Dissertation

submitted to the

Combined Faculties of the Natural Sciences and of Mathematics

of the Ruperto-Carola-University of Heidelberg, Germany

for the degree of

Doctor of Natural Sciences

Put forward by

M. A. Phys. Thomas H. Greif

born in: Munich (Germany)

Oral examination: July 23rd, 2009

The Formation of the First Galaxies

Referees: Prof. Dr. Ralf S. Klessen

Prof. Dr. Matthias Bartelmann

Zusammenfassung

Diese Arbeit befasst sich mit dem Einfluss der ersten Sterne auf die Enstehung und den Eigenschaften der ersten Galaxien. Insbesondere werden die Auswirkungen von Turbulenz, ionisierender Strahlung, Stoßwellen und chemischer Anreicherung erläutert. Aufgrund der verbesserten Empfindlichkeit der nächsten Generation von Teleskopen untersuchen wir die Rekombinationsstrahlung, Bremsstrahlung und 21 cm Emission der ersten Sterne und Galaxien. Das integrierte 21 cm Signal der ersten H II Regionen könnte mit dem geplanten SKA entschlüsselt werden, wohingegen die Rekombinationsstrahlung der ersten Sternpopulationen mithilfe von *JWST* gesehen werden könnte. Diese Beobachtungen sind ein wichtiger Schritt um die Strukturentstehung im frühen Universum besser zu verstehen.

Abstract

The primary concern of this thesis is to understand the formation and properties of the first galaxies, as well as the influence of the first stars in terms of radiative, mechanical and chemical feedback. In particular, we elucidate the role of turbulence, ionizing radiation by massive Population III stars, mechanical feedback by highly energetic supernovae, and chemical enrichment. In light of the next generation of ground- and space based telescopes, we derive their observational signature in terms of recombination radiation, bremsstrahlung and 21 cm emission. We find that the cumulative 21 cm signal of the first H II regions will likely be observable by the planned SKA, while the recombination radiation from the first starbursts might be observable by *JWST*. These probes are essential to test the theoretical framework of the first stars and galaxies and shed some light on this elusive period of cosmic history.

Dedicated to my family

Contents

Publications

The results presented in this thesis have been published in the following papers:

1. *The observational signature of the first H* II *regions*, Greif, T. H., Johnson, J. L., Klessen, R. S., Bromm, V., 2009, MNRAS, submitted (arXiv:0905.1717)

2. *The first galaxies: signatures of the initial starburst*, Johnson, J. L., Greif, T. H., Bromm, V., Klessen, R. S., Ippolito, J., 2009, MNRAS, submitted (arXiv:0902.3263)

3. *Chemical mixing in smoothed particle hydrodynamics simulations*, Greif, T. H., Glover, S. C. O., Bromm, V., Klessen, R. S., 2009, MNRAS, 392, 1381

4. *The first galaxies: assembly, cooling and the onset of turbulence*, Greif, T. H., Johnson, J. L., Klessen, R. S., Bromm, V., 2008, MNRAS, 387, 1021

5. *The First Supernova Explosions: Energetics, Feedback, and Chemical Enrichment*, Greif, T. H., Johnson, J. L., Bromm, V., Klessen, R. S., 2007, ApJ, 670, 1

6. *Local Radiative Feedback in the Formation of the First Protogalaxies*, Johnson, J. L., Greif, T. H., Bromm, V., 2007, ApJ, 665, 85

1

Introduction

This thesis is concerned with the formation and properties of the first stars and galaxies, their observational signature, and their feedback on the intergalactic medium (IGM). With the introduction of the Λ cold dark matter (ΛCDM) model, the first stars, termed Population III (Pop III), are predicted to have formed at redshifts $z \sim 20$ in 10^5 – 10^6 $M_\odot$ 'minihalos' (Barkana & Loeb, 2001; Bromm & Larson, 2004; Fuller & Couchman, 2000; Glover, 2005; Haiman et al., 1996b). These first bound objects formed after fluctuations in the dark matter density became large enough to decouple from the Hubble flow and collapse (Couchman & Rees, 1986). Understanding the origin and evolution of these perturbations has been one of the main goals in modern cosmology, following the discovery of large-scale anisotropies in the Cosmic Microwave Background (CMB) by the *Cosmic Background Explorer (COBE)*, and the analysis of these fluctuations by the *Wilkinson Microwave Anisotropy Probe (WMAP)* (Komatsu et al., 2009). Theoretical work over the last few decades has revealed that these perturbations can be attributed to quantum fluctuations in the initially extremely homogeneous fireball. Subsequently, they experienced a period of linear growth after passing through the epochs of inflation, matter-radiation-equality, and recombination. When the Universe was merely one per cent of its present size, previously independent modes coupled and structure formation left the linear regime (Couchman & Rees, 1986). At this highly interesting epoch of cosmic history, numerical simulations have become invaluable. Especially the last decade has brought a wealth of new insights, with the consensus that the first stars were typically two orders of magnitude more massive than present-day stars (Abel et al., 2000, 2002; Bromm et al., 1999, 2002; Yoshida et al., 2003a, 2008, 2006). Subsequent work focused on their radiative, mechanical and chemical feedback (Abel et al., 2007; Glover &

Brand, 2001; Greif et al., 2007; Johnson et al., 2007; Whalen et al., 2004; Wise & Abel, 2008b; Yoshida et al., 2007a), and on the formation of the first galaxies (Greif et al., 2008; Ricotti et al., 2002a; Wise & Abel, 2007a; Yoshida, 2006). These more massive systems formed at redshifts $z \sim 10$ in $\gtrsim 10^8$ $M_\odot$ halos and relied on atomic instead of molecular hydrogen cooling. A key motivation behind this development is their potential observability by the next generation of ground- and space-based instruments, such as the *James Webb Space Telescope (JWST)* and the Square Kilometer Array (SKA). In this thesis, we investigate the various feedback effects exerted by the first stars on the IGM, as well as their influence on the formation of first galaxies. Furthermore, we determine the observational signature of the first stars in terms of recombination radiation, as well as the radio background produced by bremsstrahlung and 21 cm emission. These investigations are essential in light of the numerous missions planned for the next decade, with the goal of understanding the formation of the first stars and galaxies at the end of the cosmic dark ages.

The organization of this thesis is as follows: In Chapter 2, we discuss the evolution of fluctuations from inflation to the onset of non-linearity, including the formation of the first stars. This chapter is based on Dodelson (2003), which we refer to for a more detailed account of structure formation. In Chapter 3, we concentrate on the formation and properties of the first galaxies, followed by a treatment of radiative feedback by Pop III stars in minihalos (Chapter 4), their observational signatures (Chapter 5), and the visibility and characteristics of entire starbursts (Chapter 6). Subsequently, we discuss the dynamical evolution and feedback of high-redshift supernovae (Chapter 7), and introduce a new algorithm for smoothed particle hydrodynamics (SPH) simulations for chemical mixing (Chapter 8). Finally, in Chapter 9 we give an outlook on future work. For consistency, all quoted distances are physical, unless noted otherwise.

2

From Primordial Fluctuations to the Formation of the First Stars

Understanding the evolution of perturbations from the epoch of inflation to the formation of the first structures is one of the most important issues in modern cosmology. After *COBE* found the CMB to be isotropic over all angular scales to one part in 10^5, and *WMAP* revealed the detailed distribution of these inhomogeneities, theory evolved rapidly to interpret these perturbations. In the following, we discuss first-order perturbation theory with respect to the relevant species and derive the equations governing the evolution of fluctuations. We then construct the dark matter power spectrum and briefly discuss the formation of the first stars.

2.1 The Background Universe

The Friedmann-Robertson-Walker (FRW) metric describes a homogeneous, isotropic, and flat universe, with the non-negative components of the metric given by:

$$g_{00} = -1 \tag{2.1}$$

$$g_{ii} = a^2 , \tag{2.2}$$

where a is the scale factor, and the speed of light, c, has been set to unity (we will maintain this convention throughout this chapter). The Einstein equations couple the metric to the

total energy content of the universe, resulting in the Friedmann equation:

$$H^2 = \frac{8\pi G}{3}\rho \,, \tag{2.3}$$

where G is the gravitational constant, $H = \dot{a}/a$ is the Hubble expansion rate (the overdot denotes derivative with respect to time, t), and ρ is the sum of all contributions to the energy density, i.e. matter, radiation, and a cosmological constant. We obtain an additional equation relating ρ and a by demanding that the divergence of the stress-energy tensor vanishes:

$$\frac{\partial \rho}{\partial t} = -3H\left(\rho + P\right) \,, \tag{2.4}$$

where P denotes the pressure. For matter, thermal pressure is negligible compared to the rest mass, so $\rho_m \propto a^{-3}$, whereas radiation pressure is important for the radiation density, yielding $\rho_r \propto a^{-4}$. The energy density and pressure of a given particle species may be derived directly from the distribution function f:

$$\rho = \frac{g}{(2\pi)^3}\int E(p) f\left(\mathbf{x},\mathbf{p}\right) \mathrm{d}^3 p \tag{2.5}$$

$$P = \frac{g}{(2\pi)^3}\int \frac{p^2}{3E(p)} f\left(\mathbf{x},\mathbf{p}\right) \mathrm{d}^3 p \,, \tag{2.6}$$

where g denotes the degeneracy, $\mathbf{x}$ the spatial coordinate (with absolute value x), E the energy, $\mathbf{p}$ the momentum vector (with absolute value p), and $\hbar$ has been set to unity. The distribution function plays an important role for the evolution of perturbations in the early Universe.

2.2 The Boltzmann Equation

A description of the interactions of particles in thermal, but not chemical equilibrium, requires the Boltzmann equation, which models the change in abundance of a certain species due to collisions with other particles:

$$\frac{\mathrm{d}f}{\mathrm{d}t} = C[f] \,, \tag{2.7}$$

where the total change of f is determined by the collisional term $C[f]$. This term is a complicated function of the abundances of all four species participating in the reaction, given by:

$$\begin{aligned} C[f_1(\mathbf{p}_1)] \;=\; & \frac{1}{p}\int \frac{\mathrm{d}^3 p_2}{(2\pi)^3\, 2E_2}\int \frac{\mathrm{d}^3 p_3}{(2\pi)^3\, 2E_3}\int \frac{\mathrm{d}^3 p_4}{(2\pi)^3\, 2E_4} \\ & \times (2\pi)^4\, \delta^3(\mathbf{p}_1+\mathbf{p}_2-\mathbf{p}_3-\mathbf{p}_4)\, \delta(E_1+E_2-E_3-E_4) \\ & \times |M|^2 \left(f_3(\mathbf{p}_3) f_4(\mathbf{p}_4) - f_1(\mathbf{p}_1) f_2(\mathbf{p}_2)\right) \,. \end{aligned} \tag{2.8}$$

The first line integrates the spacial momentum of the phase-space distribution for each interacting particle, excluding the particle of interest. They should actually be over the individual four-momenta, yet a transformation yields factors $1/2E$, leaving only the spatial momenta. The second line is relatively straightforward and applies conservation of energy and momentum based on the Dirac delta function. The third line contains the amplitude of the reaction, denoted by $|M|^2$, whereas the products of the distribution functions represent the change in $f_1(\mathbf{p}_1)$ due to deviations from equilibrium.

Even for a single species the Boltzmann equation is quite formidable. A full treatment requires the inclusion of all four involved reaction partners, which leads to a coupled set of integro-differential equations. These may be simplified by introducing first-order perturbations to the zero-order distribution functions (i.e. Fermi-Dirac or Bose-Einstein distributions), or by simply calculating various moments of f instead of the explicit distribution.

2.3 First-Order Perturbations

2.3.1 Photons

Perhaps the most important interaction in the early universe is Compton scattering, which couples the baryonic fluid to the photon distribution. Schematically, this reaction may be written as

$$\gamma(\mathbf{p}_1) + e^-(\mathbf{p}_2) \leftrightarrow \gamma(\mathbf{p}_3) + e^-(\mathbf{p}_4)\,, \tag{2.9}$$

where γ and e^- denote photons and electrons, respectively. The photon distribution function f_r may be written as a slightly modified Bose-Einstein distribution:

$$\frac{1}{f_r} = \exp\left(\frac{p}{T\left(1+\Theta\left(\mathbf{x},\hat{p},t\right)\right)}\right) - 1 \,, \tag{2.10}$$

where the first-order perturbation $\Theta\left(\mathbf{x},\hat{p},t\right)$ adopts the meaning of a deviation from the background temperature T, and $\hat{p}$ is the unit vector of the momentum. Since the perturbation is small, we may rewrite the above equation:

$$f_r \simeq f_r^{(0)} - p\frac{\partial f_r^{(0)}}{\partial p}\Theta \,, \tag{2.11}$$

where $f_r^{(0)}$ is the zero-order distribution function. Before elaborating on the collisional term, we explicitly expand the left-hand side of equation (2.7), taking into account various partial derivatives of f_r:

$$\frac{\mathrm{d}f_r}{\mathrm{d}t} = \frac{\partial f_r}{\partial t} + \frac{\partial f_r}{\partial x^i}\frac{\mathrm{d}x^i}{\mathrm{d}t} + \frac{\partial f_r}{\partial p}\frac{\mathrm{d}p}{\mathrm{d}t} + \frac{\partial f_r}{\partial \hat{p}^i}\frac{\mathrm{d}\hat{p}^i}{\mathrm{d}t} \,. \tag{2.12}$$

Since we are only interested in first order perturbations to f_r, we neglect the last term. Expressions for $\mathrm{d}x^i/\mathrm{d}t$ and $\mathrm{d}p/\mathrm{d}t$ require an introduction of perturbations $\Phi\left(\mathbf{x},t\right)$ and $\Psi\left(\mathbf{x},t\right)$ to the background metric, for which we choose conformal Newtonian gauge. In this case, Φ corresponds to the Newtonian potential, while Ψ is the perturbation to the spatial curvature:

$$g_{00} = -1 - 2\Phi \tag{2.13}$$

$$g_{ii} = a^2\left(1+2\Psi\right) \,. \tag{2.14}$$

After calculating the Christoffel Symbols and going through some tedious algebra, we find

$$\frac{\mathrm{d}f_r}{\mathrm{d}t} = \frac{\partial f_r}{\partial t} + \frac{\hat{p}^i}{a}\frac{\partial f_r}{\partial x^i} - p\frac{\partial f_r}{\partial p}\left(H + \frac{\partial \Psi}{\partial t} + \frac{\hat{p}^i}{a}\frac{\partial \Phi}{\partial x^i}\right) \,. \tag{2.15}$$

The first two terms on the right describe the continuity and Euler equations, while the third term dictates that photons lose energy in an expanding universe. The last two terms govern the effects of over- and under-dense regions on the photon distribution function.

Inserting the zero-order Bose-Einstein distribution function into equation (2.15), comparing with equation (2.7), and setting the collisional term to zero (collisions are expressed

in higher-order terms of f_r), results in the well known fact that $T \propto a^{-1}$. Inserting the first order expression for f_r into equation (2.15) yields

$$\frac{\mathrm{d}f_r}{\mathrm{d}t} = -p\frac{\partial f_r^{(0)}}{\partial p}\left(\frac{\partial \Theta}{\partial t} + \frac{\hat{p}^i}{a}\frac{\partial \Theta}{\partial x^i} + \frac{\partial \Psi}{\partial t} + \frac{\hat{p}^i}{a}\frac{\partial \Phi}{\partial x^i}\right) . \tag{2.16}$$

The next step consists of explicitly computing the collisional term for Compton scattering with equation (2.8). This includes some tedious algebra, which we do not discuss in detail. Instead, we outline some key assumptions:

- The energy of the electron consists only of its rest-mass.
- Very little energy is transferred by Compton scattering, greatly simplifying some terms.
- Second-order terms may be neglected.
- The amplitude of the reaction is taken to be constant, i.e. $|M|^2 = 8\pi\sigma_\mathrm{T} m_e^2$, where σ_T is the Thompson cross section and m_e the mass of the electron. Consequently, we neglect a contribution from the quadrupole moment of Θ and the polarization state. Both assumptions do not result in large dicrepancies for the purpose of determining the matter power spectrum.

With these approximations, the final expression for the collisional term is given by

$$C[f_r] = -p\frac{\partial f_r^{(0)}}{\partial p} n_e \sigma_\mathrm{T} \left(\Theta_0 - \Theta + \hat{p}\mathbf{v}_b\right) , \tag{2.17}$$

where n_e is the electron density, $\mathbf{v}_b$ the bulk velocity of the baryons, and Θ_0 the zeroth moment of Θ, i.e. $\Theta_0 = (1/4\pi)\int \Theta \,\mathrm{d}\Omega$. In the absence of bulk velocities, Θ is driven towards the value for the zeroth moment. Comparing equations (2.16) and (2.17) by means of equation (2.7), and applying a Fourier transformation to Θ, Φ, Ψ, and v_b, we finally obtain

$$\dot{\Theta} + ik\mu\Theta + \dot{\Psi} + ik\mu\Phi = -\dot{\tau}\left(\Theta_0 - \Theta + \mu v_b\right) , \tag{2.18}$$

where k is the wave number, an overdot represents a derivative with respect to conformal time η (convention from now on), μ describes the angle between $\mathbf{k}$ and $\hat{p}$, $\hat{p}\mathbf{v}_b = \mu v_b$ implies that the velocity is irrotational, and $\dot{\tau} = -n_e\sigma_\mathrm{T} a$ introduces the optical depth to Thompson scattering.

2.3.2 Dark Matter

The treatment of dark matter perturbations is fairly straightforward, since collisions may be neglected. We must therefore merely compute the left-hand side of equation (2.7). The main difference to photons is the presence of rest-mass, leading to additional velocity terms of the form p, p/E, and p^2/E in a modified version of equation (2.16):

$$\frac{\mathrm{d}f_{\mathrm{dm}}}{\mathrm{d}t} = \frac{\partial f_{\mathrm{dm}}}{\partial t} + \frac{\hat{p}^i}{a}\frac{p}{E}\frac{\partial f_{\mathrm{dm}}}{\partial x^i} - p\frac{\partial f_{\mathrm{dm}}}{\partial E}\left(H\frac{p^2}{E} + \frac{p^2}{E}\frac{\partial \Psi}{\partial t} + \frac{p\hat{p}^i}{a}\frac{\partial \Phi}{\partial x^i}\right) = 0 \,. \tag{2.19}$$

We integrate this equation over the three-momentum to extract the zeroth moment, and expand the resulting dark matter particle density to $n_{\mathrm{dm}} = n^{(0)}_{\mathrm{dm}}\,(1 + \delta\,(\mathbf{x}, t))$ around the zero-order value $n^{(0)}_{\mathrm{dm}} \propto a^{-3}$, where δ is the overdensity. This yields the first-order, Fourier-transformed equation

$$\dot{\delta} + ikv + 3\dot{\Psi} = 0 \,, \tag{2.20}$$

where the bulk dark matter velocity v is again assumed to be irrotational. This expression shows that density perturbations are sourced by bulk velocities and changes to the spatial curvature. A second equation may be obtained by multiplying equation (2.19) by $\mathbf{v}$ and integrating over the three-momentum to extract the first moment:

$$\dot{v} + Hv + ik\Phi = 0 \,, \tag{2.21}$$

showing that changes in v are generated by the Hubble flow and the Newtonian potential Φ.

2.3.3 Baryons

The tight coupling of protons and electrons by Coulomb scattering forces their overdensities and bulk velocities to common values, denoted δ_b and v_b. This allows us to concentrate on the collisional term for electrons, which is governed by Coulomb and Compton scattering. Similar to the previous section, we find

$$\dot{\delta}_b + ikv_b + 3\dot{\Psi} = 0 \,, \tag{2.22}$$

which is equivalent to equation (2.20) for dark matter density perturbations, and

$$\dot{v}_b + H v_b + ik\Phi = \dot{\tau}\frac{4\rho_r}{3\rho_b}\left(3i\Theta_1 + v_b\right) \ , \tag{2.23}$$

where ρ_r and ρ_b are the background energy density of photons and baryons, respectively, and $\Theta_1 = i/2 \int_{-1}^{1} \mu\, \Theta \, \mathrm{d}\mu$ is the first moment of Θ. Changes in the bulk velocity of the baryons are additionally sourced by the first moment of the photon distribution function. Since baryons are tightly coupled to radiation at early times, one may omit their presence without introducing significant errors to the matter power spectrum. Nevertheless, it is instructive to write down the governing equations, since an exact treatment requires their inclusion.

2.3.4 Perturbations to the Metric

In the last few sections, we have investigated the influence of perturbations to the metric on various distribution functions. To obtain the full set of equations, one must investigate how additional terms in the stress-energy tensor $T^{\mu}{}_{\nu}$, which are sourced by over- and under-densities, affect the metric itself. For this purpose we need the Einstein equations:

$$G^{\mu}{}_{\nu} = 8\pi T^{\mu}{}_{\nu} \, , \tag{2.24}$$

where $G^{\mu}{}_{\nu}$ is the Einstein tensor. Since we are mainly interested in scalar perturbations, we concentrate on the time-time component of the stress-energy tensor. After going through some tedious algebra, we obtain the first-order equation

$$G^{0}{}_{0} = -6H\frac{\partial \Psi}{\partial t} + 6H^2\Phi - 2\frac{k^2}{a^2}\Psi \ . \tag{2.25}$$

The right-hand side of equation (2.24) includes the contribution to the energy density from all species, given by

$$T^{0}{}_{0} = -\frac{G}{2}\left(\rho_{\mathrm{dm}}\delta + \rho_b\delta_b + 4\rho_r\Theta_0\right) \ . \tag{2.26}$$

Combining the above equations, we find

$$k^2\Psi + 3H\left(\dot{\Psi} - H\Phi\right) = 4\pi G a^2\left(\rho_{\mathrm{dm}}\delta + \rho_b\delta_b + 4\rho_r\Theta_0\right) \ . \tag{2.27}$$

In the absence of expansion this reduces to the well-known Poisson equation for gravity. One may extract a separate equation for anisotropic stresses by determing the spatial components of the Einstein tensor, yet they turn out to be negligible, implying that $\Psi = -\Phi$. Furthermore, the decomposition theorem shows that vector perturbations (topological defects) and tensor perturbations (gravity waves) to the metric are not sourced by first-oder perturbations to the time-time component of the stress-energy tensor. We therefore only discuss the linear perturbations quoted in equations (2.13) and (2.14).

2.4 Initial Conditions

The theory of inflation predicts the exponential growth of the scale factor over a brief period of time, caused by an almost time-invariant scalar field ϕ. Quantum-mechanical fluctuations in this field oscillate with zero mean, but non-zero root-mean-square (RMS). Modes smaller than the horizon decay $\propto \eta$, while those larger than the horizon maintain their amplitude. As inflation progresses, smaller and smaller modes exit the horizon, which gives the primordial power spectrum its characteristic shape:

$$P_\phi = \frac{H^2}{2k^3} \, . \tag{2.28}$$

Since perturbations to the spatial curvature couple directly to perturbations in the scalar field, the primordial power spectrum of Φ is given by

$$P_{\Phi_p} = \frac{8\pi G H^2}{9\epsilon k^3} \, , \tag{2.29}$$

evaluated at $aH = k$ and where ϵ describes the rate of change of the scalar field. To quantify deviations from scale invariance, the power spectrum is usually rescaled to

$$P_{\Phi_p} = \frac{50\pi^2}{9k^3}\delta_{\mathrm{H}}^2 \left(\frac{k}{H_0}\right)^{n-1} \left(\frac{\Omega_m}{D\,(a=1)}\right)^2 \, , \tag{2.30}$$

where δ_{H} is the amplitude at Horizon crossing, H_0 the present Hubble rate, n the spectral index (describes deviations from scale-invariance), Ω_m the matter density today, and D the growth function (will be defined in the next section). At the end of inflation, radiation dominates the energy content of the Universe, marking the epoch when inhomogeneities in the

matter density begin to grow. In the following, we discuss how the primordial power spectrum generates these fluctuations, and construct the resulting matter power spectrum.

2.5 The Power Spectrum

For simplicity, we constuct the matter power spectrum P_δ for a universe dominated by dark matter, setting $\rho_{\mathrm{dm}} = \rho_m = \rho_c$, where ρ_c is the critical density of the Universe. We will discuss the resulting minor inaccuracies at the end of this section. Using Poisson's equation, we relate the fluctuation power δ to the the fluctuation power of Φ when radiation no longer dominates:

$$P_\delta = \frac{4k^4a^2}{9\Omega_m^2 H_0^4} P_\Phi \,. \tag{2.31}$$

We then split $\Phi(k, a)$ into a transfer function $T(k)$, which depicts the change in amplitude of each mode through horizon-crossing and matter-radiation equality a_{eq}, and a growth function $D(a)$, which describes the scale-invariant growth after these epochs, yielding

$$\Phi(k, a) = \frac{9}{10}\Phi_p(k)T(k)\frac{D(a)}{a} \,, \tag{2.32}$$

where the factor $9/10$ accounts for the fact that even the largest scales are marginally damped through matter-radiation equality. Inserting the RMS of equation (2.32) into equation (2.31), and using the primordial power spectrum, we obtain the matter power spectrum

$$P_\delta = 2\pi^2\delta_{\mathrm{H}}^2 \frac{k^n}{H_0^{n+3}} T^2(k) \left(\frac{D_1(a)}{D_1(a=1)}\right)^2 \,. \tag{2.33}$$

To obtain the transfer function, we must follow the growth of matter perturbations through horizon crossing and a_{eq}, using the Boltzmann equations. Fortunately, this problem may be decomposed: scales that cross the horizon after a_{eq} grow $\propto a$ (independently of k), leading to $T(k) = 1$, while sub-horizon modes are significantly damped as radiation pressure washes out perturbations. In the following, we determine the damping term in detail.

In a first step, we neglect the influence of matter over- and under-densities on the potential, which is initially dominated by radiative perturbations. Higher moments of Θ are suppressed at early times, so we may concentrate on the first two moments of equation (2.18),

resulting in

$$\dot{\Theta}_0 + k\Theta_1 = -\dot{\Phi} \tag{2.34}$$

and

$$\dot{\Theta}_1 - \frac{k}{3}\Theta_0 = -\frac{k}{3}\Phi \,. \tag{2.35}$$

Together with equation (2.27) this leads to a second-order differential equation for Φ:

$$\ddot{\Phi} + \frac{4}{\eta}\dot{\Phi} + \frac{k^2}{3}\Phi = 0 \,. \tag{2.36}$$

which may be solved by the second spherical Bessel function

$$\Phi = 3\Phi_p \left(\frac{\sin b - b\cos b}{b^3} \right) , \tag{2.37}$$

where $b = k\eta/\sqrt{3}$. Evidently, the overall amplitude of Φ decays $\propto \eta^{-2}$ once it enters the horizon. From this we may now determine the evolution of δ using equation (2.20), resulting in

$$\ddot{\delta} + \frac{1}{\eta}\dot{\delta} = -3\ddot{\Phi} + k^2\Phi - \frac{3}{\eta}\dot{\Phi} \,. \tag{2.38}$$

With Green's function, the solution is approximately given by

$$\delta = 9\Phi_p \ln\left(\frac{3k\eta}{5}\right). \tag{2.39}$$

Thus, even though the gravitational potential decays, matter fluctuations still grow $\propto \ln(k\eta)$. This solution holds deep in the radiation era, yet around $a_{\rm eq}$ even small perturbations in δ begin to dominate the potential, and one must include equation (2.27) next to equations (2.20) and (2.21):

$$\delta' + \frac{ikv}{aHy} = -3\Phi' \,, \tag{2.40}$$

$$v' + \frac{v}{y} = \frac{ik\Phi}{aHy} \,, \tag{2.41}$$

$$k^2\Phi = \frac{3y}{2\,(y+1)} a^2 H^2 \delta \,, \tag{2.42}$$

where a prime denotes the derivative with respect to y, and $y = a/a_{\rm eq}$. Terms $\propto \rho_r\Theta_0$ as well as H have been dropped, since $aH/k \ll 1$. Combining the above, we obtain an equation for

the evolution of δ once the Universe becomes matter-dominated:

$$\delta'' + \frac{2+3y}{2y\,(y+1)}\delta' - \frac{3}{2y\,(y+1)}\delta = 0\ . \tag{2.43}$$

The solution to this equation is given by

$$\delta = C\,(y + 2/3)\ , \tag{2.44}$$

where C is a constant. Evidently, δ grows $\propto a$ after a_{eq}, proving the inital definition of the power spectrum useful. For the complete expression, we patch the individual solutions for δ before and after a_{eq} together, yielding the integration constant C. Comparing the resulting formula for δ with equation (2.33), we finally obtain

$$T(k) = \frac{12k_{\mathrm{eq}}^2}{k^2}\ln\left(\frac{k}{8k_{\mathrm{eq}}}\right), \tag{2.45}$$

where $k_{\mathrm{eq}} = H_0\sqrt{2/a_{\mathrm{eq}}}$.

In the presence of dark energy, the Boltzmann equations slightly change and the growth factor becomes a more complicated function:

$$D(a) = \frac{5\Omega_m H}{2H_0}\int_0^a \frac{da'}{(a'H'/H_0)^3}\ , \tag{2.46}$$

where the prime now simply denotes the integration variable. For higher accuracy, one must also account for the presence of baryons and neutrinos. However, due to their small contribution to the total energy density, they only have a small effect. In the first case, the tight coupling of baryons to photons leads to a suppression of fluctuations on small scales. This imprints oscillations on the power spectrum, similar to the ones derived in equation (2.37). A comparable effect is found for massive neutrinos, wish wash out perturbations due to their ability to free-stream over large distances. Taken together, the simple analytic solution presented in equation (2.45) is accurate to $\simeq$ 20 percent, which is quite good in light of the numerous assumptions made.

2.6 The Formation of the First Stars

In the last few sections, we have derived the dark matter power spectrum that sets the overall gravitational potential. At sufficiently late times, the baryons follow this potential, at least on scales larger than the Jeans length. As the fluctuation power approaches unity, independent Fourier modes couple and numerical simulations become indispensable to accurately calculate the subsequent evolution. In a more simplified spherical model, a region collapses once a critical overdensity of $\delta_c = 1.686$ is reached. At this point it free-falls to a virialized state of high density and forms a dark matter 'halo'. The very first of these halos, termed 'minihalos', emerge at redshifts $z \lesssim 30$ with virial masses of 10^5 – 10^6 $M_\odot$ (Tegmark et al., 1997). The gas in these systems cools via molecular hydrogen to $\simeq 200$ K and becomes Jeans-unstable at a hydrogen number density of $n_H \simeq 10^4$ cm^{-3} (Abel et al., 2000, 2002; Bromm et al., 1999, 2002). Under the influence of self-gravity, the central clump then further collapses to $n_H \sim 10^{21}$ cm^{-3}, where it becomes adiabatic and forms a protostellar seed (Yoshida et al., 2008). The later evolution is not well understood, but analytical work has indicated that heavy accretion from the circumstellar disk leads to a final stellar mass of ~ 100 $M_\odot$ (McKee & Tan, 2008; Tan & McKee, 2004). This mass scale leads to short lifetimes, but high photon yields (Bromm et al., 2001b; Schaerer, 2002), as well as extreme fates in the form of black holes (BHs) or pair-instability supernovae (PISNe) (Heger et al., 2003; Heger & Woosley, 2002). A good deal of research has therefore concentrated on their feedback and influence on the formation of the first galaxies.

3

The First Galaxies: Assembly, Cooling and the Onset of Turbulence

Understanding the formation of the first stars and galaxies at the end of the cosmic dark ages is one of the most important challenges in modern cosmology (Barkana & Loeb, 2001; Bromm & Larson, 2004; Ciardi & Ferrara, 2005; Glover, 2005). In the standard ΛCDM cosmology, the first stars are predicted to have formed at $z \lesssim 30$ in DM minihalos with virial masses of 10^5 – 10^6 $M_\odot$ (Abel et al., 2000, 2002; Bromm et al., 1999, 2002; Gao et al., 2007; Nakamura & Umemura, 2001; O'Shea & Norman, 2007; Yoshida et al., 2003a, 2006). Based on molecular hydrogen cooling, the gas can cool to $\simeq$ 200 K and become Jeans-unstable once the central clump attains $\simeq 10^3$ $M_\odot$. Such high temperatures lead to efficient accretion on to the protostellar core and imply that the first stars were predominantly very massive, with $M_* \sim 100$ $M_\odot$ (Bromm & Loeb 2004; Omukai & Palla 2003; O'Shea & Norman 2007; but see McGreer & Bryan 2008; McKee & Tan 2008; Ripamonti 2007; Tan & McKee 2004).

Due to their primordial composition, massive Pop III stars have smaller radii than their present-day counterparts and their surface temperatures can exceed $\simeq 10^5$ K, resulting in high photon yields (Bromm et al., 2001b; Schaerer, 2002; Tumlinson & Shull, 2000; Tumlinson et al., 2003). Consequently, they exert strong feedback on the IGM via radiation in the LW bands, which readily destroys molecular hydrogen (Glover & Brand, 2001; Greif & Bromm, 2006; Johnson et al., 2008; Machacek et al., 2001; Mesinger et al., 2006; Omukai & Yoshii, 2003; O'Shea & Norman, 2008; Ricotti et al., 2001; Wise & Abel, 2007b), and ionizing radiation giving rise to the first H II regions (Abel et al., 2007; Ahn & Shapiro, 2007; Alvarez

et al., 2006a; Johnson et al., 2007; Kitayama et al., 2004; Susa & Umemura, 2006; Whalen et al., 2004, 2008a; Yoshida et al., 2007a). Furthermore, a yet unknown fraction of massive, metal-free stars is expected to end in extremely violent SN explosions (Heger et al., 2003; Heger & Woosley, 2002), profoundly affecting the IGM in terms of dynamics and chemical enrichment (Bromm et al., 2003; Greif et al., 2007; Kitayama & Yoshida, 2005; Machida et al., 2005; Mackey et al., 2003; Norman et al., 2004; Salvaterra et al., 2004; Whalen et al., 2008b; Yoshida et al., 2004). Since primordial star formation initially occurs in minihalos that constitute the progenitors of the first galaxies, stellar feedback is expected to play an important role during their assembly.

When and where did the first galaxies form? According to the bottom-up character of structure formation, as described by standard Press-Schechter theory (Press & Schechter, 1974), the first $\gtrsim 5 \times 10^7$ $M_\odot$ halos assembled at $z \gtrsim 10$ via hierarchical merging. This mass scale is set by the onset of atomic hydrogen cooling once the virial temperature exceeds $\simeq 10^4$ K; these objects have therefore frequently been termed 'atomic cooling halos'. Henceforth, we will synonymously use the term 'first galaxy', as these halos can retain photoheated gas and therefore might, for the first time, maintain self-regulated star formation in a multi-phase, interstellar medium (Dijkstra et al., 2004; Mac Low & Ferrara, 1999; Madau et al., 2001; Mori et al., 2002; Oh & Haiman, 2002; Read et al., 2006; Ricotti et al., 2002a,b, 2008; Scannapieco et al., 2002; Thacker et al., 2002; Thoul & Weinberg, 1996; Wada & Venkatesan, 2003).

What types of stars are expected to form during the assembly of the first galaxies? Depending on the primordial initial mass function (IMF) and the strength of radiative and SN-driven feedback, the IGM could be heavily enriched with metals prior to the onset of second-generation star formation (Bromm et al., 2003; Greif et al., 2007; Wise & Abel, 2008b). The existence and precise value of a critical metallicity for the transition to Pop II are still vigorously debated, and has originally been discussed in the context of fine-structure versus dust cooling (Bromm & Loeb, 2003b; Frebel et al., 2007; Jappsen et al., 2007; Schneider et al., 2003; Smith & Sigurdsson, 2007). In the former case, critical metallicities of $Z_{\rm crit} \simeq 10^{-3.5}$ $Z_\odot$ have been found (Bromm et al., 2001a; Santoro & Shull, 2006), while in the latter case uncertainties in the dust composition and gas-phase depletion lead to a range of possible values, $10^{-6} \lesssim Z_{\rm crit} \lesssim 10^{-5}$ $Z_\odot$ (Omukai et al., 2005; Schneider et al., 2006; Tsuribe & Omukai, 2006). Somewhat transcending this debate, recent simulations have shown that a single SN explosion might enrich the local IGM to well above any critical metallicity (Bromm et al.,

2003; Greif et al., 2007; Wise & Abel, 2008b), forcing an early transition in star formation mode (Clark et al., 2008). However, if radiative feedback was sufficiently strong, the bulk of primordial star formation might have occurred in systems that cool via atomic hydrogen lines (Greif & Bromm, 2006; Johnson et al., 2008; O'Shea & Norman, 2008). In light of these uncertainties, we investigate the formation of a first galaxy in the limiting case of no feedback, allowing us to focus on the chemistry, cooling and development of turbulence during the assembly of the atomic cooling halo.

Theoretical investigations have recently pointed towards the existence of two physically distinct populations of metal-free stars (Johnson & Bromm, 2006; Mackey et al., 2003; Uehara & Inutsuka, 2000). Gas cooling primarily via molecular hydrogen leads to the formation of $\gtrsim$ 100 $M_\odot$ stars, termed Pop III.1, while in regions of previous ionization hydrogen deuteride (HD) likely enables the formation of $\gtrsim$ 10 $M_\odot$ stars, termed Pop III.2 (Tan & McKee, 2008). This latter mode had previously been termed Pop II.5 (Greif & Bromm, 2006; Johnson & Bromm, 2006; Mackey et al., 2003). Scenarios providing a substantial degree of ionization include relic H II regions (Nagakura & Omukai, 2005), dense shells produced by energetic SN explosions (Bromm et al., 2003; Machida et al., 2005; Mackey et al., 2003; Salvaterra et al., 2004), and structure formation shocks in the virialization of the first galaxies (Greif & Bromm, 2006; Oh & Haiman, 2002). In the former case, numerical simulations have confirmed that the gas can cool to the temperature of the CMB, reducing the Jeans-mass by almost an order of magnitude compared to the truly primordial case (Johnson et al., 2007; Yoshida et al., 2007b), while we here set out to investigate the effects of partial ionization and molecule formation during the assembly of the first galaxies. One of the key questions is therefore whether the gas can cool to the CMB limit and thus enable the formation of Pop III.2 stars.

Another important aspect concerning the baryonic collapse of the first galaxies is the development of turbulence. While turbulence does not seem to play a role in minihalos, at least on scales comparable to their virial radius (Yoshida et al., 2006), turbulent motions could become important in more massive halos, where accretion of cold gas from filaments in combination with a softened equation of state drives strong shocks (Kereš et al., 2005; Sancisi et al., 2008; Wise & Abel, 2007a), possibly leading to vigorous fragmentation and the formation of the first star clusters (Clark et al., 2008). This would mark the first step towards conditions similar to present-day star formation, where supersonic turbulent velocity fields determine the fragmentation properties of the gas. In our present study, we investi-

gate the role of turbulence by analysing the velocity field and energy content of the galaxy during virialization. We then discuss the likely fragmentation properties of the gas and the consequences for second-generation star formation.

The final ingredient of early galaxy formation is the co-evolution of massive black holes (MBHs) and the surrounding stellar system, leading in extreme cases to the formation of the highest redshift quasars observed at $z \gtrsim 6$. The most sophisticated simulations of supermassive black hole (SMBH) growth to date have been conducted by Li et al. (2007), but their resolution was insufficient to trace the origin of SMBHs below $\simeq 10^5$ $M_\odot$. Such SMBHs could form via direct collapse of isothermal gas in atomic cooling halos in the presence of a strong photo-dissociating background (Begelman et al., 2006; Bromm & Loeb, 2003a; Koushiappas et al., 2004; Lodato & Natarajan, 2006; Spaans & Silk, 2006; Wise et al., 2008), or via merging and accretion of gas on to the compact remnants of Pop III stars (Islam et al., 2003; Johnson & Bromm, 2007; Madau & Rees, 2001; Pelupessy et al., 2007; Schneider et al., 2002; Volonteri et al., 2003; Volonteri & Rees, 2005; Wise et al., 2008). Here, we investigate the fate of BHs seeded by the remnants of Pop III stars and their prospect of growing into SMBHs at the centres of the first galaxies. Finally, we provide an estimate for the amplitude of ionizing and molecule-dissociating radiation emitted by the accretion disc around the central BH.

The structure of our work is as follows. In Section 3.2, we discuss the setup of the cosmological simulations, the implementation of multiple levels of refinement and our sink particle algorithm. We then describe the hierarchical assembly of the galaxy (Section 3.3), its cooling and star formation properties (Section 3.4) and the development of turbulence (Section 3.5). In Section 3.6, we discuss the growth of the BH at the centre of the galaxy, and in Section 3.7 we summarize our results and assess their implications.

3.1 Numerical Methodology

To investigate the formation of the first galaxies with adequate accuracy, our simulations must resolve substructure on small scales as well as tidal torques and global gravitational collapse on much larger scales. We capture all the relevant dynamics by performing a preliminary simulation with a coarse base resolution, but refine around the point of highest fluctuation power. This ensures that the region containing the mass of the galaxy is well resolved and that a given number of particles is distributed efficiently.

3.1.1 Initial Setup

The simulations are carried out in a cosmological box of linear size $\simeq$ 700 kpc (comoving), and are initialized at $z = 99$ according to a concordance ΛCDM cosmology with matter density $\Omega_m = 1 - \Omega_\Lambda = 0.3$, baryon density $\Omega_b = 0.04$, Hubble parameter $h = H_0/\left(100 \text{ km s}^{-1} \text{ Mpc}^{-1}\right) = 0.7$, spectral index $n_s = 1.0$, and normalization $\sigma_8 = 0.9$ (Spergel et al., 2003). Density and velocity perturbations are imprinted at recombination with a Gaussian distribution, and we apply the Zeldovich approximation to propagate the fluctuations to $z = 99$, when the simulation is started. To capture the chemical evolution of the gas, we follow the abundances of H, H^+, H^-, H_2, H_2^+, He, He^+, He^{++}, and e^-, as well as the five deuterium species D, D^+, D^-, HD and HD^+. We include all relevant cooling mechanisms, i.e. H and He atomic line cooling, bremsstrahlung, inverse Compton scattering, and collisional excitation cooling via H_2 and HD (see Johnson & Bromm, 2006).

3.1.2 Refinement and Sink Particle Formation

In a preliminary run with 64^3 particles per species (DM and gas), we locate the formation site of the first $\simeq 5 \times 10^7$ $M_\odot$ halo. This object is just massive enough to activate atomic hydrogen cooling and fulfil our prescription for a galaxy. We subsequently carry out a standard hierarchical zoom-in procedure to achieve high mass resolution inside the region destined to collapse into the galaxy (e.g. Gao et al., 2005; Navarro & White, 1994; Tormen et al., 1997). We apply three consecutive levels of refinement centred on this location, such that a single parent particle is replaced by a maximum of 512 child particles. The particle mass in the region containing the comoving volume of the galaxy with an extent of $\simeq$ 200 kpc (comoving) is $\simeq$ 100 $M_\odot$ in DM and $\simeq$ 10 $M_\odot$ in gas. This allows a baryonic resolution of $\simeq 10^3$ $M_\odot$, such that the 'loitering state' in minihalos at $T \simeq 200$ K and $n_\text{H} \simeq 10^4$ cm^{-3} is marginally resolved (Bromm et al., 2002).

To follow the growth of BHs seeded by the collapse of Pop III.1 stars in minihalos, we apply a slightly modified version of the sink particle algorithm introduced in Johnson & Bromm (2007). Specifically, we create sink particles once the density exceeds $n_\text{H} = 10^4$ cm^{-3} and immediately accrete all particles within the resolution limit of the highest-density particle, resulting in an initial sink particle mass of $\simeq 2 \times 10^3$ $M_\odot$. Further accretion is governed by the following criteria: particles must be bound ($E_\text{kin} < \left|E_\text{pot}\right|$), have a negative

divergence in velocity and fall below the Bondi radius:

$$r_{\rm B} = \frac{\mu m_{\rm H} G M_{\rm BH}}{k_{\rm B} T} \, , \tag{3.1}$$

where μ is the mean molecular weight, $M_{\rm BH}$ the mass of the black hole, and T the temperature of the gas at the location of the sink particle, determined by a mass-weighted average over all accreted particles. Typical values for the initial Bondi radius are $r_{\rm B} \simeq 5$ pc. Here, we do not model radiative feedback that would result from accretion, and we therefore overestimate the Bondi radius and consequently the growth of the BH. We further assume that BH mergers occur instantaneously once their separation falls below the resolution limit, provided that their relative velocity is smaller than the escape velocity. Our idealized treatment provides a robust upper limit on the growth rate of BHs during the assembly of the first galaxies, but a more realistic calculation including the effects of feedback will be presented in future work.

3.2 First Galaxy Assembly

Among the key questions concerning the formation of the first galaxies are the degree of complexity associated with the halo assembly process, the role of previous star formation in minihalos, the chemical and thermal evolution of infalling gas, and the development of turbulence. To answer these questions, we first discuss the gravitational evolution of the DM with a merger tree that reconstructs the mass accretion history of the resulting atomic cooling halo, and allows us to determine the maximum amount of previous star formation in its progenitor halos.

3.2.1 Atomic Cooling Criterion

Possibly the most important characteristic distinguishing the first galaxies from their lower-mass minihalo predecessors is their ability to cool via atomic hydrogen lines, which softens the equation of state at the virial radius and allows a fraction of the potential energy to be converted into kinetic energy. At high redshift, the virial temperature of a system with virial mass $M_{\rm vir}$ can be expressed as

$$T_{\rm vir} \simeq 10^4 \, {\rm K} \left(\frac{M_{\rm vir}}{5 \times 10^7 \, {\rm M}_\odot} \right)^{2/3} \left(\frac{1+z}{10} \right) \, , \tag{3.2}$$

such that a 5×10^7 $M_\odot$ halo at $z \simeq 10$ is just massive enough to fulfil the atomic cooling criterion (Oh & Haiman, 2002). Related to this, they have the ability to retain gas photoheated by hydrogen ionization (Dijkstra et al., 2004), likely allowing self-regulated star formation for the first time. Furthermore, it is often argued that star formation in atomic cooling halos provided the bulk of the photons for reionization due to efficient shielding from LW radiation (Bromm & Loeb, 2003a; Choudhury et al., 2008; Greif & Bromm, 2006; Haiman & Bryan, 2006; Wise & Abel, 2008a). They may have been the key drivers of early IGM enrichment (Madau et al., 2001), and the host systems for the formation of the first low-mass stars that can be probed in the present-day Milky Way via stellar archaeology (Frebel et al., 2007; Karlsson et al., 2008). Their formation thus marks an important milestone in cosmic history, and in light of upcoming observations it is particularly important to understand the properties of these systems.

3.2.2 Cosmological Abundance

How common are atomic cooling halos at the redshifts we consider? A frequently used tool to estimate their abundance is the Press-Schechter mass function (Press & Schechter, 1974), which provides an analytic expression for the number of DM halos per mass and comoving volume. Even though the Press-Schechter mass function is inaccurate at low redshifts compared to other analytic estimates such as the Sheth-Tormen mass function (Sheth & Tormen, 2002), it provides a good fit to numerical simulations at the early times we are interested in (Heitmann et al., 2006; Jang-Condell & Hernquist, 2001; Reed et al., 2007). In Fig. 3.1, we show the Press-Schechter mass functions for $z \simeq 30$ and 10 (solid and dotted line, respectively), while the symbols indicate the halo distribution extracted from the simulation by the group-finding algorithm HOP (Eisenstein & Hut, 1998). The simulation and the analytic estimate generally agree, although there is a large scatter due to the finite box size. Better agreement could be expected if one accounted for the fluctuation power on scales greater than the computational box (see Yoshida et al., 2003b). At redshift $z \simeq 10$, one expects to find roughly 10 atomic cooling halos per cubic Mpc (comoving), i.e. of the order of unity in our computational box of length $\simeq 700$ kpc (comoving). Indeed, in our simulation a single 5×10^7 $M_\odot$ halo forms by $z \simeq 10$.

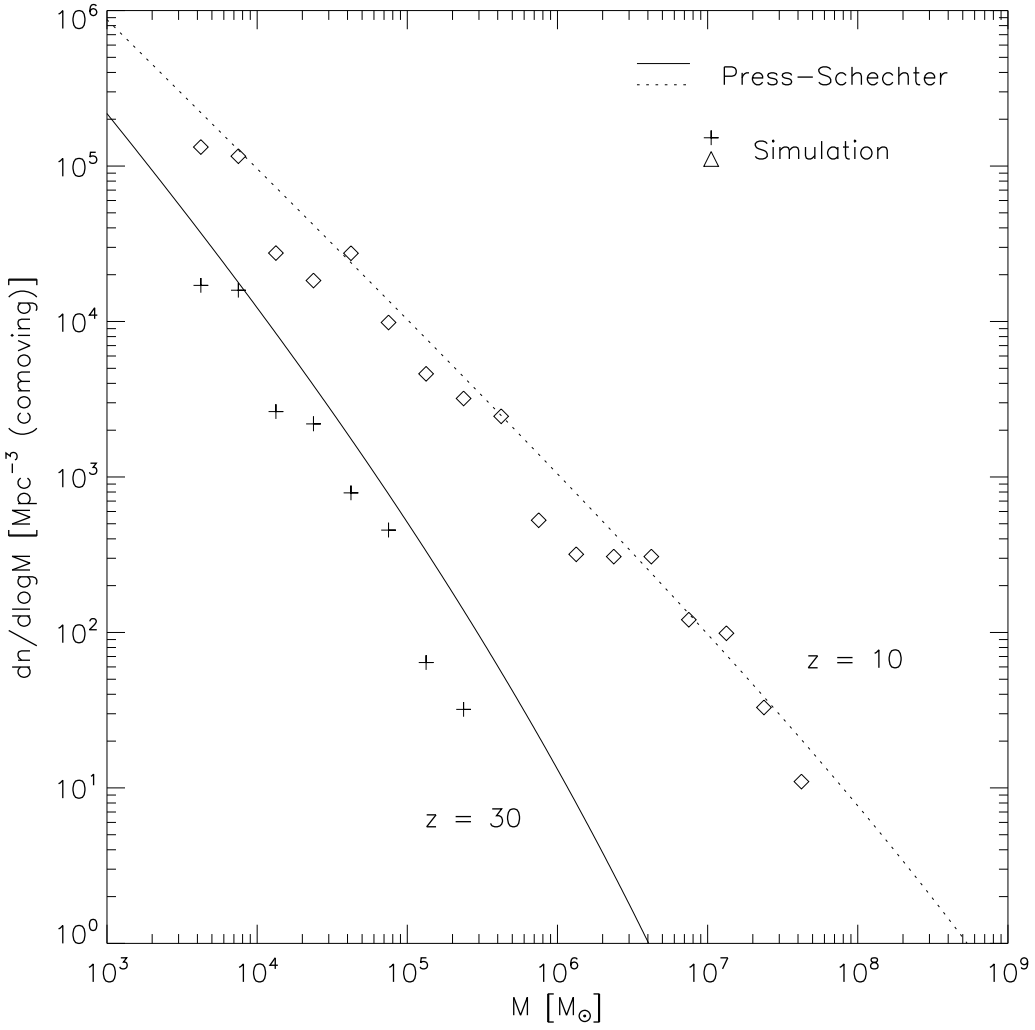

Figure 3.1: Comparison of the Press-Schechter mass function (solid and dotted line) and the simulation results (crosses and triangles) at $z \simeq 30$ (lower set) and $z \simeq 10$ (upper set). The simulation generally agrees with the analytic prediction, although there is a large scatter due to the finite box size. The expected number of atomic cooling halos per cubic Mpc (comoving) at $z \simeq 10$ is of the order of 10.

3.2.3 Assembly of Atomic Cooling Halo

In the ΛCDM paradigm, structure formation proceeds hierarchically, with small objects collapsing first and subsequently growing via merging. This behaviour eventually leads to the formation of halos massive enough to fulfil the atomic cooling criterion. In Fig. 3.2, we show the DM overdensity, gas density and temperature averaged along the line of sight at three different output times. The brightest regions in the DM distribution mark halos in virial equilibrium, according to the commonly used criterion $\rho/\bar{\rho} \simeq 178$, where ρ and $\bar{\rho}$ denote the local and background density. White crosses denote the formation sites of Pop III.1 stars in minihalos. The first star-forming minihalo at the centre of the box assembles at $z \simeq 23$ and subsequently grows into the galaxy delineated by the insets in the right panels of Fig. 3.2 and further enlarged in Figs. 3.8, 3.9, 3.10 and 3.12. Although this structure is not yet fully virialized and exhibits a number of sub-components, it has a common potential well and attracts gas from the IGM towards its centre of mass, where it is accreted by the central BH once it falls below the Bondi radius. The virial temperature of the first minihalo increases according to equation (3.2) until it reaches $\simeq 10^4$ K and atomic cooling sets in, at which point the equation of state softens and a fraction of the potential energy is converted into kinetic energy. Star formation takes place only in the most massive minihalos, with 10 Pop III.1 star formation sites residing in the volume that is destined to form the galaxy. This has important consequences for the role of stellar feedback, and will be further discussed in Section 3.4. The morphology of the galaxy can best be seen in Fig. 3.3, where we show a three-dimensional rendering of the central 150 kpc (comoving), i.e. the same field of view as in Fig. 3.2. The temperature is colour-coded such that the hottest regions with $T \simeq 10^4$ K are displayed in bright red. Here, the true spacial structure of the galaxy becomes more apparent, showing that its environment is organized into prominent filaments with a high amount of substructure. In some instances, star-forming minihalos have aligned along these filaments and will soon merge with the galaxy.

3.2.4 Merger Tree

The hierarchical assembly of the galaxy can be best described by means of a merger tree that depicts the evolution of all progenitor halos. We construct such a merger tree by tagging all DM particles that reside in the parent atomic cooling halo and track their location backwards in time. If they are part of a group at a previous timestep, they are considered to reside in

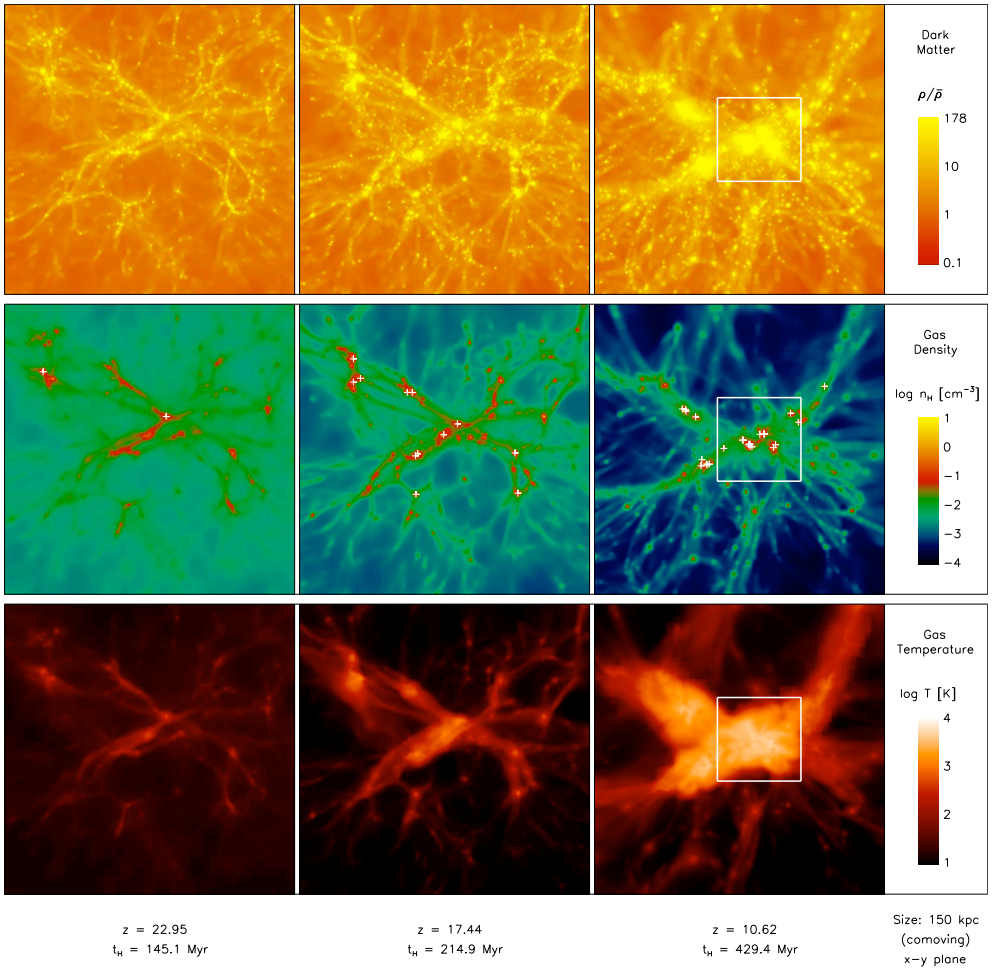

Figure 3.2: The DM overdensity, hydrogen number density and temperature averaged along the line of sight within the central $\simeq$ 150 kpc (comoving) at three different output times, from $z \simeq 23$, when the first star-forming minihalo at the centre of the box collapses, to $z \sim 10$, when the first galaxy forms. White crosses denote Pop III.1 star formation sites in minihalos, and the insets approximately delineate the boundary of the galaxy, further enlarged in Figs. 3.8, 3.9, 3.10 and 3.12. Top row: the hierarchical merging of DM halos leads to the collapse of increasingly massive structures, with the least massive progenitors forming at the resolution limit of $\simeq 10^4$ $M_\odot$ and ultimately merging into the first galaxy with $\simeq 5 \times 10^7$ $M_\odot$. The brightest regions mark halos in virial equilibrium according to the commonly used criterion $\rho/\bar{\rho} > 178$. Although the resulting galaxy is not yet fully virialized and is still broken up into a number of sub-components, it shares a common potential well and the infalling gas is attracted towards its centre of mass. Middle row: the gas generally follows the potential set by the DM, but pressure forces prevent collapse in halos below $\simeq 2 \times 10^4$ $M_\odot$ (cosmological Jeans criterion). Moreover, star formation only occurs in halos with virial masses above $\simeq 10^5$ $M_\odot$, as densities must become high enough for molecule formation and cooling. Bottom row: the virial temperature of the first star-forming minihalo gradually increases from $\simeq 10^3$ K to $\simeq 10^4$ K, at which point atomic cooling sets in.

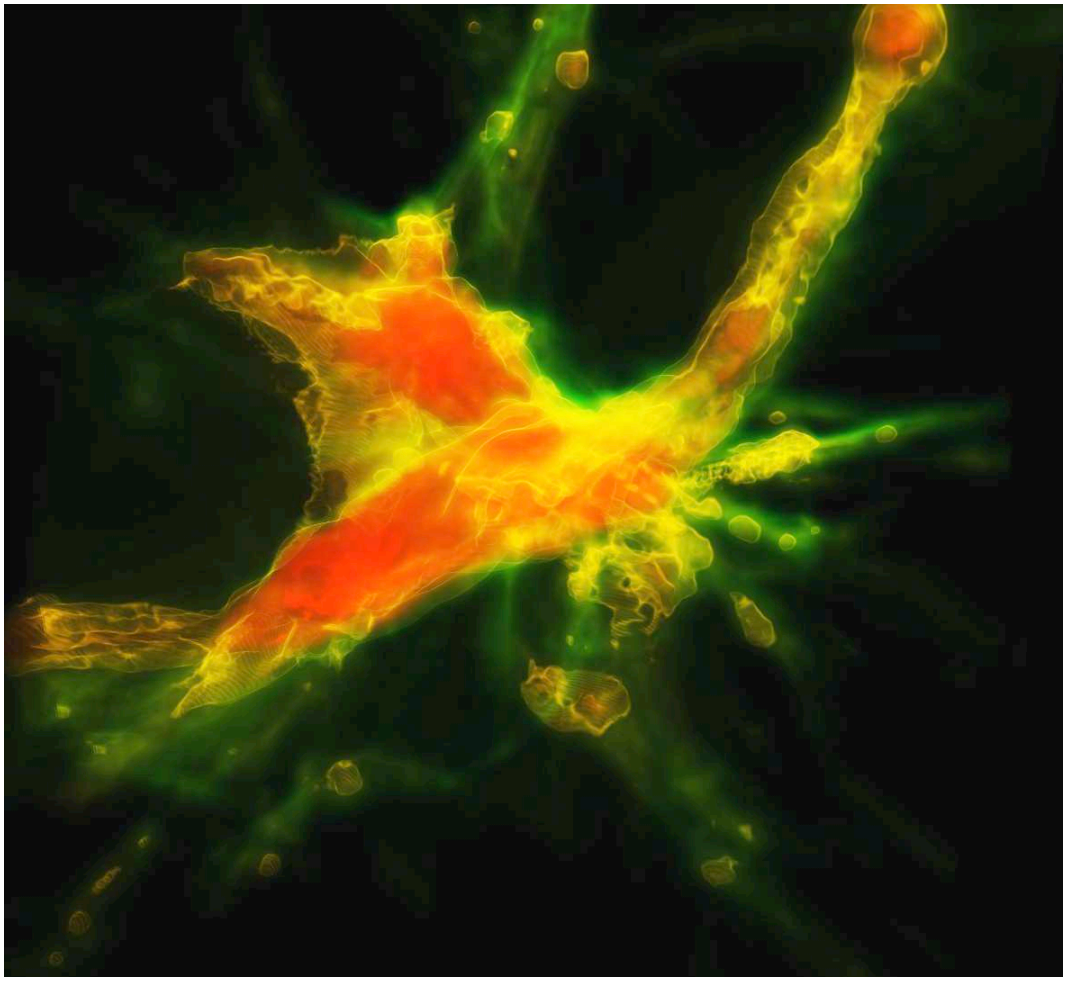

Figure 3.3: A three-dimensional rendering of the central $\simeq$ 150 kpc (comoving), showing the same field of view as in Fig. 3.2. The temperature is colour-coded such that the hottest regions with $T \simeq 10^4$ K are displayed in bright red. Here, the true spacial structure of the galaxy becomes more clear, showing that its environment is organized into prominent filaments with a high amount of substructure. In some instances, star-forming minihalos have aligned along these filaments and will soon merge with the galaxy.

a halo with mass equal to the sum of their individual masses. We repeat this process until all tagged particles are no longer part of a group or the mass falls below the resolution limit. Fig. 3.4 shows the resulting absolute and differential mass growth of the galaxy. Accretion is fuelled by minor as well as major mergers, with the latter showing the tendency to double the mass of the halo. In the course of $\simeq$ 400 Myr, the accretion rate increases from $\simeq 5 \times 10^{-3}$ $M_\odot$ yr^{-1} to $\simeq$ 0.5 $M_\odot$ yr^{-1}, but varies significantly in between due to the highly complex nature of bottom-up structure formation.

To illustrate the substantial degree of complexity involved, Fig. 3.5 shows the individual paths of all progenitor halos down to the DM resolution limit of $\simeq 10^4$ $M_\odot$. The initial widening of the tree indicates that an increasing number of minihalos collapse, while at $z \simeq 20$ merging becomes dominant and the degree of complexity decreases again. The timescale for the widening of the tree is $\simeq$ 150 Myr, while the completion of the merging process requires another $\simeq$ 250 Myr. The total number of halos above $\simeq 10^4$ $M_\odot$ that merge to form the galaxy is $\simeq$ 300. A more sophisticated analysis of the merging process is presented in Fig. 3.6, where the individual paths and masses of all progenitor halos are shown. Each line represents an individual halo, while the colour denotes its mass. The target halo seeding the first galaxy is indicated by the rightmost path. Sites of Pop III.1 star formation are denoted by star symbols, and the oval denotes the formation of the atomic cooling halo. The history of this most basic building block of galaxy formation is highly complex, further complicated by the formation of 10 Pop III.1 stars prior to its assembly. However, this is an upper limit on previous star formation activity as we do not include radiative and SN-driven feedback, which would likely reduce the net star formation rate.

The presence of DM fluctuations on mass scales below our resolution limit might imply that Pop III star formation takes place in halos with viral mass well below $\simeq 2 \times 10^4$ $M_\odot$, but pressure forces prevent gas from settling into these shallow potential wells (cosmological Jeans criterion). Moreover, gas may not be able to collapse beyond the point of virialization in $\lesssim 10^5$ $M_\odot$ halos, as temperatures and densities do not become high enough for efficient H_2 formation. Dynamical heating by mergers counteracts cooling and thus only a fraction of all minihalos will be able to form stars (Yoshida et al., 2003a). To ascertain the importance of this effect, we determine the masses of all minihalos experiencing star formation. As described in Section 3.2, the formation of a Pop III.1 star is denoted by the creation of a sink particle once the hydrogen number density exceeds $\simeq 10^4$ cm^{-3}. We implicitly assume that such a parcel of gas does not experience further subfragmentation. With this prescription,

we find the following virial masses for all star-forming minihalos shown in Fig. 3.6, from top to bottom: $M_{\rm vir} \simeq [5.8, 1.6, 7.5, 3.5, 4.3, 1.4, 3.2, 9.3, 1.4, 11.8] \times 10^5$ M$_\odot$. As expected, their masses are in the range $\simeq 10^5$ – 10^6 M$_\odot$, emphasizing the influence of dynamical heating on halos below $\simeq 10^5$ M$_\odot$. Interestingly, the fact that only a fraction of all minihalos forms stars ensures a constant inflow of cold gas into existing halos, which is crucial for the growth of the BHs at their centres.

3.3 Cooling and Star Formation

A crucial issue concerning the formation of the first galaxies is the chemical and thermal evolution of accreted gas, which ultimately determines the mode of star formation. We here briefly discuss radiative and SN-driven feedback exerted by the very first stars, followed by a discussion of the chemistry and cooling properties of an atomic cooling halo and the implications for second-generation star formation.

3.3.1 Population III.1

As shown in Section 3.3, star formation ensues in minihalos before the larger potential wells of the first galaxies assemble. This implies that radiative and SN-driven feedback influences star formation in other minihalos as well as second-generation star formation in the resulting atomic cooling halo. However, recent numerical simulations have shown that local radiative feedback via photoheating and LW radiation may not be as important as previously thought (Ahn & Shapiro, 2007; Johnson et al., 2007; Whalen et al., 2008a), and that a global LW background may only reduce the number of Pop III.1 stars by ~ 50 percent (Greif & Bromm, 2006; Johnson et al., 2008). An unknown fraction of these stars end their lives as energetic SNe and enrich the surrounding IGM to well above the critical metallicity (Bromm et al., 2003; Greif et al., 2007; Wise & Abel, 2008b), while others collapse directly to BHs and do not expel any metals (Heger et al., 2003; Heger & Woosley, 2002). Since the timescale for the recollapse of enriched gas is $\gtrsim 100$ Myr (Greif et al., 2007), and mixing is inefficient with respect to pre-established overdensities (Cen & Riquelme, 2008), subsequent star formation in minihalos prior to the assembly of the atomic cooling halo likely remains metal-free. It is much more difficult, however, to predict the character of star formation inside the first galaxies. In the following, we will first examine the consequences of pristine gas collapsing

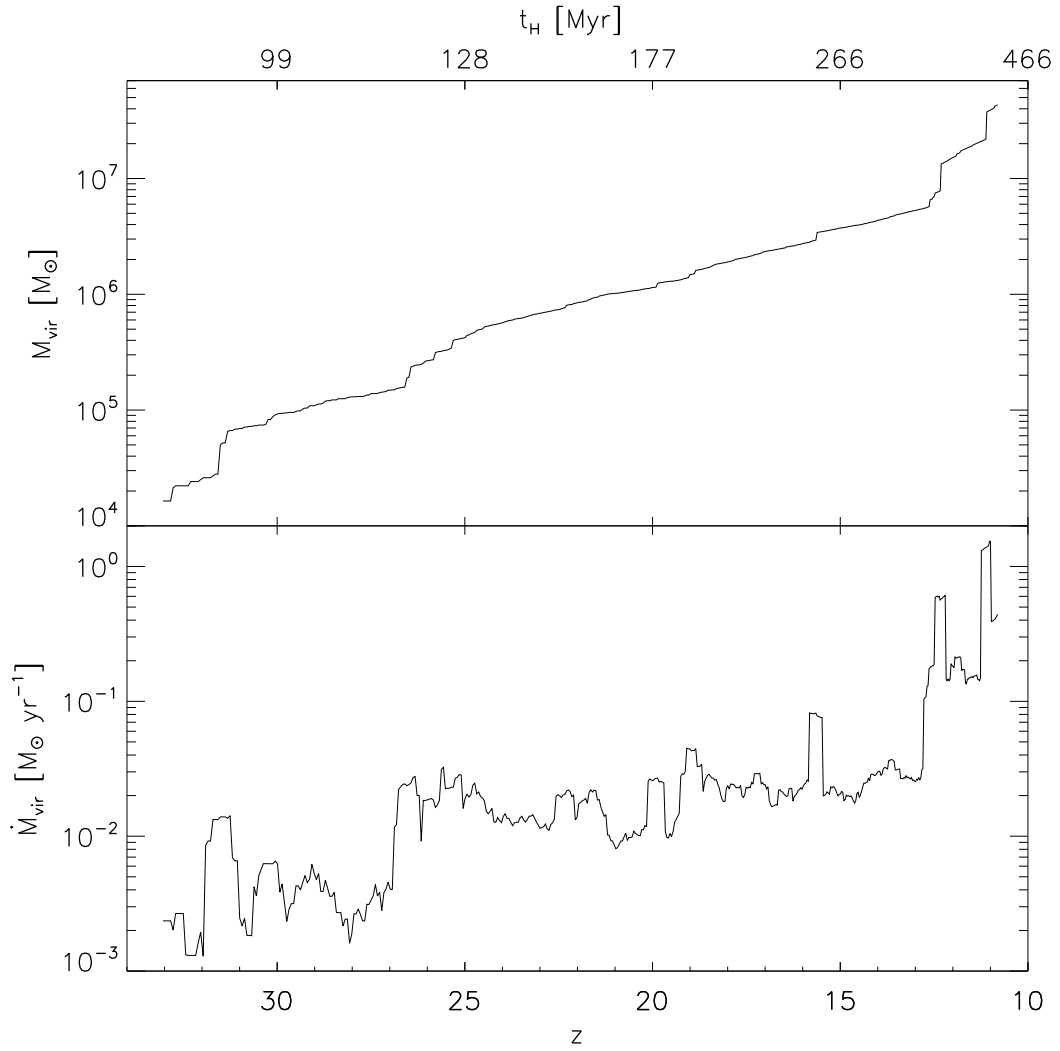

Figure 3.4: The virial mass (top panel) and accretion rate (bottom panel) of the galaxy as a function of redshift. The growth of the underlying DM halo is fuelled by minor as well as major mergers, with the latter showing the tendency to double the mass of the target halo. At $z \simeq 10$, the atomic cooling criterion is fulfilled and a galaxy is born.

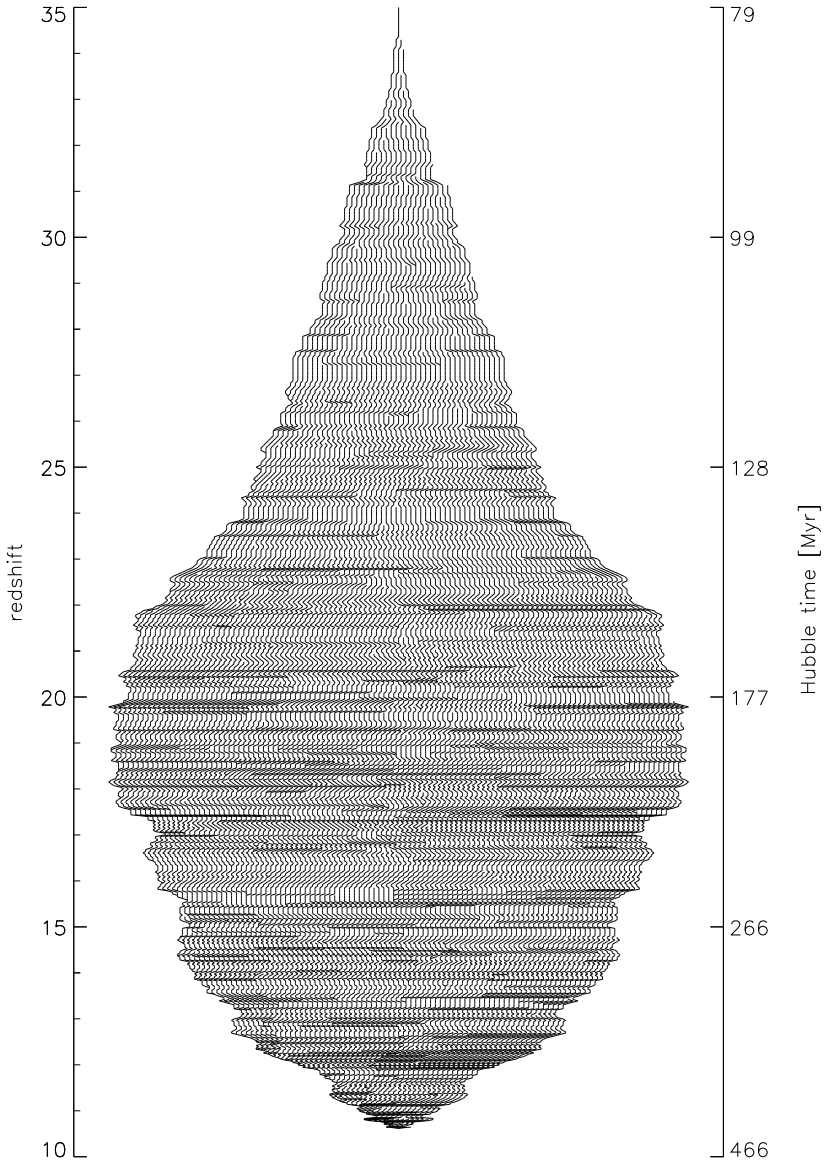

Figure 3.5: The merger tree of the galaxy, illustrating its complexity as a function of time. New branches indicate the formation of DM halos at the resolution limit of $\simeq 10^4$ $M_\odot$. The widening of the tree increases as more and more halos collapse, until merging dominates and the degree of complexity decreases again. The timescale for the former is $\simeq$ 150 Myr, while the completion of the merging process requires another $\simeq$ 250 Myr. A total of $\simeq$ 300 halos above $\simeq 10^4$ $M_\odot$ merge to form the galaxy.

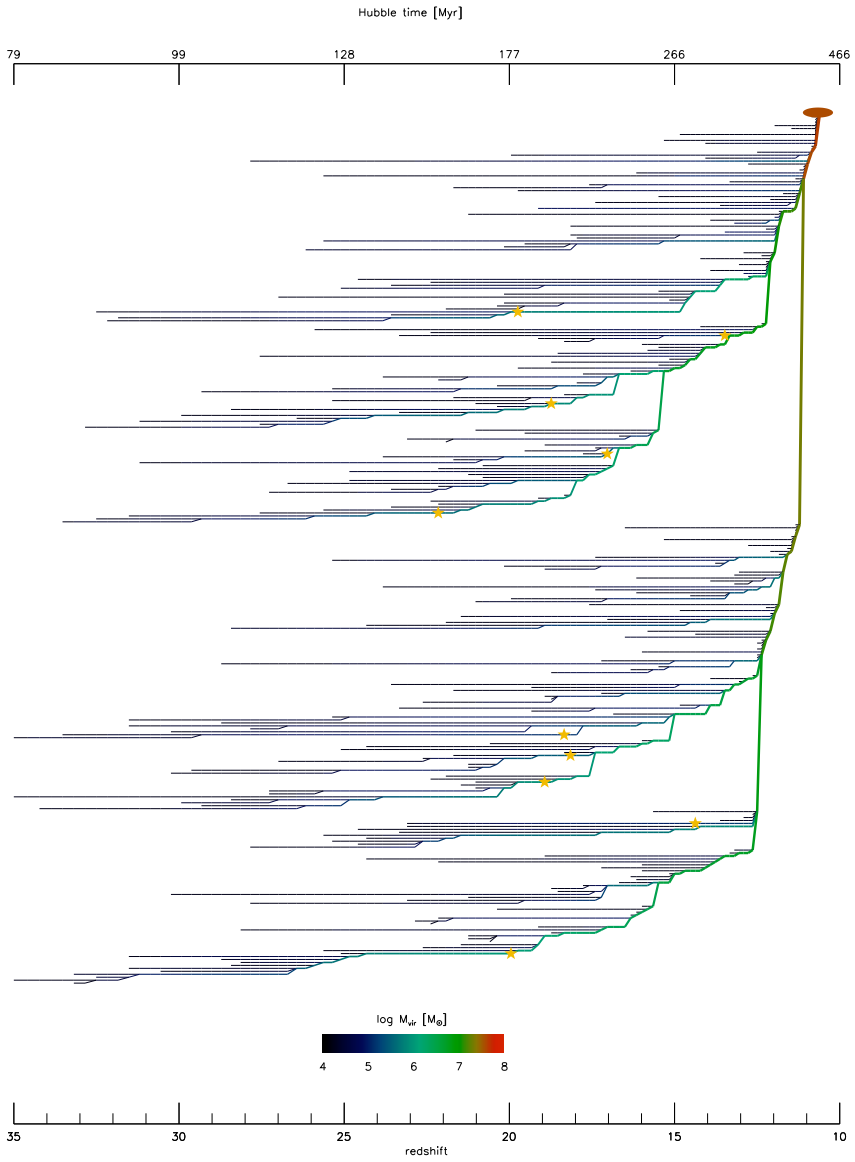

Figure 3.6: The full merger tree of the galaxy assembling at $z \simeq 10$. Each line represents an individual progenitor halo and is colour-coded according to its mass. The target halo seeding the galaxy is represented by the rightmost path, which ultimately attains $\simeq 5 \times 10^7$ $M_\odot$ and fulfils the atomic cooling criterion (denoted by the red oval). Star symbols denote the formation of Pop III.1 stars in minihalos, showing that in our specific realization 10 Pop III.1 stars form prior to the assembly of the galaxy. Only a fraction of all minihalos form stars, as dynamical heating via mergers partially offsets cooling. Depending on the detailed merger history, this ensures that star-forming minihalos are supplied with cold gas, which is crucial for the growth of the BHs at their centres.

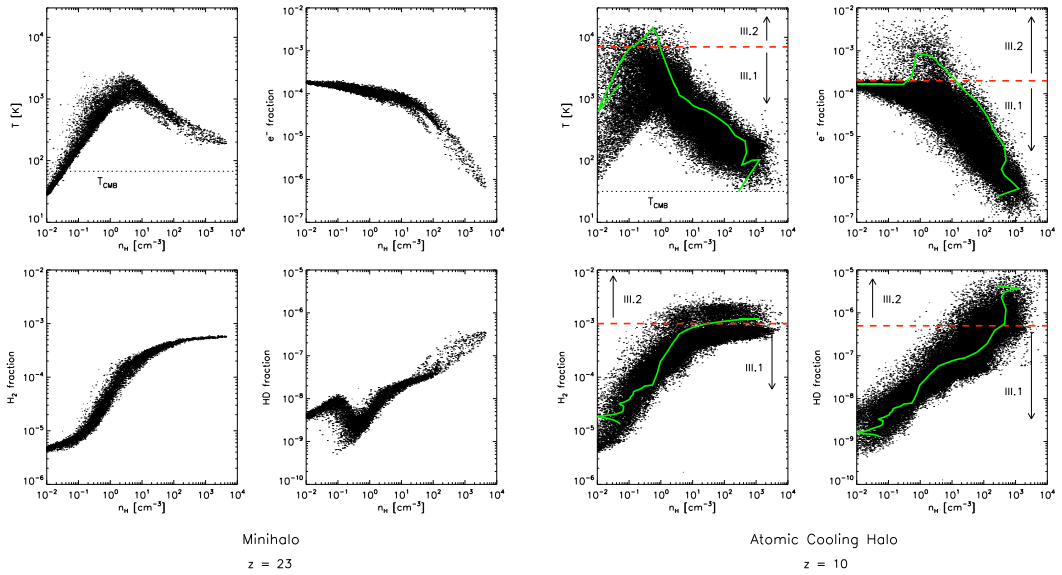

Figure 3.7: The phase-space distribution of gas inside the first star-forming minihalo (left-hand panel) and the atomic cooling halo (right-hand panel). We show the temperature, electron fraction, HD fraction and H_2 fraction as a function of hydrogen number density, clockwise from top left to bottom left. Left-hand panel: in the minihalo case, adiabatic collapse drives the temperature to $\gtrsim 10^3$ K and the density to $n_{\rm H} \gtrsim 1$ cm^{-3}, where molecule formation sets in allowing the gas to cool to $\simeq 200$ K. At this point, the central clump becomes Jeans-unstable and ultimately forms a Pop III.1 star. Right-hand panel: in the first galaxy, a second cooling channel has emerged due to an elevated electron fraction at the virial shock, which in turn enhances molecule formation and allows the gas to cool to the temperature of the CMB. The dashed red lines and arrows approximately delineate the resulting Pop III.1 and Pop III.2 channels, while the solid green lines denote the path of a representative fluid element that follows the Pop III.2 channel.

in the atomic cooling halo, and subsequently briefly address the corresponding case of pre-enriched gas.

3.3.2 Population III.2

The possible existence of a distinct population of metal-free stars in regions of previous ionization has attracted increasing attention (Greif & Bromm 2006; Johnson & Bromm 2006; Mackey et al. 2003; Tan & McKee 2008; Yoshida 2006; Yoshida et al. 2007a; but see McGreer & Bryan 2008; Ripamonti 2007). According to theory, an elevated electron fraction catalyses the formation of H_2 and HD well above the level found in minihalos and enables the gas to cool to the temperature of the CMB. This reduces the Bonnor-Ebert mass by almost an order of magnitude and likely leads to the formation of Pop III.2 stars with $\gtrsim 10\,M_\odot$ (Johnson & Bromm, 2006). Numerical simulations of star formation in relic H II regions have largely confirmed this picture (Johnson et al., 2007; Yoshida et al., 2007b), while its relevance during the virialization of the first galaxies has not yet been established (but see Greif & Bromm, 2006; Johnson et al., 2008).

The chemistry of gas contracting in an atomic cooling halo is fundamentally different from that in minihalos. The latter maintain a primordial electron fraction of $\simeq 3 \times 10^{-4}$ and form a limited amount of molecules, while the virial temperature in an atomic cooling halo exceeds $\simeq 10^4$ K and the elevated electron fraction facilitates the formation of high H_2 and HD abundances. This allows the gas to cool to the temperature of the CMB instead of the canonical $\simeq 200$ K found in minihalos. In the left panel of Fig. 3.7, we show the properties of the gas in the first star-forming minihalo at the centre of the computational box. The primordial electron fraction remains constant until densities become high enough for electron recombination. After adiabatic heating to $\gtrsim 10^3$ K, molecule formation sets in and the gas cools to $\simeq 200$ K, at which point the central clump becomes Jeans-unstable and inevitably forms a Pop III.1 star. In contrast, the right panel of Fig. 3.7 shows the density and temperature of the gas inside the atomic cooling halo. The conventional H_2 cooling channel is still visible, but a second path from low to high density has emerged, enabled by an elevated electron fraction at the virial shock, which in turn enhances the formation of H_2 and HD and allows the gas to cool to the temperature of the CMB. The dashed red lines and black arrows in Fig. 3.7 approximately delineate both channels, showing that the electron fraction in the Pop III.2 case is elevated by an order of magnitude to $\sim 10^{-3}$, and the H_2

fraction rises to $\simeq 2 \times 10^{-3}$. As already estimated in Johnson et al. (2008), the HD fraction grows to above $\simeq 10^{-6}$.

To more clearly illustrate this point, we plot the path of a representative fluid element evolving along the Pop III.2 channel (solid green lines in Fig. 3.7). Such gas indeed cools to the CMB floor, potentially enabling the formation of Pop III.2 stars. The mass fraction entering this channel is relatively low at the time considered here since the atomic cooling threshold has just been surpassed, but should quickly rise as freshly accreted material is shock-heated to $\simeq 10^4$ K. We cannot study any possible fragmentation, since the gas rapidly falls to within the Bondi radius of the central BH, and is thus accreted by the sink particle. It will be very interesting to investigate the fragmentation of the Pop III.2 mode in future, higher-resolution simulations, in particular testing the predicted mass scale of $\gtrsim 10$ $M_\odot$ (e.g. Clark et al., 2008).

What are the implications of this result? Parcels of gas that are accreted on to the galaxy through the virial shock can cool to the temperature of the CMB and possibly become gravitationally unstable, resulting in the formation of Pop III.2 stars. Including radiative feedback from previous star formation would only strengthen this conclusion, as the degree of ionization would be increased even further (Wise & Abel, 2008b). As long as the gas collapsing into the first galaxies remains pristine, primordial star formation will therefore likely be dominated by intermediate-mass (Pop III.2) stars (Greif & Bromm, 2006). The crucial question, however, is: can the gas inside the first galaxies remain metal-free?

3.3.3 Population II

In the previous sections, we have found that of order 10 Pop III.1 stars form prior to the assembly of the atomic cooling halo. In this case it appears unlikely that all of them will collapse into BHs without any metal-enrichment (Johnson et al., 2008). Even a single SN from a massive Pop III star would already suffice to reach levels above the critical metallicity, at least on average (Bromm et al., 2003; Greif et al., 2007; Wise & Abel, 2008b). More generally, at some stage in cosmic history, there must have been a transition from primordial, high-mass star formation to the 'normal' mode that dominates today. The discovery of extremely metal-poor stars in the Galactic halo with masses below one solar mass (Beers & Christlieb, 2005; Christlieb et al., 2002; Frebel et al., 2005) indicates that this transition occurs at abundances considerably smaller than the solar value. At the extreme end, these

stars have iron abundances less than 10^{-5} times the solar value, but show significant carbon and oxygen enhancements, which could be due to unusual abundance patterns produced by enrichment from BH-forming Pop III SNe (Umeda & Nomoto, 2003), or due to mass transfer from a close binary companion, whose frequency is predicted to increase with decreasing metallicity (Lucatello et al., 2005).

Identifying the critical metallicity at which this transition occurs is subject to ongoing research. One approach is to argue that low mass star formation becomes possible only when atomic fine-structure line cooling from carbon and oxygen becomes effective (Bromm et al., 2001a; Bromm & Loeb, 2003b; Frebel et al., 2007; Santoro & Shull, 2006), setting a value for $Z_{\rm crit}$ at $\simeq 10^{-3.5}$ $Z_{\odot}$. Another possibility, first proposed by Omukai et al. (2005), is that low mass star formation is a result of dust-induced fragmentation occurring at high densities, $n_{\rm H} \simeq 10^{13}$ cm^{-3}, and thus at a very late stage in the protostellar collapse. In this model, $10^{-6} \lesssim Z_{\rm crit} \lesssim 10^{-5}$ $Z_{\odot}$, where much of the uncertainty in the predicted value results from uncertainties in the dust composition and the degree of gas-phase depletion (Schneider et al., 2002, 2006). Recent numerical simulations by Tsuribe & Omukai (2006) as well as Clark et al. (2008) provide support for this picture. However, the existing data of metal-poor Galactic halo stars seems to be well accommodated by the C- and O-based fine-structure model (Frebel et al., 2007).

In the present simulation, we do not follow the metallicity evolution of the infalling gas. Thus, we can only speculate about the properties of the resulting stellar population. It appears reasonable to assume that some of the accreting material is still pristine and free of metals, triggering the formation of lower-mass metal-free Pop III.2 stars. Gas that flows in at even later times may already have experienced metal enrichment from previous Pop III SNe in nearby minihalos. Because of the high level of turbulence within the virial radius at that time (see Section 3.5), the incoming new material is likely to efficiently mix with the pre-existing zero-metallicity gas and the era of Pop III star formation could come to an end. This transition possibly occurs at the same time as the onset of significant degrees of turbulence in the atomic cooling halo. We therefore speculate that some of the extremely metal-deficient stars in the halo of the Milky Way may have formed as early as redshift $z \simeq 10$ (Clark et al., 2008).

3.4 Turbulence

The development of turbulence in gas flowing into the central potential well of the halo strongly influences its fragmentation behaviour and consequently its ability to form stars. Detailed studies of the interstellar medium in the Milky Way, for instance, tell us that turbulence determines when and where star formation occurs and that it is the intricate interplay between gravity on the one hand, and turbulence, thermal pressure and magnetic fields on the other that sets the properties of young stars and star clusters (Ballesteros-Paredes et al., 2007; Larson, 2003; Mac Low & Klessen, 2004). In the context of our work, we investigate the velocity field and energy distribution that build up during the assembly of the galaxy. As opposed to cooling flows in low-mass halos, the accretion flow on to the deep central potential well of the atomic cooling halo considered here becomes highly turbulent within the virial radius.

3.4.1 The Development of Turbulence: Hot versus Cold Accretion

One of the most important consequences of atomic cooling is the softening of the equation of state below the virial radius, allowing a fraction of the potential energy to be converted into kinetic energy (Wise & Abel, 2007a). This implies that perturbations in the gravitational potential can generate turbulent motions on galactic scales, which are then transported to the centre of the galaxy (e.g. Fig. 3.8). In this context it is important to investigate the accretion of gas on to the galaxy in more detail.

In principle, there are two distinct modes of accretion. Gas accreted directly from the IGM is heated to the virial temperature and comprises the sole channel of inflow until cooling in filaments becomes important. This mode is termed hot accretion, and dominates in low-mass halos at high redshift. In the atomic cooling halo, the formation of the virial shock and the concomitant heating are visible in Fig. 3.9, where we show the hydrogen number density and temperature of the central $\simeq 40$ kpc (comoving) around the BH at the centre of the galaxy. This case also reveals a second mode, termed cold accretion. It becomes important as soon as filaments are massive enough to enable molecule reformation, which allows the gas to cool and flow into the central regions of the nascent galaxy with high velocities. In Fig. 3.9, the cold gas accreted along filaments from the left- and right-hand is clearly distinguishable from the hot gas at the virial shock. These streams are also visible in Fig. 3.10, where we

compare the radial with the tangential velocity component, and in Fig. 3.8, where we show the Mach number of infalling gas. Evidently, inflow velocities can be as high as 20 km s^{-1}, with Mach numbers of the order of 10.

In Fig. 3.11, we compare the energy distribution and mass fraction of cold (< 500 K) versus hot (> 500 K) gas in radial shells for the first star-forming minihalo just before the formation of the sink particle, and the atomic cooling halo assembling at $z \simeq 10$. The blue, green and red lines denote the azimuthally averaged ratio of radial, tangential and thermal to potential energy, respectively. The black lines show the sum of all three components, and the dotted lines indicate the ratio required for perfect virialization. In the minihalo case, the total energy is dominated by thermal energy, although its share decreases towards the centre where cooling via molecular hydrogen becomes important. The radial kinetic energy dominates over the tangential component down to $r_{\rm tan} \simeq 5$ pc, where the mass fraction of cold gas rapidly rises and the cloud becomes rotationally supported. Efficient cooling implies that the total energy drops below that required for perfect virialization.

In the atomic cooling halo, the total energy at $r_{\rm vir} \simeq 1$ kpc is dominated by bulk radial motions. The distinction between hot and cold gas in the right panels of Fig. 3.11 shows that a large fraction of the kinetic energy injected into the galaxy comes from cold gas accreted along filaments, even though its mass fraction is initially small. The energy in tangential motions begins to dominate at $r_{\rm tan} \simeq 200$ pc, showing that the radial energy of the cold gas flowing in along filaments is converted into turbulent motions. This is fundamentally different from the collapse of gas in minihalos, where the radial energy is converted into a directed rotation along a single axis. The distinct features at $r \simeq 350$ pc are caused by a subhalo that has not yet merged with the central clump (see also Figs. 3.2 and 3.3). Once again, the total energy budget falls below that required for perfect virialization, as atomic hydrogen as well as molecular cooling are able to radiate away a significant fraction of the potential energy released. We conclude that the high energy input by cold accretion is ideally suited to drive turbulence at the centre of the galaxy, where bulk radial inflows are converted into turbulent motions on small scales.

3.4.2 Shocks and Fragmentation Properties

Shock fronts can arise where supersonic flows experience sudden deceleration and, if unorganized, indicate the presence of supersonic turbulence. As discussed above, cold accretion

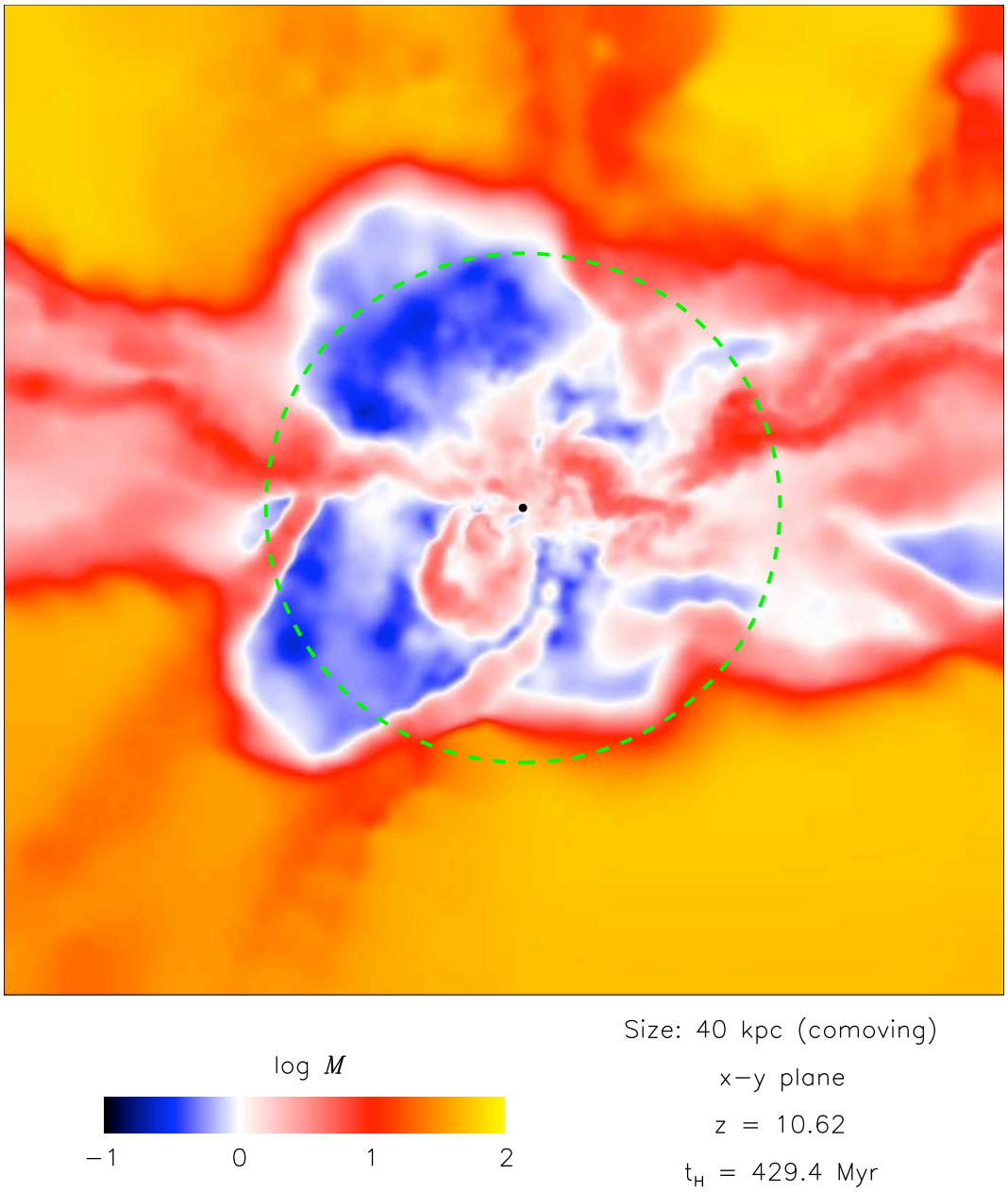

Figure 3.8: The central ≃ 40 kpc (comoving) of the computational box, roughly delineated by the insets in Fig. 3.2. Shown is the Mach number in a slice centred on the BH at the centre of the galaxy, indicated by the filled black circle. The dashed line denotes the virial radius at a distance of ≃ 1 kpc. The Mach number approaches unity at the virial shock, where gas accreted from the IGM is heated to the virial temperature over a comparatively small distance. Inflows of cold gas along filaments are supersonic by a factor of ≃ 10 and generate a high amount of turbulence at the centre of the galaxy, where typical Mach numbers are between 1 and 5.

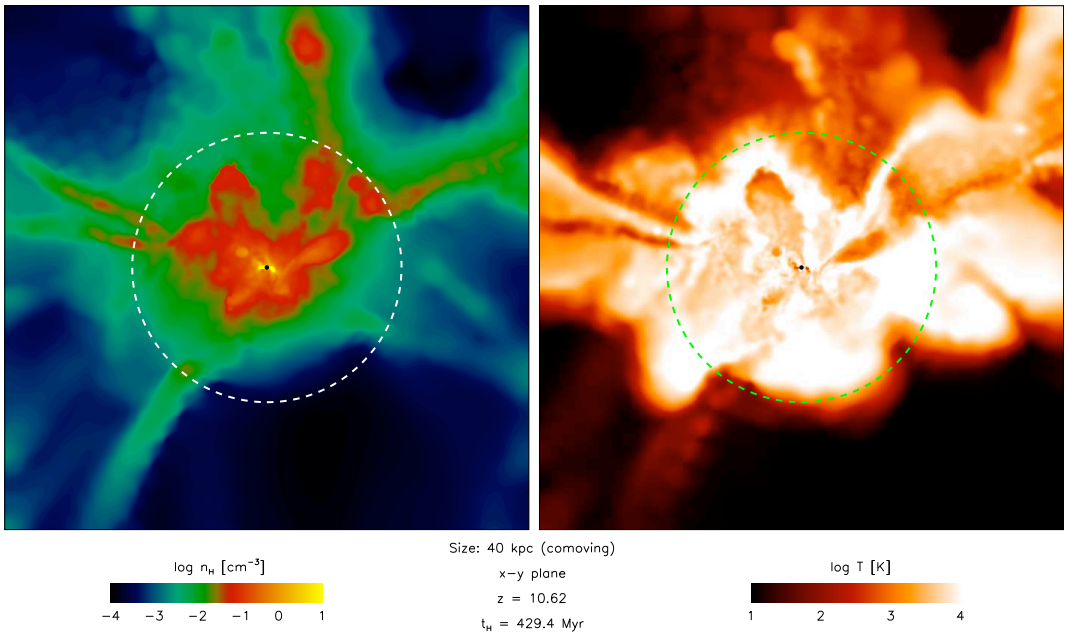

Figure 3.9: The central ≃ 40 kpc (comoving) of the computational box, roughly delineated by the insets in Fig. 3.2. Shown is the hydrogen number density (left-hand panel) and temperature (right-hand panel) in a slice centred on the BH at the centre of the galaxy, indicated by the filled black circle. The dashed lines denote the virial radius at a distance of ≃ 1 kpc. Hot accretion dominates where gas is accreted directly from the IGM and shock-heated to ≃ 10^4 K. In contrast, cold accretion becomes important as soon as gas cools in filaments and flows towards the centre of the galaxy, such as the streams coming from the left- and right-hand side. They drive a prodigious amount of turbulence and create transitory density perturbations that could in principle become Jeans-unstable. In contrast to minihalos, the initial conditions for second-generation star formation are highly complex, with turbulent velocity fields setting the fragmentation properties of the gas.

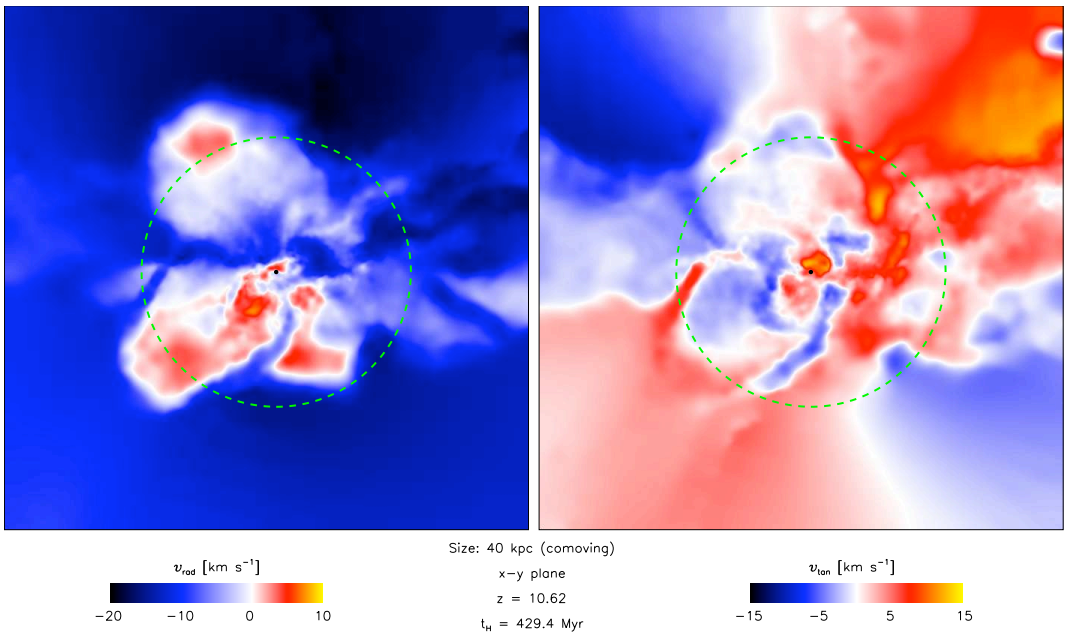

Figure 3.10: The central $\simeq$ 40 kpc (comoving) of the computational box, roughly delineated by the insets in Fig. 3.2. Shown is the radial (left-hand panel) and tangential velocity in the x-y plane (right-hand panel) in a slice centred on the BH at the centre of the galaxy, indicated by the filled black circle. The dashed lines denote the virial radius at a distance of $\simeq$ 1 kpc. Streams of cold gas from filaments, such as those coming from the left- and right-hand side, are clearly visible and can have velocities of up to 20 km s^{-1}. Some even penetrate the centre and create regions of positive radial velocities. Angular velocities are particularly high towards the centre of the galaxy, where bulk radial inflows are converted into turbulent motions on small scales. The presence of flows in both directions implies that these are unorganized instead of coherently rotating, such as is the case in minihalos (see also Fig. 3.11).

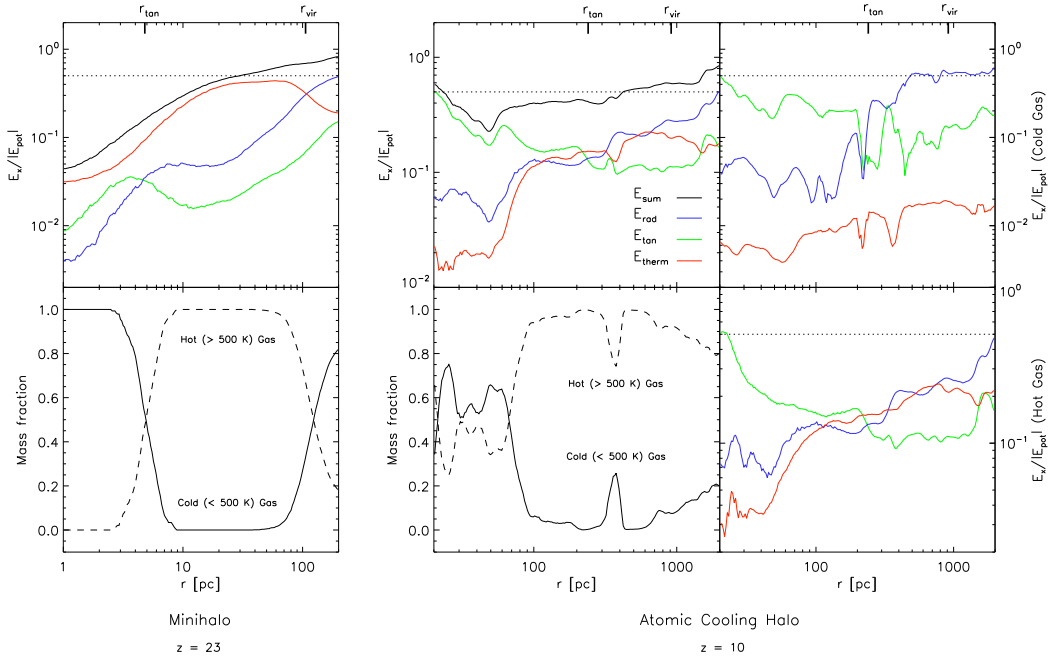

Figure 3.11: The energy distribution and mass fraction of cold (< 500 K) versus hot (> 500 K) gas in radial shells for the first star-forming minihalo just before the formation of the sink particle, and the atomic cooling halo assembling at $z \simeq 10$. The azimuthally averaged ratio of radial, tangential and thermal to potential energy are shown as blue, green and red lines, respectively. The black lines show the sum of all three components, and the dotted lines indicate the ratio required for perfect virialization. In the minihalo case, the total energy is dominated by thermal energy, although its share decreases towards the centre where cooling via molecular hydrogen becomes important. The radial kinetic energy dominates over the tangential component down to $r_{\rm tan} \simeq 5$ pc, where the mass fraction of cold gas rapidly rises and the cloud becomes rotationally supported. In the atomic cooling halo, the total energy at $r_{\rm vir} \simeq 1$ kpc is dominated by bulk radial motions. The distinction between hot and cold gas in the right panels shows that most of the kinetic energy injected into the galaxy comes from the cold gas accreted along filaments, even though its mass fraction is initially small. The tangential component begins to dominate at $r_{\rm tan} \simeq 200$ pc, where the radial flow of cold gas along filaments is converted into turbulent motions. The distinct features at $r \simeq 350$ pc are caused by a subhalo that has not yet merged with the central clump (see also Figs. 3.2 and 3.3).

is a viable agent for driving turbulence, due to the prodigious amount of momentum and kinetic energy it brings to the centre of the galaxy. In Fig. 3.12, we show the divergence and vorticity of the velocity field during the virialization of the galaxy. A comparison with Fig. 3.8 implies that there are indeed regions of supersonic flow that experience rapid deceleration and form shocks. In our case, two physically distinct mechanisms are responsible for creating these shocks. The virial shock forms where the ratio of infall velocity to local sound speed approaches unity, and is clearly visible in the left-hand panel of Fig. 3.12. The velocity divergence is negative since the gas rapidly decelerates, while the vorticity is almost negligible. In contrast, the unorganized multitude of shocks that form near the centre of the galaxy are mostly caused by accretion of cold, high-velocity gas from filaments. These are more pronounced than the virial shock and have a significantly higher angular component. They create transitory density perturbations that could in principle become Jeans-unstable and trigger the gravitational collapse of individual clumps.

How does the turbulence generated in the infalling material influence its fragmentation behaviour and control subsequent star formation? From detailed observational and theoretical studies of star formation in our Milky Way we know that turbulence plays a pivotal role in the formation of stars and star clusters. It is usually strong enough to counterbalance gravity on global scales. By the same token, however, it will usually provoke collapse locally. Turbulence establishes a complex network of interacting shocks, where regions of high density build up at the stagnation points of convergent flows. To result in the formation of stars, local collapse must progress to high enough densities on time scales shorter than the typical interval between two successive shock passages. Only then can the collapsing core decouple from the ambient flow pattern and build up a star. The accretion flow on to these objects and consequently the final stellar mass strongly depends on the properties of the surrounding turbulent flow.

In concert with the thermodynamic properties of the gas, leading to the cooling of high-density material to the CMB limit (see Section 3.4), length scale and strength of the turbulence are the most important parameters governing its fragmentation behaviour and consequently the properties of star formation, such as its timescale and overall efficiency (Klessen et al., 2000; Krumholz & McKee, 2005; Vázquez-Semadeni et al., 2003). In the atomic cooling halo discussed here, this will eventually lead to the transition to Pop II star formation. However, a quantitative understanding of the fragmentation behaviour of the turbulent gas would require dedicated high-resolution simulations, which is beyond the scope of this work.

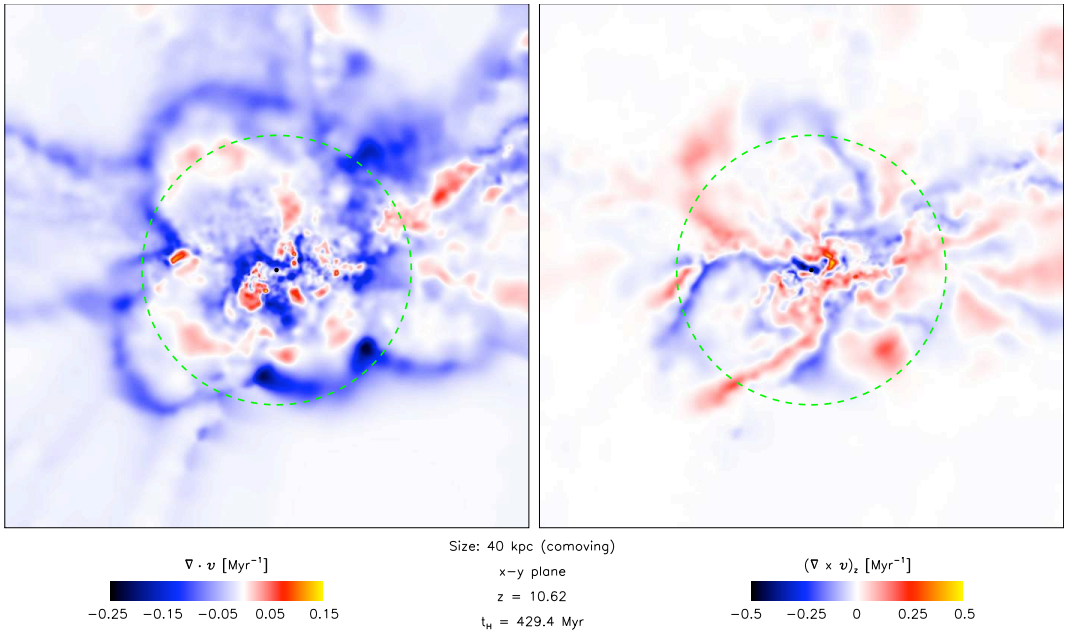

Figure 3.12: The central $\simeq$ 40 kpc (comoving) of the computational box, roughly delineated by the insets in Fig. 3.2. We show the divergence (left-hand panel) and z-component of the vorticity (right-hand panel) in a slice centred on the BH at the centre of the galaxy, indicated by the filled black circle. The dashed lines denote the virial radius at a distance of $\simeq$ 1 kpc. The most pronounced feature in the left-hand panel is the virial shock, where the ratio of infall speed to local sound speed approaches unity and the gas decelerates over a comparatively small distance. In contrast, the vorticity at the virial shock is almost negligible. The high velocity gradients at the centre of the galaxy indicate the formation of a multitude of shocks where the bulk radial flows of filaments are converted into turbulent motions on small scales.

3.5 Massive Black Hole Growth

Galaxy formation in general involves the co-evolution of a central black hole and the surrounding stellar system, the one influencing the other. Two crucial unsolved problems are: what were the seeds for BH growth, and how important was this co-evolution at very high redshifts? We here begin to address these questions. Different scenarios have been suggested to account for the seeds of BH growth (Rees, 1984): the direct collapse of gas in atomic cooling halos in the presence of a strong photodissociating background, or stellar remnants of massive, metal-free stars. In the following, we discuss the latter possibility and investigate the growth of a MBH forming at the centre of the galaxy.

3.5.1 Accretion Rate

Even though studies of stellar evolution have shown that primordial stars may explode as energetic SNe, we here assume that all Pop III.1 stars collapse directly to BHs (Heger et al., 2003; Heger & Woosley, 2002). Their initial mass is dictated by the resolution limit to $M_{\rm BH} \simeq 2 \times 10^3$ M$_\odot$, with accretion on to the BH governed by the criteria discussed in Section 3.2. Recent investigations have shown that photoheating by the progenitor star can delay efficient accretion by reducing the central density to $\lesssim 1$ cm^{-3} (Johnson & Bromm, 2007). However, the suppression of accretion also depends on the detailed merger history of the host halo. For example, a major merger occuring just after the formation of the BH could transport enough cold gas to its centre to enable accretion at the Eddington rate. As shown in Fig. 3.6, some minihalos merge shortly after forming a BH, in some cases after only a few million years. On the other hand, if mergers are absent or incoming halos are not sufficiently massive, accretion could be suppressed for $\gtrsim 100$ Myr (Johnson & Bromm, 2007). In our approach to derive an upper limit on the accretion rate, we neglect the effects of photoheating by the progenitor star such that accretion is governed solely by the supply of cold gas brought to the centre of the halo.

A more precise modelling would also require a prescription for radiation emitted by the BH-powered miniquasar and its feedback on the surrounding disc (Volonteri & Rees, 2006). In a simpler approach, one can assume a given radiative efficiency ϵ, which denotes the ratio of BH luminosity to accreted mass energy, and assume that accretion is spherically

symmetric. This leads to the Eddington accretion rate

$$\dot{M}_{\rm Edd} = \frac{1}{\epsilon}\frac{M_{\rm BH}}{t_{\rm Salp}}\,, \tag{3.3}$$

where $t_{\rm Salp}$ is the Salpeter time, defined by

$$t_{\rm Salp} = \frac{c\sigma_{\rm T}}{4\pi G m_{\rm H}} \simeq 450\ {\rm Myr}\,. \tag{3.4}$$

The mass of the BH as a function of time is thus given by

$$M_{\rm BH}(t) = M_{\rm BH}(t_0)\,\exp\left(\frac{1-\epsilon}{\epsilon}\,\frac{t-t_0}{t_{\rm Salp}}\right). \tag{3.5}$$

In Fig. 3.13, we compare the mass growth of the most massive BH with the Eddington-limited model, using a fiducial value of $\epsilon = 1/10$. We find that the accretion rate remains roughly constant at $\simeq 5\times10^{-3}$ M$_\odot$ yr^{-1}, such that the BH grows from $\simeq 2\times10^3$ to $\simeq 10^6$ M$_\odot$ in the course of $\simeq 300$ Myr. Due to our neglect of radiative feedback, the BH accretes well above the Eddington rate throughout most of its lifetime. At later times the accretion rate stagnates, most likely caused by the high kinetic energy input at the centre via cold accretion (see Fig. 3.11). Consequently, the fraction of unbound gas near the BH increases and its mass growth is slowed. We conclude that Eddington accretion is possible under the most favourable circumstances, for example, where a recent merger brings an ample supply of cold gas to the centre of the halo, but generally radiative feedback by the progenitor star and the disc around the BH will lead to sub-Eddington accretion rates (Johnson & Bromm, 2007; Pelupessy et al., 2007).

3.5.2 Accretion Luminosity

The radiation generated by the BH-powered miniquasar can have numerous effects on the formation of the first galaxies. In addition to its negative feedback on star formation via photoheating, the emitted radiation can contribute to the LW background, as well as to the reionization of the Universe (Kuhlen & Madau, 2005; Madau et al., 2004; Ricotti & Ostriker, 2004). In the following, we derive an upper limit on the photodissociating flux and the number of ionizing photons emitted by a stellar remnant BH accreting at the Eddington limit.

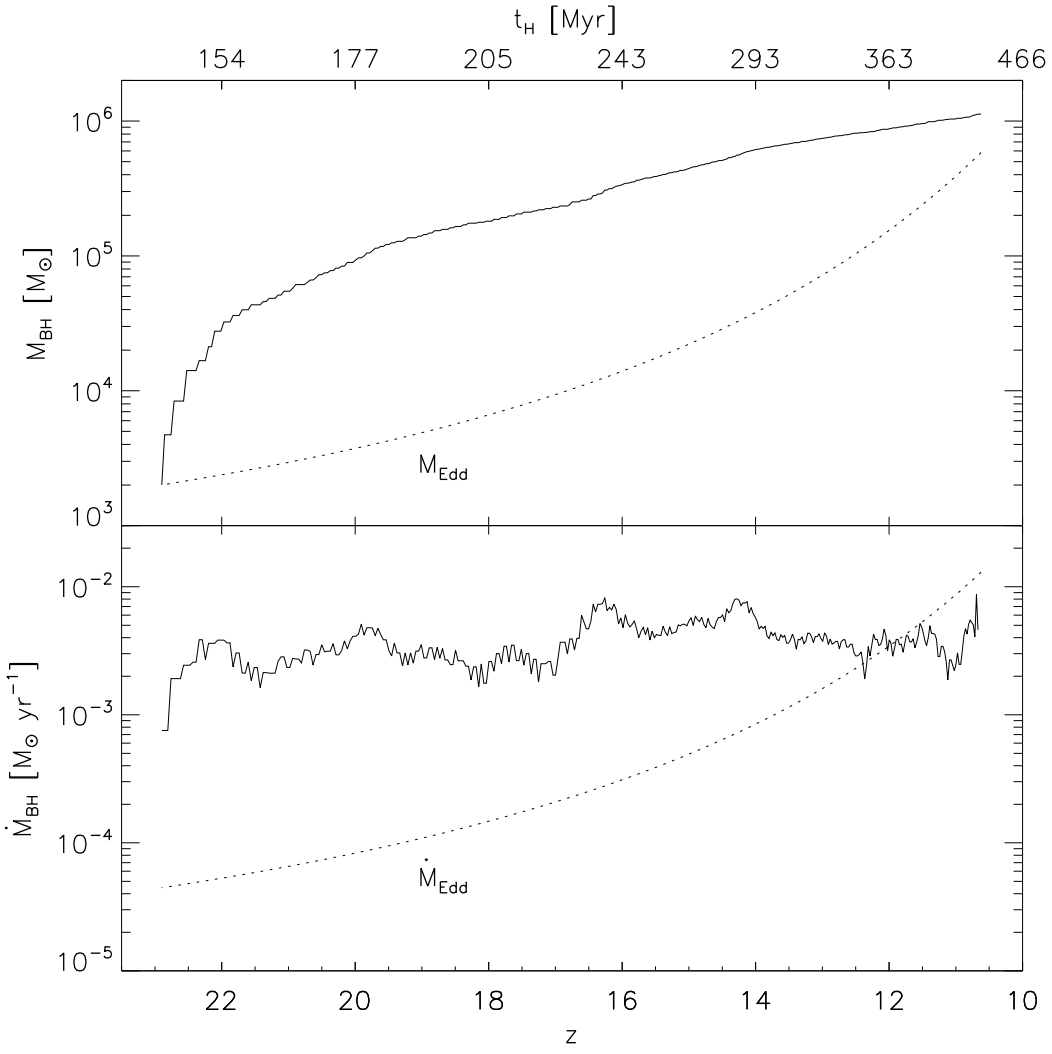

Figure 3.13: The mass (top panel) and accretion rate (bottom panel) of the central BH as a function of redshift, shown for the simulation (solid lines) and Eddington-limited accretion (dotted lines). The accretion rate remains roughly constant at $\simeq 5 \times 10^{-3}$ $M_\odot$ yr^{-1}, such that the BH grows from $\simeq 2 \times 10^3$ to $\simeq 10^6$ $M_\odot$ in the course of $\simeq 300$ Myr. This is a strict upper limit as radiation effects are not taken into account. Accretion is initially super-Eddington due to the high amount of cold gas brought to the centre of the galaxy, but stagnates once turbulence becomes important and the fraction of unbound gas increases.

Photodissociating Flux

To determine the flux of LW photons, we first model the temperature profile of the surrounding accretion disc:

$$T(r) = \left(\frac{3}{8\pi} \frac{G M_{\rm BH} \dot{M}_{\rm BH}}{\sigma_{\rm SB} r^3} \right)^{\frac{1}{4}} , \tag{3.6}$$

where r is the distance from the BH, $M_{\rm BH}$ its mass, $\dot{M}_{\rm BH}$ the accretion rate and $\sigma_{\rm SB}$ the Stefan-Boltzmann constant (Pringle, 1981). For simplicity, we have taken the disc to be a thin disc, such that each annulus radiates as a blackbody of temperature given by the above equation. The inner-most radius of the disc is given by

$$r_{\rm inner} \sim 2 \text{ km} \left(\frac{M_{\rm BH}}{\rm M_\odot} \right) , \tag{3.7}$$

corresponding to a high value for the BH spin parameter $a \gtrsim 0.9$ (Makishima et al., 2000; Vierdayanti et al., 2008), which we expect considering the large angular momentum of the accreted gas (see Fig. 3.11). We integrate the flux over the surface of the disc from $r_{\rm inner}$ to $r_{\rm outer} = 10^4 r_{\rm inner}$, where the contributions to both the photodissociating and ionizing fluxes are negligible. To determine the flux emitted in the LW bands, we evaluate the total emitted flux at 12.87 eV. In the upper panel of Fig. 3.14, we show the LW flux in units of 10^{-21} erg s^{-1} cm^{-2} Hz^{-1} sr^{-1} for the case of Eddington-limited accretion at 1 kpc distance from the BH. We consider initial BH masses of 100 and 500 $\rm M_\odot$, roughly the range expected for the direct collapse of massive Pop III stars (Heger et al., 2003; Heger & Woosley, 2002). As Fig. 3.14 shows, $J_{\rm LW}$ can greatly exceed the critical value of $\gtrsim 10^{-2}$ required for the suppression of star formation in minihalos, which mostly relies on efficient H_2 cooling (Johnson et al., 2008; Machacek et al., 2001; O'Shea & Norman, 2008; Yoshida et al., 2003a). Furthermore, even a modest LW flux can dissociate enough H_2 such that HD formation and cooling never become important, reducing the temperature to which the gas can cool (Yoshida et al., 2007b). The impact on primordial star formation in BH-hosting galaxies might thus be severe even for sub-Eddington accretion rates, implying that this effect must be taken into account in future work.

Another important issue concerns the contribution to the global LW background. We may estimate a maximum global LW background by assuming that each atomic cooling halo at $z \gtrsim 10$ hosts a BH accreting at the Eddington rate. We can then find an upper limit to the

global LW background by summing up the contributions from BHs within a distance equal to the maximum mean free path for a LW photon, $r_{\rm max} \sim 10$ Mpc at $z = 15$, following the prescription in Johnson et al. (2008). This estimate yields a maximum global LW background comparable to the LW flux from a single source, as shown in Fig. 3.14. Such a high flux could have profound consequences for further star formation in minihalos, but in most cases radiative feedback by the progenitor star will significantly delay accretion, such that a global LW background fuelled by accretion on to BHs will likely be subdominant compared to a stellar LW background (Pelupessy et al., 2007).

Ionizing Flux

The amount of ionizing radiation released by the accreting BH can be determined in analogy to our calculation of the LW flux. An integration over the temperature profile of the accretion disc yields the total number of hydrogen-ionizing photons emitted per second, shown in the bottom panel of Fig. 3.14. While massive Pop III stars emit of the order of 10^{50} hydrogen-ionizing photons per second, these stars live for only $\lesssim 3$ Myr (Bromm et al., 2001b; Schaerer, 2002). However, as Fig. 3.14 shows, if Pop III relic BHs are able to accrete efficiently, they may emit 10 – 100 times this number for $\gtrsim 100$ Myr. This enormous flux of ionizing radiation could power H II regions with radii of the order of 10 kpc, larger and longer-lived than the transient H II regions of individual Pop III stars (Johnson et al., 2007; Yoshida et al., 2007a). Star formation in minihalos within the H II region could be suppressed if accretion is continuous and drives a persistent radiative flux (Ahn & Shapiro, 2007; Whalen et al., 2008a). Due to this dramatic radiative feedback associated with high accretion rates, though, the gas in the protogalaxy is likely to be heated and driven away from the BH, once again resulting in sub-Eddington accretion rates (Pelupessy et al., 2007).

We have also calculated the number of He II-ionizing photons emitted by the accreting BH, and find that this is within a factor of $\lesssim 2$ of the number of hydrogen-ionizing photons, owing to the high temperatures of the accretion disc. Thus, if Pop III relic BHs are able to accrete efficiently, they may also contribute to the reionization of helium, driving He III regions that can be as large as their H II regions (Furlanetto & Oh, 2007).

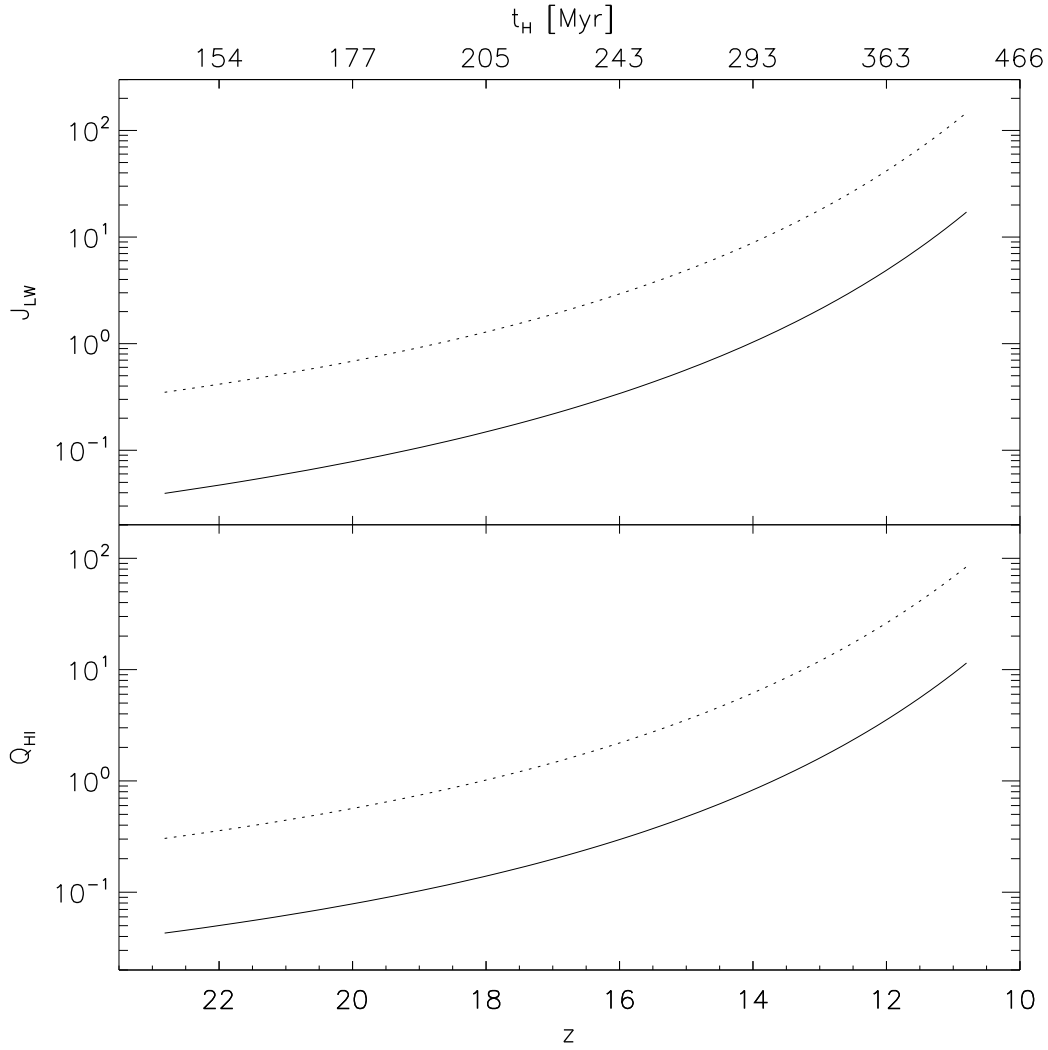

Figure 3.14: The radiation due to thermal emission from the accretion disc surrounding a Pop III relic BH accreting at the Eddington limit, for an inital mass of 100 (solid lines) and 500 $M_{\odot}$ (dotted lines). Top panel: the photodissociating flux, $J_{\rm LW}$, in units of 10^{-21} erg s^{-1} cm^{-2} Hz^{-1} sr^{-1}, at a distance of 1 kpc from the BH. Bottom panel: the number of hydrogen-ionizing photons emitted per second from the accretion disc, in units of 10^{50} s^{-1}.

3.6 Summary and Conclusions

We have investigated the formation of the first galaxies with highly resolved numerical simulations, taking into account all relevant primordial chemistry and cooling. The first galaxies form at redshifts $z \gtrsim 10$ and are characterized by the onset of atomic hydrogen cooling, once the virial temperature exceeds $\simeq 10^4$ K, and their ability to retain photoheated gas. We have described the merger history of a $\simeq 5 \times 10^7$ $M_\odot$ system in great detail and found that in the absence of stellar feedback 10 Pop III.1 stars form in minihalos prior to the assembly of the galaxy. Infalling gas is partially ionized at the virial shock and forms a high amount of H_2 and HD, allowing the gas to cool to the temperature of the CMB and likely form Pop III.2 stars with $\gtrsim 10$ $M_\odot$. Accretion on to the galaxy proceeds initially via hot accretion, where gas is accreted directly from the IGM and shock-heated to the virial temperature, but is quickly accompanied by a phase of cold accretion, where the gas cools in filaments before flowing into the parent halo with high velocities. The latter drives supersonic turbulence at the centre of the galaxy and thus plays a key role for second-generation star formation. Finally, we have investigated the growth of BHs seeded by the stellar remnants of Pop III.1 stars and found that accretion at the Eddington limit might be possible under the most favourable circumstances, but in most cases radiation emitted by the progenitor star and the accretion disc around the BH will lead to sub-Eddington accretion rates.

Depending on the strength of radiative and SN-driven feedback, some galaxies might remain metal-free and form intermediate-mass Pop III.2 stars. The inclusion of radiative feedback would likely increase the fraction of Pop III.2 material, as it enhances the degree of ionization, and, consequently, the amount of molecules formed (Johnson et al., 2007; Wise & Abel, 2008b). Observational signatures of intermediate-mass primordial stars might include gamma-ray bursts (GRBs) for the case of a rapidly rotating progenitor (e.g. Bromm & Loeb, 2006), or distinct abundance patterns produced by core-collapse SNe experiencing fallback (Umeda & Nomoto, 2003). However, since the number of Pop III.1 stars formed in minihalos prior to the assembly of the galaxy is of the order of 10, it seems much more likely that at least one star will end in a violent SN explosion and pre-enrich the halo to supercritical levels (Bromm et al., 2003; Greif et al., 2007; Wise & Abel, 2008b). In combination with the onset of turbulence, metal mixing in the first galaxies will likely be highly efficient and could lead to the formation of the first low-mass star clusters (Clark et al., 2008), in extreme cases possibly even to metal-poor globular clusters (Bromm & Clarke, 2002). Some of the

extremely iron-deficient, but carbon and oxygen-enhanced stars observed in the halo of the Milky Way may thus have formed as early as redshift $z \simeq 10$.

In future work, we plan to include the effects of radiative and SN-driven feedback by previous star formation in minihalos, as well as the distribution of metals and its concomitant cooling. We will study the fragmentation of gas accumulating at the centre of the galaxy and address the issue of turbulence-driven star formation in detail. The goal of making realistic predictions for the first generation of starburst-galaxies, to be observed with the *JWST*, is clearly coming within reach.

4

Local Radiative Feedback in the Formation of the First Protogalaxies

The formation of the earliest galaxies plays a key role in a number of the most important questions being addressed in cosmology today. The first galaxies are predicted to have been the dominant sources of the radiation which reionized the universe (Ciardi et al., 2006), and they may have hosted the majority of primordial star formation (Greif & Bromm, 2006; Jimenez & Haiman, 2006). They are the likely sites for the formation of the most metal-poor stars that have recently been found in our Galaxy (Beers & Christlieb, 2005; Christlieb et al., 2002; Frebel et al., 2005), and possibly for the first efficient accretion onto the stellar black holes (see Johnson & Bromm, 2007) which may have been the seeds for the $\sim 10^9$ $M_\odot$ black holes that are inferred at redshifts $z \gtrsim 6$ (Fan et al., 2004, 2006b). Furthermore, an understanding of the formation of the first galaxies is crucial for the interpretation of galaxies now beginning to be observed at $z \gtrsim 6$ (Bouwens & Illingworth, 2006; Iye et al., 2006; Mobasher et al., 2005), as well as of the objects at redshifts $z \gtrsim 10$ which are expected to be detected with upcoming telescopes such as *JWST* (Gardner et al., 2006). Among these systems there promise to be some of the first metal-free objects that will be observable, and as such it is important that theoretical predictions of their properties are made.

What were the effects of the radiative feedback from the first generations of stars on the formation of the first galaxies? It is now widely held that the first stars were likely very massive, and therefore emitted copious amounts of radiation which profoundly affected their surroundings (Abel et al., 2002; Bromm et al., 1999, 2002; Gao et al., 2007; Yoshida, 2006).

4. LOCAL RADIATIVE FEEDBACK IN THE FORMATION OF THE FIRST PROTOGALAXIES

Recent work has demonstrated that the H II regions surrounding the first stars were able to evacuate the primordial gas from the minihalos that hosted these objects (Abel et al., 2007; Alvarez et al., 2006a; Kitayama et al., 2004; Whalen et al., 2004). The impact of these H II regions on second generation star formation is complex (Ahn & Shapiro, 2007; Oh & Haiman, 2003; Ricotti et al., 2001; Susa & Umemura, 2006). While initially the density in these regions is suppressed and the gas within heated to $\gtrsim 10^4$ K, vigorous molecule formation can take place once the gas begins to cool and recombine after the central Pop III star has collapsed to fom a massive black hole, leading to the possibility of the formation of low-mass primordial stars (Johnson & Bromm, 2006, 2007; Nagakura & Omukai, 2005; O'Shea et al., 2005; Yoshida et al., 2007a).

An additional radiative feedback effect from the first stars is the photo-dissociation of the fragile hydrogen molecules which allow the primordial gas to cool and collapse into minihalos, with virial temperatures $\lesssim 8,000$ K (Barkana & Loeb, 2001). The effects of the molecule-dissociating radiation from the first stars can reach far beyond their H II regions (Ciardi et al., 2000), and thus star formation in distant minihalos may have been delayed or quenched altogether (Haiman et al., 2000, 1997; Mackey et al., 2003). Interestingly, however, while IGM at the epoch of the first stars becomes optically thick to LW photons only over vast distances (Glover & Brand, 2001; Haiman et al., 2000), the high molecule fraction that persists inside the first relic H II regions leads to a high optical depth to these photons, potentially allowing star formation to take place in minihalos down to lower redshifts than would otherwise be possible (Johnson & Bromm, 2007; Machacek et al., 2001, 2003; Oh & Haiman, 2002; Ricotti et al., 2001).

In the present work, we self-consistently track the formation of, and the radiative feedback from, individual Pop III stars in the course of the formation of a primordial protogalaxy. We compute in detail the H II regions and LW bubbles of each of these sources, and follow the evolution of the primordial gas as it becomes incorporated into the protogalaxy. In Section 4.2, we describe our numerical methodology. Our results are presented in Section 4.3, while we summarize our conclusions and discuss their implications in Section 4.4.

4.1 Methodology

4.1.1 Cosmological Initial Conditions and Resolution

We employ the parallel version of GADGET (version 1) for our three-dimensional numerical simulations. This code includes a tree, hierarchical gravity solver combined with the SPH method for tracking the evolution of the gas (Springel et al., 2001). Along with H, H^+, H^-, H_2, H_2^+, He, He^+, He^{++}, and e^-, we have included the five deuterium species D, D^+, D^-, HD and HD^+, using the same chemical network as in Johnson & Bromm (2006, 2007).

We carry out a three-dimensional cosmological simulation of high-z structure formation which evolves both the dark matter and baryonic components, initialized according to the ΛCDM model at $z = 100$. As in earlier work (Bromm et al., 2003; Johnson & Bromm, 2007), we adopt the cosmological parameters $\Omega_m = 1 - \Omega_\Lambda = 0.3$, $\Omega_b = 0.045$, $h = 0.7$, and $\sigma_8 = 0.9$, close to the values measured by *WMAP* in its first year (Spergel et al., 2003). Here we use a periodic box with a comoving size $L = 460\ h^{-1}$ kpc, but unless stated explicitly, we will always refer to physical distances. Our simulation uses a number of particles $N_{\rm DM} = N_{\rm SPH} = 128^3$, where the SPH particle mass is $m_{\rm SPH} \sim 740\ {\rm M}_\odot$.

We have determined the maximum density of gas that can be reliably resolved in this simulation by carrying out a cosmological simulation from $z = 100$, in which we allow the gas to cool and collapse into minihalos without including radiative effects. We then compare the minimum resolved mass, which we take to be $\sim 64\ m_{\rm SPH}$, with the Bonnor-Ebert mass, given by

$$M_{\rm BE} \simeq 700\ {\rm M}_\odot \left(\frac{T}{200\ {\rm K}}\right)^{3/2} \left(\frac{n}{10^4\ {\rm cm}^{-3}}\right)^{-1/2} , \tag{4.1}$$

where n and T are the number density and temperature of the gas, respectively. As shown in Fig. 4.1, the gas evolves according to the canonical behavior of primordial gas collapsing in minihalos (e.g. Bromm et al., 2002). We expect the gas in our simulations with radiative feedback to behave similarly as it collapses to high densities, since it is the formation of, and cooling by, molecules which will drive the collapse in both cases. Thus, we take the maximum density that we can reliably resolve to be that at which the Bonnor-Ebert mass becomes equal to the resolution mass. As is evident in Fig. 4.1, this criterion results in a maximum resolvable density of $n_{\rm res} \sim 20\ {\rm cm}^{-3}$. This density is four orders of magnitude higher than the background mean density at a redshift of $z \gtrsim 15$, and such overdensities only occur in the minihalos within which the first Pop III stars form (Bromm & Loeb, 2004; Yoshida, 2006).

We take it here that one Pop III star, assumed to have a mass of 100 $M_\odot$, will form from this dense, collapsing primordial gas inside a minihalo, consistent with recent work which shows that, in general, only single stars are expected to form in minihalos under these conditions (Yoshida, 2006). Pop III stars with this mass are predicted to directly collapse to a black hole, and therefore produce no supernova explosion (Heger et al., 2003), which allows us to self-consistently neglect the possibility of ejection of metals into the primordial gas. We will consider this possibility in future work. In the present work, we focus on the radiative feedback from the first stars.

4.1.2 Radiative Feedback

In our simulations with radiative feedback, we assume that stars are formed in minihalos which acquire densities higher than $n_{\rm res} = 20$ cm^{-3}. In order to account for the radiative feedback from a star formed in a minihalo, the gas surrounding the star is first photo-heated. We then calculate the extent of the H II region, as well as of the LW bubble around the star. We carry out this procedure every time a star forms in the simulation. The Pop III star will soon die, and we then let the simulation evolve once more, allowing recombination to take place in the relic H II region, and for molecules to reform within the relic LW bubble. We expect that this procedure will provide reliable results, as the $\lesssim 3$ Myr lifetime of a Pop III star is short compared to the typical dynamical times of the gas in this simulation.

Photoionization

To account for the presence of a 100 $M_\odot$ Pop III star in the minihalos in which the gas collapses to a density of $n_{\rm res}$, we first photoheat and photoionize the gas within 500 pc of the gas particle which first reaches this density for a duration of the lifetime of the star, using the same heating and ionization rates as in Johnson & Bromm (2007). Our choice of a 500 pc radius ensures that the entire gas within the source minihalo, with virial radius ~ 150 pc, is photoheated, but that we do not photoheat the dense, neutral gas in neighboring halos. Just as in this previous work, we reproduce the basic density and velocity structure of the gas within 500 pc of the central source that has been found in detailed one-dimensional radiation hydrodynamics calculations (Kitayama et al., 2004; Whalen et al., 2004).

Once this density structure is in place around the point source, we employ a ray-tracing technique to solve for the H II region that surrounds the star at the end of its life. We cast rays

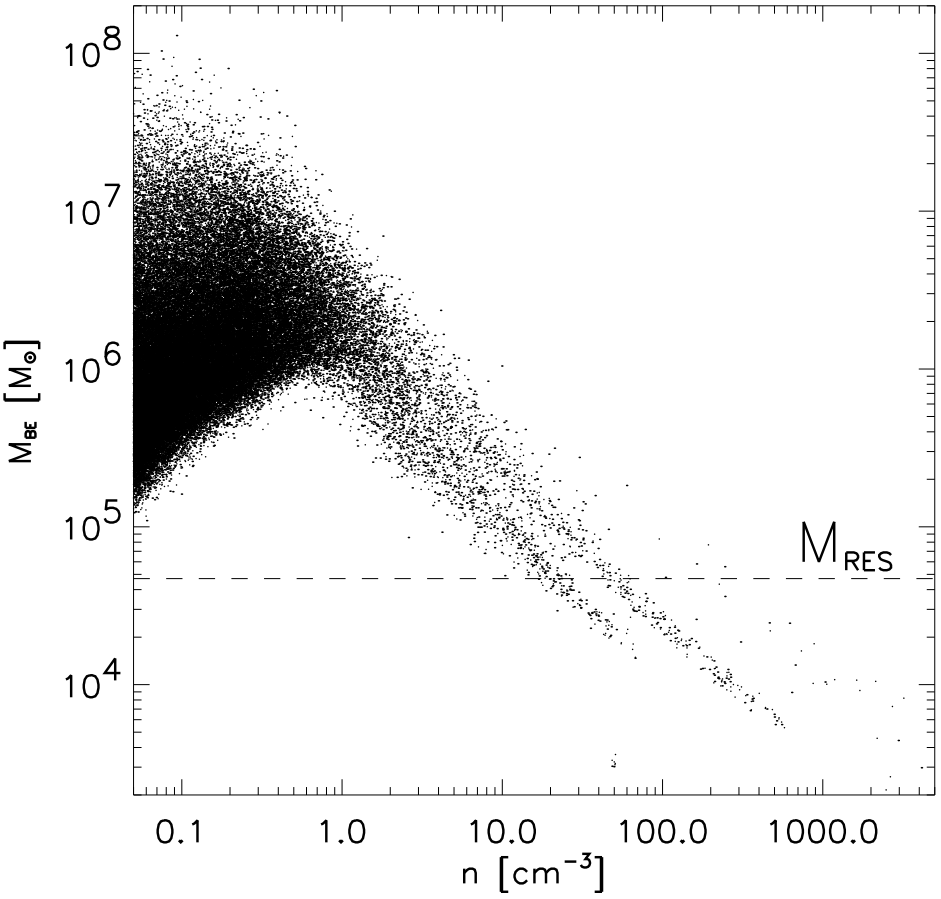

Figure 4.1: Determining the maximum density resolvable in our simulations. To reliably resolve the properties of the gas in our simulation, the Bonnor-Ebert mass, similar to the Jeans mass, must be larger than the mass in the SPH smoothing kernel. For added assurance, we take the minimum resolvable mass to be twice the mass in the kernel. This value for the resolution mass is shown by the dashed horizontal line. For densities higher than $n_{\rm res} \sim 20$ cm^{-3}, the Bonnor-Ebert mass may be exceeded by the resolution mass, and so we take it that we can only resolve the properties of the gas at densities below this value. We note that the two structures emerging at high densities are two spatially distinct halos of different mass which are undergoing collapse.

in $N_{\rm ray} \sim 100,000$ directions from the central source, and divide each ray into 500 segments. Then, we add up all of the recombinations that take place over the course of the star's lifetime in each bin along each of the $N_{\rm ray}$ rays, taking the number of recombinations to be

$$N_{\rm rec} = \alpha_{\rm B} n_{\rm mean}^2 \frac{4\pi}{N_{\rm ray}} t_* r^2 {\rm d}r \ , \tag{4.2}$$

where $\alpha_{\rm B}$ is the case B recombination coefficient, r is the distance of the bin from the star, dr is length of the bin in the direction radial to the star, and t_* is the lifetime of the star, here taken to be 3 Myr (Schaerer, 2002). We compute $n_{\rm mean}$, the average number density of hydrogen atoms in a bin, as

$$n_{\rm mean} = \frac{\sum n_{\rm H}}{N_{\rm part}} \ . \tag{4.3}$$

Here, $N_{\rm part}$ is the number of SPH particles in the bin and $n_{\rm H}$ is the number density of hydrogen of the individual SPH particles in that bin.

Next, we assume that the star radiates an equal number of photons in every direction, and we take the total number of ionizing photons that it radiates in its lifetime to be

$$N_{\rm ion} = Q_{\rm ion} t_* \ , \tag{4.4}$$

where we have chosen $Q_{\rm ion}$, the average number of ionizing photons emitted per second by the star, to be 10^{50} s^{-1} (Bromm et al., 2001b; Schaerer, 2002). We then add up the recombinations in all of the bins, along each of the rays, beginning with those closest to the star and moving outward, until the number of recombinations along a ray equals the number of ionizing photons that are emitted along that ray. If the number of recombinations in the bin falls below the number of atoms in the bin, then we count the number of atoms in the bin against the number of photons as well. Doing this for each of the rays, we solve in detail for the H II region of the star. We set the free electron fraction to unity for each of the SPH particles that lie within the H II region. We set the temperature of the SPH particles within the H II region, but outside of the 500 pc photo-heated region, to $T = 18,000$ K, roughly the value at the outer edge of the photo-heated region. As well, the fraction of molecules in the H II region is set to zero, as we assume that all molecules are collisionally dissociated at the high temperatures in the H II region.

Photodissociation

To find the region in which the LW radiation from the star destroys H_2 and HD molecules, the 'LW bubble' in our terminology, we carry out a ray-tracing procedure similar to the one used to solve for the H II region. We use the same bins as in that procedure, but now we evaluate the formation time of H_2 molecules in each bin and compare this both to the lifetime of the star and to the dissociation time of the molecules. For each bin, we compute the H_2 formation time as

$$t_{\rm form,H_2} = \sum \frac{n_{\rm H_2}}{n_{\rm H}\left(k_1 n_{\rm H_2^+} + k_2 n_{\rm H^-}\right)} / N_{\rm part} \ , \tag{4.5}$$

where $n_{\rm H_2^+}$ and $n_{\rm H^-}$ are the number densities of H_2^+ and H^-, respectively. The sum is over all the particles in the bin, $N_{\rm part}$, and k_1 and k_2 are the rate coefficients for the following two main reactions that produce H_2:

$$\rm H + H_2^+ \rightarrow H^+ + H_2 \ ,$$

$$\rm H + H^- \rightarrow e^- + H_2 \ .$$

We adopt the following values for these rate coefficients (de Jong, 1972; Haiman et al., 1996a; Karpasb) et al., 1979):

$$k_1 = 6.4 \times 10^{-10} \ {\rm cm^3 \ s^{-1}} \ , \tag{4.6}$$

$$k_2 = 1.3 \times 10^{-9} \ {\rm cm^3 \ s^{-1}} \ . \tag{4.7}$$

The dissociation time for the molecules is obtained by finding the flux of LW photons from a 100 $M_\odot$ Pop III star, assumed to be a blackbody emitter with radius $R_* \simeq 3.9 \ R_\odot$ and effective temperature $T_* \simeq 10^5$ K (Bromm et al., 2001b). The dissociation time for unshielded molecules at a distance R from the star is then given by (Abel et al., 1997)

$$t_{\rm diss,H_2} \sim 10^5 \ {\rm yr} \left(\frac{R}{1 \ {\rm kpc}}\right)^2 \ . \tag{4.8}$$

Next, we note that for molecules to be effectively dissociated by the LW radiation, the dissociation time of the molecules must be shorter than both the lifetime of the star and the formation time of the molecules. Therefore, we compare all of these timescales for each bin

along each ray and set the fraction of molecules to zero if $t_{\rm diss,H_2} \lesssim t_{\rm form,H_2}$ and $t_{\rm diss,H_2} \lesssim t_*$. If this condition is not satisfied, then the molecule fraction is left unchanged from its value before the formation of the star. This allows for the possibility of the effective shielding of H_2 molecules because it accounts for the build-up of H_2 column density, for instance, in relic H II regions or in collapsing minihalos where the formation time of H_2 is relatively short.

We take into account the effects of self-shielding by adding up the H_2 column density $N_{\rm H_2}$ along the ray contributed by each bin in which the molecules are not effectively dissociated. We then adjust the dissociation time for the molecules in shielded bins according to (Draine & Bertoldi, 1996):

$$t_{\rm diss,H_2} \sim 10^5 \text{ yr} \left(\frac{R}{1 \text{ kpc}}\right)^2 \left(\frac{N_{\rm H_2}}{10^{14} \text{ cm}^{-2}}\right)^{0.75} , \tag{4.9}$$

when the column density of molecules between the bin and the star is $N_{\rm H_2} \gtrsim 10^{14}$ cm^{-2}.

The ionic species H^- and H_2^+, which are reactants in the main reactions which form H_2, can also, in principle, be destroyed by the radiation from the star. The photo-dissociation times for these species are given in terms of the temperature of the star T_*, the source of thermal radiation in our case, and the distance from the star R, as (de Jong, 1972; Dunn, 1968; Galli & Palla, 1998)

$$t_{\rm diss,H_2^+} = 5 \times 10^{-2} T_*^{-1.59} \exp\left(\frac{82000}{T_*}\right)\left(\frac{R}{R_*}\right)^2 \text{ s} , \tag{4.10}$$

$$t_{\rm diss,H^-} = 9.1 T_*^{-2.13} \exp\left(\frac{8823}{T_*}\right)\left(\frac{R}{R_*}\right)^2 \text{ s} . \tag{4.11}$$

For the 100 $M_\odot$ star, we find that $t_{\rm diss,H_2^+} \sim 5{\times}10^3$ yr $(R/1 \text{ kpc})^2$ and $t_{\rm diss,H^-} \sim 9{\times}10^2$ yr $(R/1 \text{ kpc})^2$. The formation times for these species, on the other hand, are

$$t_{\rm form,H^-} = n_{\rm H^-} \left(\frac{{\rm d}n_{\rm H^-}}{{\rm d}t}\right)^{-1} \sim 3 \times 10^3 \text{ yr} \tag{4.12}$$

and

$$t_{\rm form,H_2^+} = n_{\rm H_2^+} \left(\frac{{\rm d}n_{\rm H_2^+}}{{\rm d}t}\right)^{-1} \sim 4 \times 10^3 \text{ yr} \tag{4.13}$$

for primordial gas at a temperature of $T = 100$ K and a density of $n_{\rm H} = 10^{-2}$ cm^{-3}, typical for gas at the outskirts of a collapsing minihalo. These formation timescales become much

shorter for gas deeper inside minihalos, where the densities and temperatures are generally higher. It is in these regions, in and around minihalos, where the presence of molecules is most important for cooling the gas. Within these regions the photo-dissociation times for these ionic species are less than their formation times only if they are located $\lesssim 2$ kpc from the star. Thus, photo-dissociation of these species will become ineffective at distances $\gtrsim 2$ kpc from the star, a distance comparable to the size of the H II region of a Pop III star (Abel et al., 2007; Alvarez et al., 2006a). Since we assume that molecules are collisionally destroyed inside the H II region, and since the LW bubble will generally be larger than the H II region, we ignore the photo-dissociation of H^- and H_2^+ in our calculations.

LW photons can also be absorbed by hydrogen atoms, through the Lyman series transitions, as discussed in detail by (Haiman et al., 2000, 1997). However, this atomic absorption will only have a significant effect on the LW flux over distances large enough that the Hubble expansion causes many of the LW photons to redshift to wavelengths of the Lyman series transitions. The light-crossing time for our cosmological box is much shorter than the Hubble time at the redshifts that we consider. Thus, LW photons will be negligibly redshifted as they cross our cosmological box and we can safely neglect the minimal atomic absorption of these photons that may take place.

It has also been found that a shell of H_2 molecules may form ahead of the expanding H II regions surrounding the first stars (see Ricotti et al., 2001). These authors find that such shells may become optically thick to LW photons. However, Kitayama et al. (2004) have discussed that such shells are likely short-lived, persisting for only a small fraction of the lifetime of the star. Thus, for our calculations we neglect the possible formation of such a shell, as we expect that the opacity to LW photons through this shell will be very small when averaged over the lifetime of the star. Additionally, as we show in Section 4.3.1, the regions affected by the LW feedback from a single Pop III star extend, at most, only a few kiloparsecs beyond the H II region of such a star, which itself extends ~ 5 kpc. If an H_2 shell forms ahead of the H II region, then the extent of the LW bubble will only be suppressed by, at most, a factor of a few in radius.

4.1.3 Sink Particle Formation

We have carried out two simulations, one with radiative feedback and one in which the simulation evolves without including radiative effects. For the former simulation, we allow

stars to form when the density reaches $n_{\rm res}$, and the expansion of the gas around the star due to photo-heating suppresses the density so that our resolution limit is not violated. For the simulation without radiative feedback we allow sink particles to form when the density of the gas reaches $n_{\rm res}$. Since the sink particles will form only in minihalos which are expected to form Pop III stars, we are able to track the star formation rate in the case without feedback by tracking the formation of sink particles. We can then compare the sites, and rates, of star formation in each of the simulations in order to elucidate the effect that radiative feedback has on Pop III star formation.

4.2 Results

In this section we discuss the evolution of the primordial gas under the influence of the radiative feedback which arises as the first stars are formed in a region destined to subsequently be incorporated into the first protogalaxy. Indeed, other effects will become important in the course of the buildup of the first galaxies. Among them is the ejection of metals into these systems by the first supernovae (Bromm et al., 2003). However, we consider the early regime in which Pop III star formation dominates, and the effects of metals might not yet be important. Initially only taking into account the stellar radiative feedback, and neglecting chemical enrichment, relies on our simplifying assumption that only 100 $M_\odot$ black hole-forming Pop III stars form, which are predicted not to yield supernovae, and therefore not to eject metals into their surroundings (Heger et al., 2003).

Although the IMF of the first generation of stars is not known with any certainty yet, there is mounting theoretical evidence that Pop III stars were very massive, and thus it is very likely that many of these stars ended there lives by collapsing directly to black holes, emitting few or no metals into the IGM (Fryer et al., 2001; Heger et al., 2003). Here we assume that all of the stars that form within our cosmological box are black hole-forming stars which do not enrich the IGM with metals, and which therefore allow subsequent metal-free star formation to occur. Eventually, however, stars which create supernovae will form, and the ejected metals will be incorporated into the first protogalaxies, thus drawing the epoch of metal-free star formation to a close. In light of this, we end our simulation after the formation of the eighth star in our box at a redshift of $z \sim 18$, as we expect that at lower redshifts the effects of the first metals ejected into the primordial gas will become important (but see Jappsen et al., 2007). Also, at lower redshifts global LW feedback, due

to star formation at distances far larger than our cosmological box, will become increasingly important. That said, by tracking the formation of individual Pop III stars in our box, we are able to find a variety of novel results concerning the local radiative feedback from the first generations of stars.

4.2.1 The First H II region and Lyman-Werner Bubble

The first star appears in our cosmological box at a redshift of $z \sim 23$. It forms inside a minihalo with a total mass $\lesssim 10^6$ $M_\odot$ and the gas within this halo is evaporated due to the photo-heating from the star. The H II region that is formed around the star can be seen in Fig. 4.2, which shows the electron fraction, H_2 fraction, temperature, and density of the gas, in projection. The H II region, which has a morphology similar to those found in previous studies, extends out to ~ 4 kpc from the star, also similar to results found in previous works (Abel et al., 2007; Alvarez et al., 2006a; Yoshida et al., 2007a).

As shown in Fig. 4.2, the molecules within ~ 5 kpc are photodissociated by the LW radiation from the first star, and the LW bubble extends to only ~ 1 kpc outside of the H II region. Noting that the formation timescale for H_2 in the neutral IGM at these redshifts is of the order of ~ 300 Myr, much longer than the lifetime of the massive stars that we consider here, we can estimate the distance through the IGM that the LW bubble should extend, $R_{\rm LW}$, by evaluating the criterion for the effective dissociation of molecules at this distance from the first star: $t_{\rm diss,H_2} = t_*$. Using equation (4.8) and taking the lifetime of the star to be 3 Myr gives $R_{\rm LW} \sim 5$ kpc, consistent with the result we find for the first star, shown in Fig. 4.2 (see also Ferrara, 1998). Outside of this LW bubble molecules will not be dissociated effectively by the single Pop III star, owing largely to its short lifetime. Only when continuous star formation sets in will the LW bubbles of the first generations of stars merge and become large enough to establish a more pervasive LW background flux (e.g. Haiman et al., 2000).

4.2.2 Thermal and Chemical Evolution of the Gas

The properties of the primordial gas within our box are strongly time-dependent, as any gradual evolution of the gas is disrupted each time a star turns on and heats the gas, ionizes atoms, and photodissociates molecules. Certain robust patterns, however, do emerge in the course of the evolution of the primordial gas. Fig. 4.3 shows the chemical and thermal properties of the gas at a redshift $z \sim 18$, just after the death of the eighth star in our cosmological box.

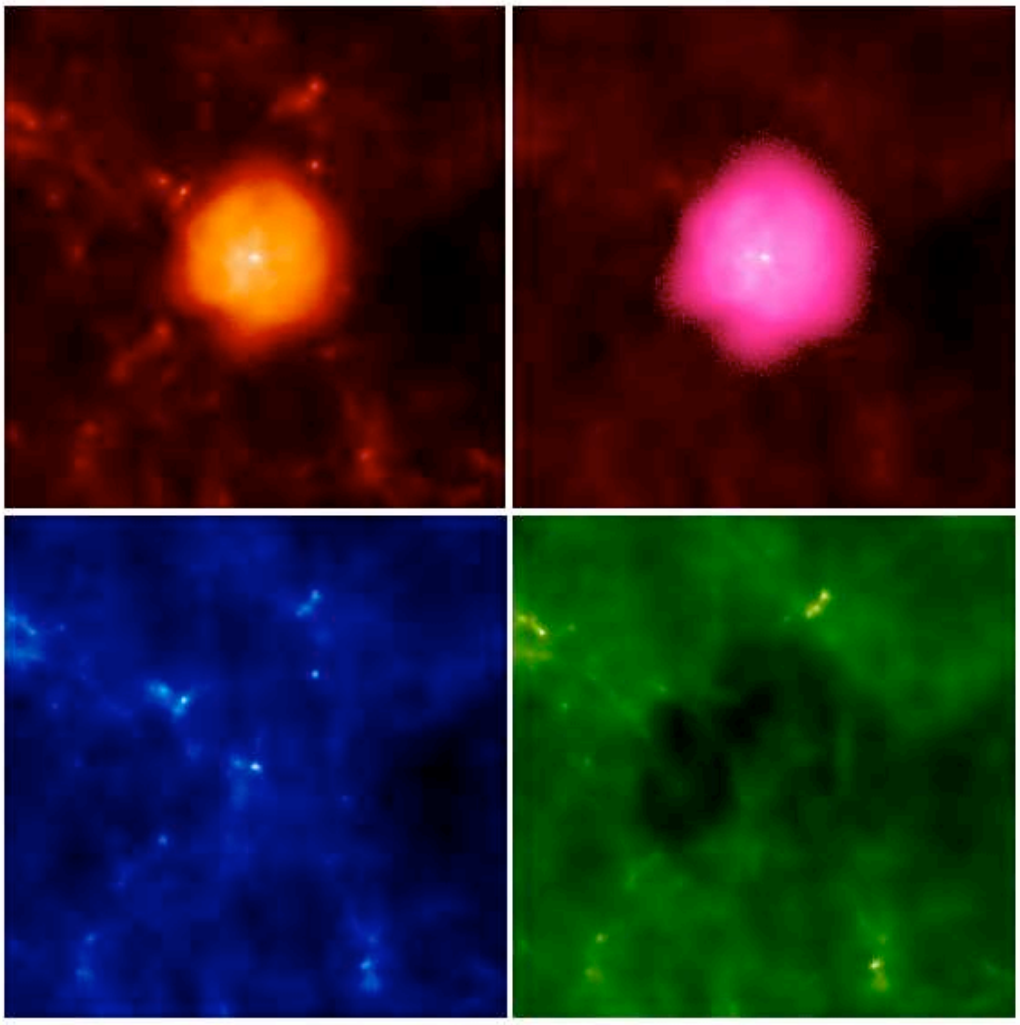

Figure 4.2: The first H II region and LW bubble. Clockwise from top-left are the temperature, electron fraction, H_2 fraction, and density, plotted in projection. While the size of our cosmological box is ~ 27 kpc at this redshift, $z \sim 23$, here we have zoomed into the inner 20 kpc, in order to see detail around the first star. The H II region extends out to ~ 4 kpc in radius, while the LW bubble extends to ~ 5 kpc, within which the molecule fraction is zero. In each panel, the lighter shades signify higher values of the quantity plotted.

Here, the light-shaded particles are those which have been contained within an H II region, and so have passed through a fully ionized phase.

The ionized gas in the H II regions begins to recombine and cool once the central star dies. The dynamical expansion of these hot regions leads to the adiabatic cooling of the gas, as can be seen in the upper left panel of Fig. 4.3. The plot shows relic H II regions at different evolutionary stages. The older ones are generally cooler, owing to the molecular cooling that has had more time to lower the temperature of the gas. Indeed, the first relic H II regions by this redshift, $\sim$ 70 Myr after the first star formed, have already cooled to near the temperature of the un-ionized gas. The electron fraction of the relic H II region gas, however, is still much higher than that of the un-ionized gas, as can be seen in the upper-right panel of Fig. 4.3. That the cooling of the gas occurs faster than its recombination leads to the rapid formation of molecules (Johnson & Bromm, 2006; Kang & Shapiro, 1992; Nagakura & Omukai, 2005; Oh & Haiman, 2003). This elevated fraction of both H_2 and HD molecules in the relic H II region gas is evident in the bottom panels of Fig. 4.3.

The high abundance of molecules in relic H II regions can lead to efficient cooling of the gas, and this has important consequences in the first protogalaxies. In particular, a high fraction of HD in these regions could allow the gas to cool to the temperature of the CMB, $T_{\rm CMB}$, the lowest temperature attainable by radiative cooling, and this effective cooling may lead to the formation of lower mass metal-free stars (Johnson & Bromm, 2006; Nagakura & Omukai, 2005; Yoshida et al., 2007b). Indeed, Fig 4.3 shows that the HD fraction can greatly exceed the minimum value needed for efficient cooling to the CMB temperature floor in local thermodynamic equilibrium (LTE), $f_{\rm HD,crit} \sim 10^{-8}$ (Johnson & Bromm, 2006).

While the LW feedback from the stars that form in our box can very effectively destroy molecules within $\sim$ 5 kpc of the stars by the end of their lives, this feedback is not continuous. Following the death of a given star, the molecules will begin to reform in the absence of LW radiation. The time required for the formation of H_2 molecules is sensitively dependent on the ionized fraction of the gas, but the formation time can be relatively short for un-ionized gas at high densities, as well. In relic H II regions the fraction of H_2 can reach 10^{-4} within $\sim$ 1 Myr (Johnson & Bromm, 2007). In collapsing minihalos, where the molecules play a key role in cooling the gas and allowing it to continue collapsing, the formation times are in general longer at the densities we consider here, $n \lesssim 20$ cm^{-3}. We find that the formation timescale for un-ionized gas collapsing in minihalos is $t_{\rm form,H_2} \sim 5 \times 10^5$ yr at a density of 1 cm^{-3} and a temperature of 900 K, and $t_{\rm form,H_2} \sim 7 \times 10^6$ yr at a density of 0.1 cm^{-3}

and a temperature of 500 K. The average time between the formation of stars in our box is $\sim$ 10 Myr, and so the molecules inside sufficiently dense minihalos can often reform and allow the gas to continue cooling and collapsing, in spite of the intermittent LW feedback from local star forming regions.

In order to evaluate the possible effects of continuous LW feedback from sources outside of our box, we have carried out simulations in which we include a LW background which destroys H_2 molecules at a rate given by (Abel et al., 1997)

$$k_{\rm diss} = 1.2 \times 10^{-12} J_{\rm LW}\ {\rm s}^{-1}\ , \tag{4.14}$$

where $J_{\rm LW}$ is the flux of LW photons in units of 10^{-21} erg s^{-1} cm^{-2} Hz^{-1} sr^{-1}. We have carried out simulations in which the value of $J_{\rm LW}$ is taken to be zero before the formation of the first star and 0.1, 10^{-2}, and 10^{-3} afterwards, when a LW background might be expected to begin building up due to distant star formation. For each of these simulations, we found the formation redshift of the second star in the box to be $z_{\rm 2nd}$ = 16.3, 20, and 20.5, respectively. In our main simulation, in which we neglect a possible background LW flux, the second star formed at $z_{\rm 2nd}$ = 20.6. This demonstrates that a background LW flux of $J_{\rm LW} \lesssim 10^{-2}$ would likely have little impact on our results, while a larger LW flux would simply delay the collapse of gas into minihalos and so lower the overall star formation rate in our box, consistent with previous findings (e.g. Machacek et al., 2001; Mesinger et al., 2006). We emphasize, however, that for a substantial LW background to be established, a relatively high continuous star formation rate must be achieved, as we have shown that individual Pop III stars can only be expected to destroy molecules within $\sim$ 5 kpc of their formation sites. In the very early stages of the first star formation, when short-lived single stars are forming in individual minihalos (e.g. Yoshida, 2006), it appears unlikely that a substantial LW background would be established, the feedback from the sources being instead largely local. It may be only later, when continuous star formation begins to occur in larger mass systems that a pervasive LW background would likely be built up (Greif & Bromm, 2006; Haiman et al., 2000).

4.2.3 Shielding of Molecules by Relic H II Regions

As star formation continues, the volume occupied by relic H II regions increases. Because of the high molecule fraction that can develop in these regions, owing to the large electron

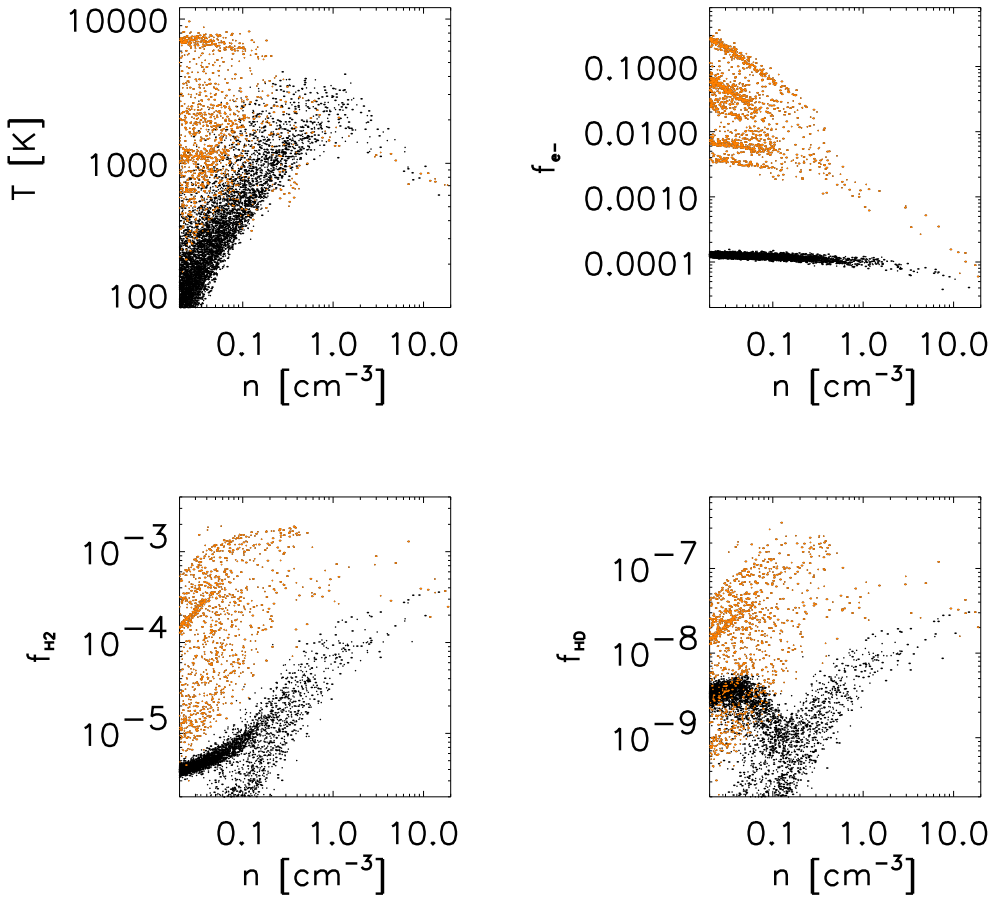

Figure 4.3: The properties of the primordial gas at redshift $z \sim 18$, at the end of the life of the eighth star. The SPH particles which have experienced an ionized phase within an H II region are colored in orange (gray), while those that have not are in black. Clockwise from the top-left, the temperature, free electron fraction, HD fraction, and H_2 fraction are plotted as functions of gas density. The relic H II region gas cools largely by adiabatic expansion, but, importantly, also by cooling facilitated by the high abundance of H_2 and HD molecules, which arises owing to the high electron fraction in this gas. The high electron fraction persists until the gas has collapsed to densities of $\gtrsim 10$ cm^{-3}, as can be seen in the top-right panel. The molecule fraction is highest at low densities for gas in which the molecules have not been destroyed by LW feedback, giving rise to the features seen at low densities in the bottom two panels.

fraction that persists for $\lesssim 500$ Myr (Johnson & Bromm, 2007), the increasing volume of the IGM occupied by relic H II regions implies an increase in the optical depth to LW photons in the vicinity of the first star formation sites. By a redshift of $z \sim 18$, eight stars have formed in our cosmological box and each has left behind a relic H II region.

As can be seen in Figs. 4.3 and 4.4, the gas inside the relic H II regions that have formed contains an H_2 fraction generally higher than the primordial abundance of 10^{-6}, and up to an abundance of $\sim 10^{-3}$ in the denser regions. This elevated fraction of H_2 inside the relic H II regions leads to a high optical depth to LW photons, $\tau_{\rm LW}$, through the relic H II regions. The column density through a relic H II region which recombines in the absence of LW radiation can become of the order of $N_{\rm H_2} \sim 10^{15}$ cm^{-2} (Johnson & Bromm, 2007). Because the molecules in the relic H II regions that we consider here are subject to LW feedback from neighboring star formation regions, the optical depth through these regions may in general be lower. However, the rapid rate of molecule formation in these regions, even considering the LW feedback from local star forming regions in our box, allows the molecule fraction to approach 10^{-4} as late as ~ 100 Myr after the death of the central star. This elevated molecule fraction combined with the growing volume-filling fraction of relic H II regions leads to an appreciable optical depth to LW photons, which generally increases with time as more stars form and create more relic H II regions. To quantify this effect, we calculate the average column density of H_2 molecules through a cubic region of side length l as the product of the length l and the volume averaged number density of H_2 molecules, given by

$$N_{\rm H_2} \simeq l \frac{\sum n_{\rm H_2} V}{\sum V} \, , \tag{4.15}$$

where the sum is over all of the SPH particles in the volume and $n_{\rm H_2}$ is the number density of H_2 at each of the SPH particles. The volume associated with each individual SPH particle, V, is estimated as $V \simeq m_{\rm SPH}/\rho$, where $m_{\rm SPH}$ is the mass of the SPH particle and ρ is the mass density of the gas at that particle. The optical depth to LW photons is then computed as (Draine & Bertoldi, 1996; Haiman et al., 2000)

$$\tau_{\rm LW} \simeq 0.75 \ln\left(\frac{N_{\rm H_2}}{10^{14}\ {\rm cm}^{-2}}\right). \tag{4.16}$$

Fig. 4.5 shows the optical depth to LW photons avergaged both over the central comoving 153 kpc h^{-1} of our cosmological box, in which the first star forms, and over the entire box,

for which the comoving side length is 460 kpc h^{-1}. Before the formation of the first star, the optical depth evolves largely owing to the cosmic expansion, following the relation $\tau_{\rm LW} \simeq n_{\rm H_2} l \propto (1+z)^2$, because the average H_2 fraction does not change appreciably. However, with the formation of the first star in our box at $z \simeq 23$ the optical depth begins to change dramatically in the inner portion of the box, first falling to a value of $\simeq 0.1$ due to the LW feedback from the first star and then steadily climbing to values $\gtrsim 2$ as copious amounts of molecules form inside the relic H II regions that accumulate as star formation continues.

The evolution of the optical depth averaged over the entire box is not as dramatic, as the fraction of the volume of the whole box occupied by relic H II regions is much smaller than the fraction of the central region that is occupied by these molecule-rich regions. However, the optical depth averaged over the whole box, which is a better estimate of the optical depth over cosmological distances, still rises to $\tau_{\rm LW} \gtrsim 1.5$ across our box, an appreciable value which will serve to impede the build-up of a cosmologically pervasive LW background.

4.2.4 Black Hole Accretion

Accretion onto Pop III relic black holes may be inefficient for some time following the formation of these objects, owing to the fact that Pop III stars photo-heat and evaporate the gas within the minihalos which host them (Johnson & Bromm, 2007; Yoshida et al., 2007a). Indeed, accretion onto Pop III relic black holes at close to the Eddington limit can only occur if the accreted gas has a density above $\sim 10^2$ cm^{-3}, and it is only in collapsing halos that such densities are achieved at the high redshifts at which the first stars formed (Johnson & Bromm, 2007). By assumption, all of the stars that are formed in our simulation are black hole-forming Pop III stars. If these black holes remain inside their host minihalos, then by tracking the evolution of the gas within these photo-evaporated host minihalos, we can learn when efficient accretion onto these Pop III relic black holes may occur.

The minihalo within which the first star forms at a redshift $z \sim 23$ resides within the relic H II region left by the first star. Due to the formation of a high fraction of molecules, and to the molecular cooling that ensues, the relic H II region gas cools down to temperatures $\sim 10^3$ K, below the virial temperature of this 10^6 M$_\odot$ minihalo. The gas then re-collapses into the minihalo, reaching a peak density of $n_{\rm res}$ at a redshift $z \sim 19$, or ~ 50 Myr after the formation of the first star. Fig. 4.6 shows the properties of the relic H II region gas as a function of distance from the center of this minihalo, at the time when the gas has collapsed

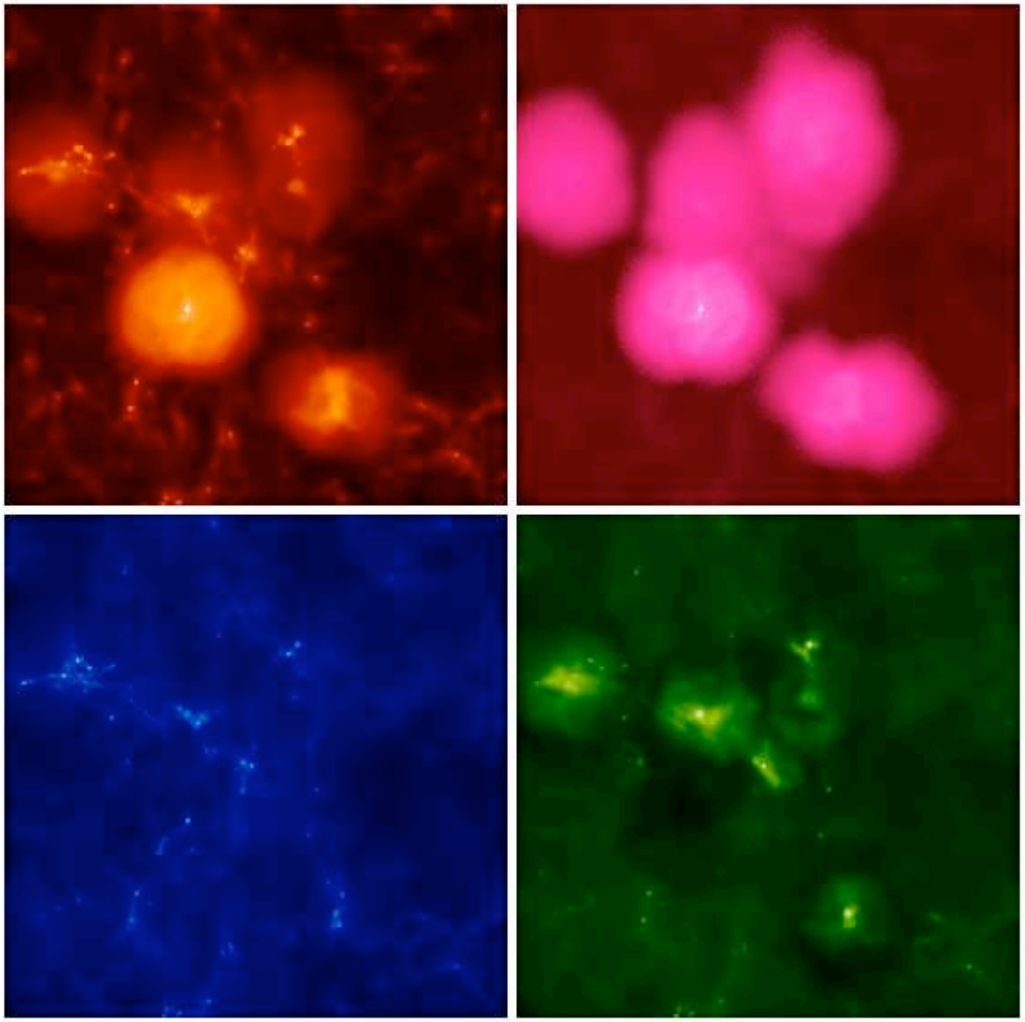

Figure 4.4: The properties of the primordial gas at the end of the life of the eighth star in our box, at redshift $z \sim 18$. Clockwise from top-left are the temperature, electron fraction, H_2 fraction, and density of the gas, in projection. Here we show the entire cosmological box, which is ~ 35 kpc. Note the high electron and H_2 fractions in the relic H II regions, where recombination is taking place. The elevated H_2 fraction in these regions raises the optical depth to LW photons through them significantly, as is illustrated in Fig. 5. The temperature in the older relic H II regions is not greatly elevated as compared to the temperature of the un-ionized gas, owing to the adiabatic and molecular cooling that takes place in these regions. The lighter shades denote higher values of the quantities plotted.

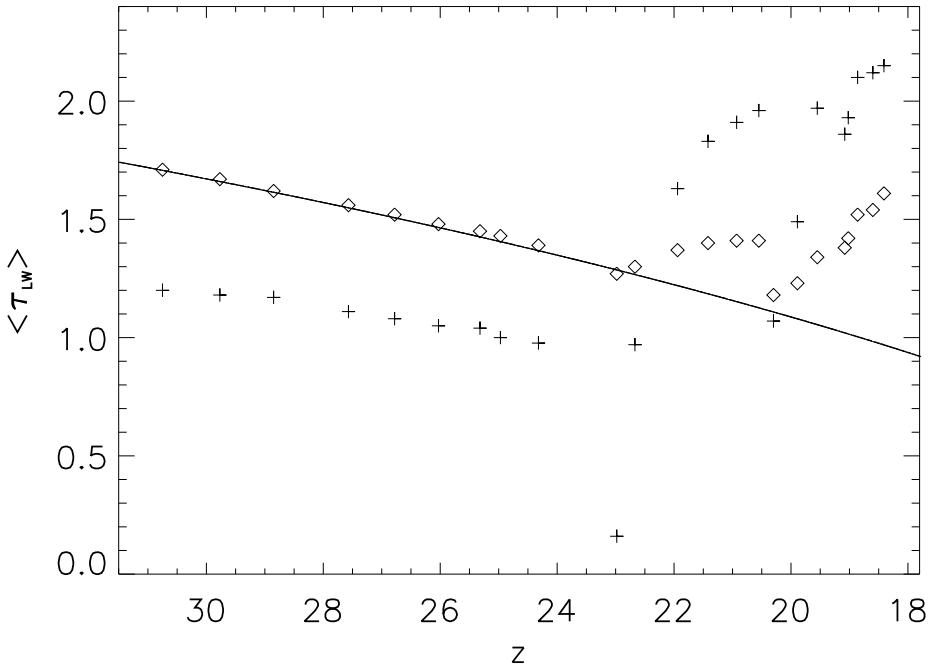

Figure 4.5: The optical depth to LW photons, $\tau_{\rm LW}$, averaged over two volumes in our box, as a function of redshift, z. The diamonds denote the optical depth averaged over the entire cosmological box, while the crosses denote the optical depth averaged only over a cube containing the inner comoving 153 kpc h^{-1} of the box, centered in the middle of the box with a volume one ninth that of the whole box. It is within this region that the first star forms and the star formation rate is higher than the average star formation rate over the whole box, and this is reflected in the higher local optical depth in this region as relic H II regions accumulate in the box. The average optical depth through the entire box also rises, but the increase is less dramatic. The solid line denotes the optical depth to LW photons, averaged over the whole box, that would be expected for the case that the gas maintains the average cosmological density everywhere and that the H_2 fraction does not change from the primordial value of 2×10^{-6}; for this case, the optical depth changes owing only to cosmic expansion. Note that the optical depth averaged over the whole box matches well this idealized case up until the first star forms at a redshift of $z \sim 23$. The temporary drops in the optical depth occur due to LW feedback when individual stars form.

to a density of $n_{\rm res}$. We cannot, with this simulation, resolve what happens once the gas collapses further and reaches higher densities. However, we can estimate the time it will take for the gas at the center of the halo to reach a density of $n \sim 10^2$ cm^{-3} as the free fall time of the gas, which is $t_{\rm ff} \sim 10$ Myr. Thus, a Pop III relic black hole at the center of this halo could be expected to begin accreting gas efficiently ~ 60 Myr after its formation. This is a significant delay, and could pose serious challenges to theories which predict that efficient accretion onto Pop III relic black holes can lead to these black holes becoming the supermassive black holes that power the quasars observed in the *Sloan Digital Sky Survey* at redshifts $z \gtrsim 6$ (Johnson & Bromm, 2007; Li et al., 2007).

4.2.5 HD Cooling in Relic H II Regions

While abundant molecules can form within relic H II regions, the LW feedback from neighboring star-forming regions can suppress the effect of this elevated fraction of molecules. The electron fraction remains high in relic H II regions for up to ~ 500 Myr in the general IGM, but in higher density regions where the gas is recollapsing, the electron fraction drops much more quickly. Figs. 4.3 and 4.6 show that the electron fraction drops to a value of $\lesssim 10^{-4}$, comparable to the electron fraction of the un-ionized gas, once the density of the relic H II region gas becomes $\gtrsim 10$ cm^{-3}. Thus, once the gas reaches these densities the ionized fraction will become too low to catalyze the formation of a high fraction of molecules, and of HD molecules in particular. Therefore, in order for HD to be an effective coolant of the primordial gas in relic H II regions, the abundanct HD molecules that are formed at densities $\lesssim 10$ cm^{-3} must not be destroyed by LW feedback from neighboring star-forming regions before the gas collapses to high densities and forms stars. If we estimate the timescale on which the relic H II region gas would collapse to form stars as the free-fall time of the gas, we find that the molecules must be shielded from photodissociating radiation for at least $t_{\rm ff} \gtrsim 10$ Myr in order for the high abundance of HD molecules to persist, so that the formation of so-called Pop II.5 stars might be enabled, with their hypothesized masses of ~ 10 M$_\odot$ (Johnson & Bromm, 2006).

We find that the relic H II region gas that re-collapses into the minihalo in which the first star formed, shown in Fig. 4.6, carries a high fraction of HD molecules, as LW feedback from neighboring stars does not effectively dissociate the molecules in this relatively dense and self-shielded gas. The HD fraction exceeds 10^{-7}, becoming an order of magnitude higher

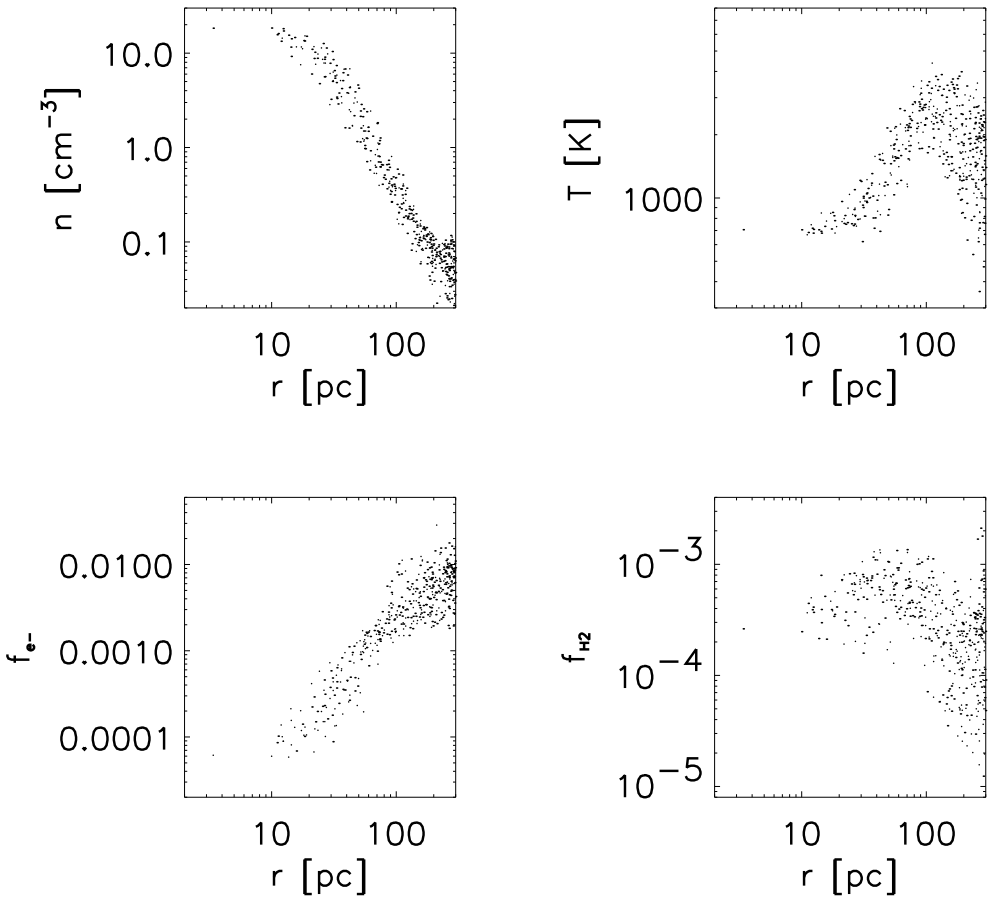

Figure 4.6: The properties of the relic H II region gas which recollapses into the minihalo which hosted the first star. Clockwise from the top-left are the density, temperature, H_2 fraction, and free electron fraction plotted as functions of distance from the center of the minihalo at the time when the density reaches $n_{\rm res}$, at a redshift of $z \sim 19$. The temperature of the gas has dropped to below 10^3 K, well below the virial temperature of the minihalo, owing to molecular cooling. Owing to the high electron fraction that persists in this relic H II region, the molecule fraction in this gas is higher than in the case of un-ionized primordial gas collapsing into a minihalo. Indeed, as can be seen in Fig. 4.3, the HD fraction is roughly an order of magnitude higher at these densities than in the case of un-ionized gas collapsing into a minihalo, which may allow for the efficient cooling of the gas to temperatures $T \gtrsim T_{\rm CMB}$ and so perhaps for the formation of metal-free stars with masses of the order of 10 $M_\odot$.

than its value for un-ionized primordial gas collapsing in a minihalo. Thus, for this case, HD cooling will likely be effective at higher densities as the gas collapses further, and we expect that a Pop II.5 star, with a mass of the order of 10 $M_{\odot}$, might form later on, if we were to run the simulation further (Johnson & Bromm, 2006; Nagakura & Omukai, 2005; Yoshida et al., 2007b). Had star formation taken place nearer this minihalo between the formation of the first star and the re-collapse of the gas into the host minihalo, then the molecule fraction would likely not be so elevated, and a higher mass metal-free star would be more likely to form. Thus, while in our simulation it appears that the first relic H II region that forms may give rise to Pop II.5 star formation, we emphasize that the possibility of the formation of Pop II.5 stars in relic H II regions is very dependent on the specific LW feedback that affects the gas in these regions.

4.2.6 Star Formation in the Presence of Radiative Feedback

To discern the effect the local radiative feedback from the first stars has on the star formation rate, we have compared the results obtained from our simulations with and without radiative feedback. By a redshift of $z \sim 18$, a total of nine star-forming regions were identified in our simulation without feedback, while at the same epoch eight stars had formed in our simulation including feedback. Thus, we find that the average star formation rate at redshifts $z \gtrsim 18$ is diminished by a factor of perhaps only $\lesssim 20$ percent due to local radiative feedback, although this result is subject to the small number statistics within our single cosmological box. Fig. 4.7 shows the locations of the sites of star formation for both cases, plotted in comoving coordinates against the projected density field. The orange squares denote sites where Pop III stars could have formed in the case without feedback, while the green dots denote sites where Pop III stars formed in the simulation including radiative feedback. Thus, the sites where star formation is suppressed by the radiative feedback are marked by the orange squares which are not filled by a green dot.

We point out, however, that we do not include LW feedback from stars which may have formed outside of our box, and hence it is possible that the overall LW feedback may be stronger than we find here. At redshift $z \sim 18$, we end the simulation, but note that star formation will likely take place at an increasing rate as the collapse fraction increases with time. This could lead to a continuous LW background produced within our box, different from the intermittent LW feedback produced by individual stars that occurs in the simulation

down to $z \sim 18$.

In addition, the limits of our resolution prohibit us from discerning the stronger shielding of H_2 molecules and I-front trapping that could occur within very dense collapsing minihalos (Ahn & Shapiro, 2007). However, we note that these authors find that the radiative feedback on collapsing minihalos from nearby stars generally does not greatly affect the final outcome of the collapse, as halos which collapse in the absence of radiative feedback generally also collapse when radiative feedback is applied (Susa & Umemura, 2006), roughly consistent with our results in the present work. Thus, our limited resolution may not substantially impact the results that we find for the slight suppression of star formation due to local radiative feedback, although higher resolution simulations will be necessary to more precisely study the full impact of radiative feedback from the first stars on the first protogalaxies.

4.3 Summary and Discussion

We have performed cosmological simulations which self-consistently account for the radiative feedback from individual Pop III stars, as they form in the course of the assembly of the first protogalaxies. We have solved in detail for the H II regions, as well as for the LW bubbles of these stars, wherein molecule-dissociating radiation effectively destroys H_2 and HD molecules. The local radiative feedback from the first stars is complex, and we find a variety of novel results on the evolution of the primordial gas, on the effects of the LW radiation from the first stars, on the nature of second generation star formation, and on black hole accretion.

While the LW radiation from the first stars can, in principle, greatly suppress Pop III star formation in the early universe, we find that a number of factors minimize the effectiveness of this negative feedback. Firstly, the LW radiation produced locally by individual stars is not uniform and constant, as LW feedback has been modeled in previous work (Ciardi & Ferrara, 2005; Mesinger et al., 2006), but rather is present only during the brief lifetimes of the individual stars that produce it. Thus, even if the molecules in collapsing minihalos and relic H II regions are destroyed by the radiation from individual stars, they will, at the early stages of Pop III star formation, have time to reform and continue cooling the primordial gas in between the times of formation of local stars. Furthermore, because the LW bubbles of individual Pop III stars extend only to $R_{\rm LW} \sim 5$ kpc from these sources, due to the short stellar lifetimes, the build up of a pervasive LW background would likely have to await the

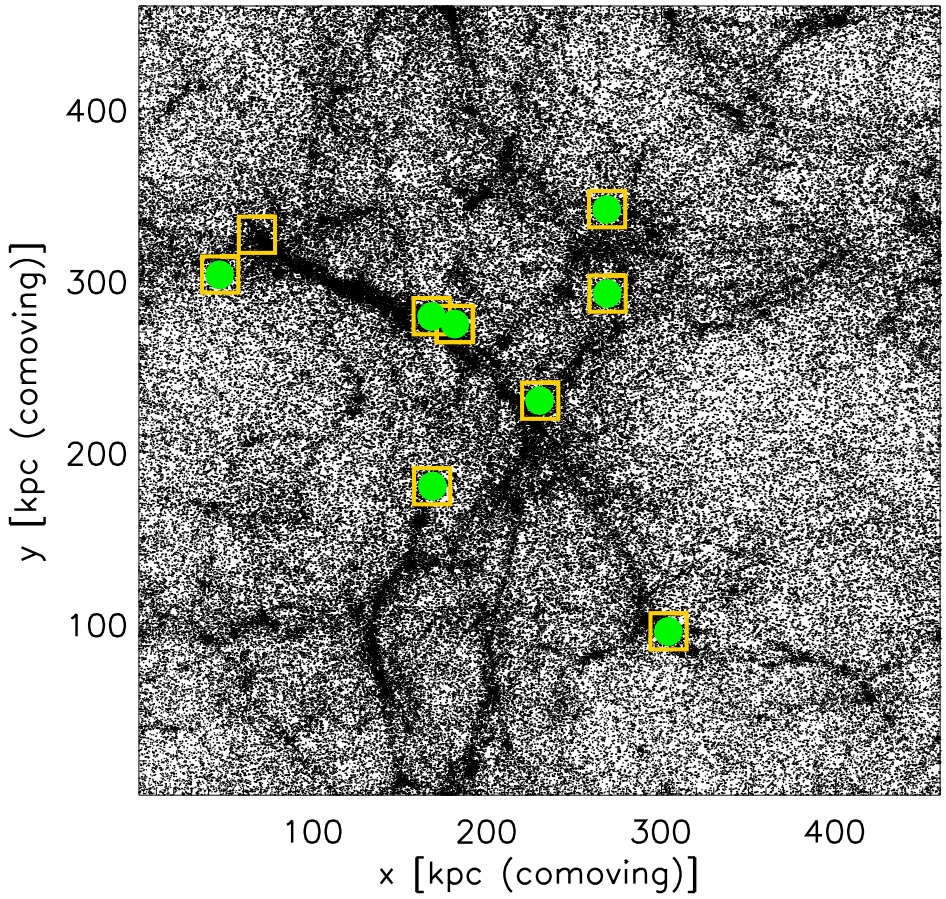

Figure 4.7: The sites of star formation with and without radiative feedback, at redshift $z \sim 18$. The black dots show the density field in our simulation box, in projection. The orange squares show the locations of minihalos in which Pop III star formation could take place, in our simulation without radiative feedback. The green dots show the sites where star formation takes place in our simulation including radiative feedback.

epoch of continuous star formation, which is fundamentally different from the epoch of the first stars, in which these sources shine for short periods within individual minihalos.

As star formation continues, the volume-filling fraction of relic H II regions increases as well, and this, combined with the high fraction of molecules that form in these regions, leads to an opacity to LW photons through the IGM which increases with time. This opacity can become of the order of $\tau_{\rm LW} \gtrsim 2$ through individual relic H II regions (Johnson & Bromm, 2007; Machacek et al., 2001, 2003; Oh & Haiman, 2002; Ricotti et al., 2001). Furthermore, as the volume-filling fraction of relic H II regions increases with time, $\tau_{\rm LW}$ through the general IGM may become similarly large, and this effect will have to be considered in future work which seeks to elucidate the effect of LW feedback on Pop III star formation.

We find that metal-free stars with masses of the order of 10 $M_{\odot}$, the postulated Pop II.5 stars (Greif & Bromm, 2006; Johnson & Bromm, 2006), might form from the molecule-enriched gas within the first relic H II regions, although we note that this may not occur in general, due to LW feedback from neighboring star-forming regions. This susceptibility to LW feedback is due to the fact that the high fraction of HD molecules which forms in the electron-rich, low density regions of relic H II regions must persist until this gas has had time to collapse to high densities and form stars. If LW feedback from neighboring star-forming regions destroys the molecules after the gas has collapsed to densities $\gtrsim 10$ cm^{-3}, then the abundance of HD molecules will not likely be elevated when the gas forms stars and Pop II.5 star formation may be suppressed. Because this implies that the molecules must be shielded from LW radiation for, at least, the free-fall time for gas with densities $\lesssim 10$ cm^{-3}, or $\gtrsim 10$ Myr, we conclude that Pop II.5 star formation in relic H II regions may occur only in the circumstances when local Pop III star formation is suppressed over such timescales. However, we also point out that the shielding provided by the high H_2 fraction in these relic H II regions may help to minimize the LW feedback from neighboring star-forming regions, and so may make Pop II.5 star formation in relic H II regions possible in many cases.

We find that the ionized primordial gas surrounding the first star formed in our simulation, at a redshift of $z \sim 23$, recombines and cools by molecular cooling to temperatures below the virial temperature of the minihalo that hosted this first star. Thus, this relic H II region gas is able to re-collapse to densities $\gtrsim 20$ cm^{-3} within this minihalo after ~ 50 Myr from the death of the star. It is predicted that many Pop III stars will collapse directly to form black holes with masses of the order of 100 $M_{\odot}$ (Heger et al., 2003), and if such a black hole resides within this host halo, then we find that it may begin accreting dense primordial gas at close

to the Eddington rate after $\sim$ 60 Myr from the time of its formation. This is an important consideration to be incorporated into models of the growth of the 10^9 $M_\odot$ black holes which have been observed at redshifts $\gtrsim$ 6, as it places constraints on the amount of matter that a given relic Pop III black hole could accrete by this redshift (Haiman & Loeb, 2001; Li et al., 2007; Volonteri & Rees, 2006).

Finally, by comparing the star formation rates which we derive from our simulation including radiative feedback with those derived from our simulation in which feedback is left out, we have seen that local radiative feedback from the first stars likely only diminishes the Pop III star formation rate by a factor of, at most, a few. In our simulation, in particular, we find that this rate is decreased by only $\lesssim$ 20 percent, although this may be less suppression than would be expected by the overall radiative feedback, as we did not include the possible effects of a global LW background. Future simulations which resolve densities higher than those reached here, and which self-consistently track the build-up of the LW background along with the IGM opacity to LW radiation, will be necessary to more fully explore the radiative effects of the first stars on the formation of the first galaxies. However, the goal of understanding the formation of the first galaxies is now clearly getting within reach, and the pace of progress is expected to be rapid.

5

The Observational Signature of the First H II Regions

One of the most important questions in modern cosmology is to understand how the first stars ended the cosmic dark ages at redshifts $z \lesssim 30$ (Barkana & Loeb, 2001; Bromm & Larson, 2004; Ciardi & Ferrara, 2005). Their emergence led to a fundamental transformation in the early Universe, from its simple initial state to one of ever increasing complexity. The emission from the hot, $T_{\rm eff} \sim 10^5$ K, photospheres of Pop III stars began the reionization of primordial hydrogen and helium in the IGM, although this process was completed only later on, when more massive galaxies formed (Fan et al., 2006a). In addition, the supernova explosions that ended the lives of massive Pop III stars distributed the first heavy elements into the IGM (Bromm et al., 2003; Greif et al., 2007; Tornatore et al., 2007; Wise & Abel, 2008b). This latter process might have had a significant impact on the physics of early star formation, as metal-enriched gas can cool more efficiently than primordial gas (Bromm & Loeb, 2003b; Jappsen et al., 2007, 2009a; Omukai et al., 2005).

Based on numerical simulations, a general consensus has emerged that the first stars formed in dark matter minihalos at $z \lesssim 30$, in isolation or at most as a small stellar multiple, and with typical masses of $M_* \sim 100$ M$_\odot$ (for a recent review, see Bromm et al., 2009). It is crucial to observationally test this key prediction. However, it has become evident that this will be very challenging. Even the exquisite near-IR ($\sim$ nJy) sensitivity of the upcoming *JWST* will not suffice to directly image such massive, single Pop III stars (Bromm et al., 2001b; Gardner et al., 2006), unless they explode as energetic pair-instability supernovae

(Heger & Woosley, 2002; Scannapieco et al., 2005b). The direct spectroscopic detection of recombination line emission from the H II region surrounding the Pop III star is beyond the capability of *JWST* as well, although such line emission might be detectable from primordial stellar populations inside more massive host halos (Johnson et al., 2009; Schaerer, 2002, 2003).

An alternative approach is to search for the global signature from many Pop III stars that formed in minihalos over large cosmic volumes (Haiman & Loeb, 1997). One such probe is the optical depth to Thomson scattering of CMB photons off free electrons along the line of sight, determined by the five-year *WMAP* measurement to be $\tau_e \simeq 0.09 \pm 0.02$ (Komatsu et al., 2009). This signal, however, is dominated by ionizing sources that must have formed closer to the end of reionization, with only a small contribution from Pop III stars formed in minihalos (Greif & Bromm, 2006; Schleicher et al., 2008). A second empirical signature is the combined bremsstrahlung emission from the H II regions around those minihalos that hosted Pop III stars. The resulting free-free radio emission leads to spectral distortions that might be detectable in the Rayleigh-Jeans part of the CMB spectrum. Recently, the ARCADE 2 experiment has attempted to measure such a free-free contribution from the epoch of the first stars (Kogut et al., 2006). The surprisingly strong signal found, however, cannot originate in early Pop III stars, and in any case would overwhelm the much weaker contribution from the first stars and galaxies (Seiffert et al., 2009). The most promising detection strategy might be to scrutinize the background from the redshifted 21 cm line of neutral hydrogen (Furlanetto et al., 2006). Once the central Pop III star has died, the relic H II region left behind would provide a bright source of 21 cm emission (Tokutani et al., 2009). Again, individual sources are much too weak to leave a detectable imprint, but the planned SKA might be able to detect the cumulative signal (Furlanetto, 2006; Lazio, 2008).

We here carry out radiation hydrodynamics simulations of the evolution of H II regions around massive Pop III stars in minihalos, giving us a detailed understanding of the properties of individual sources. We combine this with an approximate, Press-Schechter type analysis of the cosmological number density of minihalos as a function of redshift to derive the observational signature of the first H II regions, where we specifically focus on the free-free and 21 cm probes. In this sense, we organize our work as follows. In Section 5.2, we describe the simulation setup and our implementation of the radiative transfer scheme in the SPH code GADGET-2 (Springel, 2005). In Section 5.3, we discuss the properties of the first H II regions and their observational signature in terms of recombination radiation,

bremsstrahlung and 21 cm emission. Finally, in Section 5.4 we summarize our results and assess their implications. For consistency, all quoted distances are physical, unless noted otherwise.

5.1 Numerical Methodology

Our treatment of ionizing and photodissociating radiation emitted by massive Pop III stars is very similar to the methodology introduced in Johnson et al. (2007) and Yoshida et al. (2007a), with the exception that we here take the hydrodynamical response into account, self-consistently coupled to the chemical and thermal evolution of the gas. This allows us to model dense (D-type) as well as rarefied (R-type) ionization fronts, which is crucial for a proper treatment of the breakout of ionizing radiation. In the following, we describe our simulation setup, as well as the numerical implementation of the ray-tracing algorithm.

5.1.1 Simulation Setup

We perform our simulations in a cosmological box with linear size 200 kpc (comoving), and 256^3 particles per species, corresponding to a particle mass of $\simeq 17$ $M_\odot$ for dark matter and $\simeq 3$ $M_\odot$ for gas. The simulations are initialized at $z = 99$ with a fluctuation power spectrum determined by a ΛCDM cosmology with matter density $\Omega_m = 1 - \Omega_\Lambda = 0.27$, baryon density $\Omega_b = 0.046$, Hubble parameter $h = H_0/100$ km s^{-1} Mpc^{-1} $= 0.7$, where H_0 is the Hubble expansion rate today, and spectral index $n_s = 0.96$ (Komatsu et al., 2009). We use an artificially high fluctuation power of $\sigma_8 = 1.6$ to accelerate structure formation in our relatively small box, although the cosmological mean is given by $\sigma_8 = 0.81$. We take the chemical evolution of the gas into account by following the abundances of H, H^+, H^-, H_2, H_2^+, He, He^+, He^{++}, and e^-, as well as the three deuterium species D, D^+, and HD. We include all relevant cooling mechanisms, i.e. H and He collisional ionization, excitation and recombination cooling, bremsstrahlung, inverse Compton cooling, and collisional excitation cooling via H_2 and HD (Glover & Jappsen, 2007). We explicitly include H_2 cooling via collisions with protons and electrons, which is important for the chemical and thermal evolution of relic H II region gas (Glover & Abel, 2008).

We run the simulations until the first minihalo in the box has collapsed to a density of $n_H = 10^4$ cm^{-3}, at which point the gas has cooled to $\simeq 200$ K and becomes Jeans-unstable

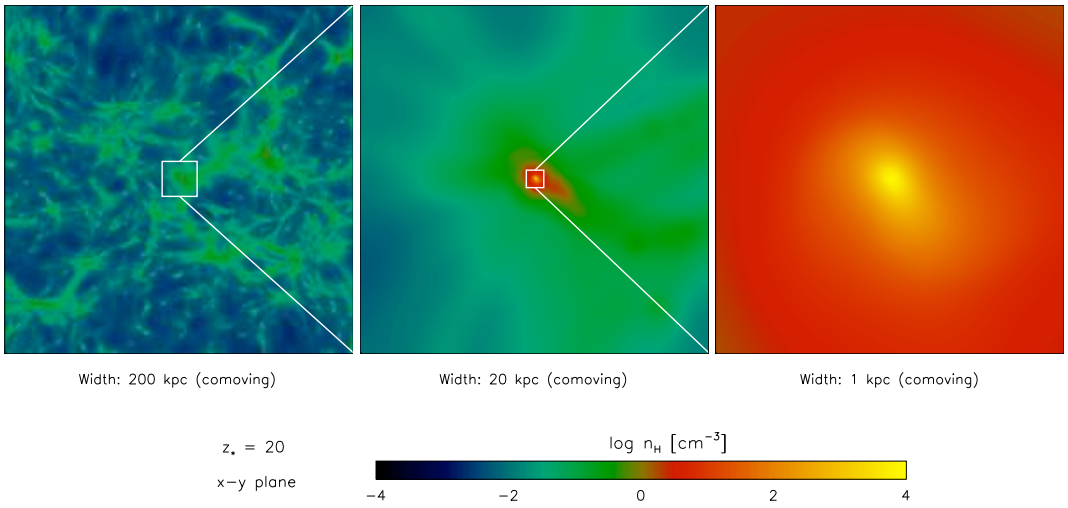

Figure 5.1: Sequential zoom-in on the first star-forming minihalo at $z_* \simeq 20$. Shown is the density-squared weighted average of the hydrogen density along the line of sight, just after the formation of the Jeans-unstable clump in a $\simeq 9.4 \times 10^5$ $M_\odot$ minihalo. The flattening of the core due to angular momentum conservation during the collapse is clearly visible, with the consequence that ionizing radiation from the central source breaks out anisotropically (see Fig. 5.3).

(Abel et al., 2002; Bromm et al., 2002). The first halo that fulfils this criterion collapses at $z_* \simeq 20$ and has a virial mass of $\simeq 9.4{\times}10^5$ $M_\odot$ and a virial radius of $\simeq 90$ pc. Highly resolved simulations have shown that at later times, the gas condenses further under the influence of self-gravity to $n_{\rm H} \sim 10^{21}$ cm^{-3}, where it becomes optically thick and forms a protostellar seed (Yoshida et al., 2008). Due to its residual angular momentum, the central clump flattens and likely evolves into an accretion disk. In our case, we find a flattened structure already at a density of $n_{\rm H} = 10^4$ cm^{-3} (see Fig. 5.1). The high temperature of the gas then leads to efficient accretion from the disk and it is commonly assumed that the protostar grows to ~ 100 $M_\odot$ within the Kelvin-Helmholtz time (Bromm & Loeb, 2004). However, we note that under certain conditions the disk may fragment to form multiple objects of smaller masses (Clark et al., 2008). Unfortunately, the details of the accretion phase and the concomitant radiative feedback are poorly understood, although some analytic investigations have been carried out (McKee & Tan, 2008; Tan & McKee, 2004). Under these circumstances it seems best to initialize the calculation of the H II region at the onset of the initial Jeans-instability, when the density exceeds $n_{\rm H} = 10^4$ cm^{-3}.

5.1.2 Ray-tracing Scheme

The procedure used to calculate the Strömgren sphere around the star for a given time-step Δt is similar to the ray-tracing scheme used in Johnson et al. (2007). We first designate an individual SPH particle as the source of ionizing radiation and create a spherical grid with typically 10^5 rays and 500 logarithmically spaced radial bins around the source particle. The minimum radius is set by the smoothing length of the central particle, while the maximum radius is chosen appropriately to encompass the entire H II region. This approach may seem crude compared to existing methods, which use adaptive grids (e.g. HEALPix; Górski et al., 2005), but the increased angular and radial resolution towards the center tend to mirror the existing density profile. However, one must proceed with care if the ionization front encounters dense clumps far from the source, where the resolution may no longer be sufficient.

In a single, parallel loop, the Cartesian coordinates of all particles are converted to spherical coordinates, such that their density and chemical abundances are mapped to the bins corresponding to their radius, zenith angle and azimuth, denoted by r, θ and ϕ, respectively. The volume of each particle is approximately given by $\Delta V \simeq h^3$, which transforms to $\Delta r = h$, $\Delta\theta = h/r$ and $\Delta\phi = h/(r\sin\theta)$. If the volume element of a particle intersects with the volume element of a bin, the particle contributes to the bin proportional to the density of the particle squared. This dependency ensures that overdense regions are not missed if the bin size is much larger than the smoothing length, which could occur far from the source where the grid resolution is poor. Accidental flash-ionization of minihalos is thus avoided. Once the above steps are complete, it is straightforward to solve the ionization front equation along each ray:

$$n_n r_{\rm I}^2 \frac{{\rm d}r_{\rm I}}{{\rm d}t} = \frac{\dot{N}_{\rm ion}}{4\pi} - \alpha_{\rm B} \int_0^{r_{\rm I}} n_e n_+ r^2 {\rm d}r \,, \tag{5.1}$$

where $r_{\rm I}$ denotes the position of the ionization front, $\dot{N}_{\rm ion}$ the number of ionizing photons emitted per second, $\alpha_{\rm B}$ the case B recombination coefficient, and n_n, n_e and n_+ the number densities of neutral particles, electrons and positively charged ions, respectively. We assume that the recombination coefficient remains constant at its value for 10^4 K, which is roughly the temperature of the H II and He III regions.

The numbers of H I/He I and He II ionizing photons are given by

$$\dot{N}_{\rm ion} = \frac{\pi L_*}{\sigma T_{\rm eff}^4} \int_{\nu_{\rm min}}^{\infty} \frac{B_\nu}{h\nu} {\rm d}\nu \,, \tag{5.2}$$

where h from now on denotes Planck's constant, σ Boltzmann's constant, and $\nu_{\rm min}$ the minimum frequency corresponding to the ionization threshold of H I and He II. We assume that massive Pop III stars emit a blackbody spectrum B_ν (in erg s^{-1} cm^{-2} Hz^{-1} sr^{-1}) with an effective temperature $T_{\rm eff}$ = dex(4.922, 4.975, 4.999) K and luminosity L_* = dex(5.568, 6.095, 6.574) L$_\odot$ for a 50, 100 and 200 M$_\odot$ star, respectively (Schaerer, 2002). This yields

$$\dot{N}_{\rm ion,HI/HeI} = [2.80, 9.14, 26.99] \times 10^{49}\ {\rm s}^{-1} \tag{5.3}$$

and

$$\dot{N}_{\rm ion,HeII} = [0.72, 4.14, 15.43] \times 10^{48}\ {\rm s}^{-1}\ . \tag{5.4}$$

We do not distinguish between the H II and He II region, which is a good approximation for massive Pop III stars (Osterbrock & Ferland, 2006). Their lifetimes are given by t_* = 3.7, 2.7 and 2.2 Myr, respectively. We neglect the effects of stellar evolution, which might lead to a decrease of the number of ionizing photons emitted at the end of the main sequence (Marigo et al., 2001; Schaerer, 2002), although recent investigations have shown that rotating Pop III stars remain on bluer evolutionary tracks and this effect might not be so strong (Vázquez et al., 2007; Woosley & Heger, 2006; Yoon & Langer, 2005).

To obtain a discretisation of the ionization front equation, we replace the integral on the right-hand side of equation (5.1) by a discrete sum:

$$\int_0^{r_{\rm I}} n_e n_+ r^2 {\rm d}r \simeq \sum_i n_{e,i} n_{+,i} r_i^2 \Delta r_i\ , \tag{5.5}$$

where Δr_i is the radial extent of bin i, and the sum extends from the origin to the position of the ionization front at the end of the current time-step Δt. The above equation describes the advancement of the ionization front due to an excess of ionizing photons compared to recombinations. Similarly, the left-hand side of equation (5.1), which models the propagation of the ionization front into neutral gas, is discretised by

$$n_n r_{\rm I}^2 \frac{{\rm d}r_{\rm I}}{{\rm d}t} \simeq \frac{1}{\Delta t} \sum_i n_{n,i} r_i^2 \Delta r_i\ , \tag{5.6}$$

where the sum now extends from the position of the ionization front at the previous time-step to its position at the end of the current time-step. We perform the above steps separately

for the H II and He III regions, since they require distinct heating and ionization rates. For the He III region, we replace the quantities n_n and n_+ in equation (5.1) with $n_n = f_{\mathrm{HeII}}\, n_{\mathrm{H}}$ and $n_+ = f_{\mathrm{HeIII}}\, n_{\mathrm{H}}$, where f_X is the number density of species X relative to n_{H}. We adopt a rate of $\alpha_{\mathrm{B}} = 1.3 \times 10^{-12}$ cm^3 s^{-1} for He III recombinations to He II (Osterbrock & Ferland, 2006). Applying the same prescription to the H II region, we find $n_n = (f_{\mathrm{HI}} + f_{\mathrm{HeI}})\, n_{\mathrm{H}}$ and $n_+ = (f_{\mathrm{HII}} + f_{\mathrm{HeII}})\, n_{\mathrm{H}}$. Similarly, we adopt a rate of $\alpha_{\mathrm{B}} = 2.6 \times 10^{-13}$ cm^3 s^{-1} for hydrogen and helium recombinations to the ground state (Osterbrock & Ferland, 2006). We initialize the calculation of the H II region at the boundary of the He III region, since hydrogen and helium are maintained in their first ionization states by recombinations of He III to He II (Osterbrock & Ferland, 2006). We note that the exact position of the ionization front is not restricted to integer multiples of our pre-defined radial bins, but may instead lie anywhere in between. For this purpose we adopt a simple linear scaling of the number of ionizations and recombinations as a function of the relative position of the ionization front. The most expensive step in terms of computing time is the assignment of the density and the chemical abundances to the grid, while the ray-tracing itself requires only a negligible amount of ressources.

5.1.3 Photoionization and Photoheating

Once the extent of the H II and He III region have been determined, the SPH particles within these regions are assigned an additional variable that stores their distance from the source. This information is then passed to the chemistry solver, which determines the relevant ionization and heating rates, given by

$$k_{\mathrm{ion}} = \int_{\nu_{\mathrm{min}}}^{\infty} \frac{F_\nu \sigma_\nu}{h\nu} \mathrm{d}\nu \tag{5.7}$$

and

$$\Gamma = n_n \int_{\nu_{\mathrm{min}}}^{\infty} F_\nu \sigma_\nu \left(1 - \frac{\nu_{\mathrm{min}}}{\nu}\right) \mathrm{d}\nu \,, \tag{5.8}$$

where F_ν and σ_ν denote the incoming specific flux and ionization cross section, respectively. For the case of a blackbody,

$$F_\nu = \frac{L_*}{4\sigma T_{\mathrm{eff}}^4 r^2} B_\nu \,, \tag{5.9}$$

where r is the distance from the source. The resulting rates are given by

$$k_{\rm ion,HI} = \frac{[0.45, 1.32, 3.69] \times 10^{-6}}{(r/{\rm pc})^2} \ {\rm s}^{-1} \ , \tag{5.10}$$

$$k_{\rm ion,HeI} = \frac{[0.42, 1.43, 4.29] \times 10^{-6}}{(r/{\rm pc})^2} \ {\rm s}^{-1} \ , \tag{5.11}$$

$$k_{\rm ion,HeII} = \frac{[0.67, 3.72, 13.57] \times 10^{-8}}{(r/{\rm pc})^2} \ {\rm s}^{-1} \ , \tag{5.12}$$

$$\Gamma_{\rm HI} = n_{\rm HI} \frac{[0.40, 1.28, 3.74] \times 10^{-17}}{(r/{\rm pc})^2} \ {\rm erg \ s^{-1} \ cm^{-3}} \ , \tag{5.13}$$

$$\Gamma_{\rm HeI} = n_{\rm HeI} \frac{[0.41, 1.57, 4.94] \times 10^{-17}}{(r/{\rm pc})^2} \ {\rm erg \ s^{-1} \ cm^{-3}} \ , \tag{5.14}$$

$$\Gamma_{\rm HeII} = n_{\rm HeII} \frac{[0.72, 4.46, 17.13] \times 10^{-19}}{(r/{\rm pc})^2} \ {\rm erg \ s^{-1} \ cm^{-3}} \tag{5.15}$$

for a 50, 100 and 200 $M_\odot$ Pop III star, respectively. These are taken into account every time-step, while the ray-tracing is performed only every fifth time-step. Since the hydrodynamic time-step is generally limited to one twentieth of the sound-crossing time through the kernel, our treatment of the coupled evolution of the ionization front and the hydrodynamic shock is roughly correct. The computational cost of runs with and without ray-tracing are typically within a factor of a few.

5.1.4 Photodissociation and Photodetachment

The final ingredient in our algorithm is the inclusion of molecule-dissociating radiation. This effect turns out to be of only minor importance in the present study, but will render our algorithm capable of addressing a general set of early Universe applications. Molecular hydrogen is the most important coolant in low-temperature, primordial gas, but is easily destroyed by radiation in the LW bands between 11.2 and 13.6 eV. The small residual H_2 fraction in the IGM leads to a very small optical depth over cosmological distances, such that even a small background can have a significant effect (Glover & Brand, 2001; Haiman et al., 2000; Johnson et al., 2007). In our implementation, we do not take self-shielding into account, which becomes important for H_2 column densities $\gtrsim 10^{14}$ cm^{-2} (Draine &

Bertoldi, 1996). Such a high column density is difficult to achieve in minihalos, and is more likely to occur within the virial radius of the first galaxies (Oh & Haiman, 2002). However, the onset of turbulence in the first galaxies likely leads to a reduction of self-shielding via Doppler shifting (Greif et al., 2008; Wise & Abel, 2007a). For this reason we treat the photodissociation of H_2 in the optically thin limit, such that the dissociation rate in a volume limited by causality to a radius $r = c\,t_*$ is given by $k_{H_2} = 1.1 \times 10^8 F_{LW}\ s^{-1}$, where F_{LW} is the integral of the specific flux F_ν over the LW bands, resulting in

$$k_{H_2} = \frac{[1.27, 3.38, 9.07] \times 10^{-7}}{(r/\mathrm{pc})^2}\ s^{-1} \tag{5.16}$$

for a 50, 100 and 200 $M_\odot$ Pop III star, respectively. Finally, we equate the photodissociation rate of hydrogen deuteride to that of molecular hydrogen. For the reasons discussed in Johnson et al. (2007), we do not explicitly include photodetachment of H^- and photodissociation of H_2^+.

5.2 Observational Signature

In the following, we discuss the direct observational signature of the first H II regions in terms of recombination radiation, as well as their indirect signature in terms of a global radio background produced by bremsstrahlung and 21 cm emission.

5.2.1 Build-up of H II Region

The build-up of the first H II regions by Pop III stars in minihalos was treated in one dimension by Kitayama et al. (2004) and Whalen et al. (2004), and in three dimensions by Alvarez et al. (2006a), Abel et al. (2007) and Yoshida et al. (2007a). They found that recombinations initially balanced ionizations within the virial radius of the host halo, leading to the formation of a D-type ionization front. Breakout occured after the density dropped sufficiently for the ionization front to race ahead of the hydrodynamic shock, becoming R-type. The hydrodynamic response of the gas is self-similar, since minihalos approximately resemble singular isothermal spheres (Alvarez et al., 2006a; Shu et al., 2002). The relevant parameters are set by the temperature of the singular isothermal sphere and the H II region, which in our case are $T \simeq 200$ and $\simeq 10^4$ K, respectively.

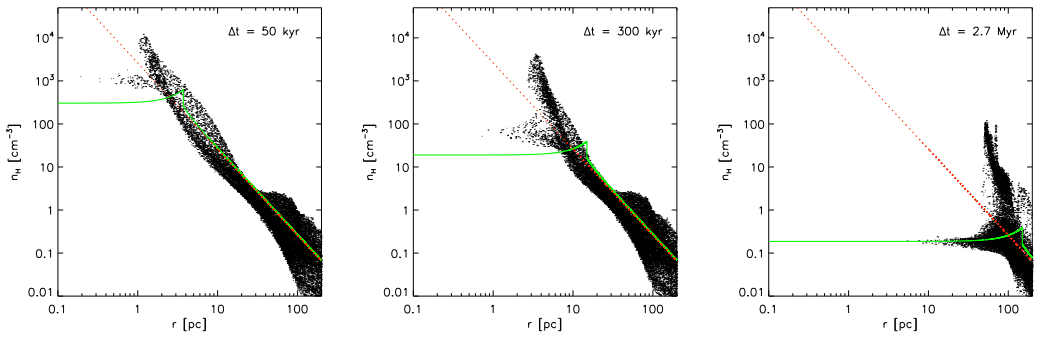

Figure 5.2: The hydrodynamic response of the gas to photoheating by a 100 $M_\odot$ Pop III star after 50 kyr, 300 kyr, and 2.7 Myr (from left to right). Shown is the hydrogen density as a function of radius for the simulation (black dots) and the analytic Shu et al. (2002) solution (green solid line), as well as the initial density profile of a singular isothermal sphere with 200 K (red dotted line). The functional form of the analytic solution is reproduced perpendicular to the disk, where the ionization front breaks out after only a few 10 kyr. However, this is not the case in the plane of the disk, where the gas remains neutral and dense until the end of the star's lifetime.

In Fig. 5.2, we compare the density profile of the Shu et al. (2002) solution to the simulation for the case of a 100 $M_\odot$ Pop III star. Interestingly, we find a clear deviation from the ideal, spherically symmetric solution already during the D-type phase, which is caused by the anisotropic collapse of the minihalo. Due to angular momentum conservation, the gas spins up and forms a flattened, disk-like structure at a density of 10^4 cm^{-3}, which can be seen in the right panel of Fig. 5.1, and in the left panel of Fig. 5.2, where it is evident that the density dispersion is almost an order of magnitude within the central $\simeq$ 10 pc. In response to this anisotropy, which is further amplified by the density-squared dependence of recombinations, the ionization front first breaks out perpendicular to the disk, where the column density is lowest. This is visible in the left and middle panels of Fig. 5.3, as well as in Fig. 5.2, where the Shu et al. (2002) solution is approximately reproduced perpendicular to the disk, while the plane of the disk remains neutral and dense. Once the ionization front becomes R-type, spherical symmetry is asymptotically restored and the H II region expands to $r_{\rm HII} \simeq$ 1.9, 2.7 and 3.7 kpc for the 50, 100 and 200 $M_\odot$ Pop III star, respectively. We find that He II ionizing photons within the He III region increase the central temperature by a factor of $\simeq$ 1.5, leaving only a small imprint on the dynamical evolution of the H II region

(see Yoshida et al., 2007a). However, the He II λ1640 recombination line within the He III region may be used as a distinct probe for the presence of massive Pop III stars (Bromm et al., 2001b; Oh, 2001; Schaerer, 2002; Tumlinson et al., 2001). In the following, we use the results obtained in this section to determine the observational signature of the first H II regions.

5.2.2 Recombination Radiation from Individual H II Regions

The strongest direct signature of the first H II regions is likely generated by recombination radiation within the H II region, since photons above the Lyman limit are absorbed by dense gas in the host halo. We here concentrate on the Hα line, since Lyα photons are scattered out of resonance by the neutral IGM, creating extended Lyα halos around high-redshift sources (Loeb & Rybicki, 1999). In the following, we estimate the total flux of the H II region in the Hα line and compare it to the expected sensitivity of the Mid-Infrared Instrument (MIRI) on *JWST* at $\sim$ 10 μm wavelengths (Gardner et al., 2006). The spatial resolution is limited by diffraction, such that a scale of $\simeq$ 1 kpc at $z = 20$ is marginally resolved, which allows us to approximate the H II region as a point source. Using the simulation output, the total luminosity is given by

$$L_{\mathrm{H}\alpha} = j_{\mathrm{H}\alpha} \sum_i \frac{m_i}{\rho_i} \left(\frac{X \rho_i}{m_{\mathrm{H}}} \right)^2 f_{e,i} f_{\mathrm{HII},i} \,, \tag{5.17}$$

where $j_{\mathrm{H}\alpha}$ is the emissivity in the Hα line at 10^4 K (Osterbrock & Ferland, 2006), $X = 0.76$ is the primordial mass fraction of hydrogen, m_{H} is the mass of the hydrogen atom, m_i and ρ_i are the mass and density of particle i, respectively, and the sum is over all particles in the simulation box. From the total luminosity, we determine the observed flux with the inverse-square law

$$F_{\mathrm{H}\alpha} = \frac{L_{\mathrm{H}\alpha}}{4\pi D_{\mathrm{L}}^2} \,, \tag{5.18}$$

where D_{L} is the cosmological luminosity distance. In Fig. 5.4, we show the observed flux for a 50, 100 and 200 $\mathrm{M}_\odot$ Pop III star as a function of time. Evidently, the H II region is brightest before breakout, when the density in the host halo is still high, and peaks around $F_{\mathrm{H}\alpha} = 10^{-23}$ erg s^{-1} cm^{-2}. For a 10 σ detection with an exposure time of 100 hours, the spectrograph on MIRI exhibits a typical limiting sensitivity of $\simeq 10^{-18}$ erg s^{-1} cm^{-2} (Panagia, 2005), implying that the first H II regions are five orders of magnitude too faint for a direct detection.

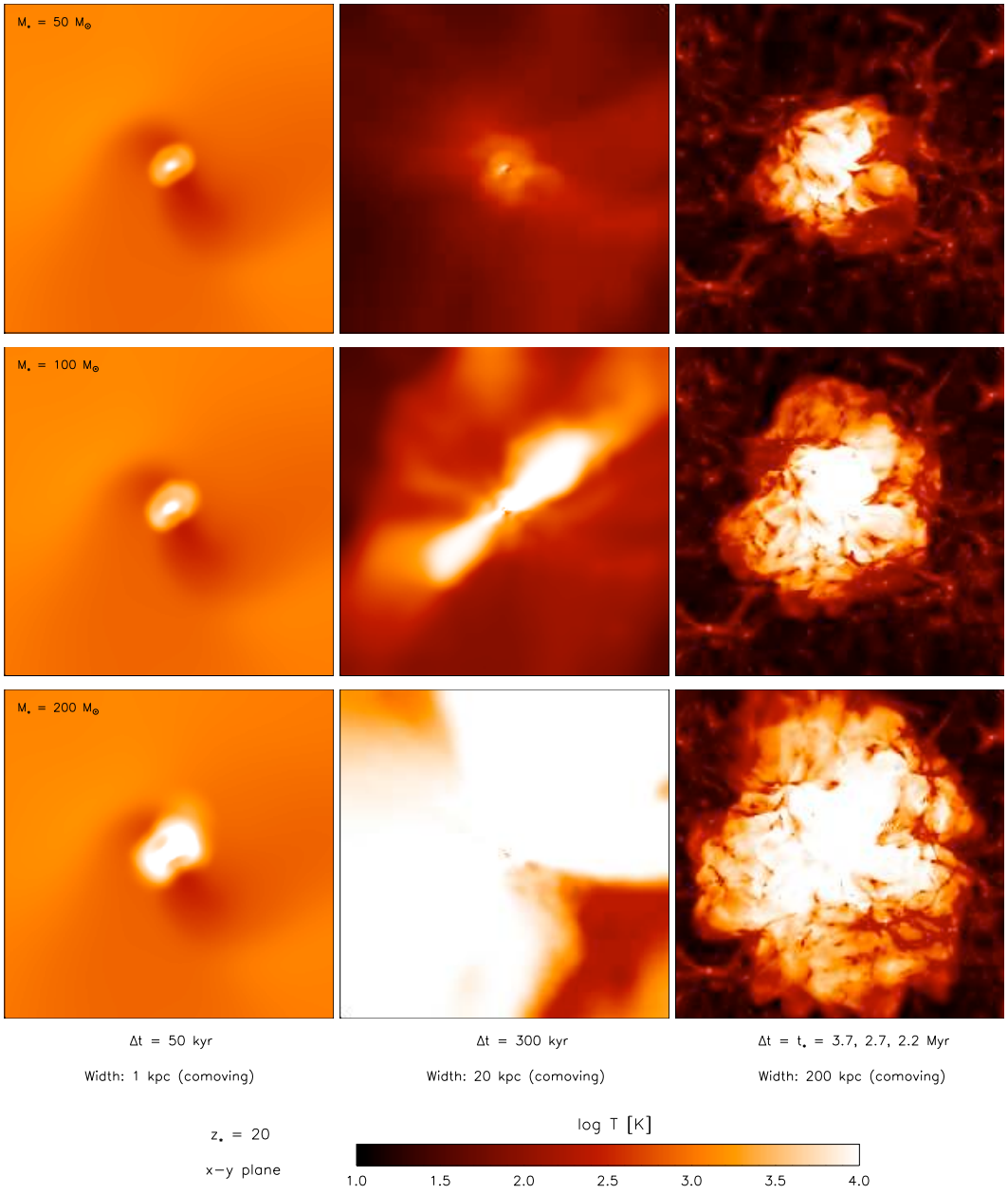

Figure 5.3: The H II region created by a 50, 100 and 200 $M_\odot$ Pop III star (from top to bottom) after 50 kyr, 300 kyr, and at the end of the star's lifetime (from left to right). Shown is the density-squared weighted average of the temperature along the line of sight. The spiral structure of the central clump as well as the resulting anisotropic breakout of the ionization front are clearly visible. For increasing stellar mass and ionizing photon output, breakout occurs earlier and is more isotropic. Once the ionization front becomes R-type, spherical symmetry is asymptotically restored and the H II region expands to a final radius of $r_{\rm HII} \simeq 1.9$, 2.7 and 3.7 kpc after 3.7, 2.7 and 2.2 Myr, respectively.

We must therefore resort to indirect methods that rely on their cumulative signal. One such signature is the cosmic infrared background (CIB), where the redshifted Lyα recombination photons from $z \sim 10$ – 20 might contribute at a detectable level (Kashlinsky et al., 2005; Santos et al., 2002). Minihalos, however, are not expected to be important sources for the CIB, as opposed to more massive dark matter halos that host the first galaxies (Greif & Bromm, 2006). This leads us to consider the radio background as a key diagnostic of the Pop III minihalo formation site.

5.2.3 Radio Background Produced by Bremsstrahlung

Next to recombination radiation, the first H II regions emit bremsstrahlung via thermal motions of electrons in an ionized medium. In line with our conlusions of the previous section, the signature from an individual H II region is much too faint to be detected. However, their cumulative radio emission might be strong enough to be detected by the upcoming SKA. We will here further explore this possibility (for a review of earlier work, see Furlanetto et al., 2006).

Solving the cosmological radiative transfer equation, it is straightforward to derive a simple expression for the observed radio background J_ν (in erg s^{-1} cm^{-2} Hz^{-1} sr^{-1}):

$$J_\nu = \int_0^{t_{H,0}} \frac{j_\nu}{(1+z)^3} c \, \mathrm{d}t \, , \tag{5.19}$$

where $t_{H,0}$ is the present Hubble time and j_ν is the specific emissivity of bremsstrahlung, given by

$$j_\nu = \epsilon_{\rm ff} \left\langle n_e^2 \right\rangle \left(T / 10^3 \, \mathrm{K} \right)^{-1/2} \, , \tag{5.20}$$

where $\epsilon_{\rm ff} \simeq 10^{-39}$ erg s^{-1} cm^3 Hz^{-1} sr^{-1}, $\left\langle n_e^2 \right\rangle$ is the volume-averaged electron density, and T is the temperature (Rybicki & Lightman, 1979). We universally assume $T = 10^3$ K, since the H II region cools quite rapidly to $\sim 10^3$ K via inverse Compton losses and adiabatic expansion once the star has died (e.g. Greif et al., 2007; Yoshida et al., 2007a). Furthermore, we assume $j_\nu = 0$ at $z < 6$, since photoheating during reionization evaporates minihalos (Dijkstra et al., 2004). This leads to:

$$J_\nu = c \, \epsilon_{\rm ff} \int_\infty^6 \frac{\left\langle n_e^2 \right\rangle}{(1+z)^3} \left| \frac{\mathrm{d}t}{\mathrm{d}z} \right| \mathrm{d}z \, , \tag{5.21}$$

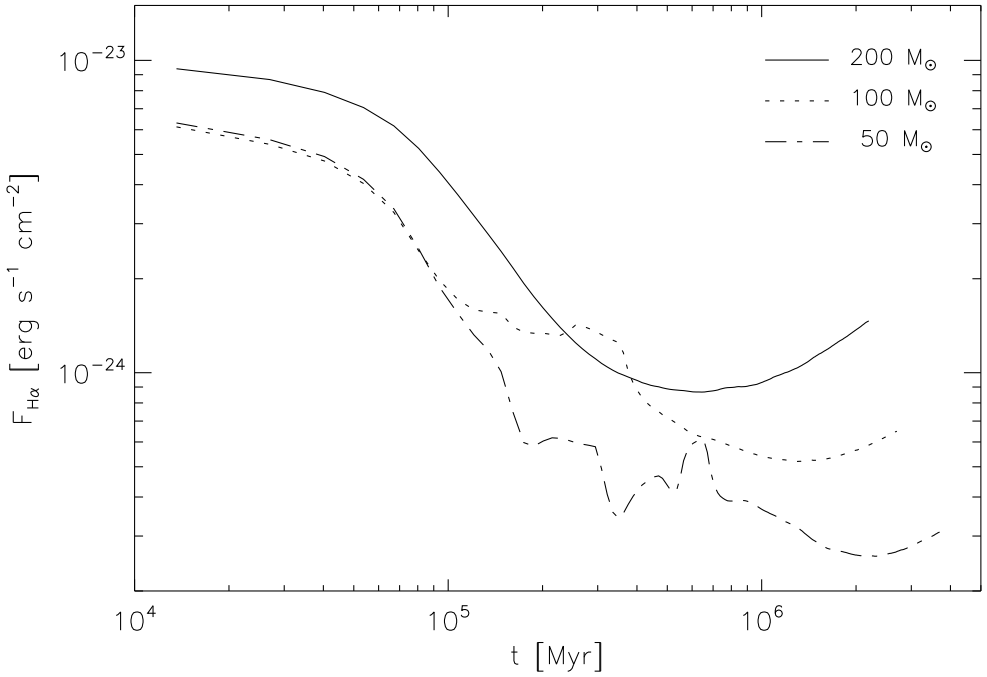

Figure 5.4: The flux in the Hα line emitted by recombination radiation from ionized gas around a 50 (dot-dashed line), 100 (dotted line) and 200 $M_\odot$ (solid line) Pop III star, shown as a function of time. Evidently, the H II region is brightest before breakout, when the density in the minihalo is still high, and peaks around $F_{\mathrm{H}\alpha} = 10^{-23}$ erg s^{-1} cm^{-2}. For a $10\,\sigma$ detection and an exposure time of 100 hours, the limiting sensitivity of the MIRI spectrograph on *JWST* is approximately 10^{-18} erg s^{-1} cm^{-2}, indicating that the first H II regions are five orders of magnitude too faint for a direct detection. The bumps in the 50 and 100 $M_\odot$ cases are caused by the ionization of dense gas near the host halo. In the 200 $M_\odot$ case, the ionization front propagates much too rapidly for a similar effect.

where we relate $\left\langle n_e^2 \right\rangle$ to the number density of minihalos according to:

$$\left\langle n_e^2 \right\rangle \simeq t_{\rm rec}\, n_{\rm H,b}^2\, V_{\rm HII} \left| \frac{{\rm d}N_{\rm ps}}{{\rm d}z} \right| \left| \frac{{\rm d}z}{{\rm d}t} \right| \,. \tag{5.22}$$

Here, $t_{\rm rec} = (\alpha_{\rm B}\, n_{\rm H,b})^{-1}$ denotes the recombination time for hydrogen atoms, $\alpha_{\rm B}$ their recombination rate for $T = 10^3$ K, $n_{\rm H,b}$ the background density, $N_{\rm ps}$ the number of minihalos per comoving volume, $V_{\rm HII} = N_{\rm ion}/n_{\rm H,b,0}$ the comoving volume of an individual H II region, which is independent of redshift, and $N_{\rm ion} = \dot{N}_{\rm ion}\, t_*$ the total number of ionizing photons emitted per Pop III star (see Section 5.2). In the above equation, we have implicitly assumed that H II regions survive for a recombination time, and that all ionizing photons escape into the IGM, which is a good approximation for massive Pop III stars in minihalos (Alvarez et al., 2006b). We note that in the range of redshifts considered here, the recombination time is larger than the stellar lifetime and smaller than the age of the Universe. In principle, one must also account for the clustering of minihalos (biasing), which reduces the net volume filling factor of H II regions (Greif & Bromm, 2006; Iliev et al., 2003; Mo & White, 1996). However, it is extremely difficult to determine the importance of this effect, since (i) the actual overlap depends on the relative separation of minihalos, and (ii) previous ionization allows a nearby H II region to become larger than usual. We therefore neglect biasing, but keep in mind that the actual signal may be somewhat lower.

In equation (5.22), the number density of minihalos is given by

$$N_{\rm ps}\,(z) = \int_{M_{\rm min}}^{M_{\rm max}} n_{\rm ps}\,(z, M)\,{\rm d}M \,, \tag{5.23}$$

where $n_{\rm ps}$ is the well-known Press-Schechter mass function (Press & Schechter, 1974). The minimum mass required for efficient cooling within a Hubble time may be found in Trenti & Stiavelli (2009):

$$M_{\rm min} \simeq 10^6\ {\rm M}_\odot \left(\frac{1+z}{10} \right)^{-2} \,, \tag{5.24}$$

while the maximum mass is set by the requirement that cooling must be dominated by molecular hydrogen, i.e. the virial temperature must not exceed $T \simeq 10^4$ K for atomic hydrogen

cooling, resulting in (e.g. Barkana & Loeb, 2001)

$$M_{\rm max} \simeq 2.5 \times 10^7 \, {\rm M}_\odot \left(\frac{1+z}{10} \right)^{-3/2} \quad . \tag{5.25}$$

We have found that our results are only marginally affected by the upper mass limit, but depend sensitively on the lower mass limit, since most minihalos reside at the lower end of the halo distribution function.

After combining the above equations, we obtain

$$J_\nu \simeq \frac{c \, \epsilon_{\rm ff} \, N_{\rm ion}}{\alpha_{\rm B}} N_{\rm ps} \, (z = 6) \ , \tag{5.26}$$

which, for an IMF consisting solely of 100 $\rm M_\odot$ Pop III stars, yields

$$J_\nu \simeq 300 \ {\rm mJy \ sr^{-1}} \ . \tag{5.27}$$

The brightness temperature, $T_b = c^2 J_\nu / 2 k_{\rm B} \nu^2$, is given by

$$T_b \simeq 1 \ {\rm mK} \left(\frac{\nu}{100 \ {\rm MHz}} \right)^{-2} \quad . \tag{5.28}$$

In the following, we investigate whether a signal of this magnitude is observable by the upcoming SKA.

The sensitivity of radio instruments is generally defined by the ratio of the effective collecting area A_e to the system temperature $T_{\rm sys}$. For the SKA with its proposed aperture array configuration at low frequencies, $A_e / T_{\rm sys} \simeq 5 \times 10^3 \ {\rm m^2 \ K^{-1}}$ at 100 MHz [1]. In this range the system temperature is dominated by Galactic synchrotron emission, for which a useful approximation is given by $T_{\rm sky} \simeq 180 \ {\rm K} \, (\nu / 180 \ {\rm MHz})^{-2.6}$ (Furlanetto et al., 2006), resulting in $T_{\rm sys} \simeq 800$ K and $A_e \simeq 4 \times 10^6 \ {\rm m^2}$. The minimum angular resolution for an array filling factor of unity at 100 MHz is approximately $15'$. At higher resolution, the sensitivity decreases much too rapidly for effective imaging. In Fig. 5.5, we compare the sensitivity of the SKA for a $10 \, \sigma$ detection, a bandwidth of $\Delta \nu_{\rm obs} = 1$ MHz, and an integration time of 1000 h to the brightness temperature and specific flux expected for free-free emission. Although the free-free signal is in principle detectable by the SKA, we have neglected biasing as well as

[1] http://www.skatelescope.org

radiative feedback in the form of a global LW background, which attenuates star formation in minihalos (Johnson et al., 2007, 2008). Another complicating issue is the overlap with 21 cm emission, which makes it nearly impossible to isolate the contribution from bremsstrahlung. In consequence, we do not believe that this signal will be observable in the near future.

5.2.4 Radio Background Produced by 21 cm Emission

Perhaps the most promising observational signature comes from 21 cm emission of the relic H II region gas once the star has died, a prospect that was already investigated by Tokutani et al. (2009). An emission signal requires the spin temperature T_S of neutral hydrogen to be greater than the temperature of the CMB, with its relative brightness determined by T_S and the size of the H II region. The spin temperature is set by collisional coupling with neutral hydrogen atoms, protons and electrons, as well as radiative coupling to the CMB. Furthermore, it may be modified by the so-called Wouthuysen-Field effect, which describes the mixing of spin states due to the absorption and re-emission of Lyα photons (Field, 1959; Wouthuysen, 1952). The color temperature of the Lyα background is determined by the ratio of excitations to de-excitations, which approaches the kinetic gas temperature at high redshifts, where the optical depth to Lyα scattering is very large (Furlanetto et al., 2006). In this case, adopting the Rayleigh-Jeans approximation and assuming $T_S \gg T_*$, where $T_* = h\nu_{21}/k_{\rm B} = 68$ mK is the temperature associated with the 21 cm transition, the spin temperature may be written as (Madau et al., 1997)

$$T_S = \frac{T_\gamma + (y_c + y_\alpha)\, T}{1 + y_c + y_\alpha} \,, \tag{5.29}$$

where T_γ is the temperature of the CMB. The collisional coupling coefficient y_c is approximately given by

$$y_c = \frac{T_*}{A_{21} T} \left(n_{\rm HI}\kappa_{\rm HI} + n_e \kappa_e\right) \,, \tag{5.30}$$

where $A_{21} = 2.85{\times}10^{-15}$ s^{-1} is the Einstein A-coefficient for the 21 cm transition, and $\kappa_{\rm HI}$ and κ_e are the effective single-atom rate coefficients for collisions with neutral hydrogen atoms and electrons, respectively. Good functional fits in the temperature range 100 K $\lesssim T \lesssim 10^4$ K are given by

$$\kappa_{\rm HI} = 10^{-11}\, T^{1/2} \text{ cm}^3 \text{ s}^{-1} \tag{5.31}$$

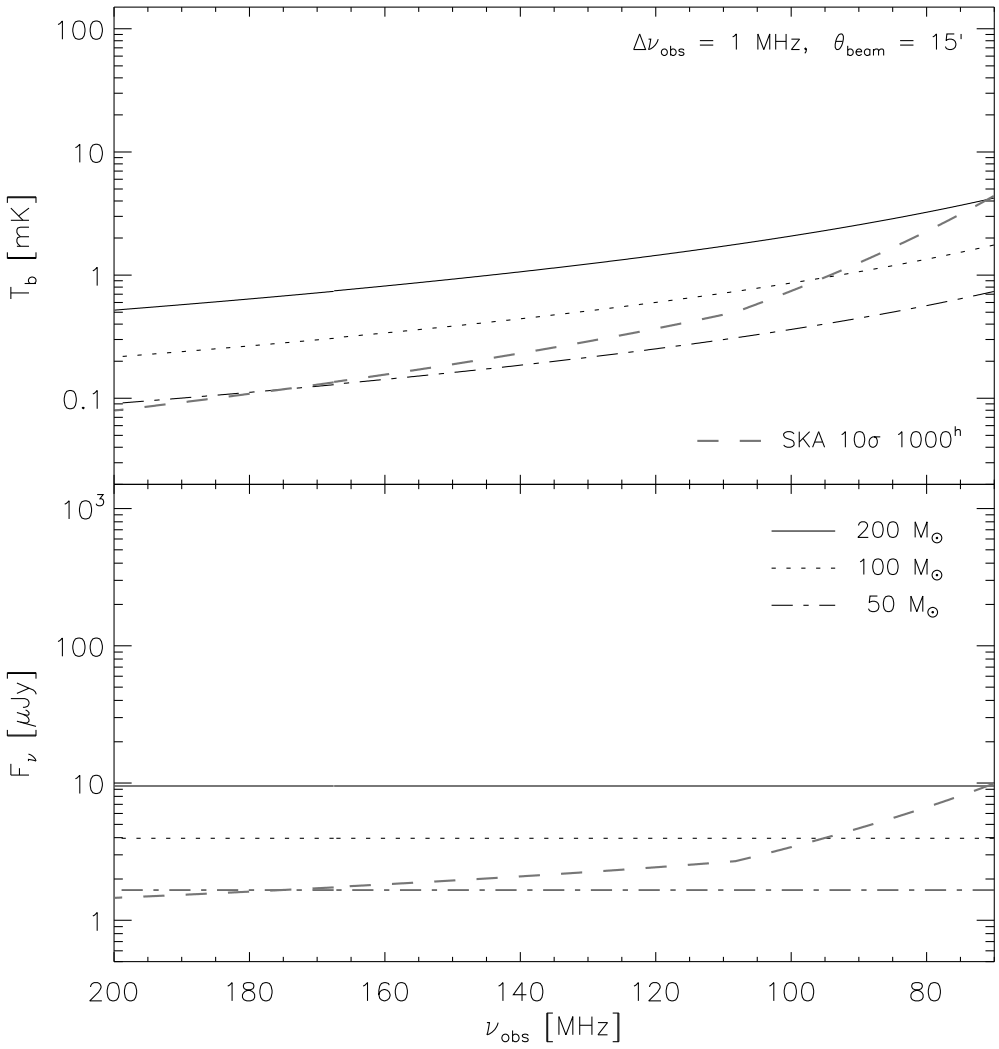

Figure 5.5: The brightness temperature (top panel) and specific flux (bottom panel) of the radio background produced by bremsstrahlung, shown as a function of observed frequency. We have chosen a beam size of 15′ to achieve the highest possible resolution and sensitivity at 100 MHz for the currently planned configuration of the SKA. The thin dot-dashed, dotted and solid lines correspond to an initial mass function consisting solely of 50, 100 and 200 $M_\odot$ Pop III stars, respectively. The thick dashed line shows the sensitivity of the SKA for a 10σ detection, a bandwidth of 1 MHz, and an integration time of 1000 h. Although the free-free signal is in principle detectable by the SKA, we have here neglected biasing and radiative feedback, which act to reduce the signal. For this reason we do not believe that the free-free signal of the first H II regions will be observable in the near future.

and

$$\kappa_e = 2 \times 10^{-10}\, T^{1/2}\ \mathrm{cm^3\ s^{-1}}\ , \tag{5.32}$$

which we have obtained from the rates quoted in Kuhlen et al. (2006). At $z \lesssim 20$, the electron fraction in the IGM remains above $f_e = 0.1$ for most of the lifetime of the relic H II region. In this case, the collisional coupling coefficient is given by

$$y_c \simeq 0.015 \left(\frac{f_e}{0.5}\right) \left(\frac{T}{10^3\ \mathrm{K}}\right)^{-1/2} \left(\frac{1+z}{10}\right)^3\ . \tag{5.33}$$

A derivation of the Lyα coupling coefficient y_α requires radiative transfer of local as well as global Lyα radiation, which is beyond the scope of this work. We therefore consider two limiting cases: one in which we only activate collisional coupling, and the other in which a strong Lyα background drives the spin temperature towards the gas temperature (i.e. $y_\alpha \gg 1$ or $T_S = T$).

The differential brightness temperature with respect to the CMB may be derived as follows. In the Rayleigh-Jeans limit and for $T_S \gg T_*$, the monochromatic radiative transfer equation for a ray passing through a cloud, evaluated in its comoving frame, may be written in terms of the brightness temperature T_b:

$$T_b = T_\gamma\, e^{-\tau} + \int_0^\tau T_S\, e^{-\tau'}\, \mathrm{d}\tau'\ , \tag{5.34}$$

where the optical depth at the 21 cm line is given by

$$\mathrm{d}\tau = \frac{3c^2 A_{21} n_{\mathrm{HI}}}{32\pi\nu_{21}^2}\, \phi(\nu_{21})\, \frac{T_*}{T_S}\, \mathrm{d}s\ . \tag{5.35}$$

Here, $\phi(\nu_{21})$ is the normalized line profile at the resonance frequency ν_{21} and $\mathrm{d}s$ is the distance traveled by the ray. In our case, the line profile is dominated by thermal broadening, with a Doppler width given by

$$\Delta\nu_{\mathrm{D}} = \nu_{21} \sqrt{\frac{2k_{\mathrm{B}}T}{\mu m_{\mathrm{H}} c^2}}\ . \tag{5.36}$$

The amplitude of the line profile at the resonance frequency may be replaced by the Doppler width, i.e. $\phi(\nu_{21}) = \Delta\nu_{\mathrm{D}}^{-1}$. With this definition, equation (5.34) yields the differential bright-

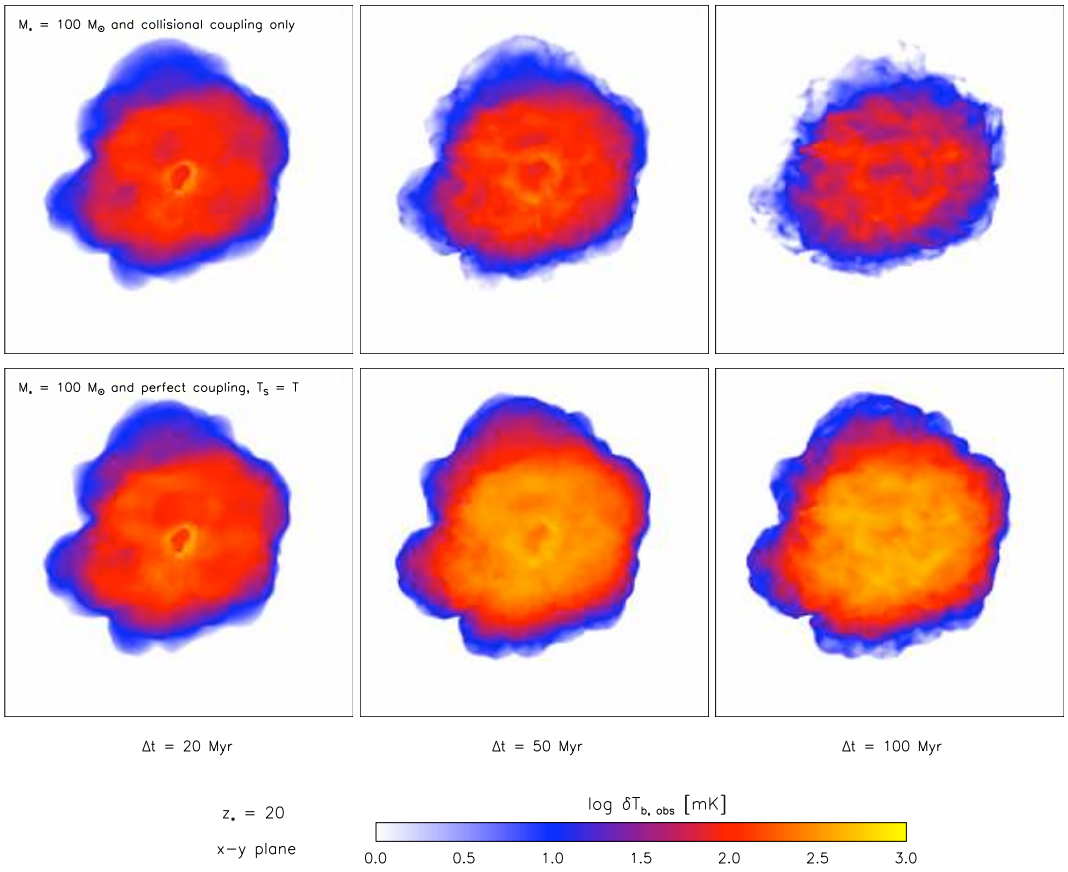

Figure 5.6: The observed differential brightness temperature of the relic H II region around a 100 $M_\odot$ Pop III star, shown 20, 50 and 100 Myr after the star has turned off. We delineate the range of possible values by showing the result for collisional coupling only (top row), as well as perfect coupling to the Lyα background, resulting in $y_\alpha \gg 1$ or $T_S = T$ (bottom row). In the first case, the observed differential brightness temperature is of order a few 10 mK for $\simeq$ 100 Myr, while in the second case the signal is of order a few 100 mK for well over $\simeq$ 100 Myr. We note that the latter is likely more relevant at $z \lesssim 20$, where the observationally accessible signal is produced (Furlanetto, 2006; Pritchard & Furlanetto, 2007).

ness temperature $\delta T_b = T_b - T_\gamma$, which becomes particularly simple for a constant spin temperature and the fact that the relic H II regions considered here are optically thin:

$$\delta T_b = (T_S - T_\gamma)\,\tau \,. \tag{5.37}$$

The observed differential brightness temperature is then simply given by $\delta T_{b,\mathrm{obs}} = \delta T_b / (1+z)$.

In Fig. 5.6, we show the observed differential brightness temperature for a 100 $\mathrm{M}_\odot$ star and the two limiting cases discussed above. Note that we have only taken into account ionized gas along the line of sight. For collisional coupling only, the observed differential brightness temperature is of order a few 10 mK for $\simeq$ 100 Myr, while for perfect coupling the signal is elevated by an order of magnitude to a few 100 mK for well over $\simeq$ 100 Myr. In reality, the expected signal lies between these extremes and is a function of redshift, since collisional coupling becomes weaker as the background density drops, while Lyα coupling becomes stronger as the Lyα background rises. At $z \lesssim 20$, where the observationally accessible signal is produced, the Lyα background is likely strong enough for the latter case to be more important (Furlanetto, 2006; Pritchard & Furlanetto, 2007).

We may now determine the radio background produced by the integrated 21 cm emission of relic H II regions. The differential specific flux observed at the redshifted 21 cm line from a single relic H II region with differential brightness temperature δT_b is given by

$$\delta F_\nu = \frac{2 k_\mathrm{B} \nu_{21}^2}{c^2}\,(1+z)^{-3}\,\Delta\Omega\,\delta T_b \,, \tag{5.38}$$

where $\Delta\Omega = A / D_\mathrm{A}^2$ denotes the solid angle subtended by the H II region, $A = \pi r_\mathrm{HII}^2$ its area, $r_\mathrm{HII} = \left(3 N_\mathrm{ion} / 4\pi n_\mathrm{H,b}\right)^{1/3}$ its radius, and D_A the angular diameter distance. The average differential specific flux $\langle \delta F_\nu \rangle$ within a beam size $\Delta\Omega_\mathrm{beam}$ and bandwidth $\Delta\nu_\mathrm{obs}$ is then given by

$$\langle \delta F_\nu \rangle = \delta F\, N_\mathrm{ps}(z)\, \frac{\mathrm{d}^2 V(z)}{\mathrm{d}z\,\mathrm{d}\Omega}\, \frac{\Delta z\,\Delta\Omega_\mathrm{beam}}{\Delta\nu_\mathrm{obs}} \,, \tag{5.39}$$

where $\delta F = \delta F_\nu\, \Delta\nu_\mathrm{D} / (1+z)$, $N_\mathrm{ps}(z)$ is the Press-Schechter mass function defined in equation (5.23), $\Delta z = \Delta\nu_\mathrm{obs}\,(1+z)^2 / \nu_{21}$, and $\mathrm{d}^2 V(z)/\mathrm{d}z\,\mathrm{d}\Omega$ is the comoving volume per unit redshift and solid angle:

$$\frac{\mathrm{d}^2 V(z)}{\mathrm{d}z\,\mathrm{d}\Omega} = \frac{c\, D_\mathrm{A}^2\,(1+z)^2}{H(z)} \,, \tag{5.40}$$

where $H(z)$ is the Hubble expansion rate. With the definition of the brightness temperature,

the average differential antenna temperature $\langle \delta T_b \rangle$ is given by

$$\langle \delta T_b \rangle = \frac{\pi c}{\nu_{21}} \frac{(1+z)^2 \, N_{\rm ps}(z)}{H(z)} \, \Delta\nu_{\rm D} \, r_{\rm HII}^2(z) \, \delta T_b(z) \, . \tag{5.41}$$

Based on our argument above, we assume that the Lyα background is strong enough for perfect coupling at all redshifts. In this case, and for $T \gg T_\gamma$, the average differential antenna temperature becomes independent of electron fraction and temperature:

$$\langle \delta T_b \rangle = \frac{9 c^3 A_{21} T_* N_{\rm ion}}{128 \pi \nu_{21}^3 H_0 \sqrt{\Omega_m}} \, (1+z)^{1/2} \, N_{\rm ps}(z) \, , \tag{5.42}$$

where we have set $n_{\rm HI} = n_{\rm H,b}$ in equation (5.35). We note that the observed frequency is related to the redshift via $\nu_{\rm obs} = \nu_{21}/(1+z)$. We have further assumed that the relic H II region produced by each star-forming minihalo persists until the Universe is reionized (i.e. $z \simeq 6$), which is a good approximation for perfect coupling and $T \gg T_\gamma$. Equation (5.42) provides a robust upper limit for the collective 21 cm emission from the first relic H II regions.

In Fig. 5.7, we compare the average differential antenna temperature and specific flux for a beam size of $\Delta\theta_{\rm beam} = 15'$ to the sensitivity of the SKA, assuming a $10\,\sigma$ detection, a bandwidth of $\Delta\nu_{\rm obs} = 1$ MHz, and an integration time of 1000 h. At all frequencies, the maximum 21 cm signal from the first relic H II regions is of order 10 mK, which is well detectable by the SKA. The effects of biasing and radiative feedback will reduce this signal, but probably not enough to fall below the sensitivity of the SKA. Compared to free-free emission, the 21 cm signal is typically an order of magnitude stronger, and offers the best prospect for indirectly probing the first stars.

5.3 Summary and Conclusions

We have introduced a general-purpose radiative transfer scheme for cosmological SPH simulations that treats ionizing and photodissociating radiation from massive Pop III stars in the early Universe. Based on this methodology, we have investigated the build-up of the first H II regions around Pop III stars formed in minihalos, and predicted their contribution to the extragalactic radio background via bremsstrahlung and 21 cm emission. Although recombination radiation from individual H II regions is too faint to be directly detectable even

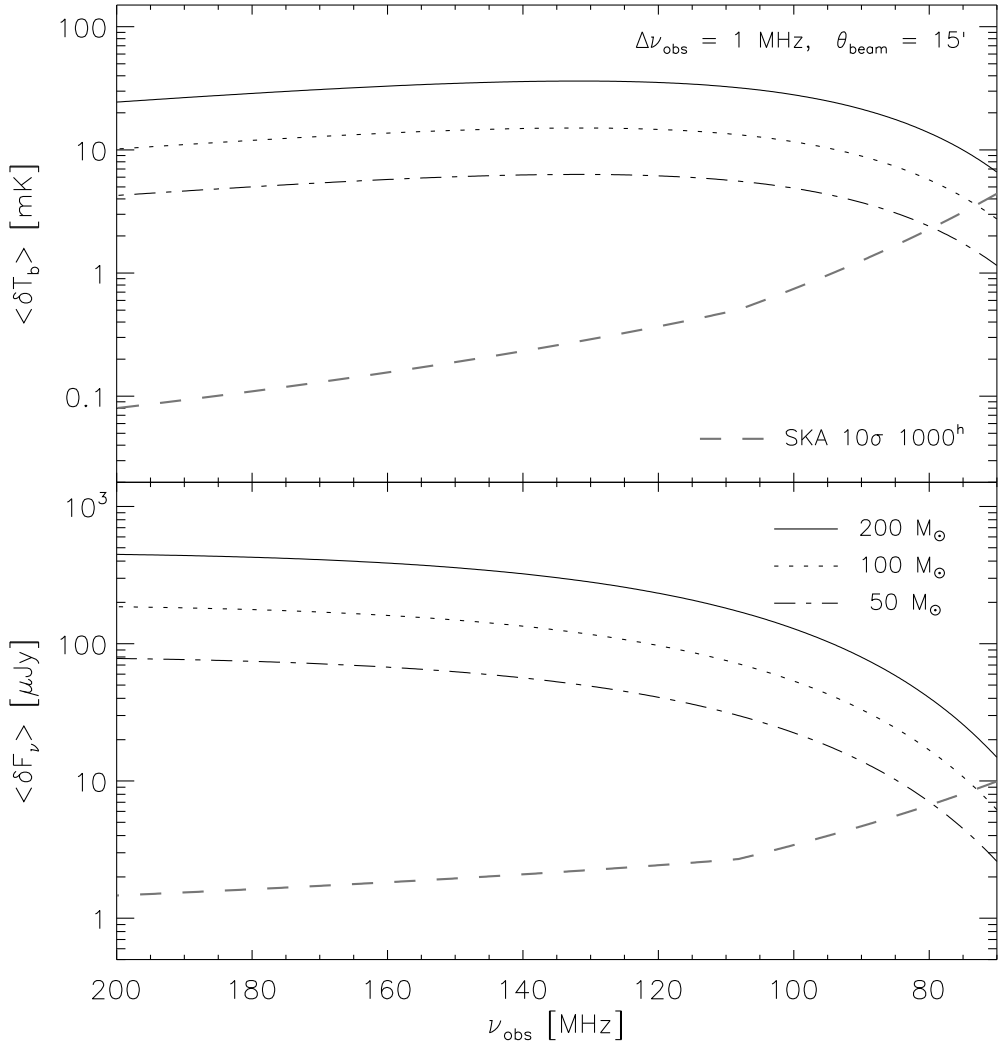

Figure 5.7: The average differential antenna temperature (top panel) and specific flux (bottom panel) of the radio background produced by 21 cm emission, shown as a function of observed frequency. We have chosen a beam size of 15′ to achieve the highest possible resolution and sensitivity at 100 MHz for the currently planned configuration of the SKA. The thin dot-dashed, dotted and solid lines correspond to an initial mass function consisting solely of 50, 100 and 200 $M_\odot$ Pop III stars, respectively. The thick dashed line shows the sensitivity of the SKA for a 10σ detection, a bandwidth of 1 MHz, and an integration time of 1000 h. In all cases, the 21 cm signal is well above the detection threshold of the SKA. The effects of biasing and radiative feedback will reduce this signal, but probably not enough to fall below the sensitivity of the SKA. Compared to free-free emission, the 21 cm signal is typically an order of magnitude stronger, and offers the best prospect for indirectly probing the first stars.

with *JWST*, their collective radio emission might be strong enough to be within reach of the planned SKA. In particular, we have found that the integrated free-free emission results in a maximum differential antenna temperature of $\simeq$ 1 mK, while the 21 cm emission is an order of magnitude stronger. Considering the effects of biasing and negative radiative feedback, which would act to reduce the predicted signal, the free-free signal is likely beyond the capability of the SKA, while the 21 cm signal will most likely be observable, providing an excellent opportunity for indirectly probing the first stars.

We note that an analysis of the angular fluctuation power spectrum will be essential to isolate the 21 cm signal from other backgrounds (Furlanetto & Oh, 2006). Among these are neutral minihalos, which appear in emission due to their enhanced density and temperature (Iliev et al., 2002), or IGM gas heated by X-rays from supernovae (Oh, 2001), X-ray binaries (Glover & Brand, 2003), or the first quasars (Kuhlen et al., 2006; Madau et al., 2004). A strong absorption signal might originate from cold, neutral gas if the Lyα background effectively couples the spin temperature to the gas temperature (Pritchard & Furlanetto, 2007). In addition, there is the signal produced by stars (primordial or already metal-enriched) formed in the first dwarf galaxies. All of these compete with each other, and more work is required to understand their relative importance. One important task is to extend the simulations to larger cosmological volumes, to measure the aggregate signal from many sources in a more robust way.

Minihalos may not have been the dominant formation sites for primordial stars, in terms of producing the bulk of the radiation that drove reionization, or of being the source for the majority of the heavy elements present at high redshifts (Greif & Bromm, 2006; Schleicher et al., 2008). Nevertheless, they are the ideal laboratory to test our current standard model of the first stars, by providing an exceedingly simple environment for the star formation process (Bromm et al., 2009). The next step in the hierachical build-up of structure, more massive systems, such as the first galaxies, is already highly complex, due to the presence of metals, turbulent velocity fields, and possibly dynamically significant magnetic fields (Greif et al., 2008; Schleicher et al., 2009; Wise & Abel, 2007a, 2008b). It is therefore crucial to empirically probe the minihalo environment, and the signature left in the radio background might provide us with one of the few avenues to accomplish this in the foreseeable future.

6

The First Galaxies: Signatures of the Initial Starburst

The epoch of the first galaxies marked a fundamental transition in the Universe, ending the Cosmic Dark Ages, beginning the process of reionization, and witnessing the rapid proliferation of star formation and black hole growth (Barkana & Loeb, 2001; Bromm & Larson, 2004). While the theory of primordial star formation and early galaxy formation has rapidly developed (Barkana & Loeb, 2007; Ciardi & Ferrara, 2005; Glover, 2005), observations of the first galaxies at redshifts $z \gtrsim 10$ have so far been out of reach (but see Stark et al., 2007). In the coming decade, *JWST* promises to provide direct observations of this critical period in cosmic history, allowing to place new constraints on the stellar IMF at high redshift, on the luminosity function of the first galaxies, and on the progress of the early stages of reionization (Barton et al., 2004; Gardner et al., 2006; Haiman, 2008; Ricotti et al., 2008; Windhorst et al., 2006).

The IMF of the stellar populations which form in the first galaxies is of central importance in determining their properties and impact on early cosmic evolution. The current theoretical consensus posits that the first stars, which formed in isolation in DM minihalos, likely had masses of the order of 100 $M_\odot$ (Abel et al., 2002; Bromm et al., 1999, 2002; McKee & Tan, 2008; Yoshida et al., 2008, 2006). In the first galaxies, which form in DM halos with masses $\gtrsim 10^8$ $M_\odot$ (Greif et al., 2008; Wise & Abel, 2007a), there is no such theoretical consensus on the IMF, as the initial conditions of the star-forming gas are uncertain (Jappsen et al., 2009a,b). A large fraction of these first galaxies are likely to already host Pop II star

formation, due to previous metal enrichment (Clark et al., 2008; Johnson et al., 2008; Trenti & Stiavelli, 2009). However, clusters of primordial stars likely form in some fraction of the first galaxies, owing to either inhomogeneities in the LW background which can suppress star formation where galaxies are strongly clustered (Ahn et al., 2008; Dijkstra et al., 2008), or to the direct collapse of the first stars to black holes, thereby locking up the metals produced in their cores (Heger et al., 2003).

Due to the hard spectra of massive metal-free stars, strong nebular emission in helium recombination lines has been suggested as an observable indicator of a population of such stars (Bromm et al., 2001b; Oh et al., 2001; Schaerer, 2002; Tumlinson et al., 2001). In particular, a high ratio of the luminosity emitted in He II λ1640 to that emitted in Lyα or Hα may be a signature of a galaxy hosting massive Pop III star formation, and has already served as the basis for searches for such galaxies (Dawson et al., 2004; Nagao et al., 2005, 2008). In addition, high equivalent widths (EWs) of Lyα and He II λ1640 are expected to characterize galaxies undergoing a Pop III starburst (Schaerer, 2003). While no definitive detections of such galaxies have been achieved to date, observations of galaxies at $3 \lesssim z \lesssim 6.5$ with large Lyα EW and strong He II λ1640 emission may indicate that some galaxies host Pop III star formation even at such relatively low redshift (Dijkstra & Wyithe, 2007; Jimenez & Haiman, 2006).

Previous analytical calculations of the recombination radiation expected from the first galaxies have been carried out under a number of idealized assumptions, namely of a static, uniform density field, and of the formation of a static Strömgren sphere. Taking a complementary approach, we study here the properties of the recombination radiation emitted by the first galaxies with a focus on how the dynamical evolution of the galaxy affects the properties of this radiation. We present high-resolution cosmological radiation hydrodynamics simulations of the production of nebular emission from a cluster of primordial stars formed within the first galaxies. We resolve the H II and He III regions generated by the stellar cluster, thereby arriving at improved predictions for the emission properties of the first galaxies, which will be tested by *JWST*.

Our paper is organized as follows. In Section 6.2, we describe our simulations and the methods used in their analysis; in Section 6.3 our results are presented, along with the implications for both IMF and SFR indicators; in the final Section 6.4, we summarize and give our conclusions.

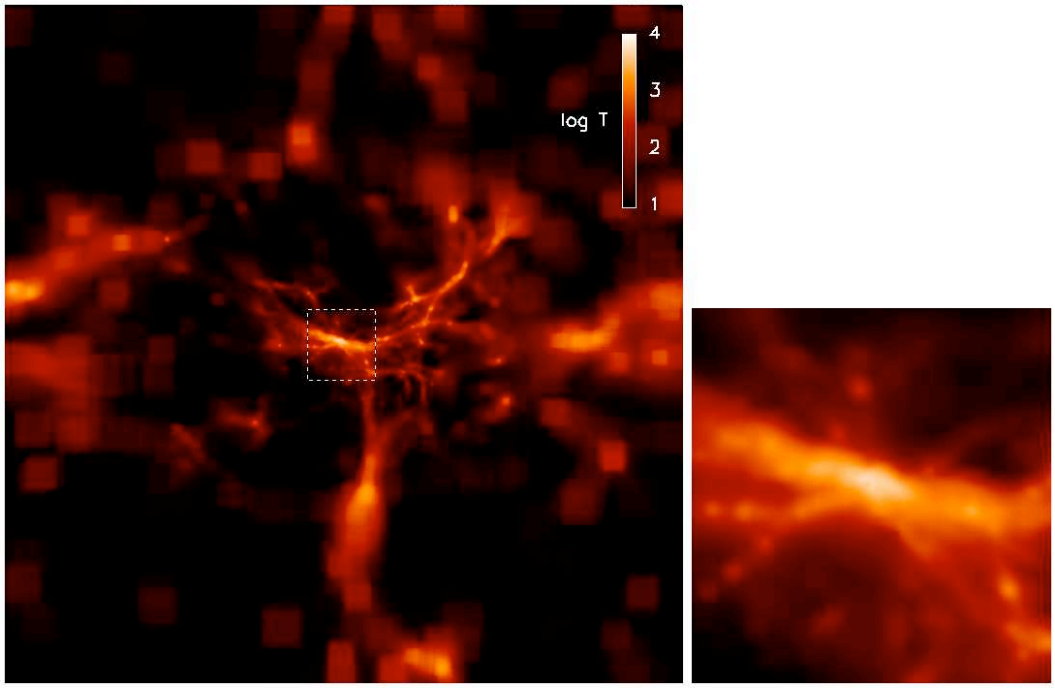

Figure 6.1: The projected gas temperature at $z = 12.7$, just before the stellar cluster turns on. Shown at left is the entire 1.4 Mpc (comoving) simulation box. The region of highest resolution is in the center of our multi-grid simulation box; magnified at right is the central ~ 10 kpc, where the $\sim 10^8$ $M_\odot$ dark matter halo hosting the stellar cluster is located. Note that the gas is heated to $\geq 10^4$ K when passing through the virialization shock.

6.1 Methodology

We carry out radiation hydrodynamics simulations which track the impact of the radiation from Pop III stellar clusters forming promptly within a dwarf galaxy at $z \sim 12.5$. In this section we describe the simulations and the calculations carried out in analyzing their outcomes.

6.1.1 The Simulations

As with previous work, for our three-dimensional numerical simulations we employ the parallel version of GADGET (version 1), which includes a tree (hierarchical) gravity solver combined with the SPH method for tracking the evolution of gas (Springel & Hernquist, 2002; Springel et al., 2001). Along with H, H^+, H^-, H_2, H_2^+, He, He^+, He^{++}, and e^-, we have included the five deuterium species D, D^+, D^-, HD and HD^+, using the same chemical network as in Johnson & Bromm (2006, 2007).

For our simulation of the assembly of a dwarf galaxy at $z \sim 12.5$, we have employed multi-grid initial conditions which offer higher resolution in the region where the galaxy forms (e.g. Kawata & Gibson, 2003). We initialize the simulation according to the ΛCDM power spectrum at $z = 100$, adopting the cosmological parameters $\Omega_m = 1 - \Omega_\Lambda = 0.3$, $\Omega_b = 0.045$, $h = 0.7$, and $\sigma_8 = 0.9$, close to the values measured *WMAP* in its first year (Spergel et al., 2003). Here, we use a periodic box with a comoving size $L = 1h^{-1}$ Mpc for the parent grid. Our simulations use $N_{\rm DM} = N_{\rm SPH} = 1.05 \times 10^6$ particles for DM and gas, where the SPH particle mass is $m_{\rm SPH} \sim 120$ $M_\odot$ in the region with the highest resolution. For further details on the technique employed to generate our multi-grid initial conditions, see Greif et al. (2008). The maximum gas density that we resolve is $n_{\rm res} \sim 10^3$ cm^{-3}, while gas at higher densities is accreted onto sink particles, as described in (Johnson et al., 2007). We have also included the effect of a LW background radiation field, at a level of $J_{\rm LW} = 0.04 \times 10^{-21}$ erg s^{-1} cm^{-2} Hz^{-1} sr^{-1}, just as in Johnson et al. (2008).

To capture the effects of the ionizing radiation emitted by a single Pop III stellar cluster within the dwarf galaxy, we approximate the cluster as a point source located at the center of the most massive DM halo in our simulation box at $z = 12.7$. The projected gas temperature in the entire simulation box at this redshift is shown in Fig. 6.1 (left panel); the right panel shows the temperature in the region of the host halo at the center of the box, which has a virial mass of 9×10^7 $M_\odot$, characteristic of the first galaxies. At each timestep, we find

the boundaries of both the H II and He III regions generated by the stellar cluster using a ray-tracing technique that improves our earlier implementation (Johnson et al., 2007).

The procedure used to calculate the Strömgren sphere around the stellar cluster for a given time-step Δt is similar to the ray-tracing scheme used in Johnson et al. (2007). We create a spherical grid centered at the location of the cluster, consisting of $\sim 1.2 \times 10^4$ rays and 1000 linearly spaced radial bins. We resolve the central kiloparsec around the source, roughly the virial radius of the host halo, with 250 radial bins, while the remaining 750 bins are linearly spaced out to ~ 20 kpc.

In a single, parallelized loop, the Cartesian coordinates of all particles are converted to spherical coordinates, such that their density and chemical abundances may be mapped to the bins corresponding to their radius, azimuth and zenith, denoted by r, θ and ϕ, respectively. To avoid missing dense clumps, particles contribute to bins independent of distance, but proportional to their density squared. Once this preliminary step is complete, it is straightforward to solve the ionization front equation along each ray:

$$n_n r_{\rm I}^2 \frac{{\rm d}r_{\rm I}}{{\rm d}t} = \frac{Q_{\rm ion}}{4\pi} - \alpha_{\rm B} \int_0^{r_{\rm I}} n_e n_+ r^2 {\rm d}r \,, \tag{6.1}$$

where $r_{\rm I}$ denotes the position of the ionization front, $Q_{\rm ion}$ the number of ionizing photons emitted per second by the stellar cluster, $\alpha_{\rm B}$ the case B recombination coefficient, and n_n, n_e and n_+ the number densities of nonionized particles, electrons and ionized particles, respectively. The numbers of H I-, He I- and He II-ionizing photons are $Q_{\rm ion} = N_* q_{\rm ion}$, where N_* is the number of stars in the cluster (here we assume that all have the same mass) and $q_{\rm ion}$ is the number of ionizing photons emitted by a single star, given by

$$q_{\rm ion} = \frac{\pi L_*}{\sigma T_{\rm eff}^4} \int_{\nu_{\rm min}}^{\infty} \frac{B_\nu}{h\nu} {\rm d}\nu \,, \tag{6.2}$$

where σ is the Stefan-Boltzmann constant, $\nu_{\rm min}$ denotes the minimum frequency corresponding to the ionization thresholds of H I, He I and He II, and we assume that massive Pop III stars emit a blackbody spectrum B_ν (in erg s^{-1} cm^{-2} Hz^{-1} sr^{-1}) with an effective temperature $T_{\rm eff}$ and a luminosity L_* (e.g. Schaerer, 2002).

To obtain a discretization of the ionization front equation, we replace the integral on the

right-hand side of equation (6.1) by a discrete sum:

$$\int_0^{r_{\rm I}} n_e n_+ r^2 {\rm d}r = \sum_i n_{e,i} n_{+,i} r_i^2 \Delta r \, , \tag{6.3}$$

where Δr is the radial extent of the individual bins. Similarly, the left-hand side of equation (6.1), which models the propagation of the ionization front into neutral gas, is discretized by

$$n_n r_{\rm I}^2 \frac{{\rm d}r_{\rm I}}{{\rm d}t} = \frac{1}{\Delta t} \sum_i n_{n,i} r_i^2 \Delta r_i \, , \tag{6.4}$$

where Δt is the current time-step and the summation is over radial bins starting with the bin lying immediately outside of $r_{\rm I,old}$, the position of the ionization front at the end of the previous time-step, and ending with the bin lying at the new position of the ionization front. We perform the above steps separately for the H II and He III regions, since they require distinct heating and ionization rates.

We have chosen the size of the bins that are used in our ray-tracing routine to roughly match the volume of gas represented by a single SPH particle within the $\sim$ 1 kpc virial radius of the halo hosting the stellar cluster, such that the boundaries of the photoionized regions are maximally resolved while also reliably conserving ionizing photons. However, in some cases it may occur that the mass contained in a bin is smaller than that of the SPH particle contained within it, such that ionizing the entire SPH particle involves ionizing more gas than is contained in the bin. In turn, this can lead to an overestimate of the number of recombinations. While this effect is minor in our simulations, in the calculations presented below we enforce that the total number of recombinations does not exceed the total number of ionizing photons available.

We carry out four simulations, each with a different combination of IMF and total cluster mass. For the IMF, we assume for simplicity, and in light of the still complete uncertainty regarding its detailed shape, that the cluster consists either entirely of 25 $M_\odot$ or 100 $M_\odot$ Pop III stars. These choices are meant to bracket the expected characteristic mass for Pop III stars formed in the first galaxies, which depending on the cooling properties of the gas may be Pop III.2 stars with masses of order 10 $M_\odot$ or, possibly, Pop III.1 stars with masses perhaps an order of magnitude higher (Greif et al. 2008; Johnson & Bromm 2006; McKee & Tan 2008; but see Jappsen et al. 2009a). For each of these IMFs, we vary the total stellar mass in the cluster, choosing either 2.5×10^3 $M_\odot$ or 2.5×10^4 $M_\odot$ for the total mass in stars.

These choices correspond to $\sim$ 1 and $\sim$ 10 percent, respectively, of the cold gas available for star formation within the central few parsecs of such a primordial dwarf galaxy (Regan & Haehnelt, 2009; Wise et al., 2008). We calculate the ionizing flux from each of these clusters, assuming blackbody stellar spectra at 7×10^4 and 10^5 K and bolometric luminosities of 6×10^4 and 10^6 $L_\odot$, for the 25 and 100 $M_\odot$ stars, respectively, appropriate for metal-free stars on the main sequence (Marigo et al., 2001).

For simplicity, we have chosen to keep the input stellar spectra constant in time over the course of the simulations. Accordingly, we run the simulations only for 3 Myr, which is roughly the hydrogen-burning timescale of a 100 $M_\odot$ primordial star, and about half that of a 25 $M_\odot$ primordial star. We note that while the H I-ionizing flux from 100 $M_\odot$ primordial stars is roughly constant over this timescale, the He II-ionizing flux decreases by a factor of $\sim$ 2 by a stellar age of 2 Myr, and by a much larger factor near the end of hydrogen-burning as the star evolves to the red (Marigo et al., 2001; Schaerer, 2002). We note, however, that stellar models accounting for the effects of rotation yield less precipitous drops in the emitted ionizing flux with time, as fast rotation, especially of low-metallicity stars, can keep the stars on bluer evolutionary tracks (Vázquez et al., 2007; Woosley & Heger, 2006; Yoon & Langer, 2005); indeed, Pop III stars may have been fast rotators (Chiappini et al., 2008). Nonetheless, the results that we derive pertaining to He II recombination emission from clusters of 100 $M_\odot$ stars may be, strictly speaking, only reliable for stellar ages $\lesssim$ 2 Myr. An in-depth study of the impact that stellar evolution has on the emission properties of primordial galaxies is given in Schaerer (2002); in the present work, we take a complementary approach and instead focus on how the emission properties are affected by the hydrodynamic evolution of the gas in the first galaxies.

We make the related simplifying assumption that the stellar cluster forms instantaneously. This is valid if the timescale for star formation $t_{\rm SF}$ is much shorter than the lifetime of the stars that we consider, or $t_{\rm SF} \ll 3$ Myr. If we assume that stars form on the order of the free-fall time $t_{\rm ff}$, and take it that the star cluster forms within the central $\sim$ 1 pc of the halo (Regan & Haehnelt, 2009; Wise et al., 2008), then we find $t_{\rm SF} \sim 5 \times 10^5$ yr, for which our assumption is marginally valid. We note that more work is needed to accurately determine the star formation timescale in the first galaxies, as the works cited here neglect, in particular, the important effect of molecular cooling on the evolution of the primordial gas.

6.1.2 Deriving the Observational Signature

The simulations described above allow us to calculate the luminosities and equivalent widths of the recombination lines emitted from high-redshift dwarf galaxies during a primordial starburst. A related quantity we obtain is the escape fraction of ionizing photons from such a galaxy. Here we describe each of these calculations.

Escape Fraction of Ionizing Photons

Photons which escape the host halo from which they are emitted proceed to reionize the IGM, where densities are generally very low, yielding long recombination times. Ionizing photons which do not escape the host halo are, however, available to ionize dense gas which recombines quickly, leading to appreciable emission in recombination lines. Therefore, the luminosity of a galaxy in recombination radiation is intimately related to the escape fraction of ionizing photons. The escape fraction of ionizing photons from the halo hosting the stellar cluster is given by subtracting the number of recombinations $Q_{\rm rec}$ per second within the virial radius from the total number of ionizing photons emitted by the cluster:

$$f_{\rm esc} = \frac{Q_{\rm ion} - Q_{\rm rec}}{Q_{\rm ion}} \,, \tag{6.5}$$

again with $Q_{\rm ion} = N_* \, q_{\rm ion}$. This equation is valid under the assumption that within the host halo the number of ionizing photons which fail to escape is balanced by the number of recombinations within the halo. This is a reasonable assumption, since the number of atoms which become ionized within the host halo is far less than the total number of recombinations that occur in the halo, the ionization of previously neutral gas being the only other sink for ionizing photons within the halo. The number of recombinations is given as

$$Q_{\rm rec} = \sum_i \alpha_{\rm B} \frac{m_i}{\rho_i} \left(\frac{\rho_i}{\mu_i m_{\rm H}} \right)^2 f_e \, f_{\rm HII} \,, \tag{6.6}$$

where $\alpha_{\rm B}$ is the case B recombination coefficient for hydrogen, $m_{\rm H}$ the mass of a hydrogen atom, while m_i, μ_i and ρ_i are the total mass, mean molecular weight, and mass density of the ith SPH particle, respectively. For each SPH particle, $f_{\rm HII}$ and f_e denote the fraction of nuclei in H II and the fraction of free electrons, respectively.

Here the summation is over all SPH particles within the virial radius of the host halo, or

within distance of ~ 1 kpc from the central stellar cluster. We calculate the escape fractions of both H I-ionizing and He II-ionizing photons. These quantities are generally not equal, and they each contribute to determining the radiative signature of the initial starbursts in the first galaxies.

Luminosity in Recombination Lines

For each of our simulations, we compute the luminosity emitted from photoionized regions in each of three recombination lines: Hα, Lyα, and He II λ1640. These luminosities are calculated by again summing up the contributions from all SPH particles within the virial radius, where virtually all of the recombination line luminosity emerges, as follows:

$$L_{\mathrm{H}\alpha} = \sum_i j_{\mathrm{H}\alpha} \frac{m_i}{\rho_i} \left(\frac{\rho_i}{\mu_i m_{\mathrm{H}}} \right)^2 f_e \, f_{\mathrm{HII}} \, , \tag{6.7}$$

$$L_{\mathrm{Ly}\alpha} = \sum_i j_{\mathrm{Ly}\alpha} \frac{m_i}{\rho_i} \left(\frac{\rho_i}{\mu_i m_{\mathrm{H}}} \right)^2 f_e \, f_{\mathrm{HII}} \, , \tag{6.8}$$

$$L_{\lambda 1640} = \sum_i j_{\lambda 1640} \frac{m_i}{\rho_i} \left(\frac{\rho_i}{\mu_i m_{\mathrm{H}}} \right)^2 f_e \, f_{\mathrm{HeIII}} \, , \tag{6.9}$$

where the j are the temperature-dependent emission coefficients for the lines (Osterbrock & Ferland, 2006), and f_{HeIII} is the fraction of helium nuclei in He III for each SPH particle.

Given the luminosity in a recombination line over an area of the sky, we may compute the flux in that line, as observed at $z = 0$ with a spectral resolution $R = \lambda/\Delta\lambda$, where λ is the wavelength at which the emission line is observed (Oh, 2001). While Lyα photons are scattered out of the line of sight in the IGM prior to reionization (Loeb & Rybicki, 1999), a process which we do treat in the present calculations, Hα and He II λ1640 photons will not suffer such severe attenuation. Assuming that the line is unresolved, the monochromatic flux in Hα, for example, is

$$f_{\mathrm{H}\alpha} = \frac{l_{\mathrm{H}\alpha} \lambda_{\mathrm{H}\alpha} \, (1+z) \, R}{4\pi c D_{\mathrm{L}}^2(z)} \sim 20 \text{ nJy} \left(\frac{l_{\mathrm{H}\alpha}}{10^{40} \text{ erg s}^{-1}} \right) \left(\frac{1+z}{10} \right)^{-1} \left(\frac{R}{1000} \right) , \tag{6.10}$$

where $l_{\mathrm{H}\alpha}$ is the luminosity in Hα along the line of sight through the emitting galaxy, $D_{\mathrm{L}}(z)$ is the luminosity distance at redshift z ($\sim 10^2$ Gpc at $z = 10$), and $\lambda_{\mathrm{H}\alpha}$ is the rest frame

wavelength of the line, 656.3 nm. If the galaxy is spatially unresolved, appearing as a point source, we may simply substitute $L_{\mathrm{H}\alpha}$ for $l_{\mathrm{H}\alpha}$ in equation (6.10), to compute the total flux from the galaxy. In terms of total (integrated) line flux, we have the equivalent expression

$$F_{\mathrm{H}\alpha} = \frac{L_{\mathrm{H}\alpha}}{4\pi D_{\mathrm{L}}^2(z)} \sim 10^{-20}\ \mathrm{erg\ s^{-1}\ cm^{-2}} \left(\frac{L_{\mathrm{H}\alpha}}{10^{40}\ \mathrm{erg\ s^{-1}}}\right)\left(\frac{1+z}{10}\right)^{-2} . \tag{6.11}$$

Recombination Line Equivalent Widths

Another observable quantity obtained from our simulations is the rest-frame EW of recombination lines. We calculate the EWs of the three recombination lines considered, following Schaerer (2002):

$$W^0_{\mathrm{H}\alpha} = \frac{L_{\mathrm{H}\alpha}}{L_{\lambda,\mathrm{neb}} + L_{\lambda,*}} , \tag{6.12}$$

$$W^0_{\mathrm{Ly}\alpha} = \frac{L_{\mathrm{Ly}\alpha}}{L_{\lambda,\mathrm{neb}} + L_{\lambda,*}} , \tag{6.13}$$

$$W^0_{\lambda 1640} = \frac{L_{\lambda 1640}}{L_{\lambda,\mathrm{neb}} + L_{\lambda,*}} , \tag{6.14}$$

where the monochromatic continuum luminosity, evaluated at the wavelength of the line, is the sum of the nebular emission $L_{\lambda,\mathrm{neb}}$ and the stellar emission $L_{\lambda,*}$. The nebular continuum luminosity is given by

$$L_{\lambda,\mathrm{neb}} = \frac{c}{\lambda^2}\frac{\gamma_{\mathrm{tot}}}{\alpha_{\mathrm{B}}} Q_{\mathrm{rec}} , \tag{6.15}$$

where λ is the wavelength in question, and Q_{rec} is again the total number of recombinations per second in the halo. The continuous emission coefficient γ_{tot} accounts for free-free, free-bound, and two-photon continuum emission, as described in Schaerer (2002). The stellar continuum luminosity is calculated assuming a blackbody stellar spectrum and is given by

$$L_{\lambda,*} = \frac{N_*}{\lambda^5} \frac{8\pi^2 h c^2 R_*^2}{\exp\left(hc/\lambda k_{\mathrm{B}} T_{\mathrm{eff}}\right) - 1} , \tag{6.16}$$

where N_* is the number of stars in the cluster, T_{eff} is the effective surface temperature of a star, and R_* is the stellar radius.

6.2 Results and Implications

We next discuss the observable characteristics of primordial dwarf galaxies. In particular, we evaluate the utility of indicators for the SFR and the stellar IMF in such galaxies.

6.2.1 Evolution of Gas inside the Galaxy

With the ignition of a stellar cluster at the center of the host halo, the gas surrounding the cluster is photoheated, raising its pressure and leading to its outward expansion. In turn, the overall recombination rate in the host halo drops, allowing the expansion of the H II region to continue for a constant rate of ionizing photon production. Fig. 6.2 shows the growth of the H II region and the concomitant expansion of the gas in the center of the host halo for the more massive 100 $M_{\odot}$ cluster. The H II region breaks out of the host halo within the first $\sim$ 1 Myr, and after 3 Myr it extends to $\lesssim$ 7 kpc, only slightly larger than the size of the H II region created by a single massive Pop III star in a minihalo (Alvarez et al., 2006a).

While the gas surrounding the formation sites of the first stars in minihalos is easily photoevacuated by a single massive Pop III star (Kitayama et al., 2004; Whalen et al., 2004), the deeper gravitational potential well of the DM halos hosting the first galaxies allows for the retention of gas even under intense photoheating; indeed, this is one criterion used to define the first galaxies (Greif et al., 2008; Johnson et al., 2008; Read et al., 2006).

As shown in Fig. 6.3, a substantial portion of the gas in the galaxy, even within $\sim$ 100 pc of the stellar cluster, remains neutral after 3 Myr. This gas is shielded from the ionizing radiation, causing the ionization front to propagate outward anisotropically in the inhomogeneous cosmological density field (Abel et al., 2007; Alvarez et al., 2006a; Shapiro et al., 2004). Even for the case of the highest ionizing flux, the fraction of ionized gas within the central $\sim$ 100 pc is $\lesssim$ 0.4, leaving the majority of the high density gas neutral. While the photodissociating radiation from the initial stellar cluster will slow the collapse of this primordial gas (Ahn & Shapiro, 2007; Susa & Umemura, 2006; Whalen et al., 2008a), some fraction of it will likely be converted into stars once the most massive stars in the cluster have died out. Indeed, the shocks engendered by the supernovae that mark the end of their lives may expedite the collapse of the gas (Greif et al., 2007; Machida et al., 2005; Mackey et al., 2003; Sakuma & Susa, 2009; Salvaterra et al., 2004). The incomplete ionization of the central gas confirms that the masses that we have chosen for the clusters are not overly

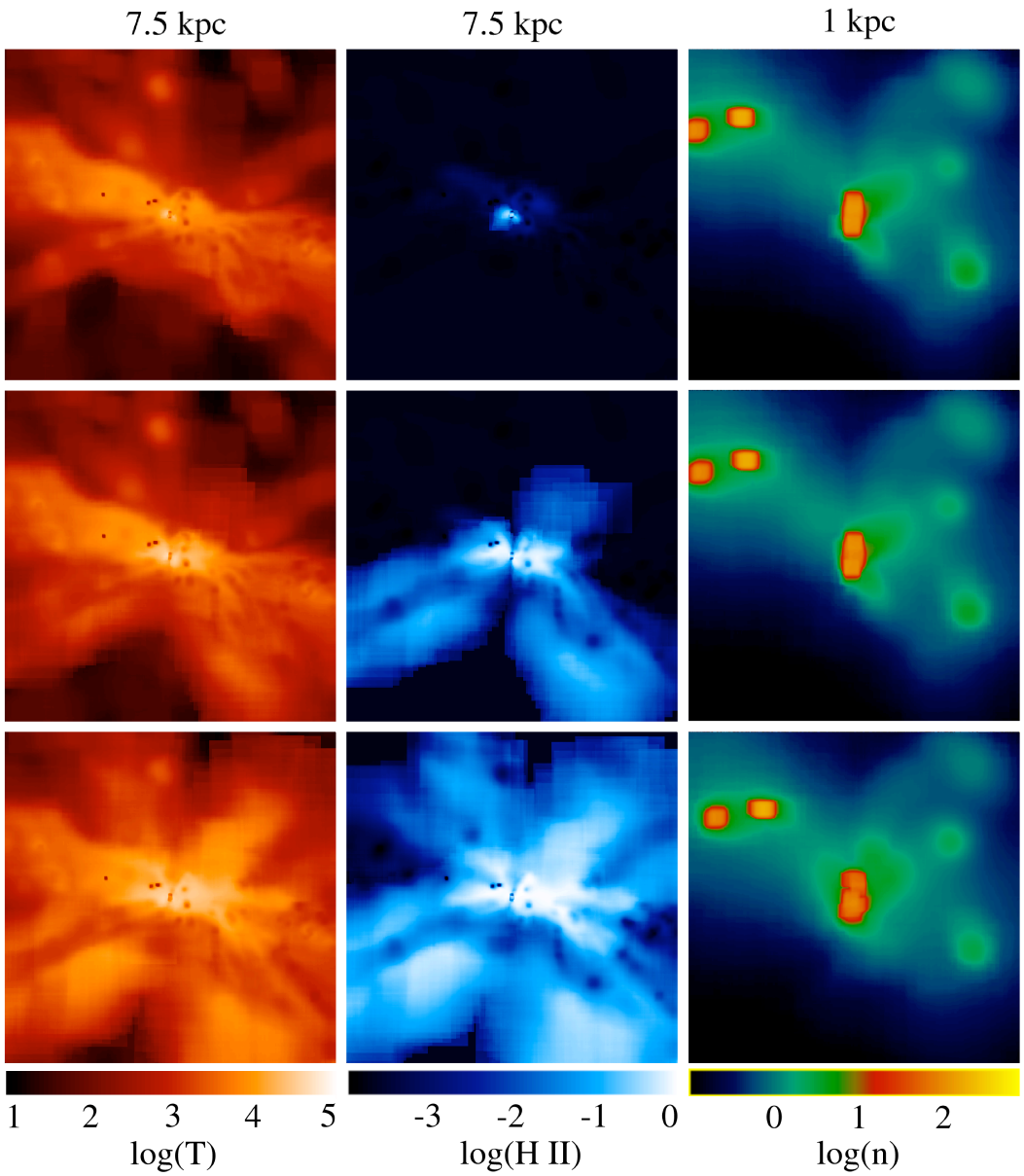

Figure 6.2: The density-weighted temperature (left column), density-weighted H II fraction (middle column), and number density (right column), each averaged along the line of sight, of the gas surrounding the more massive 100 $M_\odot$ star cluster, shown at three different times from the prompt formation of the cluster: 500,000 yr (top row), 1 Myr (middle row), and 3 Myr (bottom row). The H II region grows as the density of the gas in the center of the host halo gradually drops in response to the intense photoheating. Note the different length scale of each column; the density is shown only within the central region of the host halo.

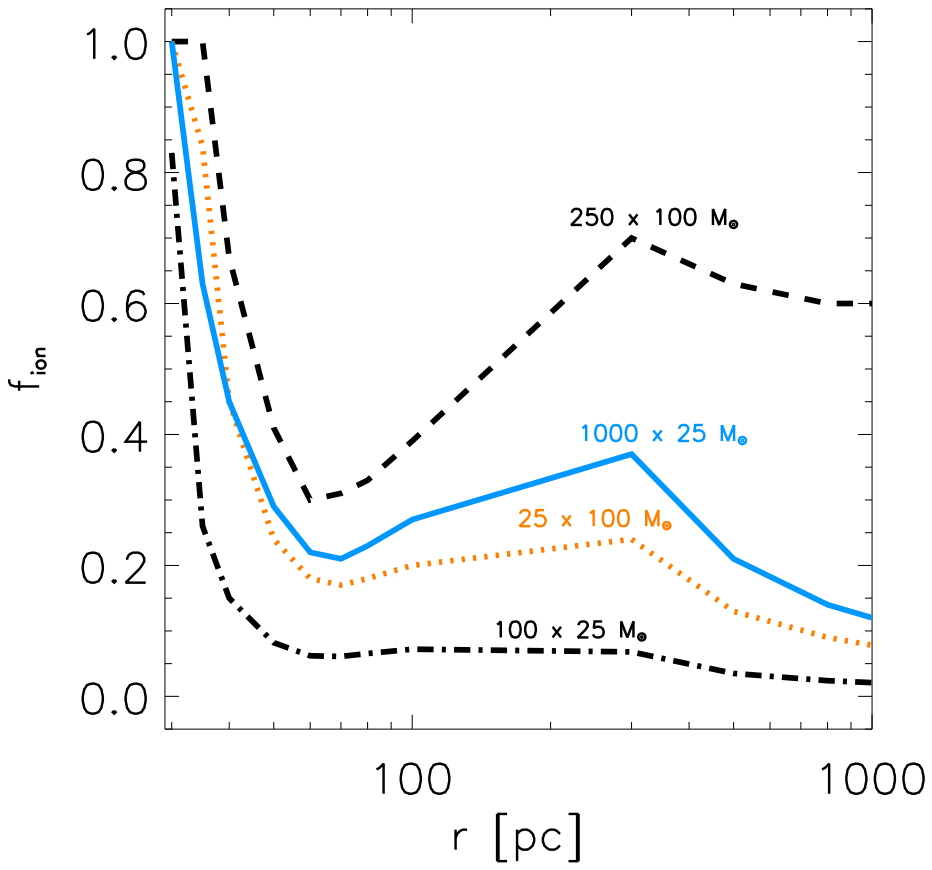

Figure 6.3: The mass fraction of enclosed gas which is photoionized, $f_{\rm ion}$, as a function of the distance from the central star cluster, after 3 Myr of photoheating. Each line corresponds to a different choice of IMF and total mass in stars, as labeled. The ionized fraction begins to drop at $\geq$ 300 pc mostly due to two minihalos at $\sim$ 400 and $\sim$ 500 pc, shown in Fig. 6.2 (right panels), which remain shielded from the ionizing radiation and are thus largely neutral. Within $\sim$ 100 pc, there is a large fraction of gas which remains un-ionized at densities $\geq$ 100 cm^{-3}. This gas will likely collapse to form stars, despite the strong radiative feedback from the central stellar cluster.

large, as there is still some neutral gas available for subsequent star formation regardless of the radiative feedback.

The gas that is photoionized, however, is gradually expelled from the center of the halo, and after 3 Myr of photoheating the density of the photoionized gas within $\sim$ 20 pc of the cluster drops to $\lesssim$ 10 cm^{-3} for the more massive cluster of 100 M$_\odot$ stars shown in Fig. 6.2. For our other choices of IMF and total cluster mass the dynamical response is less dramatic, as the ionizing flux is weaker; for example, after 3 Myr the density of the central photoionized gas is $\lesssim$ 50 cm^{-3} for the less massive cluster of 25 M$_\odot$ stars. The varying degree to which photoheating dynamically impacts the host halo leads to important differences in the properties of the emitted radiation.

Although the limited resolution of our simulations allows only to track the expansion of the H II region from an initial size of $\gtrsim$ 10 pc, we expect that after roughly a sound-crossing time of the central unresolved $\sim$ 10 pc, or after the first few 10^5 yr, the evolution of the H II region is reliably resolved. It should thus be noted that the breakout of the H II region may be delayed by of order this timescale compared to our simulations. We note that in the Milky Way the expansion of the photoheated gas in an H II region may be slowed due to turbulent pressure confinement (Mac Low et al., 2007; Xie et al., 1996), resulting in ultra-compact H II regions persisting for $\gtrsim 10^5$ yr (Wood & Churchwell, 1989), much longer than the sound-crossing timescale for such regions. As turbulence begins to play an important role in the formation of the first galaxies (Greif et al., 2008; Wise & Abel, 2007a), the initial evolution of H II regions therein may be similarly confined. This possibility notwithstanding, we expect that the spatial resolution that we do achieve suffices to track changes in the luminosity emitted in recombination lines and in the escape fraction of ionizing radiation, which we discuss in the remainder of this section.

6.2.2 Star formation Rate Indicators

The luminosity emitted in recombination lines, such as Hα, has been found to scale remarkably well with the SFR of galaxies at low redshift (Kennicutt 1983; but see Pflamm-Altenburg et al. 2007). The SFR obtained using such relations relies on some knowledge of the IMF of the stars which are forming, as well as on the escape fraction of ionizing radiation. Fig. 6.4 shows our calculations of the escape fraction $f_{\rm esc,HII}$ of H I-ionizing photons for each of our choices of IMF and total mass in stars, and Fig. 6.5 shows the escape fraction

$f_{\rm esc,HeIII}$ of He II-ionizing photons. The corresponding luminosities emitted in Hα, Lyα, and He II λ1640 are presented in Fig. 6.5.

As shown in Fig. 6.4, there is a clear trend toward higher H I-ionizing photon escape fractions for more massive stellar clusters, with the majority of the ionizing photons escaping from clusters with the larger total stellar mass. The escape fraction is not, however, independent of IMF; for a given total mass in stars, the escape fraction can differ by a wide margin. Both the variability in the escape fraction with time and the range of values that we find are in rough agreement with other recent calculations of the escape fraction of ionizing photons from dwarf galaxies at $z \gtrsim 10$ (Razoumov & Sommer-Larsen, 2009; Wise & Cen, 2009). For a recent calculation of the escape fraction of ionizing photons from more massive galaxies, see Gnedin et al. (2008).

The breakout of the H II region generated by the less massive 100 $M_\odot$ star cluster occurs after $\sim$ 1 Myr, leading to an escape fraction $\gtrsim$ 0.5 after 2 Myr. In contrast, the H II region of the equally massive 25 $M_\odot$ star cluster remains confined to the host halo for $\geq$ 3 Myr, contributing no ionizing photons to the IGM. The progress of the initial stages of hydrogen reionization, likely driven by star formation in the first galaxies, may thus depend on whether these galaxies hosted massive ($\gtrsim$ 10 $M_\odot$) or very massive stars ($\gtrsim$ 100 $M_\odot$) (Choudhury & Ferrara, 2007).

The evolution of the H I-ionizing photon escape fraction is reflected in the evolution of the luminosity of hydrogen recombination lines, as shown in Fig. 6.6. Comparing the panels on the left to those on the right, the luminosity in the Lyα and Hα lines, while generally higher for larger total mass in stars, does not scale with the total mass in stars. Indeed, owing to the increase in the escape fraction of ionizing photons, after $\sim$ 1 Myr the luminosity in hydrogen recombination lines from the clusters with greater total stellar mass drops below that of the clusters with lower total stellar mass, for a given IMF. Overall, because of the temporal evolution of the luminosity in a given line, there is no one-to-one relationship between the total mass in stars and the luminosity in a given recombination line. There is thus likely to be a relatively weak correlation between the SFR and the luminosity in the hydrogen recombination lines emitted from the first dwarf galaxies, owing to the dynamical evolution of the photoionized gas and the escape of ionizing radiation into the IGM.

Similar to the case of the hydrogen recombination lines, the luminosity in the He II λ1640 line is anticorrelated with the escape fraction of He II-ionizing photons, shown in Fig. 6.5. However, different from the case of the hydrogen lines, the luminosity emitted in He II λ1640

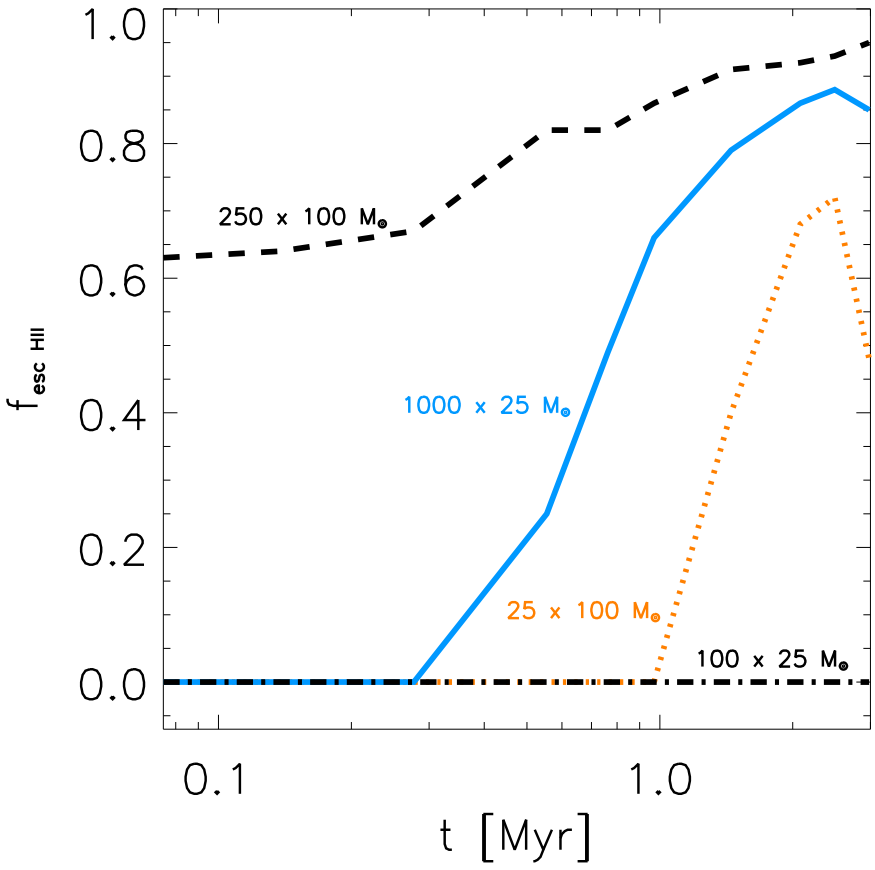

Figure 6.4: The escape fraction of hydrogen-ionizing photons, $f_{\rm esc,HII}$, from the host galaxy, each line corresponding to a different choice of IMF and total mass in stars, as labeled. Note the tight anticorrelation between the escape fraction plotted here and the luminosity in the hydrogen recombination lines shown in Fig. 6, demonstrating that the vast majority of the energy emitted in hydrogen recombination lines emanates from the dense ionized gas within the host halo, as is shown in detail in Fig. 6.10.

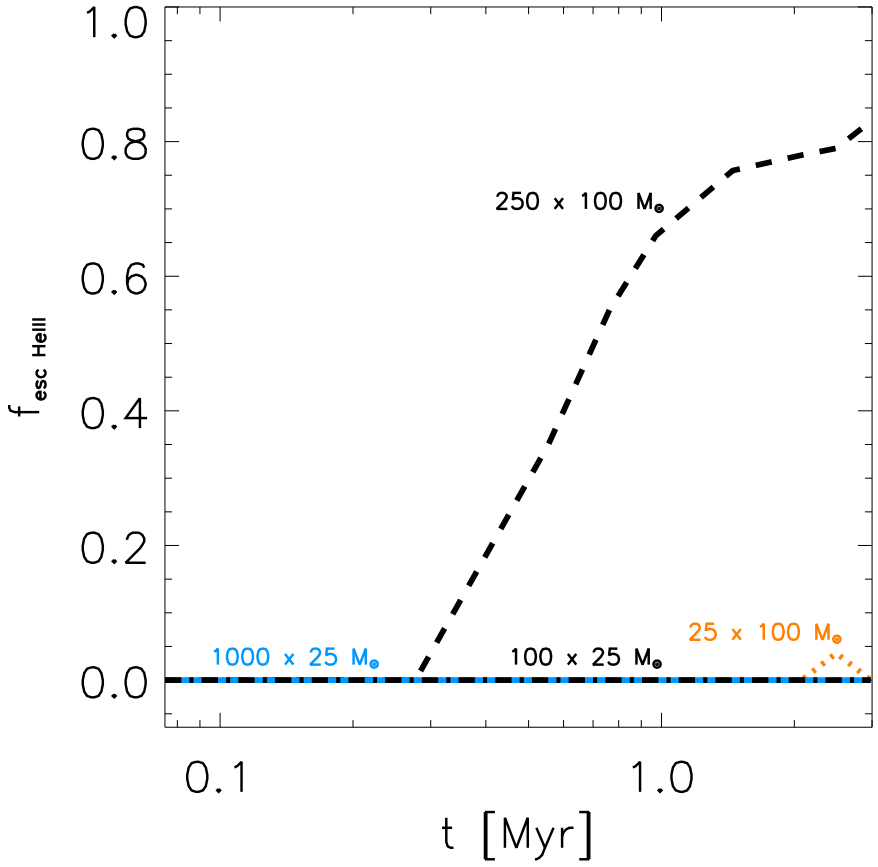

Figure 6.5: The escape fraction of He II-ionizing photons, $f_{\mathrm{esc,HeII}}$, from the host galaxy, each line labeled as in Fig. 6.4. For most cases, the negligible escape fraction leads to a tight correlation between the luminosity emitted in the He II λ1640 line and the total mass contained in stars, in contrast to the weaker correlation for hydrogen recombination lines, as discussed in Section 6.3.2.

line is generally much more strongly correlated with the total mass in stars, for a given IMF. This is due to the low escape fraction of He II-ionizing photons, which is essentially zero for every case studied here, except for the case of the more massive cluster of 100 $M_\odot$ stars. With such a high fraction of He II-ionizing photons being balanced by recombinations within the host halo, there is a near linear relation between the total mass in stars and the luminosity emitted in He II λ1640, making this line a potentially much more reliable SFR indicator than hydrogen lines such as Hα. There are slight departures from linearity due to the temperature dependence of the emission coefficient $j_{\lambda 1640}$, which varies by a factor of ~ 2 over the temperature range of the ionized gas in our simulations and is generally lower for the hotter H II regions generated by the more massive stellar clusters (Osterbrock & Ferland, 2006).

6.2.3 Initial Mass Function Indicators

The luminosity emitted from a galaxy in recombination lines depends not only on the stellar IMF, but also on the density field of the galaxy and the escape fraction of ionizing photons. Therefore, the utility of recombination line strengths as IMF indicators hinges on an understanding of the dynamical evolution of the photoionized gas, especially for the case of starbursts in the first dwarf galaxies, in which such dynamical effects can be most pronounced.

For the starbursts that we simulate here, the luminosity of the He II λ1640 emission line relative to the hydrogen recombination lines can be read from Fig. 6.6, while the equivalent widths of these lines are presented in Fig. 6.7. Comparing the top panels of Fig. 6.6 to the bottom panels, it is evident that the ratio of the luminosity emitted in He II λ1640 to that in Hα (or Lyα) can be very different depending on the IMF. Fig. 6.7 shows that there is a similar distinction in the ratios of the EWs. For the 100 $M_\odot$ star clusters the luminosity in He II λ1640 is comparable to that in Hα, while for the 25 $M_\odot$ star clusters the luminosity in He II λ1640 is up to an order of magnitude lower than that in Hα. However, as the escape fraction of H I-ionizing photons increases with time for the more massive 25 $M_\odot$ stellar cluster, the luminosities in these two lines become comparable, revealing that there is some ambiguity in the use of this ratio of line luminosities as an indicator of the IMF of young ($\lesssim 3$ Myr) stellar clusters. Thus, in some cases dynamical effects may compromise the use of this line ratio in distinguishing between clusters of Pop III.1 and Pop III.2 stars, with typical masses

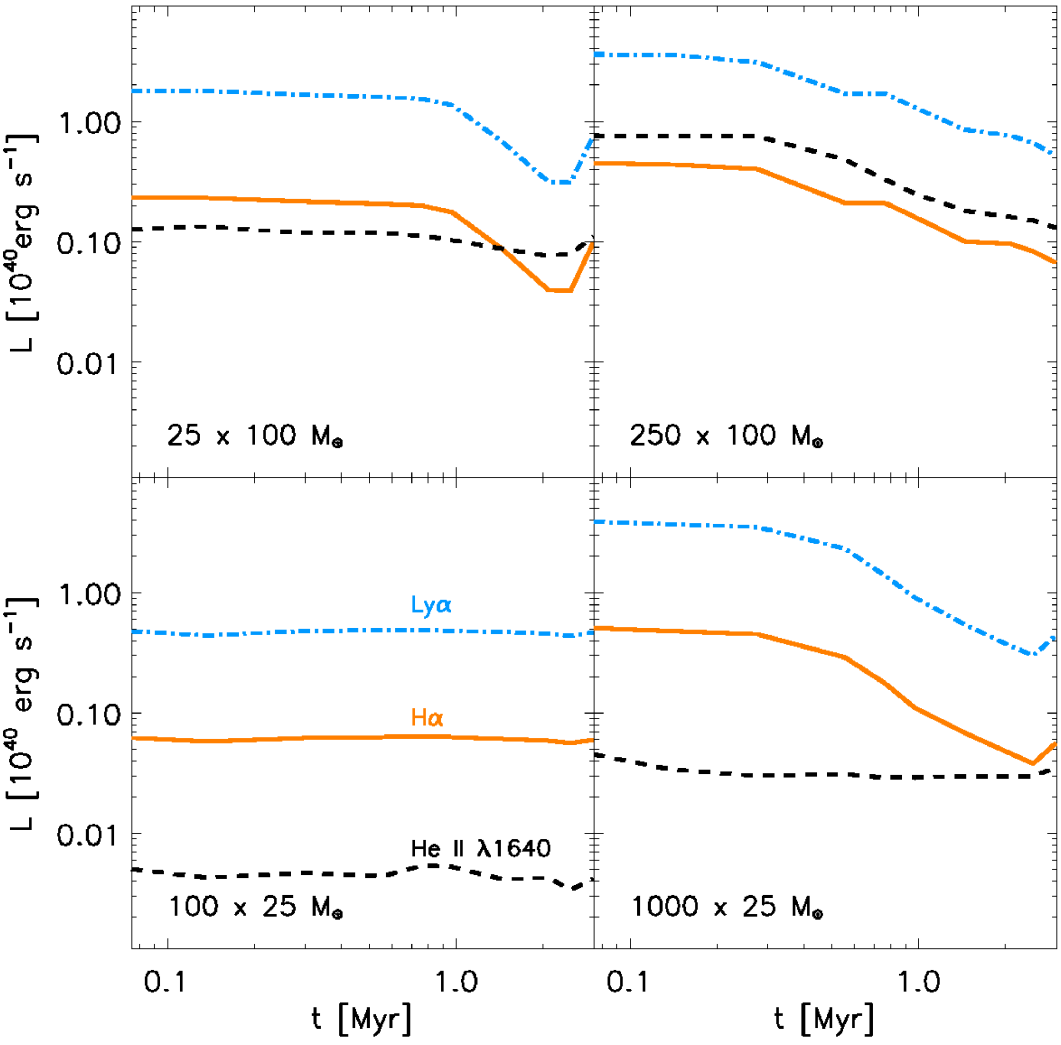

Figure 6.6: The luminosity of the galaxy, as a function of the time from the prompt formation of the cluster, in three recombination lines: Lyα (dot-dashed blue lines), Hα (solid red lines), and He II λ1640 (dashed black lines). The four panels correspond to our four different choices of IMF and total mass in stars; these are, clockwise from top-left: twenty-five 100 $M_\odot$ stars, two hundred fifty 100 $M_\odot$ stars, one thousand 25 $M_\odot$ stars, and one hundred 25 $M_\odot$ stars. The luminosities generally decrease with time, as the photoheating acts to decrease the density of the ionized gas, lowering the recombination rate. Note the different evolution of the He II λ1640 luminosity as compared to that of the hydrogen recombination lines, owing to the lower escape fraction of He II-ionizing photons (see Fig. 6.5).

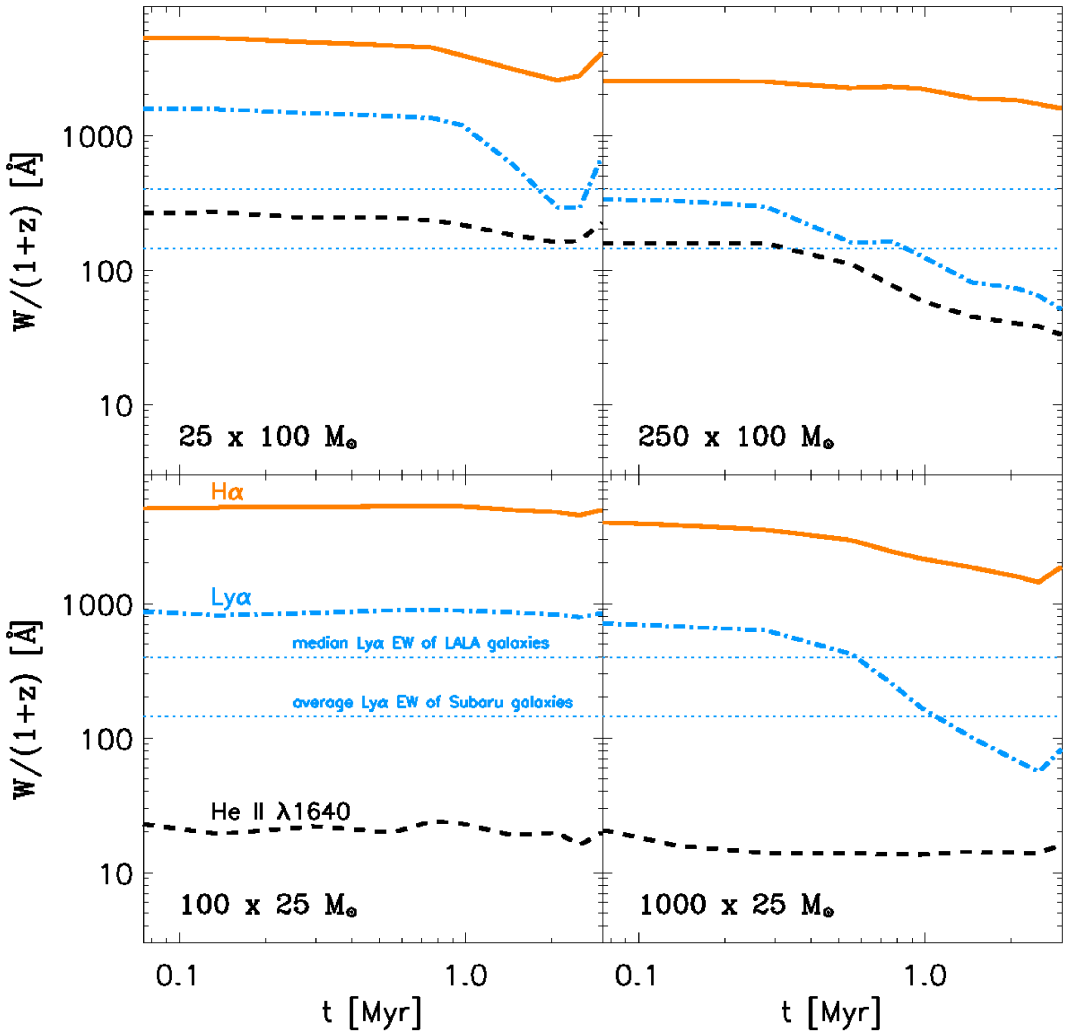

Figure 6.7: The rest frame equivalent widths, $W^0 = W/(1+z)$, where W is the observed EW, as a function of time, of the same three recombination lines shown in Fig. 6.6. For comparison, in each panel we plot the observed EWs of galaxies from two different surveys: the dotted line at 400 Ådenotes the median EW of Lyα emitters detected at $z = 4.5$ in the LALA survey (Malhotra & Rhoads, 2002), while the dotted line at 145 Ådenotes the average EW of the six Lyα emitters at $z \geq 6$ detected in the Subaru deep field (Nagao et al., 2007). Note that the Lyα EWs that we compute are upper limits, as scattering in a neutral IGM has not been accounted for.

of order 100 $M_\odot$ and 10 $M_\odot$, respectively.

The ratio of the observed fluxes in He II λ1640 and Hα, as calculated using equation (6.10), is displayed in Fig. 6.8. In this figure, it is clear that this line ratio is sensitive to the IMF, although it is not a constant for each cluster. Instead, for clusters in which the escape fraction of H I-ionizing photons increases with time dramatically, while the escape fraction of He II-ionizing photons remains roughly constant, this line ratio varies with the flux observed in Hα. While the ratio of the fluxes is a somewhat ambiguous IMF indicator, the clusters with the more top-heavy IMF do consistently exhibit larger ratios of He II λ1640 to Hα. Nagao et al. (2005) present a search for He II λ1640 emission from a strong Lyα emitter at $z = 6.33$, finding an upper limit for the ratio of He II λ1640 to Lyα. Assuming a standard value of 0.07 for the ratio of luminosity in Hα to that in Lyα (Osterbrock & Ferland, 2006), we show in Fig. 6.8 the upper limit that these authors report (Dawson et al., 2004). Although a weak upper limit, it is clear that observations with only slightly greater sensitivity will allow to differentiate between the flux ratios predicted here for massive and very massive Pop III IMFs.

Comparing the EW of Hα in the four panels of Fig. 6.7, it is clear that it is not strongly dependent on the IMF or on the total mass in stars, varying by at most a factor of three between each of the cases. While showing more variation between the four cases, the EW of Lyα also shows considerable ambiguity as an IMF indicator, its maximum value varying by about a factor of three between each of the four cases. This insensitivity of the Lyα EW to the IMF arises from two effects. Firstly, the stellar continuum luminosity $L_{\lambda,*}$ increases in a similar manner as the number of ionizing photons from the massive (25 $M_\odot$) IMF to the very massive IMF (100 $M_\odot$). This acts to keep the EW, roughly the ratio of the two, relatively constant. Secondly, while the luminosity in Lyα decreases with the increasing escape fraction of ionizing photons for the more massive clusters, the continuum luminosity remains largely unchanged, leading to a decrease in the EW with time for these clusters. We note that the Lyα EWs presented here are only upper limits, as we have not accounted for scattering of Lyα photons in the IGM (Dijkstra et al., 2007).

The EW of He II λ1640 is a more definitive indicator of IMF, being higher for the clusters of 100 $M_\odot$ stars than for the clusters of 25 $M_\odot$ stars, regardless of the total mass in stars or of the age of the cluster (up to $\gtrsim$ 3 Myr). As with the utility of He II λ1640 as a SFR indicator, this largely follows from the generally low escape fraction of He II-ionizing photons.

For comparison with observed galaxies, we plot in Fig. 6.7 the two observational results:

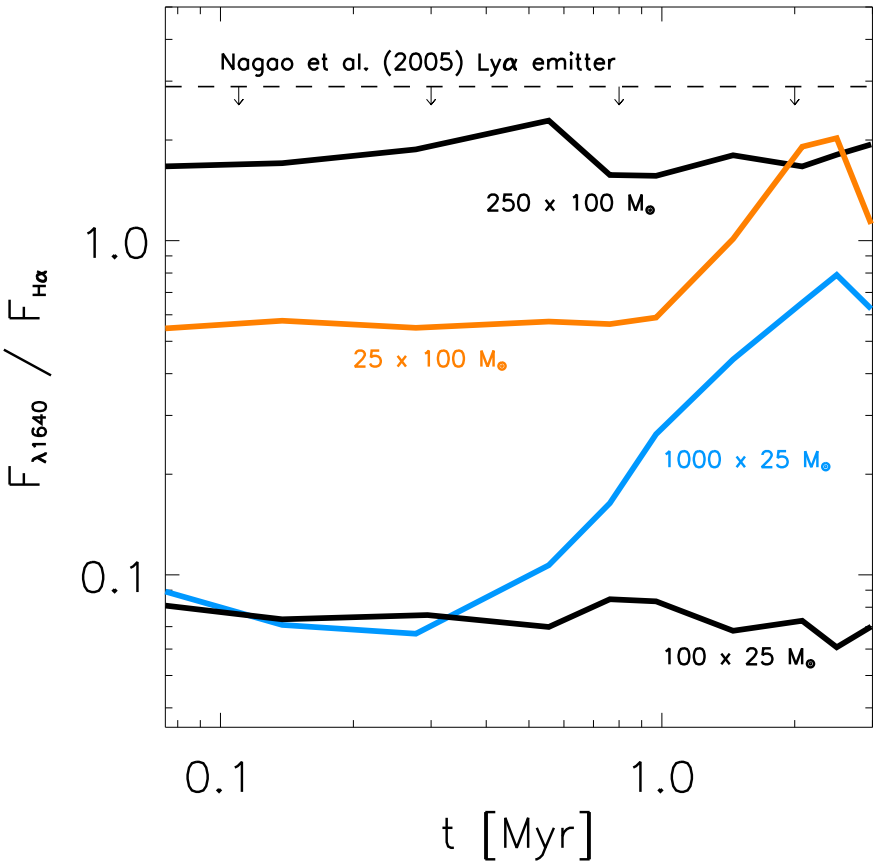

Figure 6.8: The ratio of the integrated fluxes in He II λ1640 and Hα, $F_{\lambda 1640}/F_{\mathrm{H}\alpha}$, as a function of time, for each of the four clusters simulated here, as labeled. The dashed horizontal line denotes the upper limit of this ratio for the strong Lyα emitter SDF J132440.6+273607 at $z = 6.33$, as reported by Nagao et al. (2005). Similar upper limits for Lyα emitters at $z = 4.5$ have been reported by Dawson et al. (2004).

the median Lyα EW of galaxies detected in the Large Area Lyman Alpha (LALA) survey, $W^0 \sim 400$ Å, and the average EW of six galaxies observed at $z \geq 6$ in the Subaru deep field, ~ 145 Å(Nagao et al., 2007). The large LALA EWs are comparable to what we find for primordial dwarf galaxies, although the LALA galaxies likely do not host Pop III star formation (but see Jimenez & Haiman, 2006). The detection of an EW of the He II λ1640 line $\gtrsim 10$ Åwould be a stronger indication of a galaxy hosting primordial star formation, as shown in Fig. 6.7, although none has been found as of yet. We note that observed Lyman break galaxies at $z \sim 3$ have been found to have He II λ1640 EWs of ~ 2 Å(Shapley et al., 2003), consistent with what is expected for Wolf-Rayet stars formed in starbursts (Brinchmann et al., 2008; Schaerer & Vacca, 1998).

6.2.4 Detectability of Recombination Radiation

In Fig. 6.9, we present our predictions for the observable recombination line fluxes, for each of the stellar clusters that we simulate. Fig. 6.10 shows the surface brightness in Hα as observed on the sky, for the two more massive stellar clusters, which each have a total mass in stars of 2.5×10^4 $M_\odot$. The fluxes in each plot, largely determined by our choices for the total stellar mass, are calculated using equation (6.6). While the larger H II region generated by the more massive stars encompasses more dense gas, creating more widely distributed emission in Hα, as shown in Fig. 6.10, the highest flux per square arcsecond is in the central region of the halo hosting the less massive stars. This is due again to the less dramatic dynamical response of the gas to photoheating, leading to higher densities, and thus higher recombination rates. Due to this effect, the highest fluxes are generated just after the birth of a stellar cluster, as shown in Fig. 6.9, when the density of the photoionized gas is still high, not having had time to expand in response to the concomitant heating. Indeed, Fig. 6.9 shows that the flux in Hα from the more massive 25 $M_\odot$ star cluster may reach $\gtrsim 10 \times (R/1000)$ nJy before the breakout of the H II region. Catching the first galaxies when still in the earliest stages of their initial starbursts, within the first few 10^5 yr, is thus likely to provide one of the best chances for observations of purely primordial stellar populations in the early Universe.

Aboard *JWST*, the Hα line would be observed with MIRI. Its pixel size of $\gtrsim 0.1$ arcsec would not resolve the brightest portions of the galaxies that we simulate, which, as shown in Fig. 6.10, are of order 0.01 arcsec. With a resolution capability of $R = 3000$ the MIRI has a sensitivity of $\gtrsim 200$ nJy for a signal-to-noise ratio of 10, in exposures of $\sim 10^6$ s (Panagia,

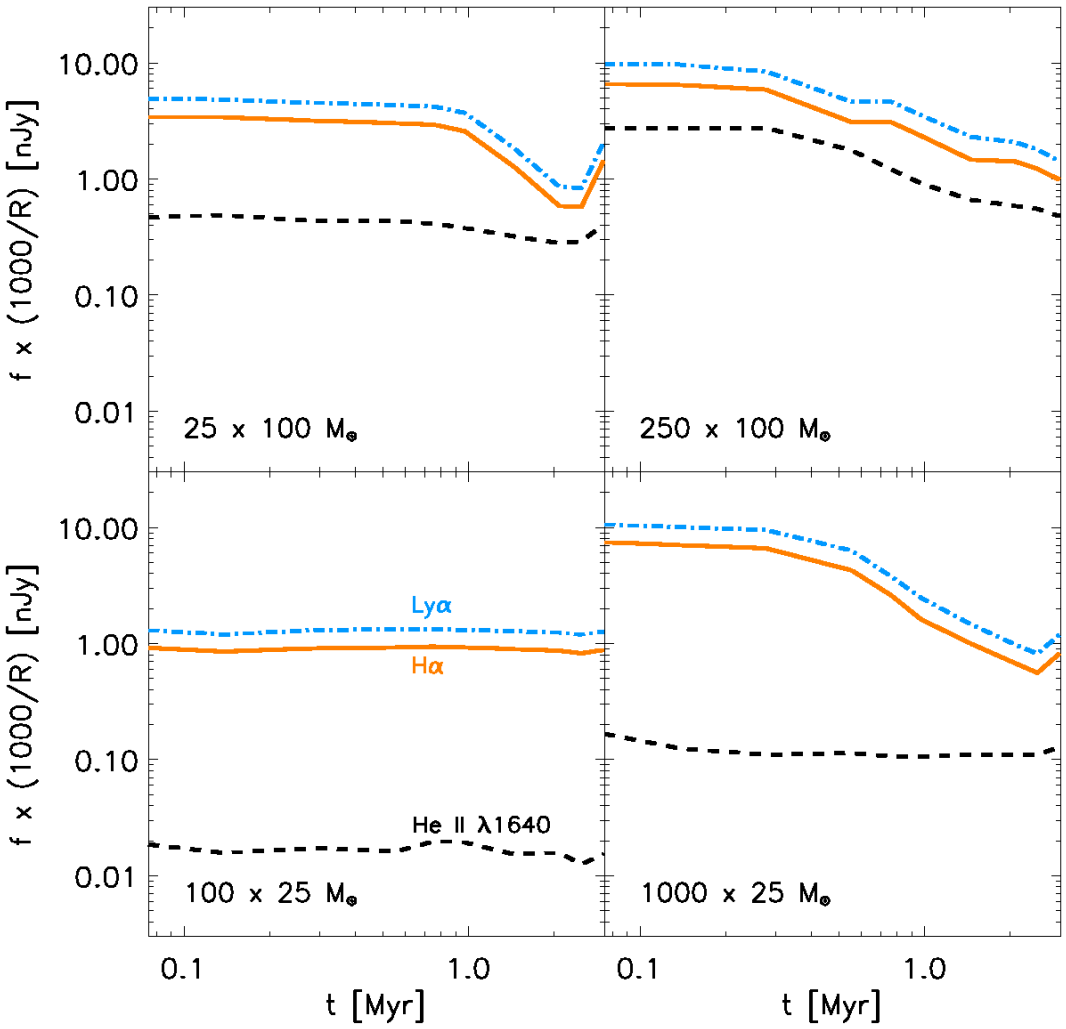

Figure 6.9: The observed fluxes, f, as a function of time, of the same three recombination lines shown in Fig. 6.6, for the galaxy we simulate at $z \sim 12.5$. The fluxes are normalized to what would be observed with a spectroscopic resolution of $R = 1000$, and are computed using equation (6.6) assuming that the galaxy appears as an unresolved point source. Note that the flux in Lyα is an upper limit, as the present calculation does not take into account scattering in a neutral IGM.

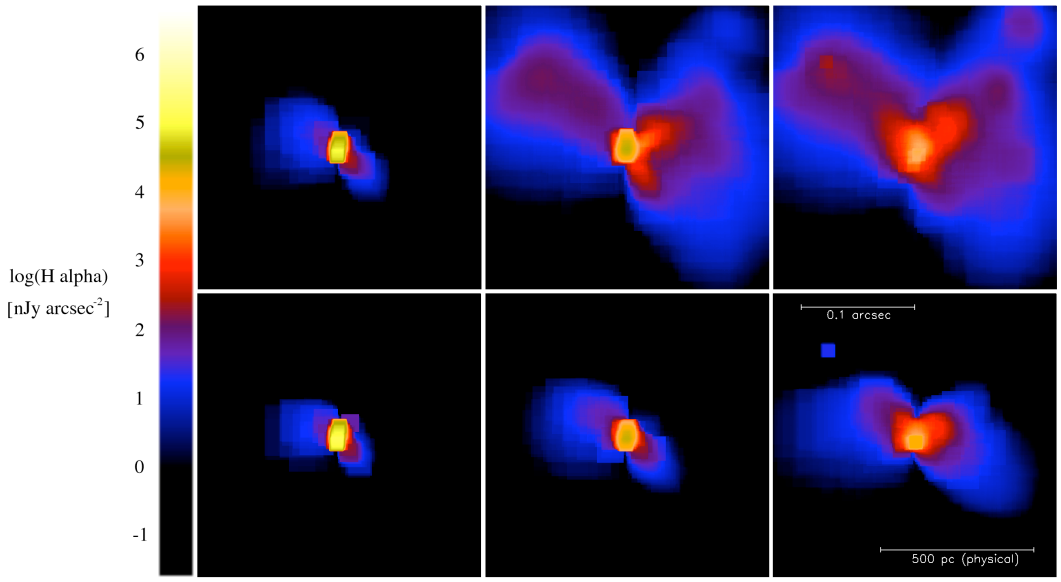

Figure 6.10: The flux in Hα, $f_{\mathrm{H}\alpha}$, per square arcsecond, emitted from a primordial dwarf galaxy, as observed on the sky at $z = 0$, assuming a spectroscopic resolution of $R = 1000$. Shown here are the two most massive of the four stellar clusters that we simulate, one containing 25 $\mathrm{M}_\odot$ stars (bottom panels), the other containing 100 $\mathrm{M}_\odot$ stars (top panels). From left to right, the clusters are shown at 10^5 yr, 1 Myr, and 3 Myr after formation. Note that the emission is concentrated in the densest photoionized regions, the filaments around the galaxy (compare the top panels to Fig. 6.2) and especially the dense gas within the inner $\sim$ 100 pc of the galaxy. The highest total fluxes occur at the earliest times, before the H II region has broken out; hence, the youngest stellar clusters are the most readily observed.

2005), making it unable to detect even the brightest galaxies that we simulate, the flux in Hα of these being $\lesssim 20$ nJy for $R = 3000$.

With a greater sensitivity of $\lesssim 100$ nJy (Panagia, 2005), the Near Infrared Spectrograph (NIRSpec) operates in the wavelength range 0.7 to 5 μm, allowing it to possibly detect Lyα out to $z \sim 40$ and He II λ1640 out to $z \sim 30$. However, the flux in He II λ1640 is always below that in Hα and, hence, is too low to be detected. The Lyα line, with the highest flux of the three recombination lines shown in Fig. 6.9, is also not directly detectable, with a flux falling well below the ~ 100 nJy sensitivity limit of NIRSpec. Furthermore, although the luminosity in Lyα is always intrinsically higher than that in Hα, before reionization the observable flux in Lyα may be dramatically decreased due to scattering in the neutral IGM (Dijkstra et al., 2007). Because we do not account for this effect in the present calculations, the Lyα fluxes presented here are only upper limits.

The Near Infrared Camera (NIRCam) aboard *JWST*, which will be used to conduct deep surveys designed to detect the first galaxies, will be capable of detecting point source fluxes as low as ~ 3.5 nJy at a signal-to-noise ratio of 10 for a 10^5 second exposure (Gardner et al., 2006). With a resolution of $\gtrsim 0.03$ arcsec per pixel, the NIRCam would also not quite resolve the galaxies that we simulate. We can evaluate the possibility that NIRCam may detect them as point sources, however, by estimating the continuum flux of the galaxies as observed at ~ 2 μm. As can be read from Figs. 6.6 and 6.7, the continuum flux, $\propto L_{\lambda 1640}/W_{\lambda 1640}$, varies only by a factor of a few between Lyα and He II λ1640. Thus, for simplicity we assume that the continuum is roughly flat and calculate the specific continuum flux, as observed at $z = 0$, as

$$f_{\rm cont} \sim \frac{L_{\lambda 1640}}{4\pi c D_{\rm L}^2(z)} \frac{\lambda_{\lambda 1640}^2 (1+z)}{W_{\lambda 1640}^0} \sim 0.03 \text{ nJy} , \tag{6.17}$$

where $W_{\lambda 1640}^0$ is the equivalent width in the rest frame of the galaxy, as defined in equations (6.12), (6.13) and (6.14). This flux is well below the sensitivity limit of the NIRCam, and so we conclude that detection of the continuum radiation from the galaxies we simulate would also be undetectable. We note, however, that under favorable circumstances, gravitationally lensed emission from a primordial galaxy undergoing an only slightly more luminous starburst may be detectable with *JWST*, given that lensing can boost the flux by a factor of order 10 (e.g. Refsdal, 1964; Stark et al., 2007).

The first dwarf galaxies could be more luminous than we find here if the efficiency of star formation $\epsilon_{\rm SF}$, defined as the fraction of the total baryonic mass in the galaxy contained

in stars, is larger than what we have assumed in our simulations, where our choices for the total mass in stars correspond to modest values of $\epsilon_{\rm SF} \sim 10^{-3} - 10^{-4}$. A larger efficiency ($\epsilon_{\rm SF} \sim 10^{-1}$), for the top-heavy IMFs considered here, would yield a cluster observable by NIRCam (Gardner et al., 2006). However, as we have demonstrated, the much higher ionizing flux from a $\sim 10^6$ $M_\odot$ cluster of massive primordial stars would induce a strong hydrodynamic response which would lead to a rapid decline in the luminosity emitted in recombination radiation. Thus, even if such clusters can be identified by their continuum emission, the detection of recombination radiation, and with it information about the stellar IMF, may be beyond the capabilities of *JWST*. Furthermore, the formation of such a massive cluster of primordial stars may face an impediment due to the strong radiative feedback within the cluster itself. Recent simulations of clustered star formation in the present-day Universe suggest that radiative feedback influences the fragmentation behavior of the gas and possibly lowers the overall star formation efficiency (Bate, 2009; Krumholz et al., 2007). However, the situation is by no means clear (Dale et al., 2005, 2007).

It is possible that more massive ($10^9 - 10^{10}$ $M_\odot$) primordial galaxies form at $z \gtrsim 12$, or form at lower redshift, making their detection feasible. However, such more massive, and therefore more luminous, galaxies are likely to also be more chemically evolved, and so may already be dominated by Pop II star formation. Thus, it may be that the galaxies which host pure Pop III starbursts, such as those we study here, will remain out of reach of even *JWST*, although this critically depends on the poorly constrained process of metal enrichment in the early Universe (Cen & Riquelme, 2008; Johnson et al., 2008; Pan & Scalo, 2007; Tornatore et al., 2007). We emphasize, however, that the dynamical effects studied here are likely to play a role even in the more luminous galaxies that will be detected, and are important to take into account in evaluating observations meant to constrain the SFR or the IMF.

6.3 Summary and Conclusions

We have presented calculations of the properties of the recombination radiation emitted from a primordial dwarf galaxy at $z \sim 12.5$, during the initial stages of a starburst. Our cosmological radiation-hydrodynamical simulations allow us to track the detailed dynamical evolution of the emitting gas in the central regions of the galaxy, and thus to study its effect on the emerging radiation. The goal of this study has been to determine the observable signatures of the initial starbursts in the first galaxies. In particular, we have aimed to find reliable

indicators of the star formation rate and of the stellar IMF.

Owing to the escape of H I-ionizing photons into the IGM, we find only a weak correlation between the total mass in stars and the luminosity in hydrogen recombination lines. This suggests that Lyα and Hα, despite the high luminosity in these lines, may not serve as strong indicators of the SFR, unlike in the low-redshift Universe (Kennicutt, 1983). The He II λ1640 line may be a more effective SFR indicator, as the luminosity in this line scales more closely with the total mass in stars, due to the lower escape fraction of He II-ionizing photons.

We confirm that the ratio of He II λ1640 to either Lyα or Hα can be used as an IMF indicator, although its utility is compromised in some cases by the unequal escape fractions of H I- and He II-ionizing photons. The most robust IMF indicator, in terms of distinguishing between populations of massive ($\gtrsim$ 10 $M_\odot$) and very massive ($\gtrsim$ 100 $M_\odot$) Pop III stars, is the EW of He II λ1640, as it is consistently higher for the more massive stars regardless of the total mass in stars. We note that while in principle the radiation emitted by a central accreting BH in a primordial dwarf galaxy could introduce complications for using He II λ1640 as IMF indicator (Tumlinson et al., 2001), recent work suggests that BH accretion is inefficient in the early Universe (Alvarez et al., 2008; Johnson et al., 2007; Milosavljevic et al., 2008; Milosavljević et al., 2009; Pelupessy et al., 2007). Such miniquasar activity may thus not result in appreciable observable radiation for the first $\sim 10^8$ yr.

In terms of the detectability of the recombination radiation from the first galaxies, we have shown that due to the dynamical response of the gas to photoheating, a top-heavy IMF or a high star formation efficiency can be self-defeating, leading to a decrease in the line luminosity of the galaxy. We conclude that the detection of purely primordial dwarf galaxies at $z \gtrsim 10$ is likely to be beyond the capabilities of *JWST*, although their detection may be just possible if the galaxies are strongly lensed. More luminous, 10^9 – 10^{10} $M_\odot$ (total mass), galaxies may thus be detected by *JWST*; however, such more massive galaxies are likely to be already chemically enriched due to previous episodes of star formation in their progenitors. These systems are then expected to host Pop II star formation, or a composite of Pop II and Pop III, depending on the still poorly understood mixing of heavy elements in the first galaxies (Karlsson et al., 2008).

Our results demonstrate how the radiation emitted from the first galaxies depends on the hydrodynamic effects of the photoionization from clusters of massive stars. This is complementary to the results of previous studies (Schaerer, 2002, 2003), which highlight the

evolution of the emitted radiation owing to the aging of a stellar population. Clearly, both effects must be considered in future work.

The initial starbursts of the first galaxies may constitute the formation sites of the only metal-free stellar clusters in the Universe, since after the first several Myr supernova feedback can quickly enrich the galaxy with metals (Kitayama & Yoshida 2005; Mori et al. 2002; but see Cen & Riquelme 2008; Tornatore et al. 2007). Also, a large fraction of the first dwarf galaxies, with masses of order 10^8 $M_\odot$, may already form from metal-enriched gas (Johnson et al., 2008; Omukai et al., 2008); it is an important open question what fraction of dwarf galaxies forming at $z \gtrsim 10$ are primordial when they begin forming stars. Future observations of those first dwarf galaxies that do host primordial star formation offer one of the few opportunities for constraining the primordial IMF.

7

The First Supernova Explosions: Energetics, Feedback, and Chemical Enrichment

One of the main goals in modern cosmology is to understand the formation of the first stars at the end of the cosmic dark ages and how they transformed the homogeneous primordial universe into a state of ever increasing complexity (Barkana & Loeb, 2001; Bromm & Larson, 2004; Ciardi & Ferrara, 2005; Glover, 2005; Miralda-Escudé, 2003). The first stars are predicted to be very massive, with $M_* \sim 100$ $M_\odot$, and formed in DM minihalos with virial masses of 10^5 – 10^6 $M_\odot$ (Abel et al., 2002; Bromm et al., 1999, 2002; Gao et al., 2007; Nakamura & Umemura, 2001; O'Shea & Norman, 2007; Yoshida et al., 2006). The first SN explosions rapidly dispersed the heavy elements that were produced during the brief lifetime of a Pop III star into the IGM, thus beginning the long nucleosynthetic build-up from a pure H/He universe to one with ubiquitous metal enrichment (Bromm et al., 2003; Daigne et al., 2006, 2004; Ferrara et al., 2000; Furlanetto & Loeb, 2003, 2005; Kitayama & Yoshida, 2005; Madau et al., 2001; Mori et al., 2002; Norman et al., 2004; Scannapieco et al., 2002; Thacker et al., 2002; Wada & Venkatesan, 2003; Yoshida et al., 2004).

The first SNe exerted important chemical and mechanical feedback effects on the early universe (Ciardi & Ferrara, 2005). First, the character of star formation changed from an early, high-mass dominated (Pop III) mode to a more normal, lower mass (Pop II) mode, once a critical level of enrichment had been reached, the so-called critical metallicity, $Z_{\rm crit} \lesssim$

$10^{-3.5}$ $Z_\odot$ (Bromm et al., 2001a; Bromm & Loeb, 2003b; Frebel et al., 2007; Omukai, 2000; Schneider et al., 2003, 2006; Smith & Sigurdsson, 2007). It is then crucially important to understand the topology of early metal enrichment and when a certain region in the universe becomes supercritical (Furlanetto & Loeb, 2005; Greif & Bromm, 2006; Mackey et al., 2003; Matteucci & Calura, 2005; Ricotti & Ostriker, 2004; Scannapieco et al., 2003; Schneider et al., 2002; Venkatesan, 2006). Second, the SN blast waves mechanically impacted the halos that hosted Pop III stars by heating and subsequently evacuating the dense gas inside them. Such a negative feedback effect, limiting the capacity for further star formation, has previously been considered for low-mass galaxies with correspondingly shallow potential wells (Dekel & Silk, 1986; Larson, 1974; Mac Low & Ferrara, 1999) but also for halos in the vicinity of a SN progenitor, where the net effect is still uncertain (Cen & Riquelme, 2008). A qualitatively different mechanical feedback effect has recently been suggested to occur in the dense, post-shock regions of the energetic blast wave (Machida et al., 2005; Mackey et al., 2003; Salvaterra et al., 2004) where secondary star formation might be induced by the onset of gravitational instabilities, thus giving rise to positive feedback.

The investigation of energetic explosions in the high-redshift universe has a long and venerable history. Most of this early work has focused on the cooling and fragmentation of astrophysical blastwaves (Bertschinger, 1985; Vishniac et al., 1985; Wandel, 1985) and the possibility of self-propagating galaxy formation (Carr et al., 1984; Ikeuchi, 1981; Ostriker & Cowie, 1981). Such explosive galaxy formation models typically implied substantial distortions to the cosmic microwave background blackbody spectrum and were thus excluded by the *COBE* (Fixsen et al., 1996). Many of the physical effects discussed in those seminal papers, however, remain relevant for our current studies.

What kind of SN explosion is expected to end the life of a massive Pop III star? According to the precise progenitor mass, the SN could be either of the conventional core-collapse type (for masses $\lesssim 40$ $M_\odot$) or it could be a PISN for masses in the range $\sim 140 - 260$ $M_\odot$ (Heger et al., 2003; Heger & Woosley, 2002). In this paper, we specifically consider a PISN with a progenitor mass of 200 $M_\odot$ and an explosion energy of $E_{\rm sn} = 10^{52}$ ergs. A PISN is predicted to completely disrupt the star, so that all the heavy elements produced will be released into the IGM (Fryer et al., 2001; Heger & Woosley, 2002), resulting in extremely high metal yields. However, our simulation would also approximately describe a hypernova explosion, in which a rapidly rotating, massive star undergoes core collapse (Tominaga et al., 2007; Umeda & Nomoto, 2002), as far as the energetics and overall dynamics of the blast

wave expansion are concerned.

Theoretically, one would expect that a PISN could only have occurred in the early universe, where Pop III stars were born massive and mass loss might have been negligible (Baraffe et al., 2001; Kudritzki, 2002). The recent discovery of the extremely luminous, relatively nearby SN 2006gy, which has tentatively been interpreted as a PISN (Smith et al. 2007; but see Ofek et al. 2007), might defy this theoretical expectation. Having such a nearby example of a PISN, in effect, would provide us with an "existence proof," opening up the exciting possibility of detecting the first SNe with the upcoming *JWST*, which will be sensitive enough to observe a single PISN out to $z \sim 15$ (Gardner et al., 2006; Mackey et al., 2003; Scannapieco et al., 2005b; Weinmann & Lilly, 2005; Wise & Abel, 2005).

In this paper, we carry out cosmological simulations of the first SN explosions, using the smoothed particle hydrodynamics code GADGET in its entropy-conserving formulation (version 1.1) (Springel et al., 2001). To address the questions outlined above, it is crucial to investigate the evolution of the SN remnant in three dimensions, starting from realistic initial conditions and including all the relevant physics. In particular, one needs to implement a comprehensive model for the cooling and the chemical evolution of the gas, as well as an efficient algorithm to treat the radiative transfer around the Pop III progenitor star (Johnson et al., 2007). Our simulations greatly improve on earlier work (Bromm et al., 2003), in that we calculate the preexplosion situation with much greater realism, using a ray-tracing method to determine the structure and extent of the H II region. In addition, we follow the evolution to much later times, allowing us to reach the point where the blast wave finally stalls and effectively dissolves into the general IGM. We are thus able to analyze the expansion and cooling properties of the SN remnant in great detail, allowing us to draw robust conclusions on the temporal behavior of the shock, its morphology, the final shock radius, and the total swept-up mass.

The structure of our work is as follows. In Section 7.2, we describe the SN progenitor and our method of initializing the SN explosion, followed by a test simulation to verify the accuracy of our results. Subsequently, we discuss the cosmological setup of the main simulation and our treatment of the H II region. We then concentrate on the evolution of the SN remnant, finding a simple analytic model that summarizes its expansion properties (Section 7.3). In Section 7.4, we investigate the mechanical feedback of the blast wave on neighboring minihalos and elaborate on the prospect of triggering gravitational fragmentation in the dense shell. In Section 7.5, we discuss the relevance of metal cooling, the coarse-grain dispersal of

metals, and the general mixing efficiency. Finally, in Section 7.6 we summarize our results and discuss important cosmological implications.

7.1 Numerical Methodology

The treatment of SN explosions in SPH simulations is a demanding problem, primarily due to the strong discontinuities arising at the shock front. One must set up the initial conditions with great care, and it is necessary to enforce strict timescale constraints in calculating the subsequent evolution. In light of these challenges, we describe the SN progenitor and our method of initializing the SN explosion, followed by a performance test to verify the correct behavior of the shock.

7.1.1 The Supernova Progenitor

Although the IMF of Pop III is poorly constrained, numerical simulations have indicated that stars forming in primordial halos typically attain 100 $M_\odot$ by efficient accretion and might even become as massive as 500 $M_\odot$ (Bromm & Loeb, 2004; Omukai & Palla, 2003; O'Shea & Norman, 2007). Heger & Woosley (2002) have discussed the fate of such massive stars and found that in the range 140 – 260 $M_\odot$ a PISN disrupts the entire progenitor, with explosion energies ranging from 10^{51} to 10^{53} ergs and yields up to $y \simeq 0.5$.

In the present work, we aim to investigate the most representative case, assuming a stellar mass of $M_* = 200\ M_\odot$. We conservatively adopt an explosion energy of $E_{\rm sn} = 10^{52}$ ergs and a yield of $y = 0.1$, to include the possibility of a less top-heavy IMF and a hypernova explosion, but we caution that such models generally predict energy input via bipolar jets, which may invalidate the assumption of a spherically symmetric blast wave. In light of the uncertain progenitor, we note that the dynamics of the SN remnant are governed mainly by the explosion energy, together with the IGM density distribution, and that the composition and metal content of the stellar ejecta become important only at very late times when the enriched gas recollapses (see Section 7.5.1).

7.1.2 Energy Injection

During the early evolution of the SN remnant, i.e., typically less than 10^4 yr after the explosion, the stellar ejecta are confined to a thin shell propagating at constant velocity into the surrounding medium, while secondary shocks quickly bring the interior to a uniform temperature (Gull, 1973). This stage in the evolution of the SN remnant is termed the free-expansion (FE) phase, and it lasts until the swept-up mass becomes comparable to the ejecta mass.

To reproduce these well-known initial conditions, we inject the kinetic energy of the SN as thermal energy into the $N_{\rm sn} = M_*/m_{\rm sph}$ innermost particles surrounding the center of the box, where $m_{\rm sph} \simeq 5$ M$_\odot$ corresponds to the SPH particle mass. This increases the thermal energy of all particles inside $r_{\rm fe}$ to $E_{\rm th} = E_{\rm sn}/N_{\rm sn}$, and the resulting temperature gradient acts as a piston on the surrounding gas. The ensuing shock accelerates the material in the vicinity of $r_{\rm fe}$ and creates a thin shell of highly supersonic material, initiating the Sedov-Taylor (ST) phase of the SN remnant. In addition, this method allows us to track the dispersal of metals, as each particle inside $r_{\rm fe}$ represents the original stellar content. Although the so-obtained resolution is crude, we can nevertheless quantify the coarse-grain chemical enrichment properties of the SN.

7.1.3 Test Simulation

To test our method of setting up the initial conditions, and also verify that the code reliably calculates the shock propagation, we compare the radial profiles of a test simulation with the well-known ST solution. For this purpose we place the SN according to the above prescriptions in a noncosmological box of length 1 kpc with 200^3 gas particles and switch off gravity, chemistry, and cooling. The particles are distributed randomly, so that the density fluctuates slightly around the mean of $n_{\rm H} = 0.5$ cm^{-3}, while the temperature is set to 2×10^4 K. This choice reflects the situation in the vicinity of a 200 M$_\odot$ Pop III star after the surrounding medium has been photoheated (Alvarez et al., 2006a; Johnson & Bromm, 2007; Kitayama et al., 2004; Whalen et al., 2004), but it also reproduces the initial conditions of the main simulation (see Fig. 7.8).

Once we initialize the simulation, the shock propagates into the surrounding medium according to the ST solution. As the duration and time-dependent properties of the gas in this phase are crucial for the late-time behavior of the SN remnant, we briefly review the

relevant details.

ST Solution

For a strong shock in an adiabatic gas, the Rankine-Hugoniot jump conditions imply for the density, velocity, pressure, and temperature directly behind the shock:

$$\rho_{\rm sh} = 4\rho \tag{7.1}$$

$$,v_{\rm sh} = \frac{3}{4}\dot{r}_{\rm sh} \tag{7.2}$$

$$,P_{\rm sh} = \frac{3}{4}\rho\dot{r}_{\rm sh}^2 \tag{7.3}$$

$$,T_{\rm sh} = \frac{3}{16}\frac{\mu m_{\rm H}}{k_{\rm B}}\dot{r}_{\rm sh}^2\,, \tag{7.4}$$

where ρ is the density of the surrounding medium, μ its mean molecular weight, $m_{\rm H}$ the mass of the hydrogen atom, and $k_{\rm B}$ Boltzmann's constant. Solving the continuity, Euler, and energy equations, one can relate these quantities at *any point* behind the shock to those *directly* behind the shock as a function of position. Fig. 7.1 shows the resulting self-similar, time-independent character of the ST solution, implying that most of the swept-up mass piles up just behind the shock and forms a dense shell, while the interior regions remain at high temperatures.

Completing the ST solution, the absolute position of the shock as a function of time is given by

$$r_{\rm sh} = \beta\left(\frac{E_{\rm sn}t_{\rm sh}^2}{\rho}\right)^{1/5}\,, \tag{7.5}$$

where $\beta = 1.17$ for an adiabatic gas. Thus, given the SN explosion energy and the density of the surrounding medium, all quantities of relevance around the progenitor are well-determined.

Test Results

Using the above results, we investigate whether the test simulation has successfully reproduced the ST solution. Fig. 7.2 compares the profiles of the test simulation after 1 Myr, when enough time has passed to enable a relaxation to the asymptotic solution, to the analytic, but dimensionalized, ST profiles shown in Fig. 7.1. Apart from minor deviations caused by

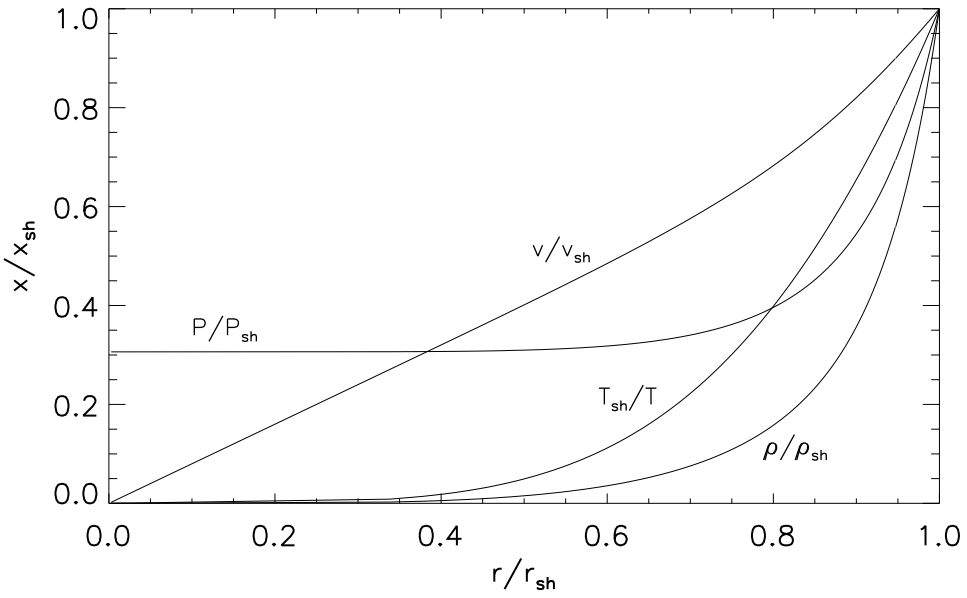

Figure 7.1: ST solution: density, velocity, pressure, and inverse temperature as a function of position relative to the shock. Most of the mass piles up just behind the shock and forms a dense shell, while the isobaric interior regions remain at high temperatures.

initial density fluctuations and higher order shocks, in particular in regard to the velocity distribution, we find that the simulation and the ST solution are in good agreement. The slight offset at the position of the shock is inevitable in light of kernel smoothing.

Being assured that we can reliably treat the propagation of shocks, we turn to the main focus of this work and describe the setup for a SN explosion in the high-redshift universe.

7.1.4 Main Simulation

Initial Setup

To investigate the long-term evolution of the SN remnant, but also to correctly calculate the structure and extent of the preceding build-up of the H II region around the progenitor, we choose a cosmological box of length $150/h$ kpc (comoving), with 200^3 particles per species (DM and gas). We initialize the simulation at $z = 100$ deep in the linear regime, adopting for this purpose a concordance ΛCDM cosmology with the following parameters: matter density $\Omega_m = 1 - \Omega_\Lambda = 0.3$, baryon density $\Omega_b = 0.04$, Hubble parameter $h = H_0/\left(100 \text{ km s}^{-1} \text{ Mpc}^{-1}\right) = 0.7$, spectral index $n_s = 1.0$, and a top-hat fluctuation power $\sigma_8 = 0.9$ (Spergel et al., 2003). Initial density and velocity perturbations are imprinted according to a Gaussian random field and grow in proportion to the scale factor until the onset of nonlinearity. At this point the detailed chemical evolution of the gas becomes crucial, and we apply the same chemical network as in Johnson et al. (2007) to track the abundances of H, H^+, H^-, H_2, H_2^+, He, He^+, He^{++}, and e^-, as well as the five deuterium species D, D^+, D^-, HD, and HD^+. All relevant cooling mechanisms in the temperature range 10 – 10^8 K are implemented, including H and He resonance processes, bremsstrahlung, inverse Compton (IC) scattering, and molecular cooling for H_2 and HD. Metal cooling does not become important for the entire lifetime of the SN remnant, yet we postpone a more detailed discussion of this issue to Section 7.5. We do not take into account the emission of radiation by the post-shock gas, which acts to create a thin layer of fully ionized material ahead of the shock and suppresses molecule formation (Kang & Shapiro, 1992; Shapiro & Kang, 1987; Shull & McKee, 1979), since (i) the SN remnant expands into an H II region, and (ii) we find that molecule formation in the post-shock gas becomes important only at late times, when it has cooled to below 10^4 K (see Section 7.3.4).

With these ingredients, the first star forms in a halo of $M_{\rm vir} \simeq 5 \times 10^5$ $M_\odot$ and $r_{\rm vir} \simeq 100$ pc at $z \simeq 20$ in the canonical fashion (Abel et al., 2002; Bromm et al., 1999, 2002). We

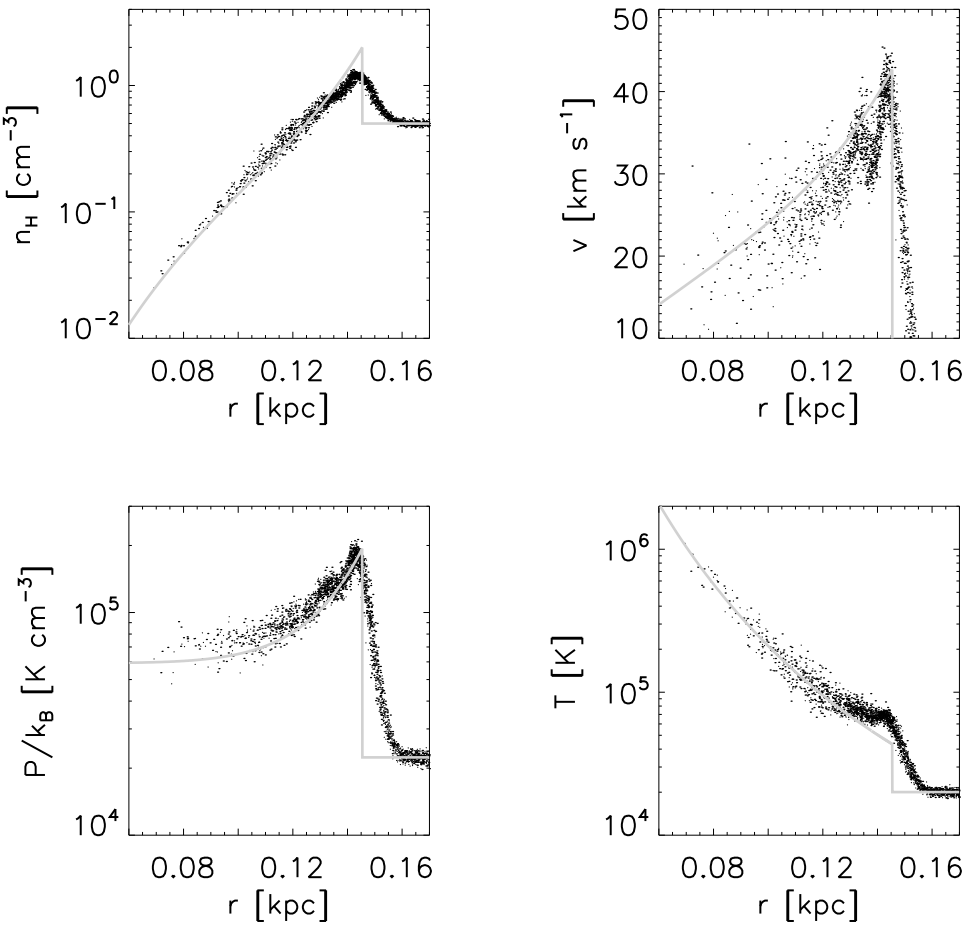

Figure 7.2: Density, velocity, pressure, and temperature of the shocked gas after 1 Myr. Black dots represent the test simulation, while the gray lines show the dimensionalized ST solution. Apart from deviations caused by higher order shocks and kernel smoothing, the simulation reproduces the analytic profiles relatively well.

determine its location by identifying the first particle that reaches a density of $n_{\rm H} = 10^4$ cm^{-3}. At this point the gas 'loiters' around a temperature of 200 K and typically attains a Jeans mass of a few 10^3 M$_\odot$ before further collapsing (Bromm et al., 2002; Glover, 2005). For simplicity, we assume that such a clump forms a single star, and we find that its location is reasonably well resolved by the minimum resolution mass, $M_{\rm res} \simeq 500$ M$_\odot$. In Fig. 7.3, we show the hydrogen number density in the x-y and y-z plane, centered on the formation site of the first star. Evidently, the host halo is part of a larger overdensity that will collapse in the near future and lead to multiple merger events. This behavior is characteristic of bottom-up structure formation, and our simulation therefore reflects a cosmological environment typical for these redshifts.

H II Region

The treatment of the H II region around the star is crucial for the early- and late-time behavior of the SN remnant. The photoevaporation of the host minihalo greatly reduces the central density and extends the energy-conserving ST phase, whereas after an intermediate stage the enhanced pressure in the H II region leads to an earlier transition to the final, momentum-conserving phase. In addition, the shock fulfills the stalling criterion (i.e. $\dot{r}_{\rm sh} = c_s$, where c_s is the sound speed of the photoheated IGM) much earlier in the H II region compared to previously unheated gas. We have found that neglecting the presence of the H II region around the star, which extends well into the IGM, leads to a final shock radius a factor of 2 larger, demonstrating its importance for the long-term evolution of the SN remnant.

To determine the size and structure of the H II region, we proceed analogously to Johnson et al. (2007). In detail, we initially photoheat and photoionize a spherically symmetric region surrounding the star up to a maximum distance of 200 pc, where we find a neighboring minihalo. We determine the necessary heating and ionization rates by using the properties of a 200 M$_\odot$ Pop III star found by Bromm et al. (2001b) and Schaerer (2002). After about 2 Myr, when the star has reached the end of its lifetime, the hydrodynamic shock has propagated to $r_{\rm vir}/2$ and photoevaporated the central regions of the host halo. Fig. 7.8*a* shows the resulting density, temperature, pressure, and velocity profiles, which display the characteristics of the analytic Shu et al. (2002) solution (i.e. pressure equilibrium throughout the interior, while the density [temperature] become almost constant at small [large] radii). In our case, the average interior density drops to $n_{\rm H} \simeq 0.5$ cm^{-3}, while the central temperatures rise

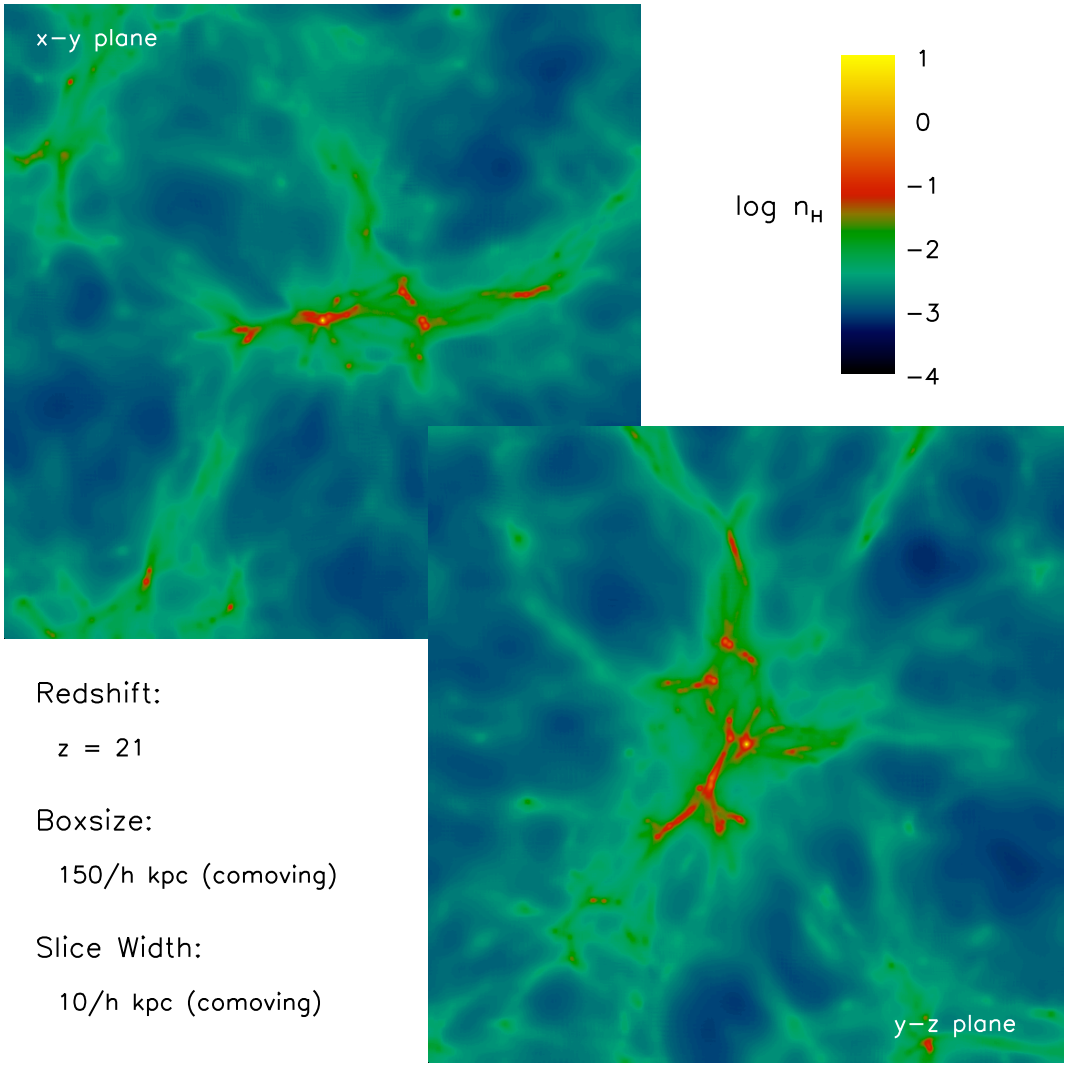

Figure 7.3: Hydrogen number density averaged along the line of sight in a slice of $10/h$ kpc (comoving) around the first star, forming in a halo of total mass $M_{\rm vir} \simeq 5 \times 10^5$ $M_\odot$ at $z \simeq 20$. Evidently, the host halo is part of a larger conglomeration of less massive minihalos and is subject to the typical bottom-up evolution of structure formation.

to roughly 4×10^4 K (see Fig. 7.8*a*). The radial profiles agree relatively well with the self-consistent radiation-hydrodynamics simulations performed in Abel et al. (2007) and Yoshida et al. (2007a), with slight differences most likely due to the harder spectrum and shorter lifetime of a 200 $M_\odot$ star compared to a 100 $M_\odot$ star (see also Johnson & Bromm, 2007).

Since ionizing radiation escapes the minihalo after only a few thousand years (Alvarez et al., 2006a), we determine the final size and structure of the H II region by performing the ray-tracing algorithm introduced in Johnson et al. (2007). This routine finds the Strömgren radius along 10^5 rays around the star, with each ray consisting of 200 radial bins. For this purpose we assume that helium has the same ionization properties as hydrogen, and we do not treat a separate He III front. Once an individual cell fulfills the Strömgren criterion, we ionize its content and set its temperature and molecule abundances to the values at the outer edge of the photoheated region. This method is appropriate for the propagation of ionization fronts in the general IGM, but it does not correctly treat the photoevaporation of neighboring minihalos, when the ionization front becomes D-type (Ahn & Shapiro, 2007). This issue is particularly important with respect to feedback on neighboring minihalos and is further discussed in Section 7.4.

Fig. 7.4 shows the gas temperature after the main-sequence lifetime of the star, and thus indirectly the size and structure of the H II region. In agreement with Alvarez et al. (2006a), we find that the H II region can be as large as 5 kpc, but efficient shielding by neighboring minihalos may limit its size to a few 100 pc in some directions. The H II region initially cools via IC scattering, while the pressure gradient at the boundary of the H II region leads to a gradual adiabatic expansion on timescales comparable to the Hubble time at $z \simeq 20$ (see Figs. 7.4 and 7.9) (Johnson & Bromm, 2007). Even though molecule fractions rise to typically $x_{H_2} \sim 10^{-3}$ and $x_{HD} \sim 10^{-7}$, molecular cooling remains inefficient due to the low densities of the photoheated gas (Johnson & Bromm, 2007). We do not treat the evolution of a separate LW front, as molecules inside the H II region are destroyed primarily by collisional dissociation and charge transfer, while they are quickly reformed in more massive, neighboring minihalos once the central source turns off (Johnson et al., 2007; Yoshida et al., 2007a).

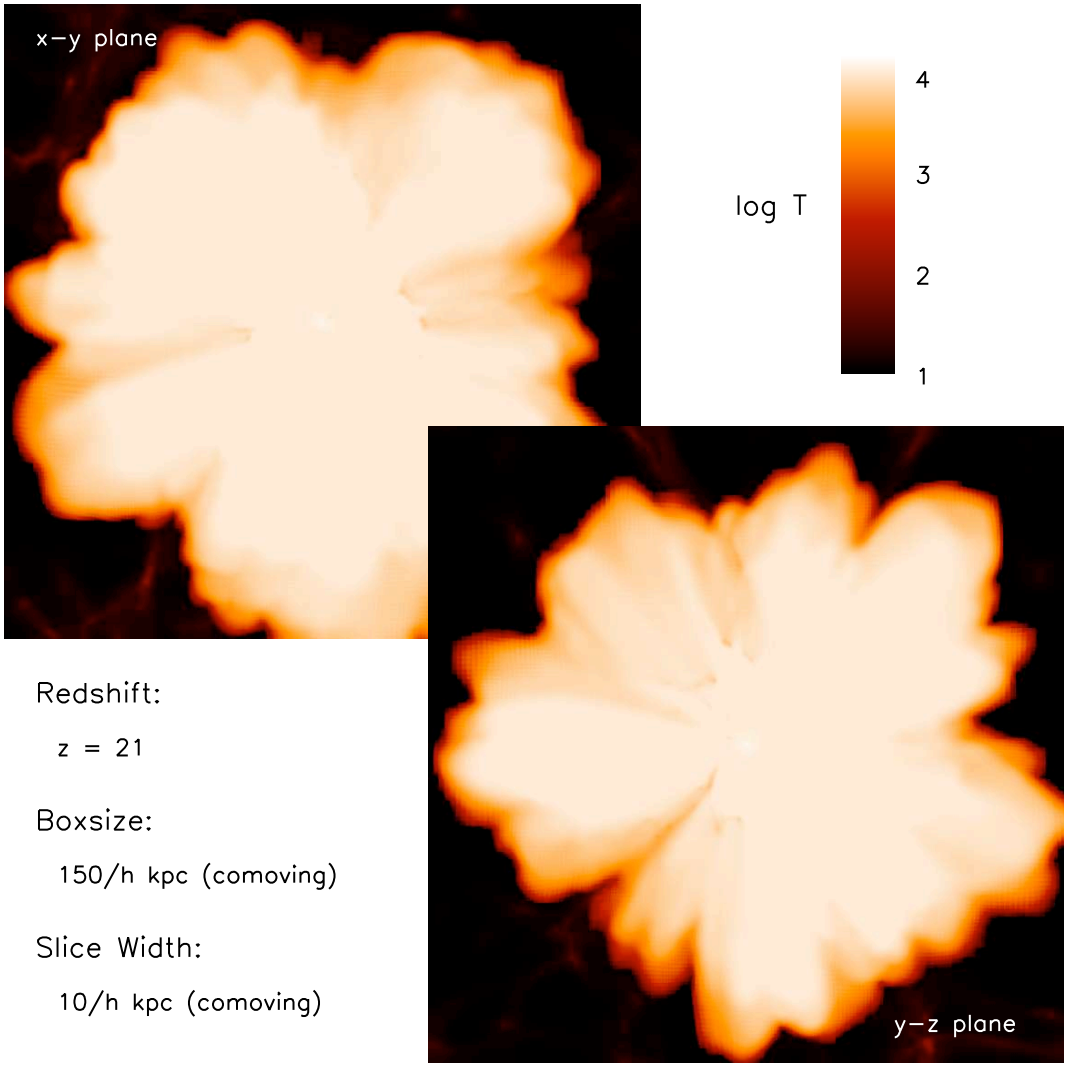

Figure 7.4: Temperature averaged along the line of sight in a slice of $10/h$ kpc (comoving) around the star after its main-sequence lifetime of 2 Myr. Ionizing radiation has penetrated nearby minihalos and extends up to 5 kpc around the source, heating the IGM to roughly 2×10^4 K, while some high-density regions have effectively shielded themselves.

Sink Particles

In the course of the simulation, neighboring minihalos might reach high enough densities to form stars, and the subsequent photoheating could significantly influence the propagation of the SN remnant. In the present work, we aim to investigate a single unperturbed SN explosion, and thus we rule out further star formation by employing the sink particle algorithm used in Johnson et al. (2007). This routine forms sink particles once the hydrogen number density exceeds 10^4 cm^{-3} and further accretes particles inside the Bondi radius (Bondi, 1952). This procedure prevents disturbances arising from the expansion of additional ionization fronts and allows us to concentrate on the feedback caused by the SN explosion.

With these preparations in place, we reinitialize the simulation at the end of the FE phase according to Section 7.2.2. In the following we discuss the evolution of the SN remnant until it effectively dissolves into the IGM.

7.2 Expansion and Cooling Properties

Throughout its lifetime, the remnant goes through four evolutionary stages, each of which is characterized by a different physical mechanism becoming dominant. Based on this chronological sequence, we discuss the expansion and cooling properties of the SN remnant with respect to the simulation results, and we summarize the remnant's behavior with a simple analytic model.

7.2.1 Phase I: Free Expansion

At very early times, the SN remnant enters the FE phase and propagates nearly unhindered into the surrounding medium. It expands with a constant velocity of $v_{\rm ej}^2 = 2E_{\rm sn}/M_{\rm ej}$, where for our case $M_{\rm ej} = M_*$. The duration of the FE phase is given by $t_{\rm fe} = r_{\rm fe}/v_{\rm ej}$, or

$$t_{\rm fe} = r_{\rm fe}\sqrt{\frac{M_{\rm ej}}{2E_{\rm sn}}}\,, \tag{7.6}$$

where $r_{\rm fe}$ is the radius at which the swept-up mass equals the mass of the original ejecta, i.e.

$$r_{\rm fe} = \left(\frac{3XM_{\rm ej}}{4\pi m_{\rm H} n_{\rm H}}\right)^{1/3}\,, \tag{7.7}$$

where $X = 0.76$ is the primordial mass fraction of hydrogen (Kitayama & Yoshida, 2005).

After $t_{\rm fe}$, the inertia of the swept-up mass becomes important, and the shock undergoes a transition to the ST phase. Since we do not explicitly model the FE phase, we use the above analytic arguments to obtain $r_{\rm fe} \lesssim 20$ pc and $t_{\rm fe} \lesssim 10^4$ yr (see Fig. 7.7).

7.2.2 Phase II: Sedov-Taylor Blast Wave

According to Section 7.2.2, the simulation begins when the shock undergoes a transition to the ST phase. Since we have already discussed the properties of the ST solution in Section 7.2.3, we can apply these results to understand the early behavior of the SN remnant. With the knowledge that the previous photoheating has created an average density profile of $n_{\rm H} \simeq 0.5$ cm^{-3} in the vicinity of the progenitor (Fig. 7.8*a*), we find with the help of equation (7.5) that the shock approaches $r_{\rm vir}/2$ after about 10^5 yr. At this point it catches up with the previously established photoheating shock, where the outlying density profile becomes isothermal. The simulation results (Fig. 7.8*b*) agree with this analytic prediction, yet the profiles do not quite resemble the ST solution, partly because not enough time has passed, but also because cooling in the dense shell becomes important, violating energy conservation. Consequently, the ST phase ends and the remnant undergoes a second transition.

To understand the origin of this transition, we elaborate on the cooling mechanisms responsible for radiating away the thermal energy of the remnant. At the high temperatures behind the shock, these are H and He resonance processes (RPs), bremsstrahlung (BS), and IC scattering, with the former consisting of collisional ionization, excitation, and recombination cooling. Fig. 7.5 shows the relevant cooling rates, normalized to a hydrogen number density of unity, where the abundances of the various species follow from assuming collisional ionization equilibrium. Evidently, IC scattering and BS are important at high temperatures, whereas RPs become significant below 10^6 K. However, BS and RPs are proportional to the density squared, while IC scattering exhibits only a linear dependence. Thus, RPs will be the most important coolant in the dense shell, while IC scattering is dominant in the hot interior.

At $z = 20$, the cooling time for IC scattering is approximately 10 Myr, independent of temperature and density, while cooling times for RPs in the dense shell are generally much lower. To determine when radiative losses affect the energetics of the SN remnant, we must equate the shell cooling time with the expansion time. Fig. 7.6 shows this analytic relation for the initial conditions of the simulation, i.e. $E_{\rm sn} = 10^{52}$ ergs and $n_{\rm H} = 0.5$ cm^{-3}. Confirming

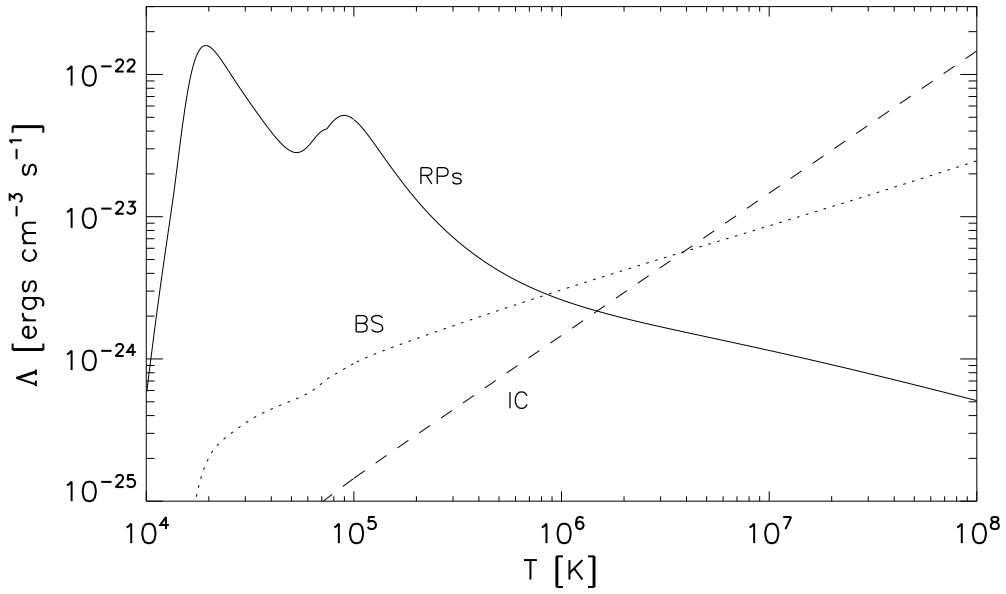

Figure 7.5: Cooling rates as a function of temperature at $z \simeq 20$ for H and He RPs (solid line), BS (dotted line), and IC scattering (dashed line) in collisional ionization equilibrium, with $n_{\rm H}$ set to unity. At low temperatures RPs dominate, while above 10^6 K IC scattering and BS become important. However, RP's and BS are proportional to the density squared, while IC scattering exhibits only a linear dependence.

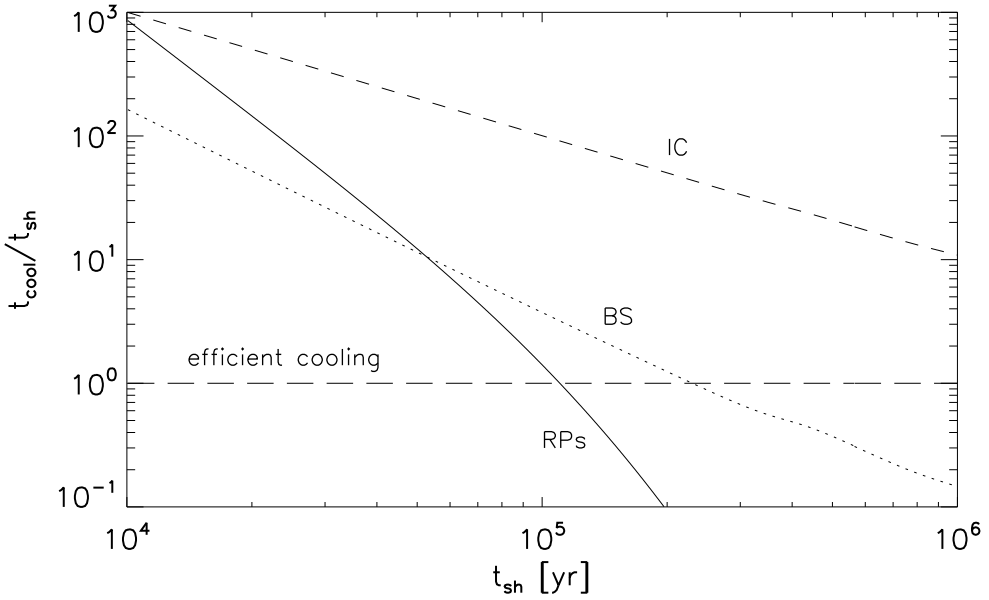

Figure 7.6: Cooling time over expansion time in the dense shell for RPs (solid line), BS (dotted line), and IC (dashed line). The long-dashed line indicates when cooling becomes efficient, implying that RPs are responsible for ending the ST phase after 10^5 yr. At $z = 20$, the cooling time for IC scattering is roughly 10 Myr, independent of temperature and density.

the simulation results, this prediction yields that RPs efficiently cool the dense shell to 10^4 K after about 10^5 yr. At this point the shocked gas separates into a hot, interior bubble with temperatures above 10^6 K and a dense shell at 10^4 K bounded by a high-pressure gradient. This multi-phase structure is clearly visible in Fig. 7.8*b*, which remains intact for $\lesssim 10$ Myr, when IC scattering becomes important and cools the last remnants of the interior bubble to the temperature of the dense shell. With energy conservation no longer valid, the ST phase ends before the shock has relaxed to the asymptotic solution, yet we nevertheless find that $r_{\rm sh} \propto t_{\rm sh}^{2/5}$ fits the temporal scaling of the mass-weighted mean shock radius relatively well (see Fig. 7.7).

7.2.3 Phase III: Pressure-Driven Snowplow

After the ST phase ends, the pressurized, interior bubble drives a dense shell, and one speaks of a pressure-driven snowplow (PDS). To analytically describe the further evolution of the

SN remnant, we assume that the entire swept-up mass $M_{\rm sw}$ is confined to an infinitely thin shell. In light of the steep density profile toward the interior, this assumption is justified, leading to an equation of motion of the form

$$\frac{d\left(M_{\rm sw}v_{\rm sh}\right)}{dt} = 4\pi r_{\rm sh}^2 P_b \,, \tag{7.8}$$

where P_b is the pressure of the hot, interior bubble, and the external pressure has been neglected (Ostriker & McKee, 1988). Since $M_{\rm sw} \propto r_{\rm sh}$ in an r^{-2} density profile and $P_b \propto r_{\rm sh}^{-5}$ in the adiabatically expanding interior, one can solve the above equation with a power law of the form $r_{\rm sh} \propto t_{\rm sh}^{2/5}$. Interestingly, this procedure yields the same temporal scaling as the ST solution, and we therefore do not expect a change in slopes after 10^5 yr. This is a direct consequence of the transition to the PDS phase once the shock approaches the isothermal density profile in the outskirts of the halo. Fig. 7.7 confirms this result, as the simulation shows only a slight deviation from the analytically derived $t_{\rm sh}^{2/5}$ slope.

Using the above model, we can further determine when the PDS phase ends. The pressure directly behind the shock after 10^5 yr can be estimated with equation (7.3) as $P_b/k_{\rm B} \simeq 3 \times 10^6$ K cm^{-3}, in agreement with the simulation (see Fig. 7.8*b*). With $P_b \propto r_{\rm sh}^{-5}$ and $r_{\rm sh} \propto t_{\rm sh}^{2/5}$, we further find $P_b \propto t_{\rm sh}^{-2}$, implying that after roughly 1 Myr the interior pressure has dropped to $P_{\rm b}/k_{\rm B} \simeq 3 \times 10^4$ K cm^{-3}. At this point pressure equilibrium between the hot interior and the dense shell has been established, and the shock is driven solely by its accumulated inertia. Fig. 7.8*c* confirms this prediction, showing that the interior pressure has indeed dropped to that of the dense shell. In contrast, the temperature only drops proportional to $t_{\rm sh}$ and remains high.

7.2.4 Phase IV: Momentum-Conserving Snowplow

With the pressure gradient no longer dominant, the SN remnant is driven by the accumulated inertia of the dense shell and becomes a momentum-conserving snowplow (MCS). In analogy to the derivation performed in Section 7.3.3, the position of the shock as a function of time can be obtained by solving equation (7.8) in the absence of a pressure term. Since the shock has not yet propagated beyond the surrounding r^{-2} density profile, this yields an initial scaling of $r_{\rm sh} \propto t_{\rm sh}^{1/2}$.

At later times, the shock finally leaves the host halo and encounters neighboring mini-

halos in the y-z plane, but underdense voids perpendicular to the y-z plane (see Fig. 7.3). This increases its radial dispersion, while at the same time the Hubble expansion becomes important and serves to expand the medium on which the SN remnant propagates, thus raising its physical shock velocity. We can therefore only estimate the temporal scaling of the mass-weighted mean shock radius based on the simulation results, finding, interestingly, that $r_{\rm sh}$ maintains its $t_{\rm sh}^{1/2}$ scaling until it fulfills the stalling criterion (see Fig. 7.7). This occurs after about 200 Myr, close to the Hubble time at $z \simeq 20$, when the shock velocity approaches the local IGM sound speed and becomes indistinguishable from sound waves. Evidently, the increased slope at late times is a fundamental difference between SNe occurring at high redshifts and in the present-day universe, where $r_{\rm sh} \propto t_{\rm sh}^{1/4}$.

In the meantime, the hot interior has expanded adiabatically for roughly 10 Myr, when IC scattering becomes important, quickly cooling the interior to temperatures of the dense shell (see Fig. 7.8*d*). Even later, the high electron fraction persisting in the interior and the dense shell leads to efficient molecule formation, and typical abundances of $x_{\rm H_2} \sim 10^{-3}$ and $x_{\rm HD} \sim 10^{-7}$ are reformed. By the end of the simulation, both phases have adiabatically cooled to $T \sim 10^3$ K, while densities in the dense shell have dropped to $n_{\rm H} \sim 10^{-2.5}$ cm^{-3} (see Figs. 7.9 and 7.14). The interior is even more underdense, and we find that the SN explosion has completely disrupted the host halo, preventing further star formation inside of it for at least a Hubble time at $z \simeq 20$. Due to the continuous adiabatic expansion of the post-shock gas, molecular cooling remains inefficient for the entire lifetime of the SN remnant.

7.2.5 Summary of Expansion Properties

Summarizing the expansion properties of the SN remnant, Fig. 7.7 shows the mass-weighted mean shock radius as a function of time, together with the analytically derived power laws. The good agreement indicates that one can quantify the evolution of the SN remnant by means of simple physical arguments and obtain relatively accurate results.

We find a final mass-weighted mean shock radius of 2.5 kpc, which is roughly a factor of 2 smaller than the H II region. Fig. 7.7 also shows the radial dispersion of the shock, indicating that the surrounding medium becomes highly anisotropic once the SN remnant leaves the host halo. After about 5 Myr, the shock encounters the first neighboring minihalos in the y-z plane and begins to stall, while it continues to propagate into the voids perpendicular to the y-z plane. The vast majority of the shocked material resides in the general IGM, as the

mass-weighted mean closely traces the maximum shock radius.

To conclude this section, Fig. 7.10 shows the swept-up gas mass as a function of time for the simulation and the analytic model, where the slopes have been determined by the relation $M_{\rm sw} \propto \rho r_{\rm sh}^3$, except at very late times when the shock structure becomes too complex for a simple analysis. We find a final swept-up mass of 2.5×10^5 $M_\odot$, which is roughly a factor of 2 smaller than the mass enclosed inside a sphere of radius 2.5 kpc, assuming the background density at $z \simeq 12$. This further demonstrates the overall asymmetry of the shock (see Fig. 7.14).

7.3 Feedback on Neighboring Halos

So far we have concentrated on the propagation of the SN remnant into the IGM and treated neighboring minihalos as disturbances to the radial density profile. In the following, we explicitly investigate the mechanical feedback of the SN on nearby minihalos and discuss possible consequences for star formation. For this purpose we have carried out two additional simulations, one without feedback and another with radiative feedback, which enable us to disentangle the effects of photoheating and the SN shock.

Combining the so-obtained results, Fig. 7.11 shows the distances of all star-forming halos from the initial SN progenitor as a function of expansion time, when they have reached the threshold density $n_{\rm H} = 10^4$ cm^{-3}. Following our argumentation in Section 7.2.4, the halo irreversibly collapses at this point and forms a star. The shades of the symbols in Fig. 7.11 indicate their affiliation to the different simulations (i.e. black, dark gray, and light gray symbols represent the no-feedback, photoheating-only, and main simulation runs), while the shapes of the symbols represent individual halos. For orientation, we show the mass-weighted mean shock radius at late times according to Fig. 7.7.

7.3.1 Delay by Photoheating

In the photoheating-only case, we find that the collapse of all three star-forming halos is delayed (see Fig. 7.11). While we do not properly resolve D-type ionization fronts that may develop within shielded minihalos, we find that ionizing radiation can penetrate deep into their cores and suppress cooling and the accretion of gas. The distance, mass, and maximum density of the halo at the onset of photoheating are all crucial for the extent of

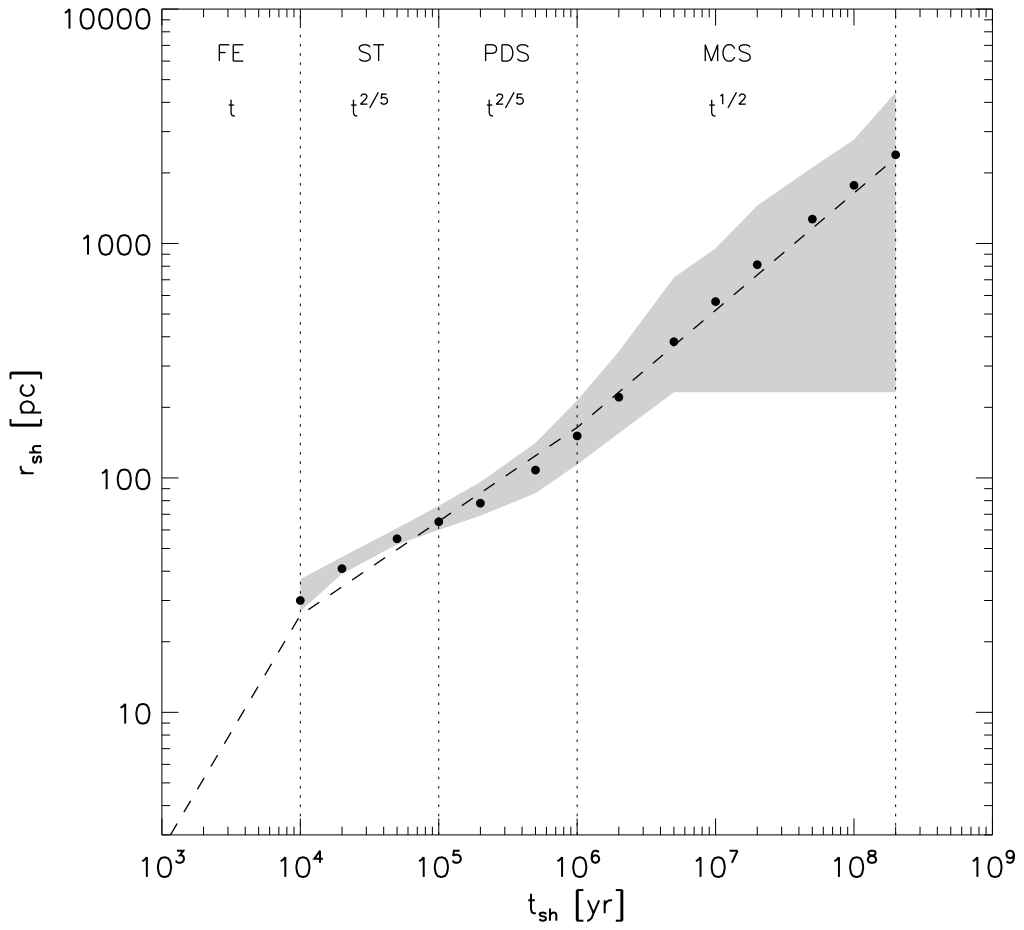

Figure 7.7: Evolution of the SN remnant in its entirety, from $z \simeq 20$, when the SN explodes, to $z \simeq 12$, when the shock finally stalls. Its total lifetime is about 200 Myr, or a Hubble time at $z \simeq 20$. The black dots indicate the mass-weighted mean shock radius according to the simulation, while the dashed line shows the analytic solution. For both we find a final mass-weighted mean shock radius of 2.5 kpc. The shaded region shows the radial dispersion of the shock, indicating that it increases significantly once the SN remnant leaves the host halo and encounters the first neighboring minihalos in the y-z plane. The bulk of the SN remnant propagates into the IGM, since the mass-weighted mean closely traces the maximum shock radius.

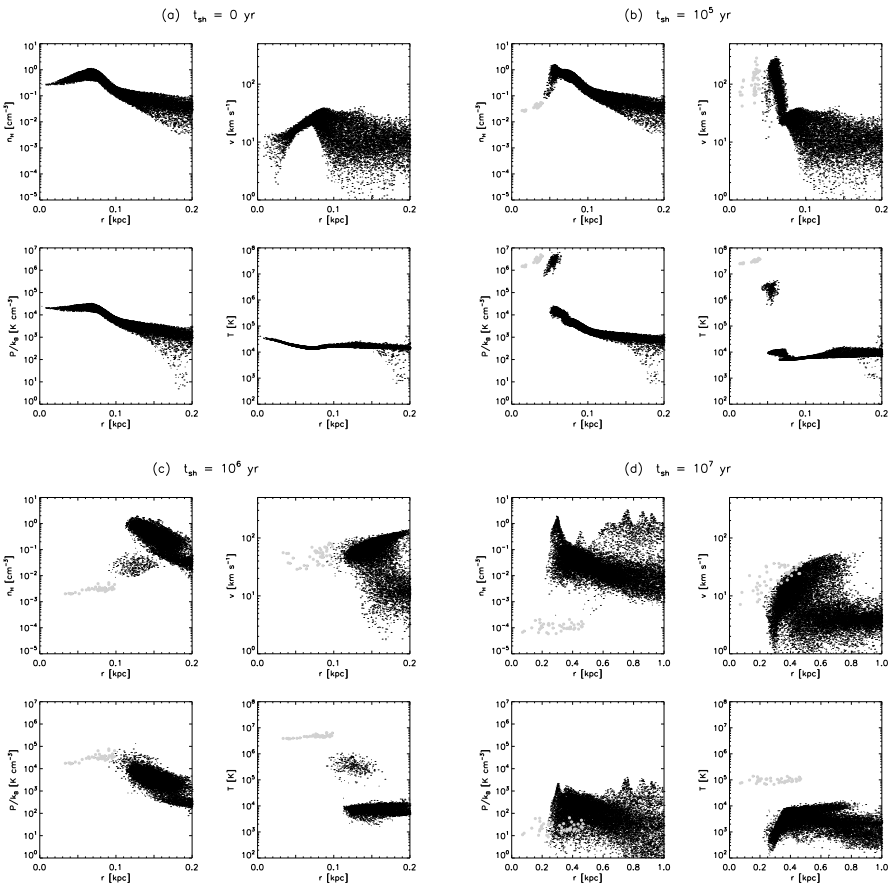

Figure 7.8: Density, velocity, pressure, and temperature around the SN progenitor star immediately before its death, and 10^5, 10^6, and 10^7 yr after the SN explosion. Black dots represent normal SPH particles, while gray dots represent the initial stellar ejecta. Panel (a): the hydrodynamic shock of the H II region has approached $r_{\rm vir}/2$ at $\simeq 50$ pc after establishing pressure equilibrium in the interior, while the density and velocity profiles assume the characteristic Shu et al. (2002) solution of a champagne flow. The temperature of the H II region is typically 2×10^4 K. Panel (b): the shock created by the SN explosion propagates into the surrounding medium according to the ST solution, with the characteristic formation of a dense shell and a hot, interior bubble. After 10^5 yr, the shock approaches the previous photoheating shock with expansion velocities well in excess of 100 km s^{-1}. At the same time, cooling in the dense shell by RPs becomes efficient and the ST phase ends. The resulting sharp temperature drop between the interior bubble at $T > 10^6$ K and the dense shell at $T \simeq 10^4$ K is clearly visible. Panel (c): the SN remnant has undergone a transition to the PDS phase and is driven by the high pressure in the interior and the momentum of the dense shell. This phase ends after about 1 Myr, when pressure equilibrium has been established. The pressure drop in comparison with Panel (b) is clearly visible, while temperatures in the interior remain high. Panel (d): after 10 Myr, the radial dispersion of the shock has increased dramatically, ranging from $\gtrsim 200$ pc where the shock encounters the first neighboring minihalos, to $\lesssim 1$ kpc perpendicular to the overdensities in the y-z plane.

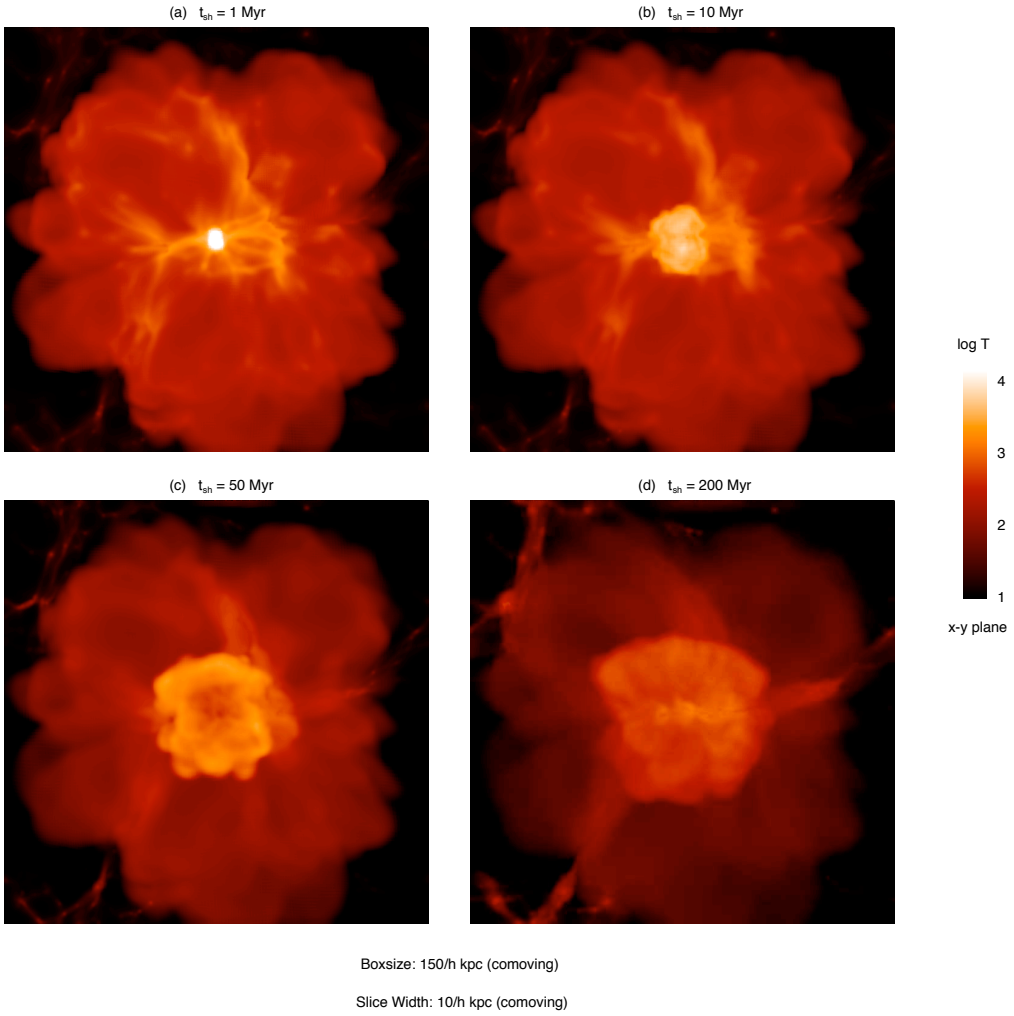

Figure 7.9: Temperature averaged along the line of sight in a slice of $10/h$ kpc (comoving) around the x-y plane after 1, 10, 50, and 200 Myr. In all four panels, the H II region and SN shock are clearly distinguishable, with the former occupying almost the entire simulation box, while the latter is confined to the central regions. Panel (a): the SN remnant has just left the host halo, but temperatures in the interior are still well above 10^4 K. Panel (b): after 10 Myr, the asymmetry of the SN shock becomes visible, while most of the interior has cooled to well below 10^4 K. Panel (c): the further evolution of the shocked gas is governed by adiabatic expansion, and its morphology develops a 'finger-like' structure (see also Fig. 7.13). Panel (d): after 200 Myr, the shock velocity approaches the local sound speed and the SN remnant stalls. By this time the post-shock regions have cooled to roughly 10^3 K.

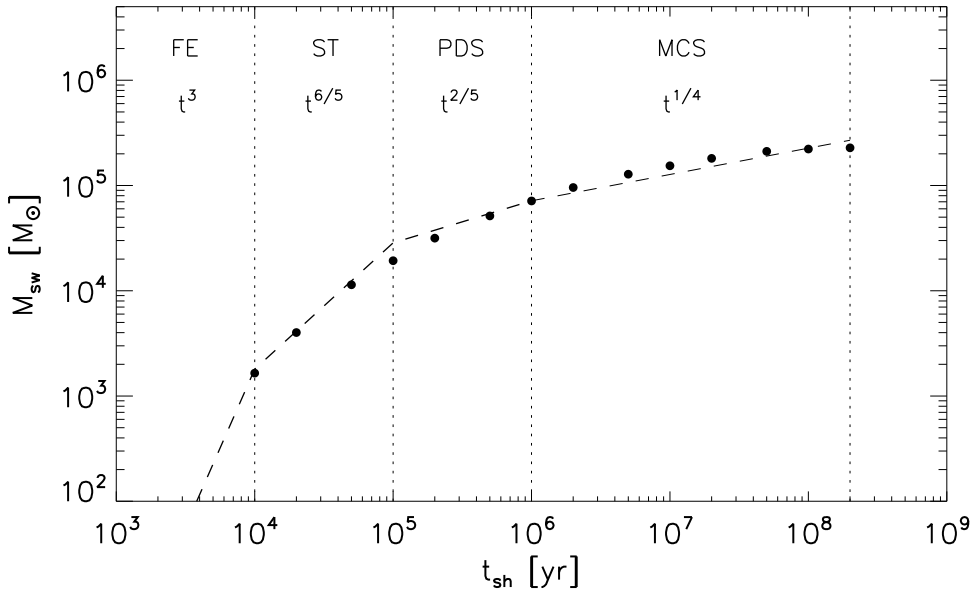

Figure 7.10: Swept-up gas mass as a function of time for the simulation (black dots) and the analytic model (dashed lines), where the latter is related to the shock radius by $M_{\rm sw} \propto \rho r_{\rm sh}^3$, except at very late times, when the shock structure becomes too complex for a simple analysis. For both we find a final swept-up mass of 2.5×10^5 M$_\odot$.

the delay. The most massive halo in our simulation, halo (a), experiences a delay of only 25 Myr, while halos (b) and (c) are less dense at the time of photoheating and experience delays in excess of 80 Myr. This is roughly consistent with the results of Ahn & Shapiro (2007) who argue that radiative feedback on neighboring minihalos strongly depends on their evolutionary stage (Mesinger et al., 2006; Susa & Umemura, 2006). For more quantitative results, one must perform self-consistent radiation-hydrodynamics simulations that include the effects of photodissociating radiation (Yoshida et al., 2007a).

Due to the inaccuracies mentioned above, we cannot draw robust conclusions on the subsequent mode of primordial star formation, i.e., Pop III or Pop II.5, but we anticipate this to be a function of the state of the collapse and the ionizing flux (Greif & Bromm, 2006; Jappsen et al., 2007; Johnson & Bromm, 2006; Mackey et al., 2003).

7.3.2 Shock-driven Collapse

In contrast to feedback by ionizing radiation, we find that in our case the shock of the SN remnant acts to enhance halo collapse and promote star formation. This behavior is evident from Fig. 7.11, as halos (a) and (b) collapse about 15 Myr earlier with respect to the photoheating-only run. In both cases, the shock compresses the dense cores of each of the halos, which serves to enhance cooling and accretion. Although our resolution is too crude for quantitative conclusions, we find that the mechanical impact of the SN remnant mitigates the delay caused by photoheating and leads to a slightly increased star formation rate. This situation might be different for star-forming halos much closer to the SN explosion, where ram pressure stripping could be sufficient to dispel a large fraction of the gas. However, in the present simulation we find that most halos massive enough to form stars are at sufficient distances from the SN progenitor.

We note that we neglect the possible effects of photodissociating radiation emanating from the relic H II region, as it has been shown that recombination radiation can only produce a relatively weak photodissociating flux, which quickly dies away as the gas in the relic H II region recombines on timescales of the order of 1 Myr (Johnson & Bromm, 2007; Yoshida et al., 2007a). In addition, we are able to neglect the radiation generated by the supernova-shocked gas as a source of photodissociating radiation concerning neighboring minihalos, since the shock is only moving at velocities $\lesssim 20$ km s^{-1} when it arrives at the star-forming minihalos mentioned above. This implies a photodissociating flux of $J_{\rm LW} \lesssim 10^{-5}$, where

$J_{\rm LW}$ is in units of 10^{-21} ergs s^{-1} cm^{-2} Hz^{-1} sr^{-1} (Shull & Silk, 1979). Such a low level of flux will not have a substantial impact on the evolution of gas in collapsing minihalos, as it implies a timescale for photodissociation of H_2 of the order of 1 Gyr, much longer than the Hubble time at the redshifts we consider (Johnson & Bromm, 2006; Oh & Haiman, 2003). However, a minihalo within $\sim$ 200 pc of the SN explosion may be subject to a significant photodissociating flux, owing to the higher shock velocity at small distances.

7.3.3 Mixing Efficiency

An important question is whether a large fraction of metals can penetrate neighboring halos and efficiently mix with their cores, thus changing the mode of star formation from Pop III/Pop II.5 to Pop II. Although a detailed quantitative analysis would require dedicated high-resolution simulations that are unavailable here, we can nevertheless estimate the mixing efficiency by applying the criterion for the operation of Kelvin-Helmholtz (KH) instabilities (Cen & Riquelme, 2008; Murray et al., 1993; Wyithe & Cen, 2007):

$$\frac{gDr_{\rm vir}}{2\pi\dot{r}_{\rm sh}^2} \lesssim 1 \, , \tag{7.9}$$

where g is the gravitational acceleration at the virial radius, and D the density ratio of gas in the halo compared to the dense shell. For the nearest star-forming halo with about 5×10^5 M$_\odot$ and $r_{\rm vir} \simeq 100$ pc, we find $D \simeq 10$ and $\dot{r}_{\rm sh} \simeq 20$ km s^{-1}. The left-hand side of equation (7.9) is thus of order $1/10$, suggesting that the gas at the outer edge of the halo will be disrupted and mix with the enriched material in the dense shell, while the core of the halo will remain pristine and stable. This is consistent with the results of the detailed simulations conducted by Cen & Riquelme (2008), and by the same arguments we find that halos b and c remain pristine as well.

Once again, we note that massive minihalos very close to the SN progenitor might experience a different behavior, as expansion velocities are of the order 100 km s^{-1} when the SN remnant leaves the host halo (see Fig. 7.8). In such cases, the shock could disrupt the dense cores and trigger efficient mixing, leading to Pop II star formation once the gas recollapses.

7.3.4 Gravitational Fragmentation

Various authors have suggested that cooling in the dense shell might lead to gravitational fragmentation and trigger secondary star formation (Machida et al., 2005; Mackey et al., 2003; Salvaterra et al., 2004). However, due to the previous photoheating, the density of the surrounding medium is sufficiently lowered such that molecule formation is initially inefficient. Even though we do not fully resolve the radiative shock front, we thus find that the continuous adiabatic expansion of the dense shell renders molecular cooling unimportant and does not trigger gravitational instabilities (see Section 7.3.4 and Fig. 7.8). We note that the potential mixing of metals into the dense shell and the associated additional cooling might affect these results but postpone a more detailed discussion of this issue to future work.

Another scenario for secondary star formation is at the interface of colliding SN remnants. If such encounters take place in significantly overdense regions and occur relatively early in the evolution of individual SN remnants, densities might become high enough for gravitational fragmentation to occur.

7.4 Chemical Enrichment

We have previously argued that mixing of enriched material with gas in existing star-forming halos is generally inefficient (see Section 7.4.3), indicating that the dispersal of metals can only occur via expulsion into the IGM. In Section 7.3.5, we have shown that the bulk of the shock propagates into the voids surrounding the host halo, and we expect that chemical enrichment proceeds via the same channel (Pieri et al., 2007). This realization is crucial, as the detailed distribution of metals not only governs the transition to secondary star formation, but also the properties of the first galaxies, when the enriched material recollapses into larger potential wells.

We shed some light on these issues by determining the influence of metal cooling on the evolution of the SN remnant and by discussing the transport of metals into the IGM. Although our resolution is too crude for a detailed analysis, we can nevertheless discuss the mixing efficiency in a qualitative manner and draw some preliminary conclusions on the ultimate fate of the expelled metals.

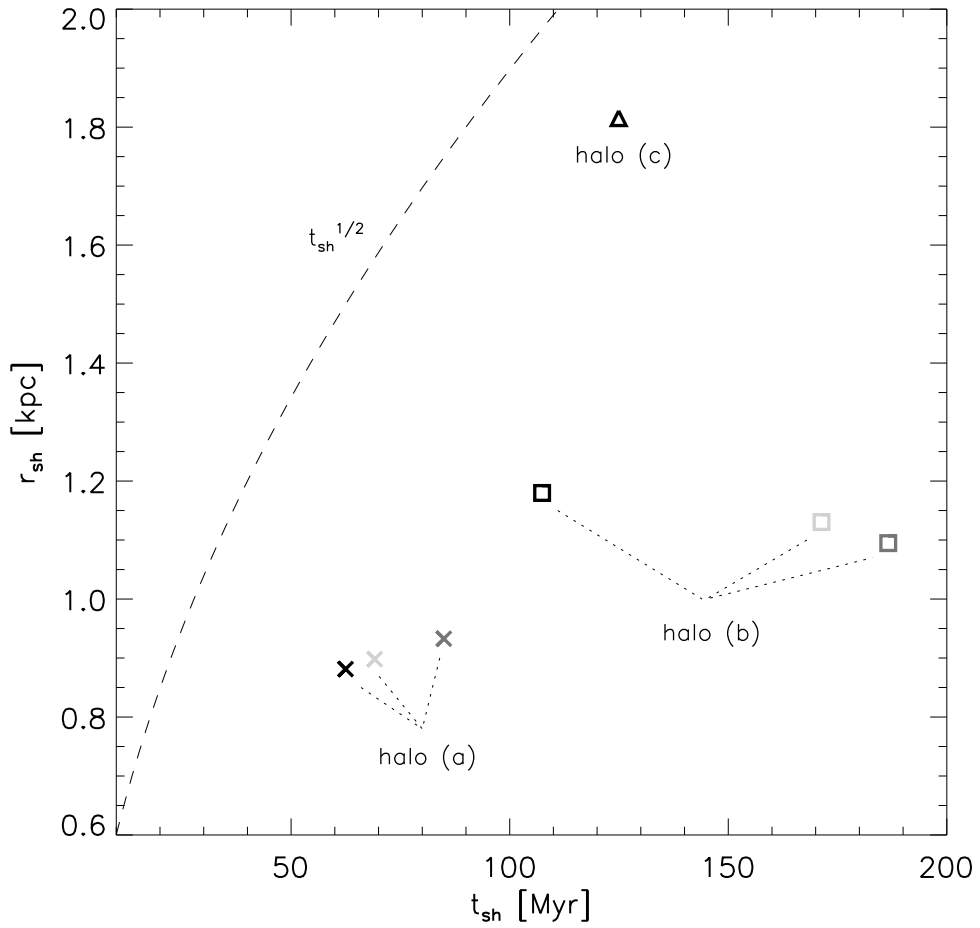

Figure 7.11: Collapse times and distances from the SN progenitor for all star-forming minihalos affected by the SN shock. The shades of the symbols indicate their affiliation, i.e. black, dark gray, and light gray symbols represent the no-feedback, photoheating-only, and main simulation runs, respectively, while the shapes of the symbols denote the individual halos. For orientation, the dashed line shows the mass-weighted mean shock radius at late times according to Fig. 7.7. In our case, photoheating significantly delays star formation, while the SN shock acts to compress gas in neighboring minihalos and slightly accelerates their collapse.

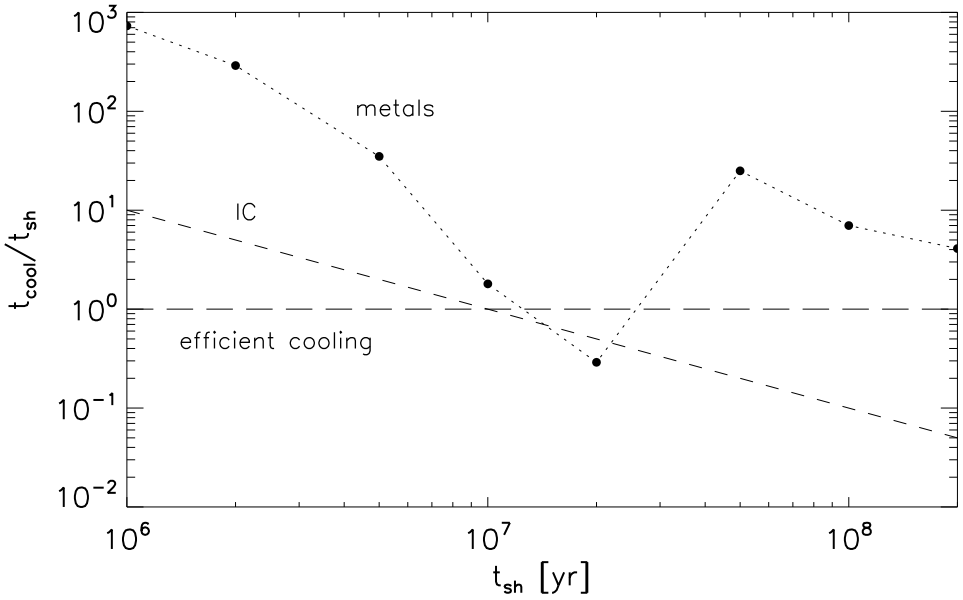

Figure 7.12: Cooling time vs. expansion time in the interior. The dotted line represents cooling by metal lines for a total metallicity of $Z = Z_{\odot}$, but consisting solely of C, O, Fe, and Si (in equal parts), while the dashed line represents IC cooling. The long-dashed line indicates when cooling becomes efficient, implying that metal cooling becomes momentarily important after 10 Myr, when the interior temperatures have dropped to 10^5 K and cooling rates peak. However, IC scattering becomes efficient at the same time and rapidly cools the enriched regions to below 10^4 K, where metal cooling rates drop by a few orders of magnitude. Consequently, the presence of metals does not effect the dynamical evolution of the SN remnant.

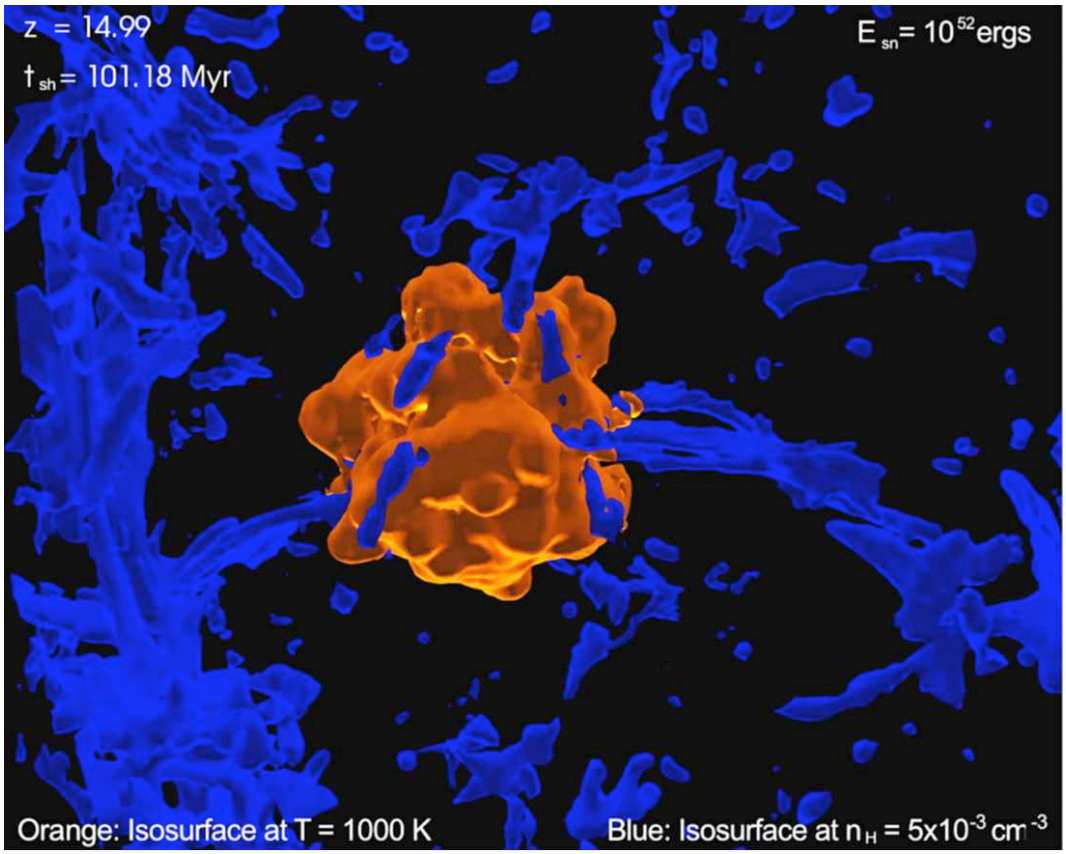

Figure 7.13: Three-dimensional view of the SN remnant at $z = 15$, or 100 Myr after the SN explosion, when it has reached a radius of 2 kpc. The finger-like morphology of the shock becomes visible as the SN remnant propagates at varying speeds in different directions, caused by an anisotropic density distribution.

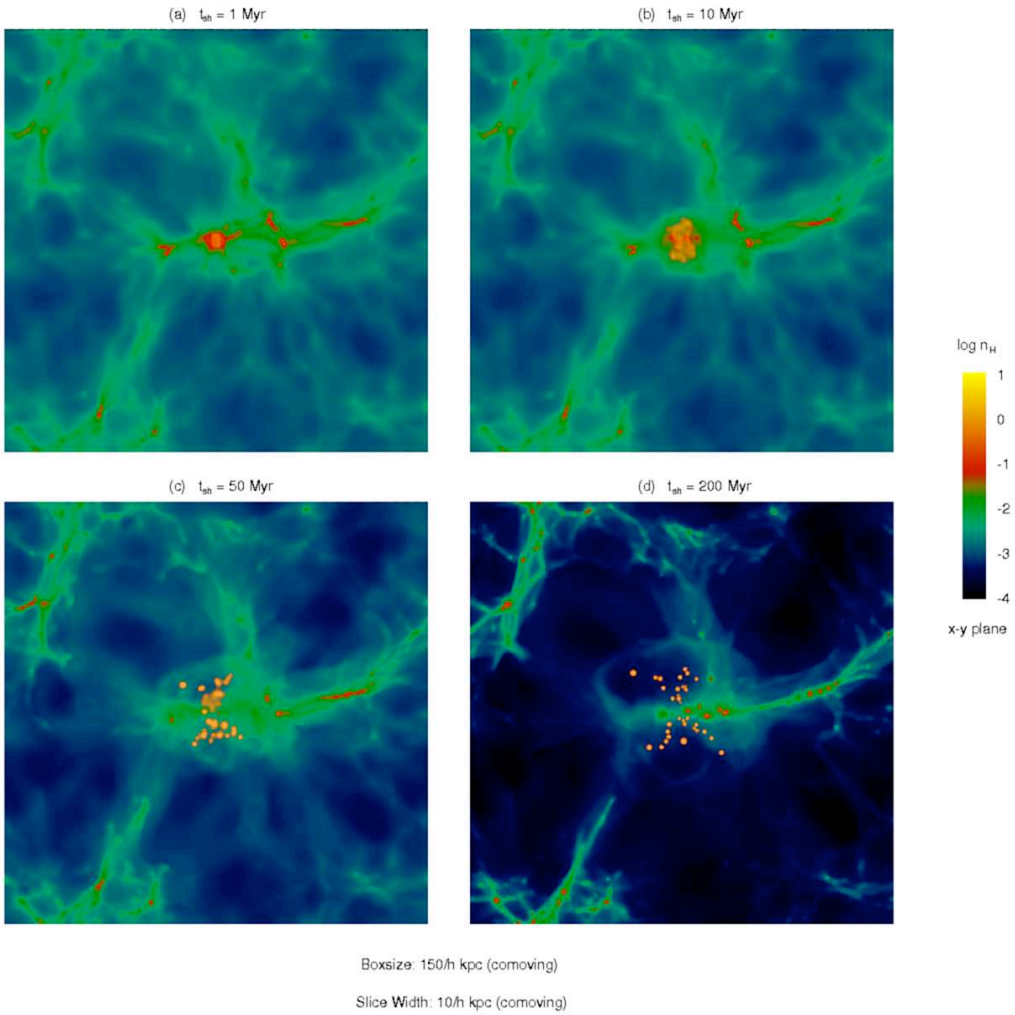

Figure 7.14: Hydrogen number density averaged along the line of sight in a slice of $10/h$ kpc (comoving) around the x-y plane, overlaid with the distribution of all metal particles (bright orange), after 1, 10, 50, and 200 Myr. The extent of each particle is set by the SPH smoothing length, while the apparent mixing within neighboring minihalos is a projection effect. Panel (a): after 1 Myr, the shock has left the host halo and enters the IGM, while the metals are still confined well within the virial radius. Panel (b): the contours of the shock have become visible as the SN remnant plows into the IGM 10 Myr after the SN explosion. The interior bubble expands adiabatically into the cavities created by the shock and begins to lose its spherical symmetry. Panel (c): after 50 Myr, the dense shell becomes distinguishable from the metal-enriched interior, which has become substantially asymmetric and expands into the voids around the y-z plane in the shape of an hourglass. Panel (d): when the SN remnant finally stalls after 200 Myr, the dense shell and the metal-enriched, interior bubble have reached their maximum extent, with the former providing a natural confinement around the interior.

7.4.1 Heat Conduction and Metal Cooling

During the first 10 Myr, the initial stellar ejecta expand adiabatically and apparently do not mix with the surrounding material (see Fig. 7.8). In reality, however, the high electron mean free path behind the shock leads to heat conduction and gas from the dense shell evaporates into the hot, interior bubble (Gull, 1973). This effect is not included in the simulation, as it would only marginally affect the dynamics of the SN remnant, but the onset of Rayleigh-Taylor (RT) and KH instabilities is predicted to efficiently mix the metals with primordial material evaporated from the dense shell, reducing the metallicity of the interior by a factor of a few to at most one order of magnitude (Madau et al., 2001). In the following, we assume that the overall metallicity has dropped by a factor of 5, to $Z = Z_\odot$, in the course of the first million years.

To determine the importance of metal cooling, we proceed analogously to Section 7.3.2 and compare the expansion and cooling timescales of the interior bubble. For this purpose we adopt the cooling rates provided in Maio et al. (2007) for gas in collisional ionization equilibrium enriched to $Z = Z_\odot$ but consisting solely of C, O, Fe, and Si (in equal parts). Although this does not represent the specific yield of a PISN or a hypernova, we here only intend to give an approximate argument and defer a more precise treatment to future work.

Assuming the time-dependent properties of the simulation, we find that metal cooling is only briefly important after 10 Myr (see Fig. 7.12), when the interior has adiabatically cooled to 10^5 K and metal cooling is most efficient. At the same time, however, IC scattering becomes important and temperatures quickly fall to 10^4 K, where cooling rates drop by a few orders of magnitude. Due to the low densities in the interior, the onset of fine structure cooling below 10^4 K also proves inefficient, and we conclude that even for initial metal yields as high as $y = 0.1$, metal cooling is unimportant for the entire dynamical evolution of the SN remnant. We emphasize that the presence of metals will become crucially important once the enriched gas has recollapsed into a sufficiently massive halo later on, thereby reaching high densities again.

7.4.2 Instabilities and Distribution of Metals

Due to inefficient cooling, the evolution of the metal-enriched, interior bubble is governed by adiabatic expansion and preferentially propagates into the cavities created by the shock (see Figs. 7.8 and 7.14). Once the shock leaves the host halo and becomes highly anisotropic, the

interior adopts the same behavior and expands into the voids surrounding the y-z plane in the shape of an hourglass, with a maximum extent similar to the final mass-weighted mean shock radius. This behavior is evident in Fig. 7.14, where we plot the hydrogen number density and distribution of metal particles at various times after the SN explosion. Furthermore, since the radius of each metal particle is determined by the smoothing length, we find that at late times the interior becomes substantially mixed with the initial stellar ejecta.

When the shock finally stalls, the interior bubble is in pressure equilibrium with its surroundings, but it stays confined within the dense shell. To investigate the importance of RT instabilities in this configuration, we estimate the mixing length $\lambda_{\rm rt}$ for large density contrasts between two media according to (Madau et al., 2001):

$$\lambda_{\rm rt} \simeq 2\pi g t_{\rm sh}^2 \,, \tag{7.10}$$

where g is the gravitational acceleration of the host halo. Estimating the distance of the dense shell from the host halo with the final mass-weighted mean shock radius, we find that mixing between the dense shell and the interior bubble takes place on scales $\lesssim 10$ pc in the course of a few times 10 Myr. In light of the substantial extent of the interior, we conclude that such mixing is generally inefficient and that much larger potential wells must be assembled to recollect and mix all components of the shocked gas. Specifically, turbulence arising in the virialization of the first galaxies could be an agent for this process (Wise & Abel, 2007a).

On the other hand, mixing could be important in the y-z plane, where, due to the progression of structure formation, material falls in along filaments toward the metal-enriched gas near the host halo. Since this mechanism will only affect a limited volume, while most metals are expelled into the voids (see Fig. 7.14), we again conclude that a fundamental transition in star formation from Pop III/Pop II.5 to Pop II requires the assembly of a DM halo with a sufficiently deep potential well.

To find the minimum mass necessary to recollect the hot and underdense post-shock gas residing at $T \sim 10^3$ K and $n_{\rm H} \sim 10^{-2.5}$ cm^{-3} (see Section 7.3.4), we estimate by means of the cosmological Jeans criterion that a DM halo of at least $M_{\rm vir} \gtrsim 10^8$ M$_\odot$ must be assembled. Assuming that in the course of its virialization the initial stellar ejecta mix with the entire swept-up mass, we find a final, average metallicity of $Z \simeq 10^{-2.5}$ Z$_\odot$. Although this value is well above $Z_{\rm crit}$, we emphasize that the final topology of metal enrichment could be highly inhomogeneous, with pockets of highly enriched material on the one hand, but regions with

a largely primordial composition on the other hand.

7.5 Summary and Conclusions

We have investigated the explosion of a 200 $M_\odot$ PISN in the high-redshift universe by means of three-dimensional, cosmological simulations, taking into account all necessary chemistry and cooling. Using a ray-tracing algorithm to determine the size and structure of the H II region around the progenitor star, we have followed the evolution of the SN remnant until it effectively dissolves into the IGM, and discussed its expansion and cooling properties in great physical detail. Specifically, we have found that a chronological sequence in its evolution, based on various physical mechanisms becoming dominant, allows the introduction of a simple analytic model summarizing its expansion properties. The SN remnant propagates for a Hubble time at $z \simeq 20$ to a final mass-weighted mean shock radius of 2.5 kpc, roughly half the size of the H II region, and in this process sweeps up a total gas mass of 2.5×10^5 $M_\odot$. We have found that its morphology becomes highly anisotropic due to encounters with filaments and neighboring minihalos in the y-z plane, but underdense voids perpendicular to the y-z plane. Based on the high explosion energy, the host halo is entirely evacuated, while in our case shock compression of neighboring minihalos partially offsets the delay in star formation due to negative feedback from photoionization heating. In contrast, we do not observe gravitational fragmentation triggered by efficient cooling behind the SN shock, which could in principle lead to secondary star formation. We have found that the metal-enriched, interior bubble expands adiabatically into the cavities created by the shock and preferentially propagates into the voids of the IGM with a maximum extent similar to the final mass-weighted mean shock radius. We have estimated that RT instabilities do not efficiently mix the dense shell with the interior, but that material falling in along filaments could mix with metal-enriched gas near the host halo. Finally, we have concluded that a DM halo of at least $M_{\rm vir} \gtrsim 10^8$ $M_\odot$ must be assembled to recollect and mix all components of the shocked gas.

Based on the simulation, we find that a single PISN can enrich the local IGM to a substantial degree. If energetic SNe were indeed a common fate for the first stars, they might have deposited metals on large scales before massive galaxies formed and outflows were suppressed by their increasingly deep potential wells. Hints on ubiquitous metal enrichment have recently been found in the low column density Lyα forest (Aguirre et al., 2005;

Songaila, 2001; Songaila & Cowie, 1996) and in dwarf spheroidal satellites of the Milky Way (Helmi et al., 2006), where the presence of a 'bedrock' metallicity was inferred. Based on these observations, various authors have argued that SNe occurring in the shallow potential wells of minihalos could substantially pre-enrich the universe (Daigne et al., 2006, 2004; Greif & Bromm, 2006; Matteucci & Calura, 2005; Yoshida et al., 2004). Although the frequency of PISNe is debated (Norman et al., 2004; Ricotti & Ostriker, 2004; Scannapieco et al., 2003; Venkatesan & Truran, 2003), we have found that the overall dynamics of the SN remnant and the distribution of metals are largely independent of the progenitor and are governed mainly by the explosion energy. Our simulations would therefore also approximately describe a hypernova explosion, where a rotating, massive star undergoes core collapse (Tominaga et al., 2007; Umeda & Nomoto, 2002). Such scenarios might better explain the peculiar yields found in extremely metal-poor stars in the Galactic halo (Christlieb et al., 2002; Frebel et al., 2005), assuming they formed out of gas enriched by a previous generation of stars (Iwamoto et al., 2005; Karlsson, 2006; Tumlinson, 2006; Tumlinson et al., 2004; Umeda & Nomoto, 2003, 2005). However, in light of the tentative identification of SN 2006gy as a PISN (Smith et al., 2007), we find that the plausibility of the PISN scenario is enhanced and that it provides a viable possibility for the ultimate fate of a very massive, metal-free star.

When and where do the first Pop II stars form? Based on the progression of structure formation, we expect that the first low-mass stars will form at the centers of the first galaxies, where primordial material streams in along filaments and mixes with the metal-enriched gas of the host halo. On the other hand, metals expelled into the voids are not so readily available, as the associated gas resides at too low densities and high temperatures. Because of this diversity, secondary star formation in the virialization of the first galaxies will likely be a highly complicated and multi-faceted process. To understand the relevant mechanisms in detail, one must perform numerical simulations that include metal cooling as well as an efficient model for their mixing. Furthermore, one must take into account the effects of multiple star-forming regions, including the expansion of additional H II regions and SN remnants. In future work, we hope to shed some light on these issues by performing detailed numerical simulations incorporating all the necessary physics and evolving them to sufficiently late times. Such investigations are key in arriving at detailed predictions for the properties of the first galaxies to be observed with *JWST*.

8

Chemical Mixing in Smoothed Particle Hydrodynamics Simulations

Understanding chemical enrichment and the dispersal of heavy elements in the wake of energetic SNe has become essential to a number of fields in astrophysics. The details of how enriched material mixes with ambient gas are not only relevant for the cooling and fragmentation properties of the interstellar medium (ISM), but also manifest themselves in the composition and dynamics of the resulting stars. As massive stars return metals to the ISM, mixing plays a key role in the overall matter cycle in galaxies. Tracing this loop back in time, one encounters the initial enrichment of the pristine, pure H/He gas at the end of the cosmic dark ages, when the very first stars ended their lives in violent SN explosions and expelled a significant fraction of their mass in metals (Greif et al., 2007; Heger et al., 2003; Iwamoto et al., 2005; Wise & Abel, 2008b). The resulting mixing in the early Universe has two aspects. The first concerns the enrichment inside the first galaxies, when the metals ejected by Pop III stars recollapsed into more massive halos that cooled by atomic hydrogen lines and vigorously mixed with pristine material in the presence of a highly turbulent medium (Greif et al., 2008; Wise & Abel, 2007a). The second relates to the enrichment of the IGM at redshifts $z > 5$ (Madau et al., 2001). The resulting metallicity distribution is a crucial ingredient in modeling the reionization history of the Universe (Furlanetto & Loeb, 2005; Yoshida et al., 2004) and in determining when cosmic star formation shifted from a predominantly high-mass, Pop III mode, to a more normal Pop II mode (Mackey et al., 2003; Schneider et al., 2002; Tornatore et al., 2007; Venkatesan, 2006).

8. CHEMICAL MIXING IN SMOOTHED PARTICLE HYDRODYNAMICS SIMULATIONS

Unfortunately, an accurate treatment of mixing, while simultaneously simulating the larger-scale environment, is presently not feasible, as the turbulent motions responsible for mixing typically cascade down to very small scales. A frequently encountered approach to this problem is to assume that the products of stellar nucleosynthesis are distributed within a fixed volume (e.g. Kobayashi et al., 2007; Norman et al., 2004; Scannapieco et al., 2005a; Tornatore et al., 2007). Significantly better results can be achieved in grid-based simulations by relating the mass flux between cells to the mixing efficiency, even though it remains unclear how much of this mixing is numerical instead of physical (e.g. Wise & Abel, 2008b). Such a direct approach is difficult to implement in SPH simulations, due to their Lagrangian nature, and instead chemical mixing has been modeled as a diffusion process (e.g. Martínez-Serrano et al., 2008). This is somewhat more accurate since the rms displacement of a fluid element in a homogeneously and isotropically driven turbulent velocity field can be described by the diffusion equation, with the diffusion coefficient set by the velocity dispersion and the typical shock travel distance (Klessen & Lin, 2003).

Prescriptions with a constant diffusion coefficient have been applied to models of the chemical evolution of the Milky Way (Karlsson, 2005; Karlsson & Gustafsson, 2005), galaxies in a cosmological context (Martínez-Serrano et al., 2008), and the environment of the first galaxies (Karlsson et al., 2008). In the present paper, we introduce an improved method that resolves chemical mixing in space and time based on the velocity dispersion within the SPH smoothing kernel. This yields results in agreement with more detailed investigations of mixing in the early phases of SN remnants, without having to explicitly resolve the hydrodynamic instabilities in the post-shock gas. In future work, we plan to use our method to investigate the long-term evolution of energetic SNe in a cosmological environment, particularly at high redshift when the Universe was enriched with the first metals. However, since our algorithm is quite generic, we hope that it will prove a valuable tool for any SPH simulation that attempts to follow the mixing of pollutants.

The structure of our work is as follows. In Section 8.2, we describe our model for diffusion and its numerical implementation in the cosmological simulation code GADGET (version 2) (Springel, 2005), followed by a series of idealized test simulations (Section 8.3). We then discuss the relation between the diffusion coefficient and the velocity dispersion and apply our prescription to the evolution of an idealized SN remnant (Section 8.4). Finally, in Section 8.5 we summarize our results and assess their implications. For consistency, all quoted distances are physical, unless noted otherwise.

8.1 Diffusion Algorithm

Diffusion plays an important role in a variety of astrophysical contexts. Among them are thermal conduction (e.g. Jubelgas et al., 2004), heat transfer in shear flows (e.g. Wadsley et al., 2008), the microscopic diffusion of particles, such as photons in stellar interiors, or the spatial correlation of individual fluid elements in a turbulent medium (Klessen & Lin, 2003). These processes are all described by the diffusion equation, commonly written in the form:

$$\frac{\mathrm{d}c}{\mathrm{d}t} = \frac{1}{\rho}\nabla \cdot (D\nabla\, c)\,, \tag{8.1}$$

where c is the concentration of a contaminant fluid per unit mass, D is the diffusion coefficient, which can be a function of space and time, and $\mathrm{d}/\mathrm{d}t$ the Lagrangian derivative, or the derivative following the motion. The diffusion coefficient has dimensions $\mathrm{M\,L^{-1}\,T^{-1}}$, suggesting that it can be represented as the product of the local density and some typical length-scale and velocity, such as the particle mean free path and velocity dispersion in a microscopic picture of diffusion.

8.1.1 Numerical Implementation

In the SPH formalism, the diffusion equation can be reduced to a discrete summation over all particles within the smoothing kernel:

$$\frac{\mathrm{d}c_i}{\mathrm{d}t} = \sum_j K_{ij}(c_i - c_j)\,, \tag{8.2}$$

with

$$K_{ij} = \frac{m_j}{\rho_i \rho_j}\frac{4D_iD_j}{(D_i + D_j)}\frac{\mathbf{r}_{ij}\cdot\nabla_i W_{ij}}{r_{ij}^2}\,, \tag{8.3}$$

where i and j denote the particle indices, m the mass, ρ the density, W_{ij} the kernel and $\mathbf{r}_{ij}$, r_{ij} the vector and absolute separations between particles i and j, respectively (for a more detailed derivation, see Monaghan et al., 2005). In the above equation, the arithmetic mean of the diffusion coefficient has been replaced by the harmonic mean, which has proven to be more robust. Furthermore, the second derivative has been replaced by a term involving the gradient and the particle separation, since a direct computation of the second derivative is problematic (Monaghan, 2005).

The solution to equation (8.2) can either be determined explicitly, which requires an additional constraint on the time-step to ensure numerical stability, or implicitly, which requires the solution of a coupled set of differential equations involving all 'active' particles (i.e. all SPH particles that are being updated on the current time-step). The explicit approach is extremely difficult to implement in a conservative fashion in an SPH code that allows individual particles to have different time-steps (e.g. GADGET-2). This is because in a code of this type, neighboring particles will sometimes have different time-steps. Consequently, the increase in concentration at particle i caused by diffusion from particle j will sometimes be computed at a different time from the corresponding decrease in concentration at particle j caused by diffusion to particle i. To ensure conservation, the increase and decrease must exactly balance, but in general they will not if i and j have different time-steps. One could, of course, avoid this problem by ensuring that all particles are synchronized before their concentrations are updated. However, the required synchronizations would have to occur very frequently, and so one would lose essentially all of the benefits gained by allowing the particles to have individual time-steps. A further undesirable feature of the explicit approach is the fact that the time-steps required to stably model the diffusion can become very small. Consideration of equation (8.1) shows that the required time-step scales with the spatial resolution – represented in an SPH code by the smoothing length h – as

$$\Delta t \propto h^2 \ . \tag{8.4}$$

In comparison, the standard Courant time-step scales only linearly with h.

An implicit approach to the solution of equation (8.2) avoids some of these problems, as it allows one to take larger time-steps without compromising numerical stability. However, this comes at a cost: the coupled differential equations representing the diffusion must be solved iteratively, and it is difficult to do this in a fashion that can be efficiently parallelized. In addition, one still has to deal with the synchronization problem discussed above.

In view of the disadvantages of both standard approaches, it is interesting to explore the viability of simpler, but more approximate approaches, such as the one presented in this paper. To obtain our approximation, we assume that the densities and concentrations of all active particles do not change significantly over a time interval Δt, allowing a direct

integration of equation (8.2):

$$c_i(t_0 + \Delta t) = c_i(t_0)e^{A\Delta t} + \frac{B}{A}(1 - e^{A\Delta t}) \,, \tag{8.5}$$

with

$$A = \sum_j K_{ij} \tag{8.6}$$

and

$$B = \sum_j K_{ij} c_j \,. \tag{8.7}$$

For large time-steps, the concentration of particle i thus tends to the average among its neighbors, while for small time-steps it remains close to its original concentration.

We implement this approach by performing the required operations at a global synchronization point in the density routine of GADGET-2. After the new densities and smoothing lengths have been computed, we update the coefficients K_{ij} and subsequently use equation (8.5) to determine the new concentrations of all active SPH particles. In a final step, we renormalize the obtained concentrations with a global factor such that the total concentration is conserved. Since the Courant condition does not allow for significant changes in density between time-steps, and diffusion generally progresses slower than the speed of sound, our implementation is quite generic and can be applied to a number of problems in astrophysics. We have found that the algorithm is remarkably stable even for very short diffusion timescales, since particles tend to equilibrate their concentrations and neighboring particles are generally active at the same time. The additional CPU consumption is minimal since we utilize the pre-existing neighbor search. By the same token, the algorithm is easy to implement in any SPH code and is not restricted to GADGET-2.

8.1.2 Test Problems

In this section we investigate the formal accuracy of the algorithm by performing a number of idealized test simulations. We initialize all simulations in a periodic, uniform density box with 1 million SPH particles and length and sound-crossing time set to unity, such that we may conveniently quote the elapsed time in units of the sound-crossing time. We adopt a hydrogen number density of $n_{\mathrm{H}} = 1\ \mathrm{cm}^{-3}$ and a mean molecular weight corresponding to that of a neutral, primordial gas. We place the particles on a grid with a very small

random displacement, and in the first test problem also consider a fully random distribution of particles, such that the density fluctuates considerably around the mean. This gives a better handle on the performance of our algorithm under more realistic circumstances. In all cases, we use the maximum diffusivity that is accurately modeled by our algorithm, determined by the Courant condition (see Sections 8.2.1 and 8.3.1):

$$D = \rho \, h \, c_\mathrm{s} \, , \tag{8.8}$$

where c_s is the sound speed and ρ and h are determined by the mean density $n_\mathrm{H} = 1 \ \mathrm{cm}^{-3}$, such that the diffusion coefficient becomes a fixed numerical value.

In the first test problem, we consider the propagation of an initial δ-distribution, to which the analytic solution is Green's function of the diffusion equation:

$$G\left(\mathbf{x}, \mathbf{x}', t\right) = \frac{1}{(2\pi\sigma^2)^{3/2}} \exp\left(\frac{-\left|\mathbf{x} - \mathbf{x}'\right|^2}{2\sigma^2}\right), \tag{8.9}$$

with variance

$$\sigma = \sqrt{2Dt} \, . \tag{8.10}$$

This configuration is reproduced by setting the concentration of the central particle to unity, and of all others to zero. In the left-hand column of Fig. 8.1, we compare the analytic solution to the simulation results at three different output times. Early on, diffusion progresses somewhat too rapidly, since the concentrations of neighboring particles differ substantially. In this case, equation (8.5) effectively breaks down, but the resulting deviations remain small and do not influence the long-term behavior, where all three curves become nearly indistinguishable. Note that the random distribution performs almost as well as the grid-based distribution, showing that the diffusivity remains unchanged even for high density fluctuations.

The second test problem consists of two individual δ-distributions initially separated by $\Delta x = 1/3$. The analytic solution can be obtained by a convolution of Green's function with the initial state of the system:

$$c\left(\mathbf{x}, t_0 + \Delta t\right) = \int G\left(\mathbf{x}, \mathbf{x}', t_0 + \Delta t\right) \, c\left(\mathbf{x}', t_0\right) \, d\mathbf{x}' \, , \tag{8.11}$$

such that the general solution is given by the superposition of two Gaussian distributions

centred at $x = 1/3$ and $2/3$. Similarly, the solution to the third test problem, consisting of a slab of uniform concentration between $x = 1/3$ and $2/3$, is given by

$$c(\mathbf{x}, t) = \frac{1}{2} \operatorname{erfc}\left(\frac{1/3 - x}{\sqrt{4Dt}}\right) \tag{8.12}$$

for $x \leq 1/2$ and

$$c(\mathbf{x}, t) = \frac{1}{2} \operatorname{erfc}\left(\frac{x - 2/3}{\sqrt{4Dt}}\right) \tag{8.13}$$

for $x > 1/2$. In the middle and right-hand columns of Fig. 8.1, we compare the simulation results to the analytic solution, showing that there are only minor deviations at early times, similar in nature to those found in the first test problem. A slice through all three boxes (Fig. 8.2) shows the solution in two dimensions.

Finally, in a series of resolution studies performed with 32^3, 64^3 and 128^3 particles, we have found no correlation between the resolution and the deviation from the analytic solution. In fact, in all cases, the deviations were comparable to those found in previous test problems. Considering its formal simplicity, the algorithm thus performs remarkably well. Although the diffusivity is initially slightly over-predicted for cases in which the diffusion time is shorter than the sound-crossing time, we nevertheless find a correct long-term behavior.

8.2 Application to Chemical Mixing

In the previous section, we introduced an SPH formalism for diffusion that can be applied to most problems that are governed by a diffusion equation. In this section, we focus on an application that is particularly relevant to astrophysics: the mixing of chemical elements.

8.2.1 Chemical Mixing as Turbulent Diffusion

As a first step towards a model for chemical mixing, one must find a connection between the diffusivity of a pollutant and the local physical conditions. Klessen & Lin (2003) have provided this link by showing that the probability of finding a parcel of gas at a given location in a homogeneously and isotropically driven turbulent velocity field can be described by the diffusion equation, with the diffusion coefficient set by the velocity dispersion $\tilde{v}$ and the

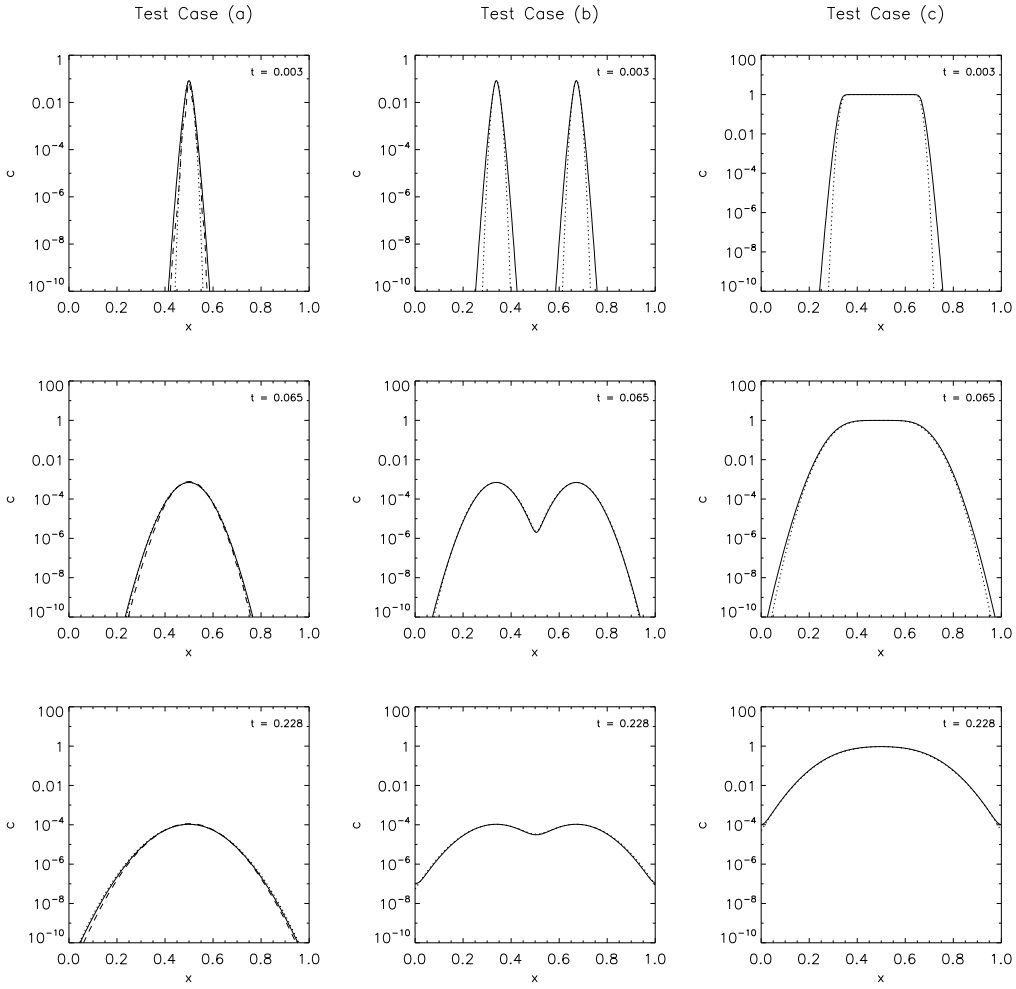

Figure 8.1: The propagation of a single δ-distribution (left-hand column), two δ-distributions (middle column) and a slab of uniform concentration (right-hand column) into an otherwise pristine medium, shown for a grid-based particle distribution (solid lines) and a random particle distribution (dashed line), compared to the analytic solution (dotted lines). The temporal evolution is depicted from top to bottom and quoted in units of the sound-crossing time. In all three cases, the simulations reproduce the analytic solution, except at early times when the underlying assumption of constant concentration for neighboring particles is not well justified (see Section 8.2). However, as is evident from the bottom two rows, this does not affect the long-term behavior.

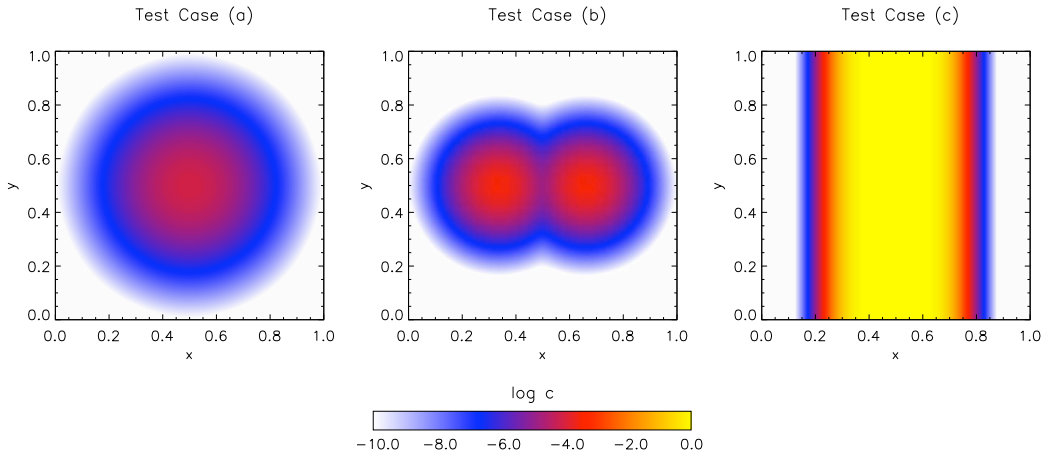

Figure 8.2: The propagation of a single δ-distribution (left-hand column), two δ-distributions (middle column) and a slab of uniform concentration (right-hand column) into an otherwise pristine medium, shown at a representative output time.

turbulent driving length $\tilde{l}$:

$$D = 2\,\rho\,\tilde{v}\,\tilde{l}\,. \tag{8.14}$$

This corresponds to the classical mixing-length approach extended into the supersonic regime. If one replaces the probability distribution with the concentration of a pollutant, this formalism can be reinterpreted to describe chemical mixing. The sole remaining task is then to provide the parameters $\tilde{v}$ and $\tilde{l}$ to the diffusion algorithm, such that the diffusion coefficient can become a function of space and time.

To obtain the necessary parameters, we determine the rms velocity dispersion for particle i within its smoothing length:

$$\tilde{v}_i^2 = \frac{1}{N_{\mathrm{ngb}}} \sum_j \left|\mathbf{v}_i - \mathbf{v}_j\right|^2 \,, \tag{8.15}$$

where N_{ngb} is the number of neighbors and $\mathbf{v}_i$ and $\mathbf{v}_j$ are the bulk velocities of particles i and j. Finally, we equate the turbulent driving length with the smoothing length, since this is the minimum scale where turbulent motions can be resolved. This then yields for the diffusion coefficient:

$$D_i = 2\,\rho_i\,\tilde{v}_i\,h_i\,. \tag{8.16}$$

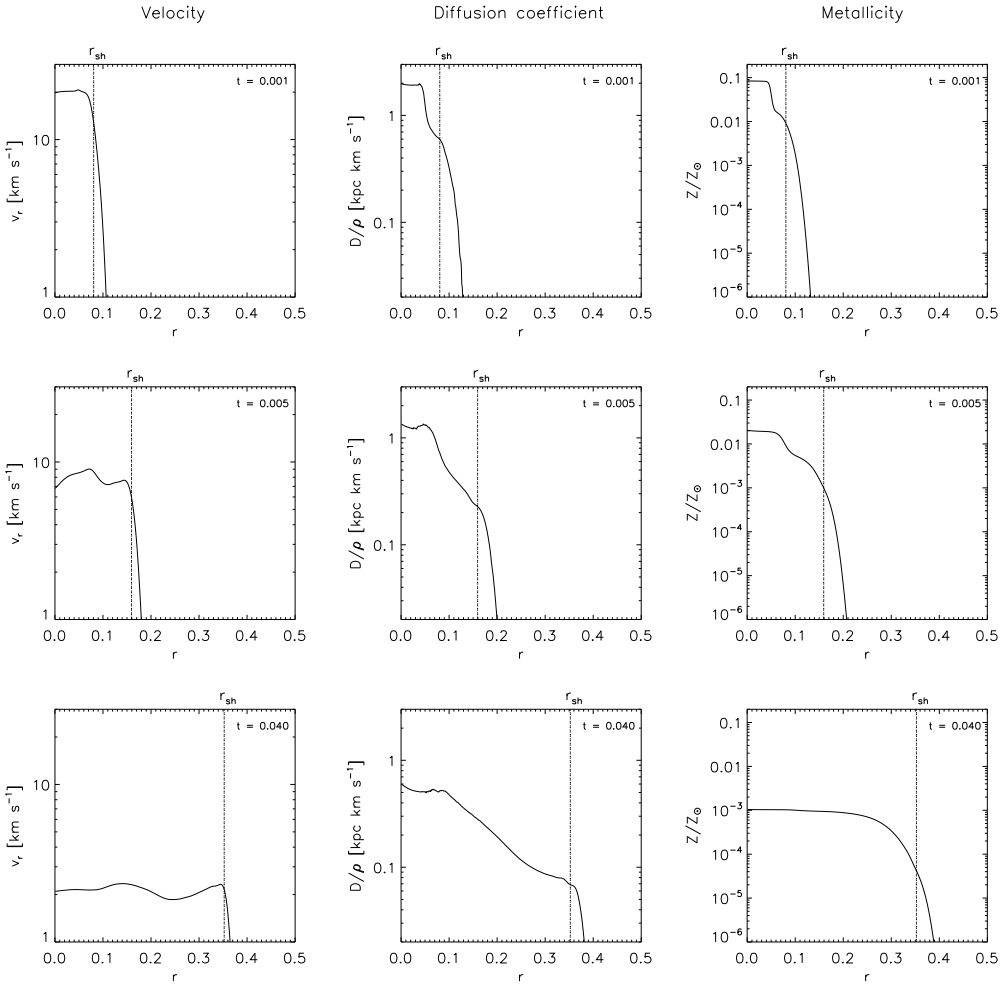

Figure 8.3: The radial velocity (left-hand column), diffusion coefficient (middle column) and metallicity (right-hand column) as a function of distance from the SN progenitor, with the position of the forward shock denoted by the dotted line. The temporal evolution is depicted from top to bottom and quoted in units of the sound-crossing time. The high velocity dispersion near the main shock leads to an elevated diffusion coefficient and thus very efficient chemical mixing. Due to the dependence on velocity dispersion, mixing by hydrodynamic instabilities in the remnant is implicitly accounted for.

As desired, the efficiency of chemical mixing is now governed entirely by local physical quantities.

An important underlying assumption of this method is that the velocity field on subresolution scales corresponds to a homogeneously and isotropically driven turbulent medium, i.e. only the magnitude of the velocity dispersion and not its three-dimensional structure is taken into account. A further implicit assumption is that the mixing efficiency on subresolution scales is set by the corresponding value on the scale of the smoothing kernel. For these reasons our method yields an upper limit to the amount of mixing that can occur, and does not capture the details of a real turbulent cascade. However, since turbulent motions on scales larger than the smoothing length are explicitly resolved, our approach should suffice for most practical purposes.

We implement the above steps in our algorithm by performing a previous neighbor search that finds the velocity dispersion for all active SPH particles, which is then used in equation (8.3) to obtain the coefficients K_{ij}. This closes the required set of equations, and in the following subsection we use our complete model to investigate the mixing of metals in a SN remnant.

8.2.2 Mixing in Supernova Remnants

The mixing of gas in the post-shock regions of SN remnants has previously been investigated, leading to the consensus view that secondary shocks trigger Rayleigh-Taylor and Kelvin-Helmholtz instabilities that mix pristine gas from the dense shell with already enriched material (e.g. Chevalier et al., 1992; Gull, 1973). The aim of our algorithm is to capture this mixing without having to explicity resolve the corresponding hydrodynamic instabilities, which cannot easily be modeled using SPH (e.g. Agertz et al., 2007; Price, 2008). To verify its ability to do this, we perform a test simulation of an idealized SN explosion with the same setup as in Section 8.2.2. We distribute an explosion energy of 10^{51} erg as thermal energy to the $N_{\rm ngb}$ nearest neighbors around the centre of the box, which results in the formation of a shock and reproduces the ideal Sedov-Taylor solution of a blast wave in a uniform medium (see Greif et al., 2007). Furthermore, we set the initial metallicities of the central particles to unity.

In Fig. 8.3, we show the radial velocity, diffusion coefficient and metallicity as a function of distance from the SN progenitor at three different output times. The high velocity disper-

sion near the forward shock is responsible for the elevated diffusion coefficient, which leads to efficient chemical mixing of pristine gas passing through the shock. As is evident from Fig. 8.3, most parcels of gas behind the shock have nearly equilibrated their metallicities. Our algorithm thus implicitly accounts for mixing due to the dependence of the diffusion coefficient on the local velocity dispersion. Intriguingly, we also find metals ahead of the forward shock. Although this initially seems unphysical, it should be remembered that our algorithm aims to capture mixing caused by unresolved instabilities, and that in a real SN remnant, it is these instabilities that would transport metals ahead of the mean position of the shock. Even further out, the degree of enrichment drops roughly exponentially, since the velocity dispersion, and hence the diffusion coefficient, tend to zero.

A second mechanism becomes important once the SN remnant has stalled: gas from the dense shell ahead of the shock falls back on to the remnant, becomes Rayleigh-Taylor unstable, and vigorously mixes with the interior gas. This is especially effective in a realistic cosmological setting, where the central potential well deepens as the SN remnant expands (Greif et al., 2007; Wise & Abel, 2008b). However, we postpone a detailed treatment of this issue to dedicated high-resolution simulations in future work.

8.3 Summary and Conclusions

We have introduced a simple and efficient algorithm for diffusion in SPH simulations and investigated its accuracy with a number of idealized test cases. Although the algorithm is quite generic and can be applied to most problems involving diffusion, we have here focused on a model for the dispersal of enriched material in supernova explosions. Adopting the mixing length approach discussed by Klessen & Lin (2003), we link the diffusivity of the pollutant to the local physical conditions and can thus describe the space- and time-dependent mixing process. We have applied our prescription to an idealized SN explosion and found that we can properly describe the mixing process without having to explicitly resolve the hydrodynamic instabilities in the post-shock gas. Instead, this process is implicitly governed by the dependence on the local velocity dispersion. Our method can thus be used in any SPH simulation that attempts to follow the mixing of a pollutant but lacks the necessary resolution on small scales. This will be relevant, in particular, for simulations that aim at simultaneously representing the large-scale environment of the SN explosion and the fine-grained mixing. A crucial assumption of our model is that resolved motions cascade down to subresolution

scales which then homogeneously mix the gas. For this reason our method yields an upper limit to the mixing efficiency and the resulting degree of homogeneity, and cannot capture the details of a real turbulent cascade. However, since turbulent motions on scales larger than the smoothing length are explicitly resolved, this approximation should generally be valid.

Our new algorithm ties in well with the current generation of radiation-hydrodynamical simulations of star formation, both at high redshifts and in the local Universe. The ultimate goal is to describe the interrelated cycle of gas fragmentation and stellar feedback. To achieve adequate realism, radiative effects have to be considered together with the mechanical and chemical feedback due to SN explosions. The methodology developed here allows us to include chemical feedback, suitable even for extremely large simulations. We will report on specific applications in future studies.

8. CHEMICAL MIXING IN SMOOTHED PARTICLE HYDRODYNAMICS SIMULATIONS

9

Outlook

Understanding the formation of the first galaxies marks the frontier of high-redshift structure formation. It is crucial to predict their properties in order to develop the optimal search and survey strategies for upcoming instruments such as the SKA or *JWST*. Whereas *ab-initio* simulations of the very first stars can be carried out from first principles, and with virtually no free parameters, one faces a much more daunting challenge with the first galaxies. Now, the previous history of star formation has to be considered, leading to enhanced complexity in the assembly of the first galaxies. One by one, all the complex astrophysical processes that play a role in more recent galaxy formation appear back on the scene. Among them are external radiation fields, comprising UV and X-ray photons, as well as local radiative feedback that may alter the star formation process on small scales. Perhaps the most important issue, though, is metal enrichment in the wake of the first SN explosions, which fundamentally alters the cooling and fragmentation properties of the gas. Together with the onset of turbulence, chemical mixing might be highly efficient and could lead to the formation of the first low-mass stars and stellar clusters.

In future work, we plan to address a number of outstanding issues. Among them are the chemical enrichment of the first galaxies and the influence of metals on neighboring star formation sites. Another crucial question is whether the transition from Pop III to Pop II stars is governed by atomic fine-structure or dust cooling. Theoretical work has indicated that molecular hydrogen dominates over metal-line cooling at low densities (Jappsen et al., 2009a,b), and that fragment masses below $\sim 1\ \mathrm{M}_{\odot}$ can only be attained via dust cooling at high densities (Clark et al., 2008; Omukai et al., 2005). On the other hand, observational studies seem to be in favor of the fine-structure based model (Frebel et al., 2007), even though

existing samples of extremely metal-poor stars in the Milky Way are statistically questionable (Beers & Christlieb, 2005; Christlieb et al., 2002; Frebel et al., 2005). Moreover, these studies assume that their abundances are related to primordial star formation – a connection that is still debated (Lucatello et al., 2005). In light of these uncertainties, it is essential to push numerical simulation to ever lower redshifts and include additional physics in the form of radiative feedback, metal dispersal, chemisty and cooling, and the effects of magnetic fields. We are confident that a great deal of interesting discoveries, both theoretical and observational, await us in the rapidly growing field of early galaxy formation.

Acknowledgements

First of all, I would like to thank my advisors Ralf Klessen and Volker Bromm for their dedicated support throughout these last three years. Without their help none of my work would have been possible. I am also indepted to my co-advisor Matthias Bartelmann for assisting in various administrative issues, taking part in my doctoral committee, and providing essential help in cosmology. I am grateful to my collaborators Jarrett Johnson, Simon Glover and Paul Clark for their input and work concerning numerous joint projects, many of which are part of this thesis.

Outside of physics, I would like to thank my flatmates Roy, Susanne, Angelika, Jessica and Bianca for a wonderful stay in Heidelberg. I had lots of fun and will certainly miss the time we spent together! Finally, I am grateful to my family for supporting me throughout this time and providing emotional backup whenever I needed it.

Bibliography

Abel, T., Anninos, P., Zhang, Y., & Norman, M. L. 1997, New Astronomy, 2, 181

Abel, T., Bryan, G. L., & Norman, M. L. 2000, ApJ, 540, 39

—. 2002, Science, 295, 93

Abel, T., Wise, J. H., & Bryan, G. L. 2007, ApJ, 659, L87

Agertz, O., et al. 2007, MNRAS, 380, 963

Aguirre, A., Schaye, J., Hernquist, L., Kay, S., Springel, V., & Theuns, T. 2005, ApJ, 620, L13

Ahn, K., & Shapiro, P. R. 2007, MNRAS, 375, 881

Ahn, K., Shapiro, P. R., Iliev, I. T., Mellema, G., & Pen, U.-L. 2008, ApJ, accepted (arXiv:0807.2254)

Alvarez, M. A., Bromm, V., & Shapiro, P. R. 2006a, ApJ, 639, 621

Alvarez, M. A., Shapiro, P. R., Ahn, K., & Iliev, I. T. 2006b, ApJ, 644, L101

Alvarez, M. A., Wise, J. H., & Abel, T. 2008, ApJ, submitted (arXiv:0811.0820)

Ballesteros-Paredes, J., Klessen, R. S., Mac Low, M.-M., & Vazquez-Semadeni, E. 2007, in Protostars and Planets V, ed. B. Reipurth, D. Jewitt, & K. Keil, 63–80

Baraffe, I., Heger, A., & Woosley, S. E. 2001, ApJ, 550, 890

Barkana, R., & Loeb, A. 2001, Phys. Rep., 349, 125

—. 2007, Reports on Progress in Physics, 70, 627

Barton, E. J., Davé, R., Smith, J.-D. T., Papovich, C., Hernquist, L., & Springel, V. 2004, ApJ, 604, L1

Bate, M. R. 2009, MNRAS, 392, 1363

Beers, T. C., & Christlieb, N. 2005, ARA&A, 43, 531

Begelman, M. C., Volonteri, M., & Rees, M. J. 2006, MNRAS, 370, 289

Bertschinger, E. 1985, ApJ, 295, 1

Bondi, H. 1952, MNRAS, 112, 195

Bouwens, R. J., & Illingworth, G. D. 2006, Nature, 443, 189

Brinchmann, J., Pettini, M., & Charlot, S. 2008, MNRAS, 385, 769

Bromm, V., & Clarke, C. J. 2002, ApJ, 566, L1

Bromm, V., Coppi, P. S., & Larson, R. B. 1999, ApJ, 527, L5

—. 2002, ApJ, 564, 23

Bromm, V., Ferrara, A., Coppi, P. S., & Larson, R. B. 2001a, MNRAS, 328, 969

Bromm, V., Kudritzki, R. P., & Loeb, A. 2001b, ApJ, 552, 464

Bromm, V., & Larson, R. B. 2004, ARA&A, 42, 79

Bromm, V., & Loeb, A. 2003a, ApJ, 596, 34

—. 2003b, Nature, 425, 812

—. 2004, New Astronomy, 9, 353

—. 2006, ApJ, 642, 382

Bromm, V., Yoshida, N., & Hernquist, L. 2003, ApJ, 596, L135

Bromm, V., Yoshida, N., Hernquist, L., & McKee, C. F. 2009, Nature, 459, 49

Carr, B. J., Bond, J. R., & Arnett, W. D. 1984, ApJ, 277, 445

Cen, R., & Riquelme, M. A. 2008, ApJ, 674, 644

Chevalier, R. A., Blondin, J. M., & Emmering, R. T. 1992, ApJ, 392, 118

Chiappini, C., Ekström, S., Meynet, G., Maeder, A., & Hirschi, R. 2008, in American Institute of Physics Conference Series, Vol. 990, First Stars III, ed. B. W. O'Shea & A. Heger, 325–329

Choudhury, T. R., & Ferrara, A. 2007, MNRAS, 380, L6

Choudhury, T. R., Ferrara, A., & Gallerani, S. 2008, MNRAS, L15+

Christlieb, N., Bessell, M. S., Beers, T. C., Gustafsson, B., Korn, A., Barklem, P. S., Karlsson, T., Mizuno-Wiedner, M., & Rossi, S. 2002, Nature, 419, 904

Ciardi, B., & Ferrara, A. 2005, Space Science Reviews, 116, 625

Ciardi, B., Ferrara, A., Governato, F., & Jenkins, A. 2000, MNRAS, 314, 611

Ciardi, B., Scannapieco, E., Stoehr, F., Ferrara, A., Iliev, I. T., & Shapiro, P. R. 2006, MNRAS, 366, 689

Clark, P. C., Glover, S. C. O., & Klessen, R. S. 2008, ApJ, 672, 757

Couchman, H. M. P., & Rees, M. J. 1986, MNRAS, 221, 53

Daigne, F., Olive, K. A., Silk, J., Stoehr, F., & Vangioni, E. 2006, ApJ, 647, 773

Daigne, F., Olive, K. A., Vangioni-Flam, E., Silk, J., & Audouze, J. 2004, ApJ, 617, 693

Dale, J. E., Bonnell, I. A., Clarke, C. J., & Bate, M. R. 2005, MNRAS, 358, 291

Dale, J. E., Clark, P. C., & Bonnell, I. A. 2007, MNRAS, 377, 535

Dawson, S., Rhoads, J. E., Malhotra, S., Stern, D., Dey, A., Spinrad, H., Jannuzi, B. T., Wang, J., & Landes, E. 2004, ApJ, 617, 707

de Jong, T. 1972, A&A, 20, 263

Dekel, A., & Silk, J. 1986, ApJ, 303, 39

Dijkstra, M., Haiman, Z., Mesinger, A., & Wyithe, J. S. B. 2008, MNRAS, 391, 1961

Dijkstra, M., Haiman, Z., Rees, M. J., & Weinberg, D. H. 2004, ApJ, 601, 666

Dijkstra, M., Lidz, A., & Wyithe, J. S. B. 2007, MNRAS, 377, 1175

Dijkstra, M., & Wyithe, J. S. B. 2007, MNRAS, 379, 1589

Dodelson, S. 2003, Modern Cosmology. Academic Press, San Diego

Draine, B. T., & Bertoldi, F. 1996, ApJ, 468, 269

Dunn, G. H. 1968, Physical Review, 172, 1

Eisenstein, D. J., & Hut, P. 1998, ApJ, 498, 137

Fan, X., Carilli, C. L., & Keating, B. 2006a, ARA&A, 44, 415

Fan, X., et al. 2004, AJ, 128, 515

—. 2006b, AJ, 131, 1203

Ferrara, A. 1998, ApJ, 499, L17+

Ferrara, A., Pettini, M., & Shchekinov, Y. 2000, MNRAS, 319, 539

Field, G. B. 1959, ApJ, 129, 536

Fixsen, D. J., Cheng, E. S., Gales, J. M., Mather, J. C., Shafer, R. A., & Wright, E. L. 1996, ApJ, 473, 576

Frebel, A., Johnson, J. L., & Bromm, V. 2007, MNRAS, 380, L40

Frebel, A., et al. 2005, Nature, 434, 871

Fryer, C. L., Woosley, S. E., & Heger, A. 2001, ApJ, 550, 372

Fuller, T. M., & Couchman, H. M. P. 2000, ApJ, 544, 6

Furlanetto, S., & Oh, S. P. 2008, ApJ, 681, 1

Furlanetto, S. R. 2006, MNRAS, 371, 867

Furlanetto, S. R., & Loeb, A. 2003, ApJ, 588, 18

—. 2005, ApJ, 634, 1

Furlanetto, S. R., & Oh, S. P. 2006, ApJ, 652, 849

Furlanetto, S. R., Oh, S. P., & Briggs, F. H. 2006, Phys. Rep., 433, 181

Galli, D., & Palla, F. 1998, A&A, 335, 403

Gao, L., White, S. D. M., Jenkins, A., Frenk, C. S., & Springel, V. 2005, MNRAS, 363, 379

Gao, L., Yoshida, N., Abel, T., Frenk, C. S., Jenkins, A., & Springel, V. 2007, MNRAS, 378, 449

Gardner, J. P., et al. 2006, Space Science Reviews, 123, 485

Glover, S. 2005, Space Science Reviews, 117, 445

Glover, S. C. O., & Abel, T. 2008, MNRAS, 388, 1627

Glover, S. C. O., & Brand, P. W. J. L. 2001, MNRAS, 321, 385

—. 2003, MNRAS, 340, 210

Glover, S. C. O., & Jappsen, A.-K. 2007, ApJ, 666, 1

Gnedin, N. Y., Kravtsov, A. V., & Chen, H.-W. 2008, ApJ, 672, 765

Górski, K. M., Hivon, E., Banday, A. J., Wandelt, B. D., Hansen, F. K., Reinecke, M., & Bartelmann, M. 2005, ApJ, 622, 759

Greif, T. H., & Bromm, V. 2006, MNRAS, 373, 128

Greif, T. H., Johnson, J. L., Bromm, V., & Klessen, R. S. 2007, ApJ, 670, 1

Greif, T. H., Johnson, J. L., Klessen, R. S., & Bromm, V. 2008, MNRAS, 387, 1021

Gull, S. F. 1973, MNRAS, 161, 47

Haiman, Z. 2008, submitted (arXiv:0809.3926)

Haiman, Z., Abel, T., & Rees, M. J. 2000, ApJ, 534, 11

Haiman, Z., & Bryan, G. L. 2006, ApJ, 650, 7

Haiman, Z., & Loeb, A. 1997, ApJ, 483, 21

—. 2001, ApJ, 552, 459

Haiman, Z., Rees, M. J., & Loeb, A. 1996a, ApJ, 467, 522

—. 1997, ApJ, 476, 458

Haiman, Z., Thoul, A. A., & Loeb, A. 1996b, ApJ, 464, 523

Heger, A., Fryer, C. L., Woosley, S. E., Langer, N., & Hartmann, D. H. 2003, ApJ, 591, 288

Heger, A., & Woosley, S. E. 2002, ApJ, 567, 532

Heitmann, K., Lukić, Z., Habib, S., & Ricker, P. M. 2006, ApJ, 642, L85

Helmi, A., et al. 2006, ApJ, 651, L121

Ikeuchi, S. 1981, PASJ, 33, 211

Iliev, I. T., Scannapieco, E., Martel, H., & Shapiro, P. R. 2003, MNRAS, 341, 81

Iliev, I. T., Shapiro, P. R., Ferrara, A., & Martel, H. 2002, ApJ, 572, L123

Islam, R. R., Taylor, J. E., & Silk, J. 2003, MNRAS, 340, 647

Iwamoto, N., Umeda, H., Tominaga, N., Nomoto, K., & Maeda, K. 2005, Science, 309, 451

Iye, M., et al. 2006, Nature, 443, 186

Jang-Condell, H., & Hernquist, L. 2001, ApJ, 548, 68

Jappsen, A.-K., Glover, S. C. O., Klessen, R. S., & Mac Low, M.-M. 2007, ApJ, 660, 1332

Jappsen, A.-K., Klessen, R. S., Glover, S. C. O., & MacLow, M.-M. 2009a, ApJ, 696, 1065

Jappsen, A.-K., Low, M.-M. M., Glover, S. C. O., Klessen, R. S., & Kitsionas, S. 2009b, ApJ, 694, 1161

Jimenez, R., & Haiman, Z. 2006, Nature, 440, 501

Johnson, J. L., & Bromm, V. 2006, MNRAS, 366, 247

—. 2007, MNRAS, 374, 1557

Johnson, J. L., Greif, T. H., & Bromm, V. 2007, ApJ, 665, 85

—. 2008, MNRAS, 388, 26

Johnson, J. L., Greif, T. H., Bromm, V., Klessen, R. S., & Ippolito, J. 2009, MNRAS, submitted (arXiv:0902.3263)

Jubelgas, M., Springel, V., & Dolag, K. 2004, MNRAS, 351, 423

Kang, H., & Shapiro, P. R. 1992, ApJ, 386, 432

Karlsson, T. 2005, A&A, 439, 93

—. 2006, ApJ, 641, L41

Karlsson, T., & Gustafsson, B. 2005, A&A, 436, 879

Karlsson, T., Johnson, J. L., & Bromm, V. 2008, ApJ, 679, 6

Karpasb), Z., Anicich, V., & Huntress, W. T. 1979, J. Chem. Phys., 70, 2877

Kashlinsky, A., Arendt, R. G., Mather, J., & Moseley, S. H. 2005, Nature, 438, 45

Kawata, D., & Gibson, B. K. 2003, MNRAS, 340, 908

Kennicutt, Jr., R. C. 1983, ApJ, 272, 54

Kereš, D., Katz, N., Weinberg, D. H., & Davé, R. 2005, MNRAS, 363, 2

Kitayama, T., & Yoshida, N. 2005, ApJ, 630, 675

Kitayama, T., Yoshida, N., Susa, H., & Umemura, M. 2004, ApJ, 613, 631

Klessen, R. S., Heitsch, F., & Mac Low, M.-M. 2000, ApJ, 535, 887

Klessen, R. S., & Lin, D. N. 2003, Phys. Rev. E, 67, 046311

Kobayashi, C., Springel, V., & White, S. D. M. 2007, MNRAS, 376, 1465

Kogut, A., et al. 2006, New Astronomy Review, 50, 925

Komatsu, E., et al. 2009, ApJS, 180, 330

Koushiappas, S. M., Bullock, J. S., & Dekel, A. 2004, MNRAS, 354, 292

Krumholz, M. R., Klein, R. I., & McKee, C. F. 2007, ApJ, 656, 959

Krumholz, M. R., & McKee, C. F. 2005, ApJ, 630, 250

Kudritzki, R. P. 2002, ApJ, 577, 389

Kuhlen, M., & Madau, P. 2005, MNRAS, 363, 1069

Kuhlen, M., Madau, P., & Montgomery, R. 2006, ApJ, 637, L1

Larson, R. B. 1974, MNRAS, 169, 229

—. 2003, Reports of Progress in Physics, 66, 1651

Lazio, J. 2008, in American Institute of Physics Conference Series, Vol. 1035, The Evolution of Galaxies Through the Neutral Hydrogen Window, ed. R. Minchin & E. Momjian, 303–309

Li, Y., et al. 2007, ApJ, 665, 187

Lodato, G., & Natarajan, P. 2006, MNRAS, 371, 1813

Loeb, A., & Rybicki, G. B. 1999, ApJ, 524, 527

Lucatello, S., Tsangarides, S., Beers, T. C., Carretta, E., Gratton, R. G., & Ryan, S. G. 2005, ApJ, 625, 825

Mac Low, M.-M., & Ferrara, A. 1999, ApJ, 513, 142

Mac Low, M.-M., & Klessen, R. S. 2004, Reviews of Modern Physics, 76, 125

Mac Low, M.-M., Toraskar, J., Oishi, J. S., & Abel, T. 2007, ApJ, 668, 980

Machacek, M. E., Bryan, G. L., & Abel, T. 2001, ApJ, 548, 509

—. 2003, MNRAS, 338, 273

Machida, M. N., Tomisaka, K., Nakamura, F., & Fujimoto, M. Y. 2005, ApJ, 622, 39

Mackey, J., Bromm, V., & Hernquist, L. 2003, ApJ, 586, 1

Madau, P., Ferrara, A., & Rees, M. J. 2001, ApJ, 555, 92

Madau, P., Meiksin, A., & Rees, M. J. 1997, ApJ, 475, 429

Madau, P., & Rees, M. J. 2001, ApJ, 551, L27

Madau, P., Rees, M. J., Volonteri, M., Haardt, F., & Oh, S. P. 2004, ApJ, 604, 484

Maio, U., Dolag, K., Ciardi, B., & Tornatore, L. 2007, MNRAS, 379, 963

Makishima, K., et al. 2000, ApJ, 535, 632

Malhotra, S., & Rhoads, J. E. 2002, ApJ, 565, L71

Marigo, P., Girardi, L., Chiosi, C., & Wood, P. R. 2001, A&A, 371, 152

Martínez-Serrano, F. J., Serna, A., Domínguez-Tenreiro, R., & Mollá, M. 2008, MNRAS, 388, 39

Matteucci, F., & Calura, F. 2005, MNRAS, 360, 447

McGreer, I. D., & Bryan, G. L. 2008, ApJ, 685, 1

McKee, C. F., & Tan, J. C. 2008, ApJ, 681, 771

Mesinger, A., Bryan, G. L., & Haiman, Z. 2006, ApJ, 648, 835

Milosavljevic, M., Bromm, V., Couch, S. M., & Oh, S. P. 2008, ApJ, submitted (arXiv:0809.2404)

Milosavljević, M., Couch, S. M., & Bromm, V. 2009, ApJ, 696, L146

Miralda-Escudé, J. 2003, Science, 300, 1904

Mo, H. J., & White, S. D. M. 1996, MNRAS, 282, 347

Mobasher, B., et al. 2005, ApJ, 635, 832

Monaghan, J. J. 2005, Reports of Progress in Physics, 68, 1703

Monaghan, J. J., Huppert, H. E., & Worster, M. G. 2005, Journal of Computational Physics, 206, 684

Mori, M., Ferrara, A., & Madau, P. 2002, ApJ, 571, 40

Murray, S. D., White, S. D. M., Blondin, J. M., & Lin, D. N. C. 1993, ApJ, 407, 588

Nagakura, T., & Omukai, K. 2005, MNRAS, 364, 1378

Nagao, T., Motohara, K., Maiolino, R., Marconi, A., Taniguchi, Y., Aoki, K., Ajiki, M., & Shioya, Y. 2005, ApJ, 631, L5

Nagao, T., et al. 2007, A&A, 468, 877

—. 2008, ApJ, 680, 100

Nakamura, F., & Umemura, M. 2001, ApJ, 548, 19

Navarro, J. F., & White, S. D. M. 1994, MNRAS, 267, 401

Norman, M. L., O'Shea, B. W., & Paschos, P. 2004, ApJ, 601, L115

Oh, S. P. 2001, ApJ, 553, 499

Oh, S. P., & Haiman, Z. 2002, ApJ, 569, 558

—. 2003, MNRAS, 346, 456

Oh, S. P., Haiman, Z., & Rees, M. J. 2001, ApJ, 553, 73

Omukai, K. 2000, ApJ, 534, 809

Omukai, K., & Palla, F. 2003, ApJ, 589, 677

Omukai, K., Schneider, R., & Haiman, Z. 2008, ApJ, 686, 801

Omukai, K., Tsuribe, T., Schneider, R., & Ferrara, A. 2005, ApJ, 626, 627

Omukai, K., & Yoshii, Y. 2003, ApJ, 599, 746

O'Shea, B. W., Abel, T., Whalen, D., & Norman, M. L. 2005, ApJ, 628, L5

O'Shea, B. W., & Norman, M. L. 2007, ApJ, 654, 66

—. 2008, ApJ, 673, 14

Osterbrock, D., & Ferland, G. 2006, Astrophysics of Gaseous Nebulae and Active Galactic Nuclei. University Science Books, Sausalito

Ostriker, J. P., & Cowie, L. L. 1981, ApJ, 243, L127

Ostriker, J. P., & McKee, C. F. 1988, Reviews of Modern Physics, 60, 1

Pan, L., & Scalo, J. 2007, ApJ, 654, L29

Panagia, N. 2005, in Astrophysics and Space Science Library, Vol. 327, The Initial Mass

Function 50 Years Later, ed. E. Corbelli, F. Palla, & H. Zinnecker, 479–+

Pelupessy, F. I., Di Matteo, T., & Ciardi, B. 2007, ApJ, 665, 107

Pflamm-Altenburg, J., Weidner, C., & Kroupa, P. 2007, ApJ, 671, 1550

Pieri, M. M., Martel, H., & Grenon, C. 2007, ApJ, 658, 36

Press, W. H., & Schechter, P. 1974, ApJ, 187, 425

Price, D. J. 2008, Journal of Computational Physics, 227, 10040

Pringle, J. E. 1981, ARA&A, 19, 137

Pritchard, J. R., & Furlanetto, S. R. 2007, MNRAS, 376, 1680

Razoumov, A. O., & Sommer-Larsen, J. 2009, ApJ, submitted (arXiv:0903.2045)

Read, J. I., Pontzen, A. P., & Viel, M. 2006, MNRAS, 371, 885

Reed, D. S., Bower, R., Frenk, C. S., Jenkins, A., & Theuns, T. 2007, MNRAS, 374, 2

Rees, M. J. 1984, ARA&A, 22, 471

Refsdal, S. 1964, MNRAS, 128, 307

Regan, J. A., & Haehnelt, M. G. 2009, MNRAS, 393, 858

Ricotti, M., Gnedin, N. Y., & Shull, J. M. 2001, ApJ, 560, 580

—. 2002a, ApJ, 575, 33

—. 2002b, ApJ, 575, 49

—. 2008, ApJ, 685, 21

Ricotti, M., & Ostriker, J. P. 2004, MNRAS, 350, 539

Ripamonti, E. 2007, MNRAS, 376, 709

Rybicki, G. B., & Lightman, A. P. 1979, Radiative Processes in Astrophysics. Wiley-Interscience, New York

Sakuma, M., & Susa, H. 2009, ApJ, accepted (arXiv:0904.2355)

Salvaterra, R., Ferrara, A., & Schneider, R. 2004, New Astronomy, 10, 113

Sancisi, R., Fraternali, F., Oosterloo, T., & van der Hulst, J. M. 2008, A&AR, 15, 189

Santoro, F., & Shull, J. M. 2006, ApJ, 643, 26

Santos, M. R., Bromm, V., & Kamionkowski, M. 2002, MNRAS, 336, 1082

Scannapieco, C., Tissera, P. B., White, S. D. M., & Springel, V. 2005a, MNRAS, 364, 552

Scannapieco, E., Ferrara, A., & Madau, P. 2002, ApJ, 574, 590

Scannapieco, E., Madau, P., Woosley, S., Heger, A., & Ferrara, A. 2005b, ApJ, 633, 1031

Scannapieco, E., Schneider, R., & Ferrara, A. 2003, ApJ, 589, 35

Schaerer, D. 2002, A&A, 382, 28

—. 2003, A&A, 397, 527

Schaerer, D., & Vacca, W. D. 1998, ApJ, 497, 618

Schleicher, D. R. G., Banerjee, R., & Klessen, R. S. 2008, Phys. Rev. D, 78, 083005

Schleicher, D. R. G., Galli, D., Glover, S. C. O., Banerjee, R., Palla, F., Schneider, R., & Klessen, R. S. 2009, ApJ, submitted (arXiv:0904.3970)

Schneider, R., Ferrara, A., Natarajan, P., & Omukai, K. 2002, ApJ, 571, 30

Schneider, R., Ferrara, A., Salvaterra, R., Omukai, K., & Bromm, V. 2003, Nature, 422, 869

Schneider, R., Omukai, K., Inoue, A. K., & Ferrara, A. 2006, MNRAS, 369, 1437

Seiffert, M., et al. 2009, ApJ, submitted (arXiv:0901.0559)

Shapiro, P. R., Iliev, I. T., & Raga, A. C. 2004, MNRAS, 348, 753

Shapiro, P. R., & Kang, H. 1987, ApJ, 318, 32

Shapley, A. E., Steidel, C. C., Pettini, M., & Adelberger, K. L. 2003, ApJ, 588, 65

Sheth, R. K., & Tormen, G. 2002, MNRAS, 329, 61

Shu, F. H., Lizano, S., Galli, D., Cantó, J., & Laughlin, G. 2002, ApJ, 580, 969

Shull, J. M., & McKee, C. F. 1979, ApJ, 227, 131

Shull, J. M., & Silk, J. 1979, ApJ, 234, 427

Smith, B. D., & Sigurdsson, S. 2007, ApJ, 661, L5

Smith, N., et al. 2007, ApJ, 666, 1116

Songaila, A. 2001, ApJ, 561, L153

Songaila, A., & Cowie, L. L. 1996, AJ, 112, 335

Spaans, M., & Silk, J. 2006, ApJ, 652, 902

Spergel, D. N., et al. 2003, ApJS, 148, 175

Springel, V. 2005, MNRAS, 364, 1105

Springel, V., & Hernquist, L. 2002, MNRAS, 333, 649

Springel, V., Yoshida, N., & White, S. D. M. 2001, New Astronomy, 6, 79

Stark, D. P., Ellis, R. S., Richard, J., Kneib, J.-P., Smith, G. P., & Santos, M. R. 2007, ApJ, 663, 10

Susa, H., & Umemura, M. 2006, ApJ, 645, L93

Tan, J. C., & McKee, C. F. 2004, ApJ, 603, 383

Tan, J. C., & McKee, C. F. 2008, in American Institute of Physics Conference Series, Vol. 990, First Stars III, 47–62

Tegmark, M., Silk, J., Rees, M. J., Blanchard, A., Abel, T., & Palla, F. 1997, ApJ, 474, 1

Thacker, R. J., Scannapieco, E., & Davis, M. 2002, ApJ, 581, 836

Thoul, A. A., & Weinberg, D. H. 1996, ApJ, 465, 608

Tokutani, M., Yoshida, N., Oh, S. P., & Sugiyama, N. 2009, MNRAS, 395, 777

Tominaga, N., Umeda, H., & Nomoto, K. 2007, ApJ, 660, 516

Tormen, G., Bouchet, F. R., & White, S. D. M. 1997, MNRAS, 286, 865

Tornatore, L., Ferrara, A., & Schneider, R. 2007, MNRAS, 382, 945

Trenti, M., & Stiavelli, M. 2009, ApJ, 694, 879

Tsuribe, T., & Omukai, K. 2006, ApJ, 642, L61

Tumlinson, J. 2006, ApJ, 641, 1

Tumlinson, J., Giroux, M. L., & Shull, J. M. 2001, ApJ, 550, L1

Tumlinson, J., & Shull, J. M. 2000, ApJ, 528, L65

Tumlinson, J., Shull, J. M., & Venkatesan, A. 2003, ApJ, 584, 608

Tumlinson, J., Venkatesan, A., & Shull, J. M. 2004, ApJ, 612, 602

Uehara, H., & Inutsuka, S.-i. 2000, ApJ, 531, L91

Umeda, H., & Nomoto, K. 2002, ApJ, 565, 385

—. 2003, Nature, 422, 871

—. 2005, ApJ, 619, 427

Vázquez, G. A., Leitherer, C., Schaerer, D., Meynet, G., & Maeder, A. 2007, ApJ, 663, 995

Vázquez-Semadeni, E., Ballesteros-Paredes, J., & Klessen, R. S. 2003, ApJ, 585, L131

Venkatesan, A. 2006, ApJ, 641, L81

Venkatesan, A., & Truran, J. W. 2003, ApJ, 594, L1

Vierdayanti, K., Watarai, K.-y., & Mineshige, S. 2008, PASJ, 60, 653

Vishniac, E. T., Ostriker, J. P., & Bertschinger, E. 1985, ApJ, 291, 399

Volonteri, M., Haardt, F., & Madau, P. 2003, ApJ, 582, 559

Volonteri, M., & Rees, M. J. 2005, ApJ, 633, 624

—. 2006, ApJ, 650, 669

Wada, K., & Venkatesan, A. 2003, ApJ, 591, 38

Wadsley, J. W., Veeravalli, G., & Couchman, H. M. P. 2008, MNRAS, 387, 427

Wandel, A. 1985, ApJ, 294, 385

Weinmann, S. M., & Lilly, S. J. 2005, ApJ, 624, 526

Whalen, D., Abel, T., & Norman, M. L. 2004, ApJ, 610, 14

—. 2008a, ApJ, 679, 925

Whalen, D., van Veelen, B., O'Shea, B. W., & Norman, M. L. 2008b, ApJ, 682, 49

Windhorst, R. A., Cohen, S. H., Jansen, R. A., Conselice, C., & Yan, H. 2006, New Astronomy Review, 50, 113

Wise, J. H., & Abel, T. 2005, ApJ, 629, 615

—. 2007a, ApJ, 665, 899

—. 2007b, ApJ, 671, 1559

—. 2008a, ApJ, 684, 1

—. 2008b, ApJ, 685, 40

Wise, J. H., & Cen, R. 2009, ApJ, 693, 984

Wise, J. H., Turk, M. J., & Abel, T. 2008, ApJ, 682, 745

Wood, D. O. S., & Churchwell, E. 1989, ApJS, 69, 831

Woosley, S. E., & Heger, A. 2006, ApJ, 637, 914

Wouthuysen, S. A. 1952, AJ, 57, 31

Wyithe, J. S. B., & Cen, R. 2007, ApJ, 659, 890

Xie, T., Mundy, L. G., Vogel, S. N., & Hofner, P. 1996, ApJ, 473, L131+

Yoon, S.-C., & Langer, N. 2005, A&A, 443, 643

Yoshida, N. 2006, New Astronomy Review, 50, 19

Yoshida, N., Abel, T., Hernquist, L., & Sugiyama, N. 2003a, ApJ, 592, 645

Yoshida, N., Bromm, V., & Hernquist, L. 2004, ApJ, 605, 579

Yoshida, N., Oh, S. P., Kitayama, T., & Hernquist, L. 2007a, ApJ, 663, 687

Yoshida, N., Omukai, K., & Hernquist, L. 2007b, ApJ, 667, L117

—. 2008, Science, 321, 669

Yoshida, N., Omukai, K., Hernquist, L., & Abel, T. 2006, ApJ, 652, 6

Yoshida, N., Sokasian, A., Hernquist, L., & Springel, V. 2003b, ApJ, 598, 73